

Investigation of micromachining using a high repetition rate femtosecond fibre laser

A thesis submitted to the University of Manchester for the degree of
Doctor of Philosophy
in the Faculty of Engineering and Physical Sciences

2013

Joerg Schille

School of Chemical Engineering and Analytical Science

**THE UNIVERSITY OF MANCHESTER - APPROVED ELECTRONICALLY
GENERATED THESIS/DISSERTATION COVER-PAGE**

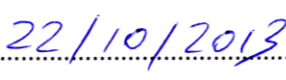
Electronic identifier: uk-ac-man-etd:10113

Date of electronic submission: 22/10/2013

The University of Manchester makes unrestricted examined electronic theses and dissertations freely available for download and reading online via Manchester eScholar at <http://www.manchester.ac.uk/escholar>.

I hereby declare that this print version of my thesis/dissertation is a TRUE and ACCURATE REPRESENTATION of the electronic version submitted to the University of Manchester's institutional repository, Manchester eScholar.

Author's signature 

Date signed 

List of contents

List of contents	3
List of figures	8
List of tables	18
List of symbols	20
List of publications	22
Abstract	23
Declaration by candidate	24
Copyright statement	25
Acknowledgements	26
1 Introduction	27
1.1 Motivation for research	27
1.2 Aims and objectives	28
1.3 ‘Split-site’ PhD project.....	30
1.4 Organisation of the thesis	31
2 A background into ultrashort pulse laser processing	33
2.1 Introduction	33
2.2 Ultrashort laser pulses in micro processing.....	33
2.3 Fundamentals of laser matter interaction in ultrashort pulse laser processing .	36
2.3.1 Introduction	36
2.3.2 Laser beam absorption	38
2.3.3 Energy transfer	40
2.3.4 Physical mechanism of laser ablation	43
2.3.5 Ablation regimes	47
2.4 Laser induced surface structures	50
2.4.1 LIPSS	50
2.4.2 Cone-like micro structures	51
2.5 High-PRF laser processing	54

2.5.1	Introduction	54
2.5.2	Heat accumulation.....	55
2.5.3	Particle shielding.....	57
2.5.4	Actual state, prospects and limitations in three-dimensional micro structuring using high-PRF ultrashort laser pulses	58
2.6	Summary	60
3	Materials and methodology	62
3.1	Materials	62
3.1.1	Investigated materials.....	62
3.1.2	Optical material properties	62
3.1.3	Thermo-physical material properties	69
3.2	Experimental setup	70
3.2.1	Micromachining work station	70
3.2.2	Laser system.....	73
3.2.3	Scan systems	77
3.3	Machining process.....	80
3.3.1	Laser processing regimes	80
3.3.2	Definition of raster-scan parameter.....	86
3.4	Measurement systems.....	88
3.4.1	Introduction	88
3.4.2	Measurements in X-Y-plane	88
3.4.3	Topography measurement.....	89
3.4.4	Roughness measurement.....	89
4	Ablation results and discussion.....	90
4.1	Introduction	90
4.2	Ablation threshold	91
4.2.1	Introduction.....	91
4.2.2	Results and discussion	93

4.3	Material removal	99
4.3.1	Determination of the material removal parameter and design of the material removal calculation model	99
4.3.2	Ablation rate	105
4.3.3	Process parameter optimisation.....	107
4.3.4	Volume ablation rate	114
4.4	Material removal efficiency	120
4.5	Surface roughness.....	122
4.6	Summary	125
5	Enhanced study of high-PRF laser ablation	126
5.1	Introduction	126
5.2	High speed camera imaging of material ablation	127
5.2.1	Camera trigger scheme.....	127
5.2.2	High speed camera photographs and discussion	128
5.3	Interplay between heat accumulation and particle shielding.....	131
5.4	Material removal in high-PRF laser ablation	134
5.4.1	Evaluation criterion.....	134
5.4.2	Cavity depth and material removal rate - results and discussion.....	135
5.5	Material ablation and repetition rate.....	140
5.6	Summary	142
6	Heat accumulation and energy balance – a phenomenological consideration	144
6.1	Introduction	144
6.2	Temperature calculation model	145
6.3	Temperature calculation under consideration of the remaining energy	152
6.3.1	Aluminium	152
6.3.2	Copper.....	154
6.3.3	Stainless steel	156

6.4	Temperature calculation considering thermal energy coupling	159
6.5	Energy balance	163
6.6	Summary	167
7	Laser-induced surface structures	168
7.1	Introduction	168
7.2	Ripple structures	169
7.3	Cone-like structures	171
7.4	Potential application of laser-induced surfaces structures	178
7.5	Summary	179
8	Machining examples	180
8.1	Introduction	180
8.2	Line-scan laser ablation	180
8.3	3D laser micro structuring	187
8.4	Micro mould fabrication	190
8.5	Technical limitations of the high-PRF laser technology in micromachining ..	192
8.6	Summary	195
9	Main conclusions and recommendations for future work	196
9.1	Conclusion of research work and summary of contribution to the body of knowledge	196
9.2	Recommendations for future work	200
	Annex 1: Determination of reflectivity and absorptivity of laser processed metal surfaces	202
	Annex 2: Ablation crater diameter used in ablation threshold calculations	204
	Annex 3: Ablation threshold calculation	206
	Annex 4: Ablation rate calculation	207
	Annex 5: Calculation program to calculate the accumulated irradiated laser fluence ..	209
	Annex 6: Cavity depth and ablation rate calculation	210
	Annex 7: Volume ablation rates	213

List of contents

Annex 8: Cavity depth depending on the repetition rate and percentage increase	214
Annex 9: Calculation of energy losses induced by convective heat transfer and heat radiation.....	215
Annex 10: Heat affected volume.....	217
Annex 11: Surface temperature calculated considering the remaining energy.....	218
Annex 12: Surface temperature calculated considering enhanced energy coupling.....	219
Annex 13: Energy balance calculation.....	220
References	222

Word count: 56,901

List of figures

Figure 2-1: Laser manufacturing processes distinguished depending on their characteristic pulse duration and intensity; the category <i>Laser micro processing</i> includes micro processing technologies, such as laser micro drilling, laser micro cutting, laser micro ablation etc.	34
Figure 2-2: <i>ISHIKAWA</i> -diagram indicating material removal process influencing parameters.	35
Figure 2-3: Overview of the mechanisms and effects occurring in laser matter interaction.....	37
Figure 2-4: Absorption of a laser beam travelling through an absorbing media taken from reference [25], the exponential decrease of the intensity follows <i>Beer's law</i> , the optical penetration depth is marked as l_a	39
Figure 2-5: Fundamental energy transfer mechanism in metals upon irradiation of a single femtosecond laser pulse, two characteristic time regimes are clearly recognisable – the non-thermal and the thermal regime.	41
Figure 2-6: Temperature profiles for the electron subsystem and the lattice, calculated by <i>FISCHER</i> [40] under the assumption that a single laser pulse of 180 fs pulse duration and 2.7 μ J pulse energy irradiates Iron.	42
Figure 2-7: Energy distribution and energy transport mechanism following laser irradiation as presented by <i>WELLERSHOF et al.</i> [41]; top: ballistic energy transport, centre: electron diffusion, bottom: thermal diffusion.	43
Figure 2-8: Snapshots of the ablated area representing the atomic distribution following femtosecond laser irradiation of Nickel, obtained using molecular dynamic simulation with respect to both different laser fluence and time [48].	45
Figure 2-9: Dynamic of material ablation for single pulse irradiation (1.8 J/cm ² , 80 fs, 820 nm) of Aluminium targets by time-resolved pump-probe shadowgraphs [59].....	46
Figure 2-10 left: Ablation depth per pulse versus fluence obtained on Copper [60]; right: in a separate view the transition area between the low-fluence and the high-fluence is extracted from the plot to highlight the conflict in the model appearing in the transition area with a fluence between 0.5 J/cm ² and 1.5 J/cm ²	47
Figure 2-11: Ballistic energy transport following femtosecond laser irradiation as presented in [64], skin depth and ballistic range can be related to the optical and effective penetration depth.....	49
Figure 2-12: SEM images of micro structures grown in Stainless steel under different irradiation conditions, captured at a tilt of view of 75°: 10 ⁴ pulses (left) and 10 ⁵ pulses	

(centre) irradiated at atmospheric air pressure, and 10^5 (right) pulses irradiated in air at a lower pressure of 10^{-3} Pa, (taken from reference [87]).	53
Figure 2-13 left: Glass temperature versus exposure, calculated at a radial position of $2 \mu\text{m}$ from the centre of the laser beam, taken from [95], right: heating of Aluminium foil by remaining energy left in the material under consideration that 10 % of the in-coupled 10 W laser power is converted to heat, modelled in [93].	55
Figure 2-14: Results achieved in high-repetition rate laser drilling of Stainless steel (left) and Copper (right) using constant pulse energy ($30 \mu\text{J}$) and wavelength (515 nm) but different repetition rates, taken from reference [2].	56
Figure 2-15: Beam transmission through a laser induced plasma/particle plume, obtained in pump-probe beam experiments on Aluminium (left), Copper and Steel (right) [96], in addition reduced laser beam transmission at 1 MHz repetition rate is indicated by red dotted lines.	57
Figure 2-16: Repetition rate versus number of laser pulses to drill through 0.5 mm thick Stainless steel, the pulse energy was $20 \mu\text{J}$ (left) and $30 \mu\text{J}$ (right), taken from reference [1].	58
Figure 2-17 left: Experimental and calculated ablation rates as a function of the repetition rate using an average laser power of 3 W; right: Ablation depths calculated for single pulse ablation (blue line) and multiple pulse irradiations, red dots represent ablation depths achieved with a total amount of irradiated laser fluence of 10 J/cm^2 , taken from reference [100].	59
Figure 2-18 left: Machining setup presented in reference [98] for fast laser beam deflection consisting of a fast rotating cylinder engraving system in combination with an acousto-optical deflector (AOD), right: pulse distance and ablation volumes as a function of the scan frequency, obtained using the presented “cross-scan” technique.	60
Figure 3-1 top: Schematic of the integrating sphere assembly used in reflectivity measurements on both virgin and laser-treated metal sheet surfaces.	63
Figure 3-2: Reflectivity calculated from photodiode signals recorded for pump laser irradiations of Stainless steel; StSt_0 to StSt_5 represent differently reflective surface characteristics as described in Table 3-1 .	64
Figure 3-3: Absorptivity and reflectivity versus temperature; top: literature data presented for Steel 35CD4 (left) [29] as well as Aluminium and Copper (right) [26], bottom: percentage increase of the absorptivity for near-infrared laser radiation versus the temperature, derived from the literature data given above.	67
Figure 3-4: Impact of the substrate temperature on ablation depth and roughness, presented for Stainless steel by <i>YAHNG et al.</i> [30].	68
Figure 3-5: Thermal conductivity versus temperature, presented for the main alloy constituents of the investigated metal sheets, taken from reference [29].	70

Figure 3-6: Schematic of the laser micromachining work station. 71

Figure 3-7: A view into the laboratory, micromachining work station (top), laser system / laser beam alignment / measurement equipment (bottom left), and processing chamber (bottom right). 72

Figure 3-8: Average laser output power and pulse energy versus pulse repetition rate. 73

Figure 3-9 left: Autocorrelation trace of a laser pulse with a pulse duration of 176 fs (sech^2); **centre:** beam caustic measurement of the focused laser beam using 56 mm f-theta objective, obtained utilising the *MicroSpotMonitor*, **right:** intensity distribution (top) and size (bottom) of the laser pulse in the focal plane. 74

Figure 3-10: Laser peak fluence available at laser source beam exit and impinging on the work piece surface versus single pulse energy..... 76

Figure 3-11 left: Operation scheme of laser beam deflection using galvanometer scan systems, taken from website of Scanlab AG; **right:** detail view of laser scan technology, taken from reference [113]. 77

Figure 3-12: Resonant scan technology: (a) schematic of the resonant scanner assembly consisting of a movable mirror driven by resonant scanner and a fixed reflection mirror; (b) lateral pulse spacing along a single line-scan; (c) lateral mismatch between two laser processed lines of one oscillation period; (d) constant lateral pulse spacing enclose the zero-crossing position of the scan mirror. 78

Figure 3-13: Machining results obtained by utilising different machining regimes; top left: single pulse laser ablation of a thin Copper layer on glass substrate; top right: repetitive line-scan laser ablation on Stainless steel; bottom left: 2.5D laser ablation on Stainless steel; and bottom right: step pyramid in Stainless steel obtained by 3D laser micro structuring. 81

Figure 3-14: Process chain illustrating distinct processing steps in 3D laser micro structuring. 82

Figure 3-15: Definition of acceleration and deceleration paths; **top left:** schematic of non-uniform overlapping pulses due to low scan speeds; **top right:** ablation profile obtained in the start area in top view (above) and cross section profile; **bottom:** empirical determination of the length of both acceleration path (left) and deceleration path (right) using digital microscope images. 83

Figure 3-16: Effective scan speed versus travelling distance obtained for various nominal scan speeds; the linear relation between the travelling distance, where the maximum scan speed was reached first time, and nominal scan speed is fitted by a red line. 84

Figure 3-17: Machining strategy developed to avoid non-uniform pulse overlap in high-PRF laser processing at the start and the end of laser processed lines; **left:** schematic of the process regime, acceleration and deceleration paths are added to the laser processing

path; right: determination of the Laser ON delay.	85
Figure 3-18: Effect of different machining strategies, illustrated by means of one processed layer of a 3D test structure; left: dark coloured areas indicate deep and inhomogeneous ablation zones due to spatially undefined laser pulse irradiations; right: well-defined laser ablation structure, obtained by using acceleration and deceleration paths.	85
Figure 3-19: Schematic of raster-scan regime.	86
Figure 3-20 (I): Schematic of overlapping laser pulses to visualise the total number of incident laser pulses n_i ; (II): schematic of laser pulses string together to visualise a scan pattern which is completely filled with single laser pulses; in this view a rectangular instead of a circular pulse shape is shown; the equations used to calculate the quantity of incident laser pulses in one distinct layer are presented.	87
Figure 4-1 left: Semi-logarithmical plot of irradiated laser fluence versus the outer radii (○) and the inner radii (●) of amorphous ring patterns, obtained on (111) silicon surface as well as radii of burn spots on polaroid films (■), induced by 20 ps pulses at 532 nm; taken from reference [121]; in the figure the laser fluence and the focal spot radius are referred to as E_0 and ρ	92
Figure 4-2: Semi-logarithmic plot of the squared ablation crater diameter D^2 versus the laser peak fluence H_0 , obtained for stationary irradiated bursts consisting of 50 individual laser pulses; the temporal distance between the pulses was 50 μ s (20 kHz); in this study the focal spot diameter was 26.2 μ m.	94
Figure 4-3: Laser fluence H_0 versus the squared ablation diameter D^2 to emphasize the impact of the repetition rate on the ablation diameter, stationary irradiated bursts consisting of 50 individual laser pulses have been irradiated on Aluminium (top), Copper (centre) and Stainless steel (bottom) metal sheets.	96
Figure 4-4: Impact of the temporal laser pulse-to-pulse distance on the ablation threshold in a standardised display format, the ablation threshold values are normalised to the 20 kHz value, measurement uncertainties are derived from the standard deviations of the averaged ablation crater diameters.	99
Figure 4-5 left: Digital microscopy photograph of cavities laser processed in Stainless steel for depth evaluation, three columns with constant processing parameter sets but increasing laser fluence from top to bottom were made; top right: schematic of the standardised laser processed cavity where l_x is the cavity length, l_y is the cavity width, and l_z is the cavity depth, bottom right: <i>µsurf Explorer</i> profilometer measurements showing the profile view of cavities obtained with increasing laser fluence.	100
Figure 4-6: Schematic view of ablation structures applying stationary (left) and overlapping (right) laser processing, in any case 5 laser pulses (P1 ... P5) irradiate the sample surface, different orders of magnitude in depth and width dimension are	

displayed by the black arrow.	101
Figure 4-7 left: Schematic of the ablation crater obtained following single pulse laser irradiation with cross section plane; right: cross section view of irradiated laser intensity profile (black line) and resulting ablation crater profile (red line), I_{th} and r_{th} denote the ablation threshold and the threshold radius, respectively.	102
Figure 4-8: Intensity distribution $I(r, z = 0)$ and $I(r = 0, z)$ calculated in both radial (left) and depth (centre) direction, Gaussian laser pulse irradiation on Stainless steel with 5 μJ pulse energy, a pulse duration of 176 fs (sech ²) and 15 μm focal spot radius, the optical penetration depth of 15 nm was taken into calculation; the ablation crater profile $d_z(r)$ shown on the right was obtained by taking the ablation threshold of 0.55 TW/cm^2 (0.11 J/cm^2) into account.	103
Figure 4-9: Ablation rate versus laser fluence obtained on Aluminium, Copper and Stainless steel by applying multi pulse processing with 25 scan passes, 5 μm lateral pulse spacing and 205 kHz repetition rate, measurement values and standard deviations are given in <i>Annex 4</i>	105
Figure 4-10: Graphical view of both accumulated laser energy input per area (top) and laser processed Copper surface (bottom); results were achieved considering a constant laser pulse energy of 3.88 μJ , focus spot diameter of 30 μm and peak fluence of $H_0 = 1.07 \text{ J}/\text{cm}^2$; the lateral pulse spacing was varied between 5 μm , 10 μm and 15 μm	107
Figure 4-11: Digital optical photographs of laser processed Aluminium surfaces, obtained with 10 scan passes; the laser peak fluence and the lateral pulse spacing were varied, ranging between 0.27 J/cm^2 and 1.88 J/cm^2 , and 2.5 μm and 20 μm , respectively.	108
Figure 4-12: Digital optical photographs of laser processed Copper surfaces, obtained with 10 scan passes; the laser peak fluence and the lateral pulse spacing were varied, ranging between 0.27 J/cm^2 and 1.88 J/cm^2 , and 2.5 μm and 20 μm , respectively.	109
Figure 4-13: Digital optical photographs of laser processed Copper surfaces, obtained with 10 scan passes; the laser peak fluence and the lateral pulse spacing were varied, ranging between 0.27 J/cm^2 and 1.88 J/cm^2 , and 2.5 μm and 20 μm , respectively.	110
Figure 4-14: Ablation rate depending on both the lateral pulse spacing and irradiated fluence, illustrated for Aluminium (top), Copper (centre), and Stainless steel (bottom).	112
Figure 4-15: Theoretically predicted and experimentally determined volume ablation rates versus fluence on Aluminium; theoretical values were calculated considering different energy transport mechanism, such as optical penetration (dotted line), effective penetration depth (solid line), mean-free path length of electrons (dashed), and molten layer (rough-dashed line); the experimentally obtained data are indicated by the black	

rhombus (\diamond).....	115
Figure 4-16: Theoretically predicted and experimentally determined volume ablation rates versus fluence on Copper; theoretical values were calculated considering different energy transport mechanism, such as optical penetration (dotted line), effective penetration depth (solid line), and mean-free path length of electrons (dashed line); the experimentally obtained data are indicated by the black rhombus (\diamond).....	118
Figure 4-17: Volume ablation rate versus peak fluence obtained on Stainless steel; theoretically values were calculated considering two different energy transport mechanisms: optical penetration depth (dashed line), and the effective penetration depth (solid line); experimentally determined ablation rates are indicated by the black rhombus.....	119
Figure 4-18: Material removal efficiency calculated for Aluminium, Copper, and Stainless steel; the green coloured fields represent the highest efficiency, the red coloured fields highlight the lowest level of energy efficiency.	121
Figure 4-19: Surface roughness R_a measured on laser processed cavities utilising the DEKTAK surface profiler; laser fluence and lateral pulse spacing were varied.	124
Figure 5-1: Trigger scheme applied in double shutter high speed camera imaging (top) and sequence of impinging laser pulses indicated by the black bars (bottom); exposure time of each record was 240 ns, indicated by the blue rectangles.	128
Figure 5-2: Ablation particle/plasma plumes arising in high-PRF femtosecond laser irradiation of Aluminium (top), Copper (entre), and Stainless steel (bottom); different repetition rates were applied; exposure time of each camera record was 240 ns.	129
Figure 5-3: Volume ablation rate versus lateral pulse spacing on Stainless steel; the pulse energy and the repetition rate were varied.....	132
Figure 5-4: Volume ablation rate versus lateral pulse spacing on Copper; the repetition rate was varied.....	134
Figure 5-5: Cavity depth versus repetition rate obtained on Aluminium (top), Copper (centre), and Stainless steel (bottom) by using constant processing parameters except the repetition rate; in addition the percentage increase of the cavity depth obtained with various repetition rates in relation to the 26 kHz cavity depth measurement are presented.	136
Figure 5-6: Experimentally determined material removal rates (indicated by <i>exp</i>) obtained on Aluminium, Copper and Stainless steel versus the repetition rate, the scattered lines reveal the up-scaled material removal rates considering the 26 kHz ablation volume rate (indicated by <i>_scal</i>).	138
Figure 5-7: SEM images of trench-like structures processed on Aluminium, Copper and Stainless steel in order to evaluate the quantity and size of re-solidified particles deposited close to the processing areas; the structures were achieved with 10 scans,	

5.5 μJ pulse energy and 2 μm pulse spacing, the temporal pulse-to-pulse distances were varied.....	141
Figure 6-1: Laser fluence profile and ablation depth profile for a Gaussian laser pulse; fraction of optical energy below the ablation threshold represents the amount of remaining energy; fraction of optical energy greater than the ablation threshold is deposited in the ablation volume.....	147
Figure 6-2: left: Schematic view to approximate the thermally affected volume, the laser spot area is indicated by a red line; right: heat affected volume and colour-coded temperature as a result of 5 consecutive incident laser pulses.	148
Figure 6-3: Expansion of isotherms in Stainless steel, induced by 5 consecutive incident laser pulses; the thermal diffusion length calculates to 17.6 μm at 20 μs , 8.8 μm at 5 μs and 3.9 μm at 1 μs temporal pulse-to-pulse distance, which correspond to repetition rates of 51 kHz, 205 kHz, and 1.024 MHz, respectively.....	149
Figure 6-4: Logarithmical plot of the heat diffusion length l_d versus pulse number, calculated on industrial grade Aluminium, Copper and Stainless steel for 100 pulses and three repetition rates (51 kHz, 205 kHz, 1.024 MHz).....	150
Figure 6-5: Surface temperature versus pulse number, calculated for Aluminium and 100 incident laser pulses, three different repetition rates, and irradiated pulse energy of 7 μJ	153
Figure 6-6: Surface temperature versus pulse number, calculated for Copper and 100 incident laser pulses, three different repetition rates, and irradiated pulse energy of 7 μJ	155
Figure 6-7: Ablation craters in Copper (left) and Stainless steel (right), each crater was obtained by irradiating a burst of 50 single laser pulses, both temporal pulse-to-pulse distance and single pulse energy are varied.	156
Figure 6-8: Surface temperature versus pulse number, calculated for Stainless steel and 100 consecutive incident laser pulses, three different repetition rates, and irradiated pulse energy of 7 μJ	157
Figure 6-9: Ablation depth per pulse versus laser fluence, obtained on ablation craters on Stainless steel by using the digital microscope VHX-100 for depth measurement.	158
Figure 6-10: Enhanced surface temperature calculation on Aluminium, according to reference [130] 80 % of in the plot depicted incident single pulse laser energy Q_P was taken into in calculation, the repetition rate was 1.024 MHz.	161
Figure 6-11: Enhanced surface temperature calculation on Stainless steel, according to reference [136] 70 % of in the plot depicted incident single pulse laser energy was taken into in calculation, the repetition rate was 1.024 MHz.	162
Figure 6-12: Energy balance calculated to remove a volume of 16.5 μm^3 Stainless steel	

with the mass of $1.37 \cdot 10^{-10}$ g; **top:** required energy for material evaporation including thermal coupling (70 %) are plotted by taking into account different levels of surface reflectivity and fractions of evaporation, **bottom:** energy balance as the difference between the total required energy for material removal and the irradiated pulse energy of 5 μ J..... 165

Figure 7-1: Characteristic laser induced surface structures on Stainless steel, **left:** (a) ripple, (b) micro groove, (c) deep micro hole, (d) hillocks / cone-like shaped micro structure; **right:** ripple and cone-like structures originated at the same time..... 168

Figure 7-2: SEM photographs taken on Stainless steel to show the dependence of both ripple orientation and superior micro-scaled groove structure on laser beam polarisation; the electrical field vector is highlighted as a white arrow..... 170

Figure 7-3: Ripple disordering induced by micro-scaled particles, observed on Stainless steel (left) and Copper (right)..... 170

Figure 7-4: Highly-regular ripple formation on Stainless steel surface (top left); light diffraction due to white-light illuminations of ripple phase gratings are shown; the polarisation direction of the laser beam is indicated by the arrow; the photographs showing light diffraction were taken by **M. KOCH** (ThyssenKrupp Steel Europe AG). 171

Figure 7-5: Cone-like shaped micro structures obtained on Stainless steel after 100 scans and 7.5 μ m hatch distance, the varied processing parameters repetition rate, pulse energy and lateral pulse spacing are given in **Table 7-1**. 173

Figure 7-6: Polarisation dependence of micro cones, the preferred direction of cone orientation is illustrated by bar graphs determined in graphical analyses; the electrical field vector of the laser beam is indicated by a white arrow..... 174

Figure 7-7: Micro cone formation on Stainless steel: (a) micro crater development, (b) initial state of micro structure formation, (c) micro cone spreading, (d) surface covered with cone-like shaped micro structures..... 175

Figure 7-8 top: Schematic of micro droplet formation mechanisms occurring in nanosecond laser irradiation, taken from reference [7], with Kelvin-Helmholtz instabilities (left) and Rayleigh-Taylor instabilities (right); **bottom:** micro structure formation upon high-PRF femtosecond laser processing of Stainless steel. 177

Figure 7-9: Contact angle measurements on Stainless steel surfaces, **left:** laser untreated material surface with a contact angle of 85°, **centre:** low-fluence laser processed surface, the contact angle of 34° indicates a hydrophilic character; **right:** cone-like shaped Stainless steel surface, the contact angle of 147° indicates a super hydrophobic character. 178

Figure 8-1 left: Machining example in Stainless steel to evaluate laser line-scan ablation, processed with 0.92 μ J pulse energy, 100 scan passes, 102 kHz repetition rate,

increasing line distance; **right:** determination of evaluation parameters *kerf width* and *kerf depth*. 181

Figure 8-2: Kerf width versus number of line-scan passes at various pulse energies (0.92 μJ , 2.7 μJ , 6.81 μJ) and repetition rates (102 kHz, 1.02 MHz, 4.1 MHz). 182

Figure 8-3: Cross section view of laser ablated kerfs processed with different machining parameters in Stainless steel: pulse energy 0.92 μJ , 2.76 μJ , 6.81 μJ ; number of line-scan passes 100, 500, 1000; repetition rate 102 kHz, 1.02 MHz, 4.1 MHz. 182

Figure 8-4: Ablation kerf development at the bottom of line-scan laser ablation structures, processed with 100 scan passes, 4.1 MHz repetition rate and different pulse energies; a) 0.92 μJ , b) 1.84 μJ and c) 2.76 μJ ; d) deep micro craters obtained with 250 scans and 1.84 μJ 183

Figure 8-5: Kerf depth versus number of line-scans obtained with different pulse energies (0.92 μJ , 2.76 μJ , 6.81 μJ) and rep. rates (102 kHz, 1.02 MHz, 4.1 MHz). 184

Figure 8-6: Cross section of kerf structures obtained using various laser processing conditions. 184

Figure 8-7 left: Trench-like ablation structure obtained by overlapping line-scans; the dimension is 1 mm width, 1 mm length and 90 μm in height; **right:** detailed view. ... 185

Figure 8-8: SEM photographs showing a detailed view on trench-like ablation structures obtained using unidirectional (left) and bidirectional (right) processing regimes; processing parameters were: pulse energy: 2.5 μJ , repetition rate: 1.02 MHz. 186

Figure 8-9: Trench-like structures obtained by using different pulse energies of either 2.5 μJ (top) or 3.75 μJ (bottom). 187

Figure 8-10: A pyramid demonstrator structure made in Stainless steel, different step heights were obtained for the repetition rate of either 205 kHz or 1.02 MHz, respectively. 188

Figure 8-11: High-PRF laser fabricated demonstrator structures made in (a) Stainless steel, (b) Copper, and (c) Aluminium; for comparison a similar structure made in Stainless steel, taken from reference [142]. 189

Figure 8-12: Micro featured mould processed in Aluminium; the drawing of the demonstrator and the manufactured Aluminium mould are shown on top, a detailed view of the micro features is given by means of both SEM (centre) and optical microscope photographs (bottom). 191

Figure 8-13: Plastic replica of the microfluidic demonstrator mould; the channel was 80 μm deep with a width of 60 μm at the bottom (left) and 116 μm at the surface, respectively. 191

Figure 8-14: Plastic replica of a ripple structured Stainless steel mould; structure size

was 20 by 20 mm² with the ripple period of approx. 1 μm; diffraction of light is clearly recognisable, induced by white light illumination; the replicated ripple pattern is shown (left)..... 192

Figure 8-15: Positioning error on Copper caused by the limited spatial resolution of the galvanometer scan technology. 193

Figure 8-16: Processing time versus scan speed and nominal pass length, calculated for 1 cm² processing area and 4 μm lateral pulse spacing in width and length, the scan direction was unidirectional. 194

List of tables

Table 3-1: Reflectivity and absorptivity calculated from voltage levels obtained in integrating sphere measurements on differently reflective Aluminium, Copper, and Stainless steel surfaces.	65
Table 3-2: Optical penetration depths for near-infrared laser irradiation of Aluminium, Copper and Iron, calculated by using Equation 2-4 and Equation 2-6	68
Table 3-3: Thermo-physical properties of industrial grade metal alloys and both pure Aluminium and Copper; ^[1] [104], ^[2] [105], ^[3] [106], ^[4] [107], ^[5] [108], ^[6] calculated according to Equation 6-5 ; missing values for Aluminium 6083-T6 are supplemented by data achieved for Aluminium alloy 6061-T as a material with comparable alloy composition, indicted by ^{*)}	69
Table 3-4: Laser parameters.....	76
Table 3-5: Scanner parameter; ¹⁾ scan speed with a constant lateral pulse spacing of $d_x = 32 \mu\text{m}$ @ 4.1 MHz, ²⁾ scan speed with constant lateral pulse spacing $d_x = 4 \mu\text{m}$ @ 4.1 MHz, ³⁾ irradiating the work piece surface.	80
Table 4-1: Ablation thresholds H_{th} depending on the repetition rates, calculated from the plots presented in Figure 4-3 , ablation threshold values achieved elsewhere are presented.	98
Table 4-2: A summary of different depth of energy transport, used in volume ablation rate calculations on Aluminium.	116
Table 4-3: A summary of different depths of energy transport, used in volume ablation rate calculations on Copper.....	118
Table 4-4: A summary of different depths of energy transport used in volume ablation rate calculations on Stainless steel.	120
Table 5-1: Processing parameters and maximal percentage increase of the cavity depths obtained experimentally at 1,024 kHz, related to the 26 kHz value.	137
Table 5-2: Material removal rates MRR determined for different repetition rates: MRR_{theo} is the theoretically calculated material removal rate by taking into account the ablation threshold H_{th} ; MRR_{exp} is the experimentally determined material removal rate calculated from the cavity depth; MRR_{scal} is the up-scaled material removal rate calculated by the product of the material removal rate obtained with 26 kHz and the repetition rate.	139
Table 6-1: Input values for surface temperature calculations on Aluminium.....	153
Table 6-2: Input values for surface temperature calculations on Copper.	154

Table 6-3: Input values for temperature calculations on Stainless steel.	156
Table 7-1: Processing parameter used in studying formation of cone-like micro structures on Stainless steel; number of scan passes and hatch distance were kept constant of 100 and 7.5 μm	172
Table 8-1: Depths of trench-like structures obtained with different processing regimes.	186

List of symbols

α	Absorption coefficient	m^{-1}
δ_e	Electron diffusion length	m
δ_{eff}	Effective penetration depth	m
δ_{opt}	Optical penetration depth	m
$\Delta\nu$	Spectral width in frequency space	Hz
θ	Angle	$^\circ$
κ	Absorption index	-
λ	Wavelength	m
λ	Thermal conductivity	$\text{W m}^{-1} \text{K}^{-1}$
Λ	Ripple periodicity	m
ρ	Density	kg m^{-3}
Ω_{vap}	Mass specific enthalpy of evaporation	J kg^{-1}
τ_H	Pulse duration	s
A	Absorptivity	-
c_p	Specific heat capacity	$\text{J kg}^{-1} \text{K}^{-1}$
c_{mol}	Molar heat capacity	$\text{J mol}^{-1} \text{K}^{-1}$
D	Thermal diffusivity	$\text{m}^2 \text{s}^{-1}$
D	Diameter	m
d_x	Lateral pulse spacing	m
d_Y	Hatch distance	m
d_Z	Ablation rate, ablation depth per pulse	m/pulse
e	Euler's number	-
H, H_0	Fluence, peak fluence	J cm^{-2}
H_{th}	Threshold fluence	J cm^{-2}
f	Focal length	m
f_R	Repetition rate	Hz
I, I_0	Intensity, peak intensity	W cm^{-2}
I_{th}	Threshold intensity	W cm^{-2}
j	Imaginary unit	$j^2 = -1$
k	Extinction coefficient	-
K	Thermal coupling coefficient	-
L	Latent heat	J kg^{-1}

List of symbols

l_{acc}	Length of acceleration/deceleration path	m
l_d	Heat diffusion length	m
l_x, l_y, l_z	Length, width and depth of a standardised cavity	m
m	Mass	kg
M	Molar mass	kg mol ⁻¹
M^2	Beam quality factor	-
MRR	Material removal rate	m ³ s ⁻¹
n	Refraction index	-
\tilde{n}	Complex refractive index	-
n_A	Number of pulses per area	-
n_P	Effective number of irradiated laser pulses	-
n_S	Number of scan passes	-
n_t	Total number of irradiated laser pulses	-
n_X	Number of laser pulses in X-direction	-
n_Y	Number of laser pulses in Y-direction	-
P, P_{max}	Power, maximum peak power	W
P_{av}	Average laser power	W
Q_P	Single pulse energy	J
Q_{abl}	Laser energy above the ablation threshold	J
Q_{rem}	Remaining laser energy	J
r	Radius	m
r_{th}	Threshold radius	m
R	Reflectivity	-
R_a	Arithmetical mean roughness	µm
R_{eff}	Material removal efficiency	m ³ J ⁻¹
t	Time	s
T	Temperature	°C, K
T_0	Ambient temperature	°C
T_{surf}	Surface temperature	°C
U	Voltage	V
v_S	Scan speed	m s ⁻¹
V	Volume	m ³
V_{SP}	Volume ablation rate	m ³ /pulse
V_{tot}	Total laser removed cavity volume	m ³
w, w_0	Beam radius, focus radius (86 % method)	m
X, Y, Z	Axes of the three-dimensional Cartesian coordinate system	m

List of publications

J. Schille, R. Ebert, U. Loeschner, P. Regenfuß, T. Suess, H. Exner: *Microstructuring with highly repetitive ultrashort laser pulses*, Proceedings of LPM2008 - the 9th Int. Symposium on Laser Precision Microfabrication, 16.-20.6.2008, Quebec, Canada.

J. Schille, R. Ebert, H. Exner, U. Loeschner, L. Schneider, N. Walther, P. Scully, N. Goddard: *3D micro machining with a high repetition rate ultrashort fibre laser*, Proceedings of the 5th Int. WLT-Conference on Laser in Manufacturing, June 2009, Munich, Germany, pp. 549-554.

J. Schille, R. Ebert, U. Loeschner, L. Schneider, N. Walther, P. Regenfuss, P. Scully, N. Goddard, H. Exner: *An ultrafast femtosecond fibre laser as a new tool in Rapid Microtooling*, Proceedings of LAMP2009 - the 5th Int. Congress on Laser Advanced Materials Processing, 29 June – 2 July 2009, Kobe, Japan.

J. Schille, L. Schneider, U. Loeschner, R. Ebert, H. Exner: *Mikrobearbeitung mit hochrepetierender Ultrakurzpuls-Laserstrahlung*, 20th International Scientific Conference Mittweida, Scientific Reports Nr. 4, 2009, pp. 50-56.

J. Schille, R. Ebert, L. Hartwig, U. Loeschner, P. Scully, N. Goddard, H. Exner: *Rapid micro processing of metals with a high repetition rate femtosecond fibre laser*, Proceedings of LPM2010 - the 11th Int. Symposium on Laser Precision Microfabrication, 2010, Stuttgart, (Germany).

J. Schille, U. Loeschner, R. Ebert, P. Scully, N. Goddard, H. Exner: *Laser micro processing using a high repetition rate femto second laser*, Proceedings of ICALEO - 29th International Congress on Applications of Lasers & Electro-Optics, Anaheim, Ca. (USA), 2010.

J. Schille, L. Schneider, U. Loeschner, R. Ebert, P. Scully, N. Goddard, B. Steiger, H. Exner: *Micro processing of metals using a high repetition rate femtosecond laser: from laser process parameter study to machining examples*, Proceedings of ICALEO - 30th International Congress on Applications of Lasers & Electro-Optics, Anaheim, Ca. (USA), 2011.

J. Schille, R. Ebert, U. Loeschner, H. Exner: *Wechselwirkungsmechanismen beim Einsatz eines hochrepetierenden UltrakurzpulsLasers zur 3D Mikrostrukturierung von Metallen*, DVS-Bericht Lasermaterialbearbeitung - Innovationen und Trends, Vorträge und Posterbeiträge der 8. Jenaer Lasertagung 2012, 2012, p. 117 - 119.

J. Schille, L. Schneider, M. Mueller, U. Loeschner, R. Ebert, N. Goddard, P. Scully, H. Exner: *Highspeed laser micro processing using ultrashort laser pulses*, Proceedings of LPM2013 - the 14th Int. Symposium on Laser Precision Microfabrication, Niigata (Japan), 2013.

Abstract

This thesis investigates laser micromachining using a high pulse repetition frequency (high-PRF) femtosecond fibre laser. Three different types of industrial-grade metals, Stainless steel, Copper, and Aluminium are investigated. The impact of the processing parameters on material removal is studied. Finally the feasibility of the technology in three dimensional micro structuring is explored.

The thesis contributes to clarify the main interaction mechanisms occurring in high-PRF femtosecond laser processing. Heat accumulation and particle shielding are identified as main material removal influencing mechanisms. As a result of heat accumulation, lowered ablation thresholds are detected for Aluminium (0.16 J/cm^2 at 1.02 MHz versus 0.33 J/cm^2 at 20 kHz) and Stainless steel (0.088 J/cm^2 at 1.02 MHz versus 0.11 J/cm^2 at 20 kHz). For the high heat conductive Copper heat accumulation is largely ruled out. Particle shielding is investigated by ultra high speed camera imaging. It is shown that the ablation plumes enlarge at the higher pulse repetition rates.

A parameter study investigates material ablation. From this study, appropriate machining parameters are derived with regard to both high ablation rate and removal efficiency, and small roughness: Aluminium: $5 \mu\text{m}$ pulse spacing / $5 \mu\text{J}$ pulse energy, Copper: $7.5 \mu\text{m}$ pulse spacing / $7 \mu\text{J}$ pulse energy, Stainless steel: $5 \mu\text{m}$ pulse spacing / $3 \mu\text{J}$ pulse energy. In addition experimentally and theoretically determined volume ablation rates are compared. For this, a material removal calculation model is designed. Good agreements between theoretical and experimental values are obtained by taking into account effective penetration instead of optical penetration for energy transport.

A surface temperature calculation model is designed, providing useful insights into heat accumulation. Heat accumulation observed for Aluminium and Stainless Steel is confirmed by surface temperature rise, calculated based on the remaining energy. Improvement of the model by enhanced energy coupling yields surface temperatures above the melting temperature. This is conclusive to experimental observations.

Finally the feasibility of the high-PRF femtosecond laser technology in micromachining is demonstrated by micro mould fabrication. Utilising these moulds, micro-fluidic plastic demonstrators are fabricated by micro-injection moulding.

Declaration by candidate

I hereby declare that no portion of the work referred to in the thesis has been submitted in support of an application for another degree or qualification of this or any other university or other institute of learning.

Date: 28.06.2013

Signature:

A handwritten signature in blue ink, appearing to read 'B. Klein', is written over a faint, illegible watermark.

Copyright statement

- i. The author of this thesis (including any appendices and/or schedules to this thesis) owns certain copyright or related rights in it (the “Copyright”) and s/he has given The University of Manchester certain rights to use such Copyright, including for administrative purposes.
- ii. Copies of this thesis, either in full or in extracts and whether in hard or electronic copy, may be made only in accordance with the Copyright, Designs and Patents Act 1988 (as amended) and regulations issued under it or, where appropriate, in accordance with licensing agreements which the University has entered into. This page must form part of any such copies made.
- iii. The ownership of certain Copyright, patents, designs, trade marks and other intellectual property (the “Intellectual Property”) and any reproductions of copyright works in the thesis, for example graphs and tables (“Reproductions”), which may be described in this dissertation, may not be owned by the author and may be owned by third parties. Such Intellectual Property and Reproductions cannot and must not be made available for use without the prior written permission of the owner(s) of the relevant Intellectual Property and/or Reproductions.
- iv. Further information on the conditions under which disclosure, publication and commercialisation of this thesis, the Copyright and any Intellectual Property and/or Reproductions described in it may take place is available in the University IP Policy (see <http://documents.manchester.ac.uk/display.aspx?DocID=487>), in any relevant Thesis restriction declarations deposited in the University Library, The University Library’s regulations (see <http://www.manchester.ac.uk/library/aboutus/regulations>) and in The University’s Guidance for the Presentation of Theses.

Acknowledgements

For giving me the opportunity to pursue this ‘split-site’ PhD, first I would like to express my gratitude to my supervisors Prof. Nicholas Goddard (University of Manchester, GB) and Prof. Dr.-Ing. Dr. h.c. Horst Exner (University of Applied Sciences Mittweida, Germany) for remarkable guidance, mentoring and encouragement during the course of this work. Further, with their reference and support, I was awarded research student scholarship from the Faculty. Many thanks go to the School of Chemical Engineering and Analytical Science and The University of Manchester, GB, as well as the Laser Institute and the University of Applied Sciences in Mittweida, Germany, for financial and technical support of my work, including travelling to many conferences.

I am very grateful to Dr. Patricia Scully and Dr. Marc Schmidt, who always share their valuable experience, and dedicated enormous amount of time offering me help and proofreading this thesis.

Further, I would especially like to thank our excellent team members, Prof. Dr.-Ing. Udo Löschner, Lars Hartwig, Sascha Klötzer, Lutz Schneider and Mathias Müller, who assist me in setting up the equipment and experiments, and for the many inspiring discussions.

The acknowledgements would be incomplete without giving special thanks to my friends in Manchester Dr. Shijie Liang and Dr. Akmez Nabeerasool for their friendship, encourage, and intelligent conversation over the years and in future.

Finally my gratitude is given to my beloved Susan and Hannes, who motivated me to study in Manchester and gave me permanent support through this work. Completing this PhD would not have been possible without your encouragement and understanding.

1 Introduction

1.1 Motivation for research

The unique advantages of ultrashort laser pulses in micromachining are high efficiency, fast and localized energy deposition, and minimal thermal load of the irradiated work piece. These benefits suggest initially a great potential of the ultrashort pulse laser technology in laser micro processing with respect to accuracy, precision and machining quality. Moreover, by using the recently developed high-repetition rate femtosecond laser technology, a great leap in terms of processing speed and machining throughput can be expected.

However, although ultrashort pulse laser processing utilising kilohertz repetition rate systems has been widely investigated so far, there is still a knowledge gap by using femtosecond lasers with high pulse repetition rates. Up to now, only little research has been done using high-PRF (pulse repetition frequency) femtosecond laser systems [1-4], mainly focused on fundamental investigations. In these studies, heat accumulation and particle shielding have been identified as new interaction phenomena for ultrashort laser pulses, caused by the short temporal distance between consecutive incident pulses. Nevertheless, the interplay between these interaction mechanisms as well as the influence of the thermo-physical properties of the irradiated materials are still hardly investigated and insufficiently understood. This is the case in particular for high-PRF laser processing of metals.

Furthermore, the literature review revealed that the impact of the temporal pulse-to-pulse distance on heat accumulation and surface temperature rise has not yet been adequately studied. The two-temperature model is established to calculate the temperature rise following single pulse ultrashort laser irradiations. Due to the complexity of laser material interaction as well as thermal energy transport, the model cannot easily be transferred to high-PRF laser processes.

Another knowledge gap exists in terms of implementation of the high-PRF femtosecond laser technology in industry-compatible micromachining production processes. The full available laser power can only be effectively utilised, when high-PRF femtosecond

lasers will be used in combination with fast beam deflection systems.

In addition, in order to use high-PRF femtosecond lasers in high-precision laser micromachining, good knowledge in terms of both accumulation of heat and laser beam shielding is of great importance. Process parameter optimisation along with development of appropriate machining strategies can potentially reduce the thermal impact and increase the process efficiency. Providing these, high-PRF femtosecond laser machining can be regarded as key enabling technology for 21st Century micro-manufacturing, capable of substituting standard machining methods in numerous micromachining applications.

1.2 Aims and objectives

The overall aim of the thesis work is the study of micromachining using a high-PRF femtosecond laser to evaluate the possibilities and limits of the promising ultrashort pulse laser technology in three-dimensional micro structuring. The implementation of the high-PRF laser technology in the machining process, the systematic study of the laser matter interaction phenomena, as well as determination of optimised processing parameters are of major interest in this work.

A secondary aim is to demonstrate the feasibility of the high-PRF femtosecond laser technology in micromachining by means of micro-scaled demonstrator devices.

The main objectives of the research in this thesis are summarised as follows:

- The study of *material removal* induced by high-PRF femtosecond laser pulses with special focus on the transition area between the “low-fluence“ and the “high-fluence” ablation regimes to enhance the existing knowledge about the fundamental mechanisms occurring in laser metal interaction,
- Investigation of the *impact of heat accumulation* and *particle shielding* on metal ablation occurring in high-PRF laser processing with a particular emphasis on the time between consecutive incident laser pulses,

- Design of a *temperature calculation model* to evaluate the impact of heat accumulation, induced by high-PRF irradiated laser pulses, on the thermal load of the work piece,
- Determination of *optimised processing parameters* with regard to the ablation rate, ablation efficiency and surface roughness,
- Investigation of the *origin of laser induced periodical surface structures* upon high-PRF laser irradiations (ripple structures, cone-like shaped structures) to elucidate the formation mechanism,
- Development of *innovative laser processing strategies* to facilitate the use of the high-PRF femtosecond laser technology in micromachining mass production processes,
- Fabrication of *three-dimensional micro-featured demonstrator structures* to point out the possibilities and limitations of the high-PRF femtosecond laser technology in micromachining,
- Fabrication of a *micro mould demonstrator* in Aluminium for micro-fluidic sensor fabrication to demonstrate the feasibility of the high-PRF femtosecond laser technology in rapid prototyping.

All experiments throughout this thesis have been performed on three industrial-grade metals with different thermo-physical characteristics: 0.5 mm thick Stainless steel metal sheet (X5CrNi18-10, 1.4301, AISI 304), 0.4 mm thick 99 % pure Copper metal sheet, and Aluminium alloy metal bar (Aluminium 6082-T6).

Stainless steel and Copper have been selected as materials of special interest in this work because of their significantly different thermo-physical material properties. This is regarded as notably beneficial to evaluate heat accumulation in high-PRF laser machining. In addition, the Aluminium alloy metal bar was investigated because this material is used in micro mould production for micro-fluidic sensor fabrication.

1.3 ‘Split-site’ PhD project

This application-orientated PhD project was undertaken as a ‘split-site’ PhD that is established within the framework of the *University of Manchester’s 2015 Agenda* as an opportunity for extending research collaborations. The project was based on the cooperation agreement of institutions of higher education between the *Hochschule Mittweida – University of Applied Sciences*, Germany and *The University of Manchester*, UK. In the ‘split-site’ PhD scheme, the graduate was registered for a University of Manchester PhD and has attended a number of seminars, including personal and professional development programmes as well as research skill training courses.

Most of the experimental research work has been performed at the partner institution in Mittweida, Germany. A brief overview about resources and facilities used in Mittweida is given below:

- Laser micromachining was investigated by using a laser micromachining work station, containing a high-PRF femtosecond fibre laser, galvanometer scan systems with 56 mm focusing lens, a high resolution translation stage, machining software,
- Ablation depth profiles were determined by means of surface topography measurement systems,
- Surface roughness was measured by a tactile surface profiler,
- Dimensions of ablated structures were evaluated by using both optical digital microscope and scanning electron microscope (SEM),
- Laser material removal was characterised by using an intensified high speed camera.

On successful completion, the PhD degree will be awarded by the University of Manchester.

1.4 Organisation of the thesis

Chapter 1 introduces this thesis work with the motivation for research, and the overall aims and objectives are pointed out. Further the applied ‘split-site’ PhD scheme is explained, established at The University of Manchester for extending research collaborations. In addition, the experimental resources and facilities used in this work are summarised. The chapter concludes with the organisation of the thesis.

The background into ultrashort pulse laser processing in *Chapter 2* reviews fundamentals of ultrashort pulse laser processing based on the outcomes of the literature research. A brief overview presents the state of the art of the laser micro processing technologies and the advantage of ultrashort laser pulses in micromachining. In addition, the physical principles of ultrashort pulse laser ablation are pointed out, followed by a summary of mechanisms causing formation of laser induced micro-scaled surface structures. The chapter concludes with an overview about the actual state, prospects and limitations in three-dimensional micro processing using high-PRF ultrashort pulse laser systems.

Materials and methodologies are presented in *Chapter 3* including a short description of the investigated materials and experimental setup. Furthermore the applied machining regime is introduced, the processing parameters are defined, and the evaluation methods are determined. Finally the utilised measurement equipment is described.

Chapter 4 presents results achieved in studying ultrashort pulse laser ablation. Experimental results are evaluated and the impact of the processing parameters on the ablation threshold and material removal are discussed. As a result, optimised processing parameters are identified with particular respect to material removal efficiency and surface roughness.

The enhanced study of high-PRF laser ablation in *Chapter 5* is focussed on the impact of the temporal pulse-to-pulse distance on material removal. Ablation plume formation induced by high-PRF laser pulses is evaluated by means of high speed camera photographs. In addition to this the interplay between heat accumulation and particle shielding is analysed. Therefore the lateral pulse spacing is varied.

Heat accumulation is phenomenologically studied in *Chapter 6*. A temperature

calculation model is presented. In a first approximation the temperature rise is calculated based on the fraction of remaining energy which does not contribute to material ablation. The model is enhanced by taking into account thermal energy coupling. Finally the model is proven by energy balance calculations.

Chapter 7 investigates the origin of laser induced micro structures appearing upon high-PRF laser irradiation. Formation of ripples and cone-like shaped micro structures is presented. In addition potential industrial applications of these structures are demonstrated.

Machining examples achieved in high-PRF femtosecond laser processing are shown in *Chapter 8*. Micro-scaled demonstrator structures indicate the feasibility of the high-PRF femtosecond laser technology in high-precision micromachining, i.e. in Rapid Tooling. For example, a micro structured Aluminium mould is fabricated in order to produce micro-fluidic sensors by using micro-injection moulding technology. Finally technical limitations of the investigated high-PRF laser micromachining technology are presented.

Finally, *Chapter 9* summarises the main conclusions from the research. A summary of contribution to the body of knowledge is presented. The chapter concludes with recommendations for future work.

2 A background into ultrashort pulse laser processing

2.1 Introduction

Chapter 2 is focused on the fundamental principles of ultrashort pulse laser processing of metals. After the introduction, *Section 2.2* presents a brief overview about the state of the art of the ultrashort pulse laser technology in laser micro processing. Next, *Section 2.3* is focussed on the phenomena and effects occurring in laser matter interaction, and particular interest is referred to as laser beam absorption, energy transport, and material ablation. The conclusions of this analysis will be included in the design of the material removal calculation model. Continuing on, scientifically accepted formation mechanisms for laser induced surface structures are summarised in *Section 2.4*. This knowledge is helpful to elucidate the origin of micro structures induced by high-PRF ultrashort laser pulses. The *Section 2.5* deals with the first results achieved in high-PRF ultrashort pulse laser processing of metals. The actual state, prospects and limitations in three-dimensional micro structuring using high-PRF ultrashort pulse lasers are presented. The chapter concludes with a short summary in *Section 2.6*.

2.2 Ultrashort laser pulses in micro processing

Since the invention of the ruby-laser by Theodor Maiman [5] in 1960, laser technology has attracted growing interest as a powerful manufacturing tool in medical and industrial applications, including automotive, aerospace, electro-optics, photonics, biomedical, semiconductor, etc. Moreover, in sheet metal cutting, drilling, welding as well as marking and engraving, the laser technology has substituted already traditional manufacturing techniques.

However, modern micro-manufacturing demands progressively product miniaturisation and hence high-accuracy and high-precision material removal. Furthermore, industrial

2.2 Ultrashort laser pulses in micro processing

processes require highly flexible manufacturing technologies and short processing times to achieve cost effective processes and products. These ambitious aims cannot be fulfilled satisfactorily by conventional micromachining techniques, such as micro-EDM (Electrical Discharge Machining), micro-turning, micro-drilling or micro-milling. For that the laser technology provides a genuine alternative.

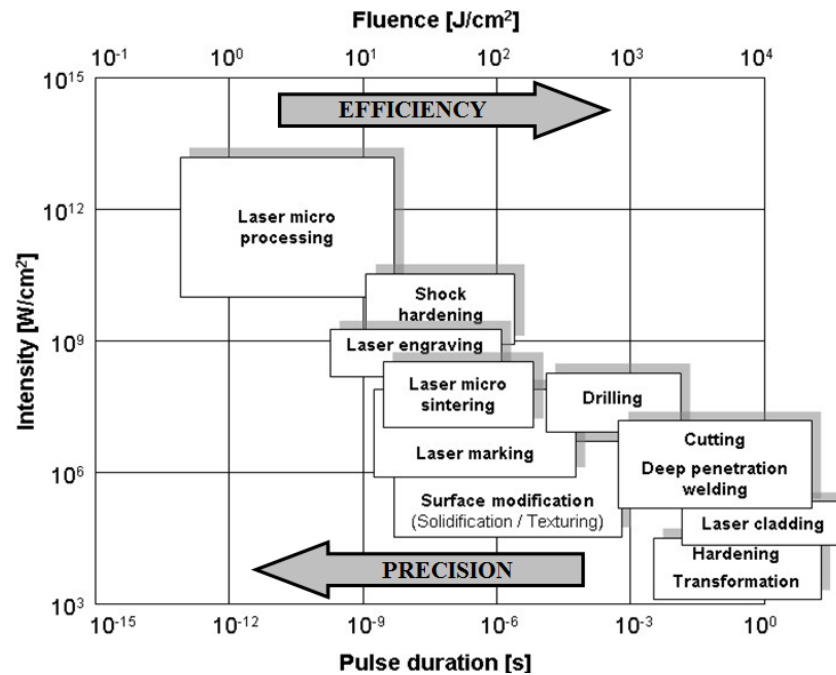


Figure 2-1: Laser manufacturing processes distinguished depending on their characteristic pulse duration and intensity; the category *Laser micro processing* includes micro processing technologies, such as laser micro drilling, laser micro cutting, laser micro ablation etc.

Different categories of operating regimes of industry-related laser-based manufacturing processes [6-8] are summarised in **Figure 2-1**, complemented by innovative laser machining technologies developed recently. The major categories are distinguished depending on their typical characteristics in terms of laser pulse duration and laser intensity. In reality the subtle distinctions between the technologies are blurred and the intended application determines the laser processing parameters to be selected. The figure indicates that machining precision increases with shorter pulse durations, whilst the material removal efficiency decreases. Laser micro processing can be typically found with pulse durations ranging between femtoseconds and nanoseconds, and pulse energies from microjoules to millijoules. By focussing the laser beam to tens of micrometre spot size, laser fluence of a few joules per square centimetre and laser intensities up to some tera watts per square centimetre can be achieved. This is considerably larger than ablation thresholds of metals and hard materials.

2.2 Ultrashort laser pulses in micro processing

However, the wide industrial application of femtosecond lasers was limited so far by inadequate levels of machining throughputs due to low average laser power and limited pulse repetition rates [9]. Further, the state of the technological development of the commercially available femtosecond laser technology has failed to meet industrial standards. Thus the picosecond laser technology was recommended by some research groups to be preferable in laser micro processing of metals [9, 10]. This is due to the better trade-off between precision and efficiency, obtainable with commercial laser systems. With the recent development of high average power high-PRF femtosecond lasers, this drawback on limited machining throughput can potentially be overcome. The available laser systems emit laser pulses with repetition rates of megahertz and pulse energies sufficiently high for metal ablation. As a result, the high-PRF femtosecond laser technology constitutes a genuine alternative in micro processing.

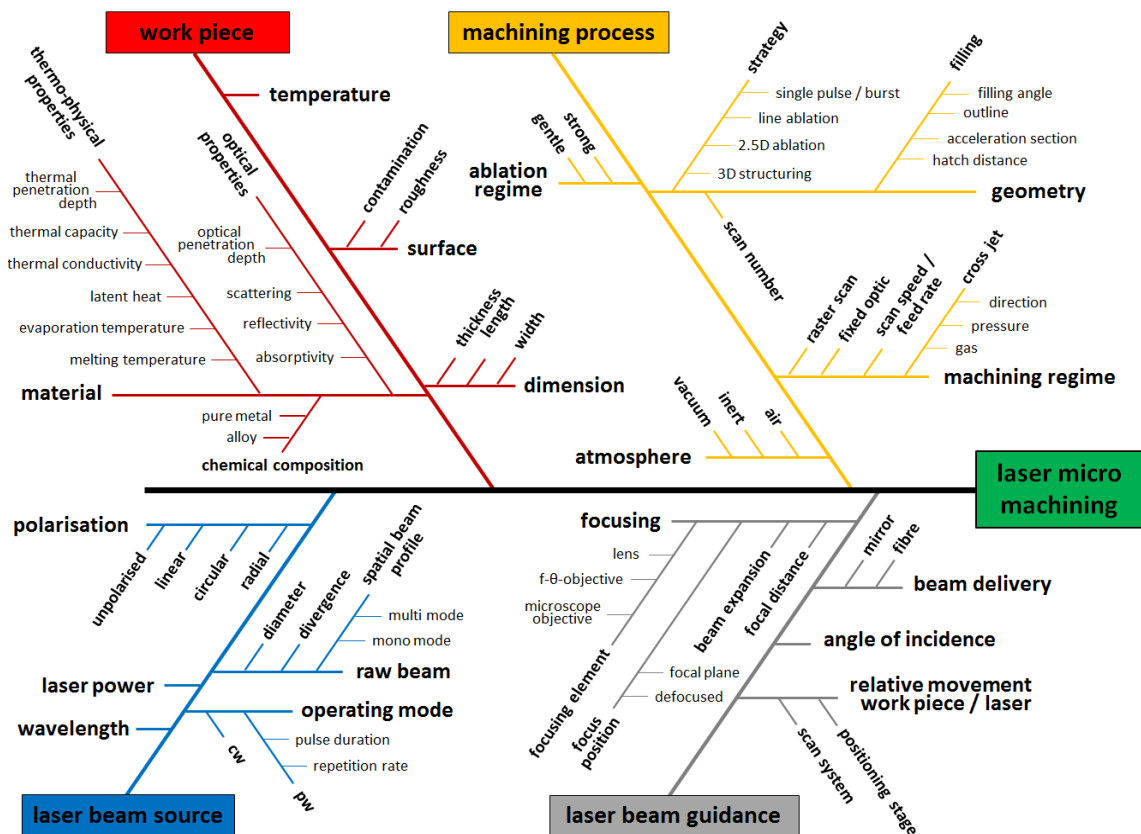


Figure 2-2: ISHIKAWA-diagram indicating material removal process influencing parameters.

Laser micromachining as the manufacturing technology of interest in this thesis is influenced by a great many of parameters, indicated in the *ISHIKAWA* diagram in **Figure 2-2**. It can be seen that material removal is determined by the laser parameters, the optical performance of the laser beam, the processing regime as well as the specific

thermo-physical and optical parameters of the work piece. Thus an effort should be spent optimising the machining process.

However, ultrashort pulse laser processing has been of interest since the development of the *Chirped Pulse Amplification* technology (CPA) in the middle of the 1980s [11]. Employing the CPA-method, femtosecond laser pulses of millijoule energies can be generated by stretching, amplification and recompressing to its original pulse width without excessive nonlinear pulse distortions or optical damage. The ultrashort pulse laser technology provides a range of advantages in laser micro processing, defined by *HERTEL et al.* [12] as follows:

- *Thermal load of the work piece is reduced by minimised and highly localised laser energy deposition,*
- *Very clean microstructures can be achieved due to little debris deposition,*
- *No interaction between the incident laser pulse and the ablated particle plume due to the shortness of the laser pulse,*
- *Avoidance of secondary effects (plume heating, plasma shielding).*

These key findings are supported by the results achieved in comparative studies using laser pulses of different pulse durations, ranging between femtoseconds, picoseconds and nanoseconds [9, 10, 13-22]. For metal machining it has been demonstrated that both considerably higher processing qualities and higher ablation efficiencies can be achieved with the shorter pulse duration, accompanied by almost negligible thermal load of the surroundings.

2.3 Fundamentals of laser matter interaction in ultrashort pulse laser processing

2.3.1 Introduction

Pulsed laser ablation of solids is a highly dynamic process, wherein the material undergoes a change of the fundamental aggregation states from solid matter to volatile phases, e.g. gas or plasma [23]. Material removal includes complex physical

mechanisms which depend on the thermal and optical material properties as well as the parameters of the incident laser beam, such as intensity, wavelength respective photon energy, and pulse duration. According to this **Figure 2-3** gives an overview about the main interacting effects and mechanisms, starting from laser beam irradiation, to reflection, scattering and absorption of the laser beam, to material removal accompanied by origin of shock waves, pressure waves and plasma. Further, as shown on the right, the energy balance close to the processing zone is influenced by heat conduction, heat radiation and convective heat transfer.

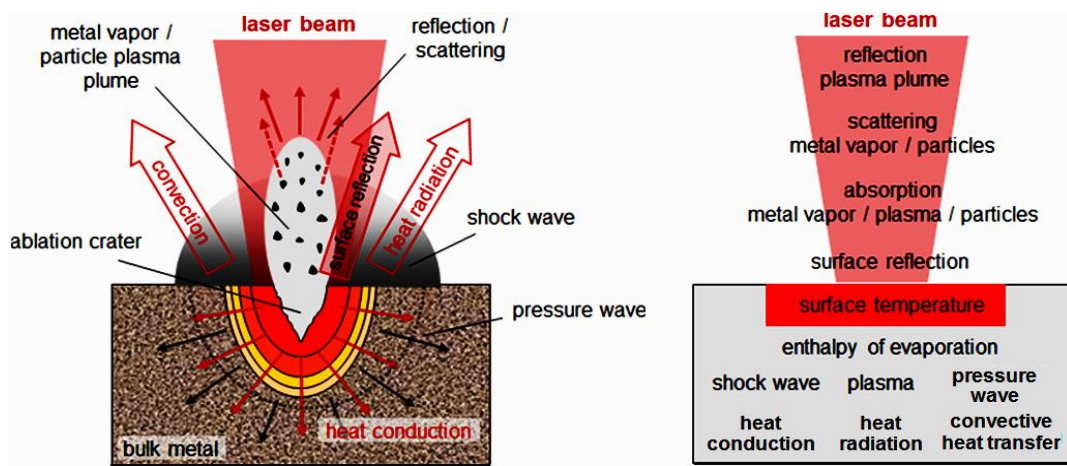


Figure 2-3: Overview of the mechanisms and effects occurring in laser matter interaction.

However, when the absorbed laser energy is sufficiently high, material ablation takes place. In general, the material removal process can be divided into four principal phases considering the fundamental effects and mechanisms as

- I - Laser beam absorption by free electrons,
- II - Energy transfer to the lattice,
- III - Heat propagation into the bulk metal,
- IV - Material ablation.

The first step in laser matter interaction is the deposition of energy by laser beam absorption, which excites the free electrons from the equilibrium state. This initial electron excitation is followed by a complex hierarchy of secondary processes which finally ends in the temperature equalisation between the electrons and the lattice. In case of a sufficient amount of deposited energy, the laser matter interaction leads to structural modifications, melting, evaporation or the ablation of the irradiated material. Thereby material modification strongly depends on the total deposited laser energy.

2.3.2 Laser beam absorption

In general laser beam absorption is characterised by different types of mechanisms, i.e. single photon absorption, non-linear absorption mechanism such as multi photon absorption or avalanche ionisation, as well as electromagnetic field enhancements due to surface roughness, nucleation centres, excitation of surface polaritons or interference phenomena [7].

In metals, the absorption of the laser beam is mainly governed by two mechanisms. Firstly in the case of a low degree of ionisation, free carrier absorption is related to the free electron gas in the conduction band. Considering the *Drude model*, the valence electrons are completely detached from ions and form the electron gas, and electron-electron as well as electron-phonon interaction is ignored. Optical absorption takes place by the conduction electrons in states close to the Fermi level, but in real metals the number of free electrons is modified by interband transitions. Thus *von ALLMEN* [24] described that the total absorptivity of metals is governed by free electrons, interband transitions, and surface effects. Moreover, in practice, the optical properties of metals change during laser irradiation, and influencing effects of temperature and phase transitions on the absorptivity have been identified in several publications [8, 25-30].

A second absorption mechanism is indicated by highly ionised gases and hot plasmas induced by high-intense laser irradiation. Therein laser beam absorption is dominated by photo-ionisation of thermally excited atoms as well as inverse Bremsstrahlung mechanism [7, 24, 31]. Thus the electron concentration rises exponentially (avalanche ionisation) and results in stronger plasma formation or optical breakdown.

Figure 2-4 illustrates schematically the absorption of a laser beam travelling through an absorbing medium as presented by *BERGSTRÖM* [25]. In metals the total amount of laser energy deposited in the solid yields the deduction of the reflected beam ratio from the incident laser intensity **I**.

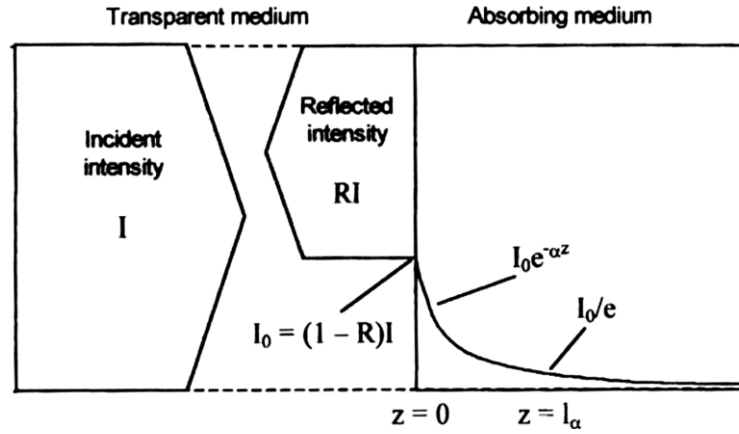


Figure 2-4: Absorption of a laser beam travelling through an absorbing media taken from reference [25], the exponential decrease of the intensity follows *Beer's law*, the optical penetration depth is marked as l_α .

Considering the laser beam propagation direction perpendicular to the sample surface, the absorbed fraction of intensity I_0 decreases exponentially with increasing penetration depth Z accordingly *Beer's law*:

$$I(z) = (1 - R) I e^{-\alpha z} = I_0 e^{-\alpha z} \quad \text{Equation 2-1}$$

where R is the reflectivity and α is the absorption coefficient.

The reflectivity R defines the reflected part of the incident laser beam and can be calculated by the *Fresnel equation*

$$R = \frac{(n - 1)^2 + k^2}{(n + 1)^2 + k^2} \quad \text{Equation 2-2.}$$

In this form, irradiation of metals by normally incident laser beam in air atmosphere is considered. Further, for metals as absorbing media, the complex refractive index \tilde{n} has taken into account [32], given as

$$\tilde{n} = n - jk = n(1 - j\kappa) \quad \text{Equation 2-3.}$$

The real part of the complex refractive index indicates the refraction n of the medium; the imaginary part is related to the absorption of the propagating laser beam. Laser beam absorption is determined by either the extinction coefficient k or the absorption index κ . The absorption coefficient, the absorption index, the refraction index, the extinction coefficient, and the wavelength of the incident laser beam correlates to each other [33] as:

$$\alpha = \frac{4 \pi k}{\lambda} \quad \text{Equation 2-4,}$$

where k is

$$k = \frac{\alpha \lambda}{4 \pi} = n \kappa \quad \text{Equation 2-5.}$$

The reciprocal of the absorption coefficient indicates the optical penetration depth δ_{opt} . This specific value gives the depth of laser beam penetration into a solid, where the intensity drops to the 1/e-level of the irradiated peak intensity. It calculates to as

$$\delta_{opt} = \frac{1}{\alpha} \quad \text{Equation 2-6,}$$

The optical behaviour of virgin metals can be summarised as follows, small optical penetration depth in the range of a few hundredth of the wavelength of the laser beam accompanied by a high reflectivity between 70 % and 95 % [34].

For laser processed surfaces, by contrast, considerably lower reflectivity levels have been reported in the literature for near-infrared laser beams. Laser beam absorptivity of 15 % has been demonstrated for low-intense laser irradiations of femtosecond laser processed Copper surfaces [35, 36]. This is considerably higher than the absorptivity of virgin Copper of almost 5 % [34]. Moreover, the papers report even higher absorptivity up to 50 % for high-intense laser beam irradiations of laser processed Copper. High absorptivity levels for infrared laser radiation are also confirmed on laser processed Stainless steel. *KAAKKUNEN et al.* [37] indicated absorptivity values for Stainless steel ranging between 70 % and 90 %.

2.3.3 Energy transfer

The fundamental mechanisms of energy transfer occurring in metals following femtosecond laser irradiation are chronologically shown in **Figure 2-5**, starting from electron excitation to thermal melting and material ablation. The figure distinguishes the non-thermal and thermal regime as two characteristic regimes which are referred to the thermal behaviour of the laser irradiated system.

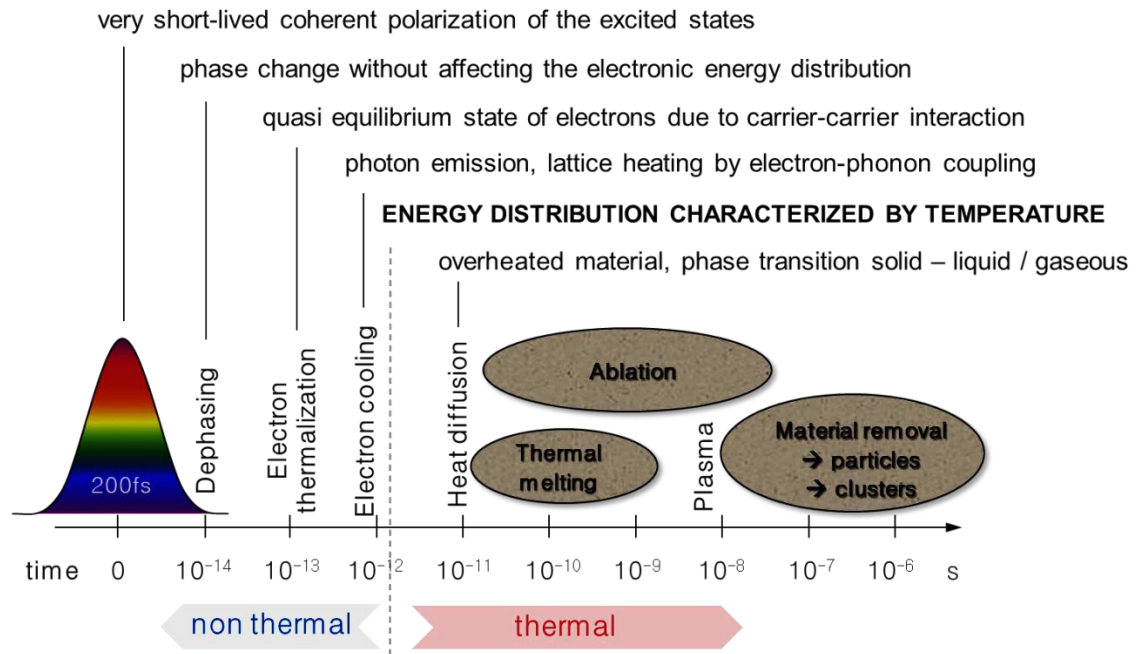


Figure 2-5: Fundamental energy transfer mechanism in metals upon irradiation of a single femtosecond laser pulse, two characteristic time regimes are clearly recognisable – the non-thermal and the thermal regime.

Electron excitation takes place in timescales of a few femtoseconds after pulse irradiation. This is followed by a dephasing process that destroys the very short-lived coherent polarisation of the material without affecting the electronic energy distribution [38]. In timescales of 10^{-13} s after pulse irradiation, a quasi-equilibrium state of the electron subsystem is reached due to electron thermalisation. At this state the energy distribution can be described by the Fermi-Dirac distribution with an electron temperature much higher than the lattice temperature. Electron cooling is driven by emission of photons and lattice heating due to electron – phonon coupling [39] until both the electrons and the lattice are thermalised.

At the final stage of thermalisation the energy distribution is close to the thermal equilibrium and can be related to the temperature (in the principal physical sense) for the first time. In metals the non-thermal interaction process changes to the thermal process at times in the range of 10^{-12} s. In accordance with this time domain, in **Figure 2-6** the thermalisation time of Iron, which is a core element of Stainless steel, can be estimated of about 2 picoseconds. Furthermore the temperature profiles of both the electrons and the lattice is plotted in this figure, calculated by *FISCHER and LICKSCHAT* [40] assuming single pulse laser excitation (180 fs pulse duration, $2.7 \mu\text{J}$ pulse energy). These parameters represent the experimental conditions applied in this thesis work.

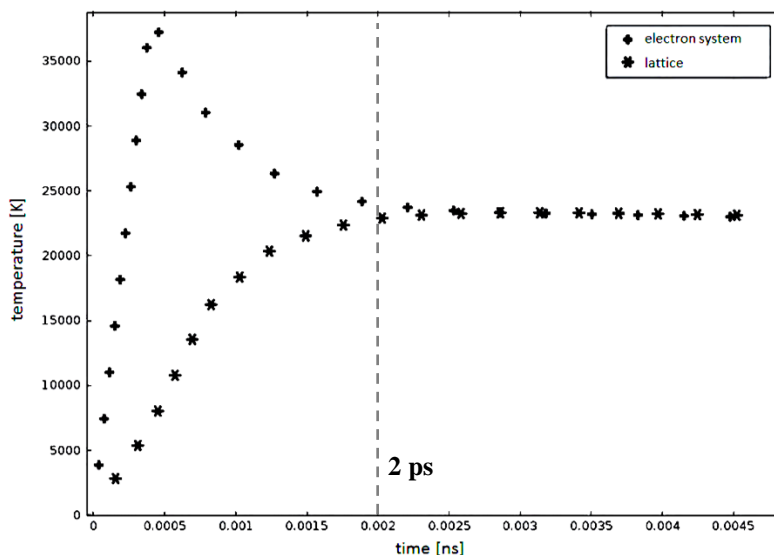


Figure 2-6: Temperature profiles for the electron subsystem and the lattice, calculated by *FISCHER* [40] under the assumption that a single laser pulse of 180 fs pulse duration and 2.7 μJ pulse energy irradiates Iron.

After thermalisation steep temperature gradients exist which induce thermal diffusion of the deposited laser energy into the bulk. The temperature rises fast and the material is superheated also in deeper regions. As a result solid liquid/gaseous phase transition takes place induced by strong material heating, phase explosion and critical point phase separation (these will be discussed more in detail in the next subsection 2.3.4). Here the removal mechanism strongly depends on the laser fluence. Thermal melting and material ablation accompanied by removal of particles and clusters take place in times between ten and some 100 picoseconds.

However, in addition to energy transport by electron diffusion (**Figure 2-7**, centre) and thermal diffusion (**Figure 2-7**, bottom) a number of authors suggested energy transport by ballistic electrons (**Figure 2-7**, top) as another significant mechanism [41-46]. Therein the ballistic energy transport is referred to diffusion of highly non-equilibrium electrons within a range determined by the electron-phonon coupling strength, excitation energy, and the density of states (DOS) at the Fermi-level. In noble metals the ballistic range can reach 100 nanometers, whilst in transition metals the ballistic energy transport is in the range of the optical penetration depth due to the large d-band electron densities and strong electron-phonon coupling.

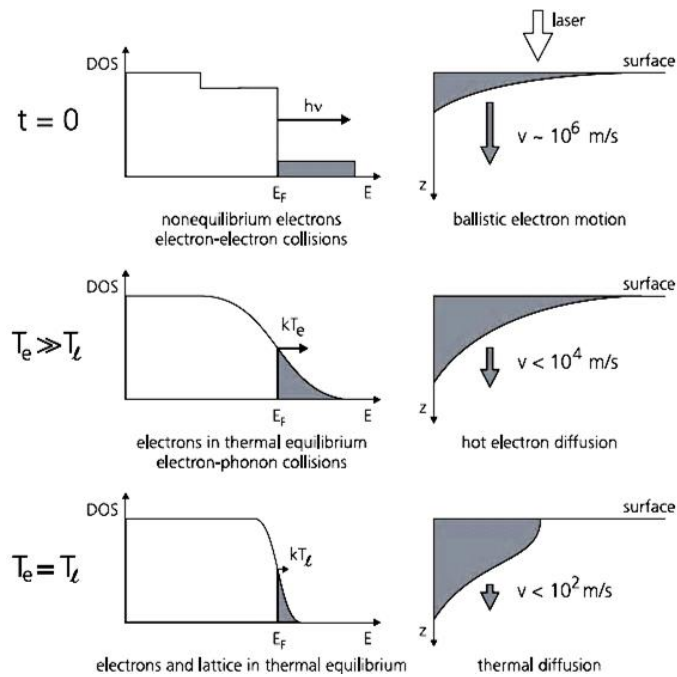


Figure 2-7: Energy distribution and energy transport mechanism following laser irradiation as presented by *WELLERSHOF et al.* [41]; **top:** ballistic energy transport, **centre:** electron diffusion, **bottom:** thermal diffusion.

2.3.4 Physical mechanism of laser ablation

Femtosecond laser ablation of metals is determined by complex and complicated interacting processes [47-51]. In very short time scales the material is heated to extremely high temperatures, resulting in pressures with entirely unknown thermal and mechanical material properties. Material ablation includes normal vaporisation, phase explosion, critical point phase separation, spallation and fragmentation or, in most cases, a mixture of all. This is in contrast to material ablation using longer laser pulses which is dominated by thermal processes including normal vaporisation, homogeneous boiling, and phase explosion [23, 52-54].

Ultrashort pulse laser processing is classified into two distinctive laser fluence regimes depending on the mechanism of material ablation. At first in the “low-fluence” regime, irradiation of low-fluence laser pulses initiates formation of gas bubbles inside the material, which grow larger due to laser heating, thermal expansion and the propagation of tensile stress waves. When the bubble size is large enough, the material will be separated and turns into a meta-stable phase consisting of a mixture of liquid, vapour

and droplets at temperatures below the thermodynamic critical temperature [48]. Explosive transition of the meta-stable metal-fluid into a stable two-phase state is caused by the loss of the thermodynamic stability and can be related to phase explosion mechanism as introduced by *MARTYNYUK* [55]. According to that *MANNION et al.* [56, 57] points out that phase explosion is the most probable and efficient mechanism for material removal in the “low-fluence” regime and both vaporisation and normal boiling are not significant.

However, in contrast to low-fluence femtosecond laser ablation, where phase explosion is dominant, in the “high-fluence” regime critical point phase separation is revealed as the main material decomposition process [48, 49, 51]. Induced by the high energy density, material ablation is completely different due to extraordinary heating directly from the solid phase to a temperature above the critical temperature. Thereby the thermodynamic critical temperature denotes that point where equilibrium vaporisation and also the liquid metal in the equilibrium state with saturated metal vapour correspond to the limit of liquid superheating.

Relaxation of the supercritical fluid decreases the temperatures below the critical point and causes thermodynamic unstable layers, consisting of a mixture of liquid droplets and gas phases, which coalesce into big liquid clusters. Accordingly, results obtained by *NEDIALKOV et al.* [58] using molecular dynamics simulations reveal, that material overheating above the critical point due to the higher incident laser fluence resulted in higher material ablation. The ablation depth increased because of areas located in deeper regions than the optical penetration depth becomes overheated, primarily due to electron heat diffusion.

To support this observation, snapshots of ablation areas are presented in **Figure 2-8**, indicating the atomic distribution on a metal surface at different times. These snapshots were obtained by *CHENG et al.* [48] studying material decomposition upon femtosecond laser irradiation. In molecular dynamic simulations by taking into account atom motion induced by thermal expansion and material ablation, the fluence was varied in the range between 0.3 J/cm², 1.0 J/cm², and 1.5 J/cm².

The snapshots presented in the figure below give evidence of different ablation phenomena. The impact of the laser fluence on the ablation mechanism is clearly recognisable.

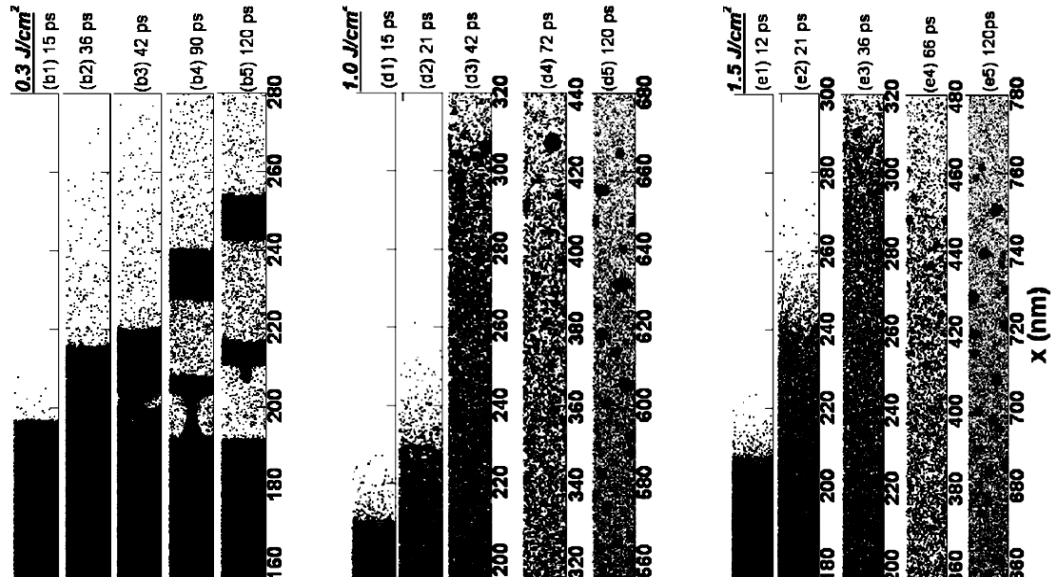


Figure 2-8: Snapshots of the ablated area representing the atomic distribution following femtosecond laser irradiation of Nickel, obtained using molecular dynamic simulation with respect to both different laser fluence and time [48].

Laser irradiation using low fluence of 0.3 J/cm^2 will generate gas bubbles inside the material. The bubbles grow larger with time, until the material is separated. In the figure it can be observed that gas bubbles appear inside the material at a depth of about 18 nm from the surface. This is caused by phase explosion mechanisms, where tensile stress is generated by laser heating.

By contrast, material removal induced by critical point phase separation can be seen by using the higher fluence. Phase separation is suggested as the dominant mechanism in the “high-fluence” regime because of the extraordinary heating of the solid to temperatures above the critical point, followed by the expansion into thermodynamic unstable zones. As a result the initially homogeneous phase is transferred into a large-scaled mixture of gas and liquid droplets, which coalesced into big liquid clusters.

Further, with regard to laser beam shielding as one of the important interaction mechanisms already reported in high-PRF laser processing, the temporal development of the particle / plasma plume forms an interest in this work. *MINGEREEV et al.* [59] studied the dynamic of single pulse laser ablation on Aluminium targets by time-resolved pump-probe shadowgraphy for time delays between 3 ns and 1.1 μs . The authors defined three distinctive time regions, separated by the characteristics of laser matter interaction. The effects occurring in the first region were related to photo-induced emission including expansion of highly pressurised heated material and

shockwave formation, shown in **Figure 2-9** (a) and (b). In the second region explosive material ejection caused by nucleation were detected at times between 200 ns and 700 ns, illustrated in **Figure 2-9** (c) to (e). At time delays larger than 700 ns massive melt ejection expanding vertically upwards up to 50 μm was observed, representing the third time region as indicated in **Figure 2-9** (f) to (h).

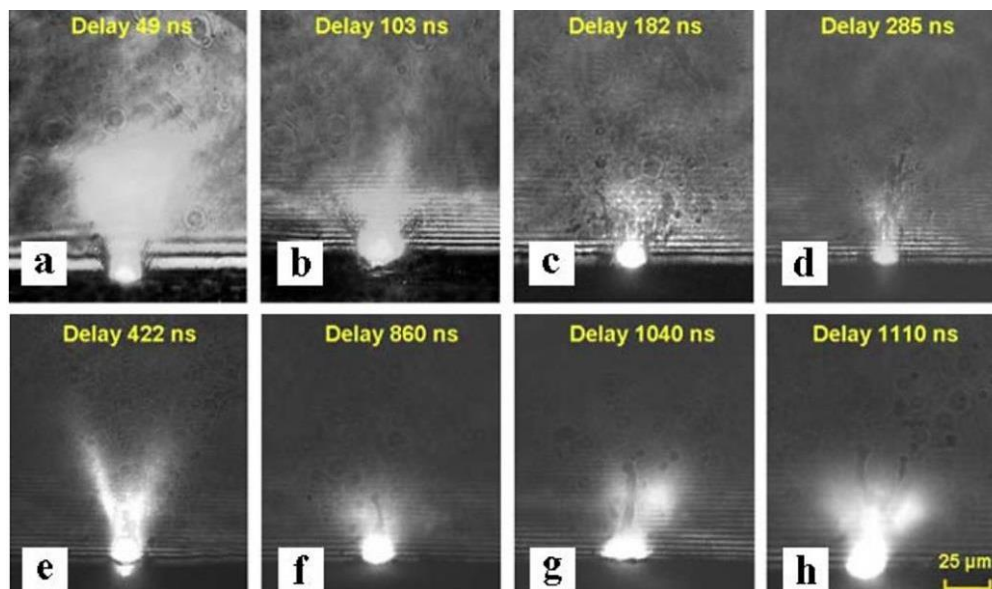


Figure 2-9: Dynamic of material ablation for single pulse irradiation (1.8 J/cm^2 , 80 fs, 820 nm) of Aluminium targets by time-resolved pump-probe shadowgraphs [59].

In addition vapour-cloud expansion induced by irradiation of high-intense ultrashort laser pulses of 1 kHz repetition rate on Aluminium has been investigated [9]. A considerable amount of ablated material remained above the processing zone for up to several milliseconds after the end of the pulse irradiated the Aluminium surface. Further it was observed, the ablated matter strongly accumulates with increasing pulse number.

From these studies, it can be derived, the ablation plume consisting of particles and vapour is still apparent at timescales of one microsecond after the onset of the laser beam. Moreover, that time corresponds to the temporal pulse-to-pulse distance in laser irradiation with repetition rates in the range of megahertz. As a result, particle shielding must be taken into account as a major influencing effect occurring in high-PRF laser processing. It can be assumed that the next following laser pulses will be scattered or/and absorbed by the dense ablation vapour / particle plume, which was induced by the previous incident laser pulses.

2.3.5 Ablation regimes

The two distinct ablation regimes, the “low-fluence” and the “high-fluence” regime as pointed out in the previous *Section 2.3.4*, have been previously established by *NOLTE et al.* [60]. Meanwhile this ablation behaviour has been scientifically proven in numerous experimental studies [14, 56-58, 61, 62]. As shown in **Figure 2-10**, the “low-fluence” and the “high-fluence” regime can be related to the regression lines, obtained by interpolating the ablation depth per pulse and the logarithmic scale of the laser fluence H_0 .

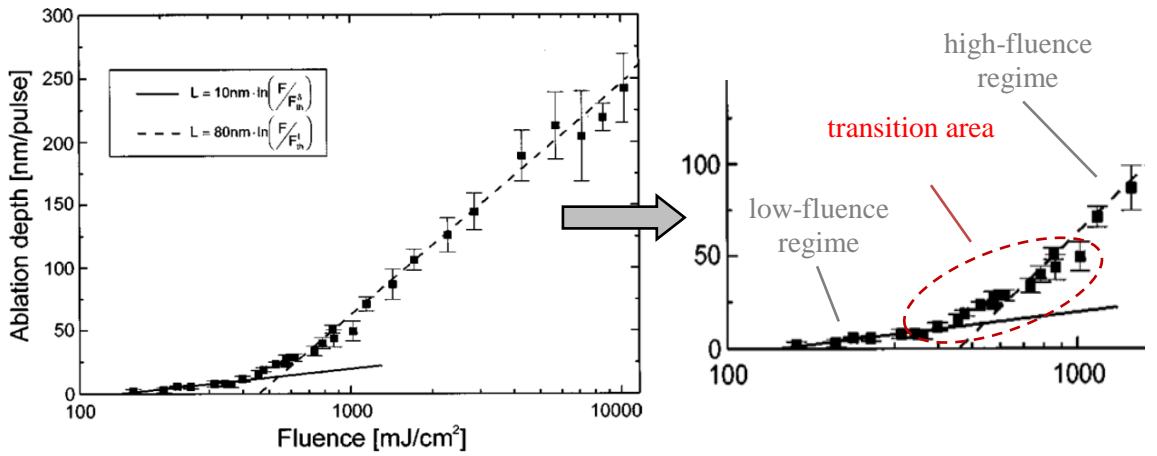


Figure 2-10 left: Ablation depth per pulse versus fluence obtained on Copper [60]; **right:** in a separate view the transition area between the low-fluence and the high-fluence is extracted from the plot to highlight the conflict in the model appearing in the transition area with a fluence between 0.5 J/cm² and 1.5 J/cm².

In the “low-fluence processing” regime, the relatively small obtained ablation depth correlates to the optical penetration depth δ_{opt} . The ablation depth per pulse d_z , in this thesis also denoted as ablation rate, can be estimated by *Beer’s law*. It calculates accordingly **Equation 2-1** by taking into account both the peak fluence H_0 instead of the peak intensity and the threshold fluence H_{th} to as

$$d_z = \frac{1}{\alpha} \cdot \ln\left(\frac{H_0}{H_{th}}\right) = \delta_{opt} \cdot \ln\left(\frac{H_0}{H_{th}}\right) \quad \text{Equation 2-7.}$$

The “high-fluence” regime indicates laser processing with the peak fluence higher than 1 J/cm². In this regime energy transport is determined by the diffusivity of the electrons rather than optical penetration. Thus the ablation rate was proposed as a function of the electron diffusion length δ_e as

$$d_z = \delta_e \cdot \ln\left(\frac{H_0}{H_{th}}\right) \quad \text{Equation 2-8.}$$

With respect to the processing quality the two distinct ablation regimes have been also referred to as the “gentle” and “strong” ablation regime [12, 57, 63]. Laser machining in the “low-fluence” regime is characterised by mild, so-called “gentle” material ablation. This is characterised by small ablation rates and smooth ablated surfaces. Surface ripple structures can emerge due to the negligible material melting phase. By contrast, laser processing using high-intense laser pulses will potentially cause “strong” material ablation and considerably higher material removal rate can be achieved. However, the ablated surfaces appeared rough and polluted due to molten and re-solidified recast layers deposited around the processing area.

In this thesis, the fluence regime between 0.3 J/cm² and 1.9 J/cm² was studied more precisely because of the overall aim to fabricate smooth micro-featured structures in adequate processing times. This fluence range correlates very well to the transition fluence range determined above in **Figure 2-10** (right). As highlighted in this figure, the statements made for both the “low-fluence” and the “high-fluence” regime do not sufficiently clarify material ablation in the fluence transition regime. The ablation depth of Copper increased disproportionately from the values predicted in the “low-fluence” regime, but it is lower than material ablation in the “high-fluence” regime. According to this, the semi-log graph plotting the ablation depth versus fluence on Stainless steel, presented in [56], verified the mismatch in the ablation depth model. The analysis of the given experimental data with particular regard to the transition fluence area, revealed the nonlinear increase of the ablation depth with the fluence in a range between 0.5 J/cm² and 2.5 J/cm².

However, in contrast to the well-established scientific assumptions that optical penetration and thermal diffusion determines material ablation, in *Section 2.3.3* it is suggested that ballistic electron diffusion is the most significant energy transport mechanism in noble metals. As a result the effective depth of optical energy diffusion is determined by the optical penetration depth aided by energy transport due to ballistic electron diffusion [41]. Emphasising this nature of energy deposition, a schematic view of energy transfer induced by femtosecond laser irradiation is presented in **Figure 2-11**, taken from reference [64]. The skin depth and the ballistic range indicated in this figure

correspond to the optical and effective penetration depth, respectively. Furthermore a number of electrons will be emitted from the metal surface. It can be seen that the energy will be deposited in regions considerably deeper than the optical penetration due to ballistic motion of free electrons.

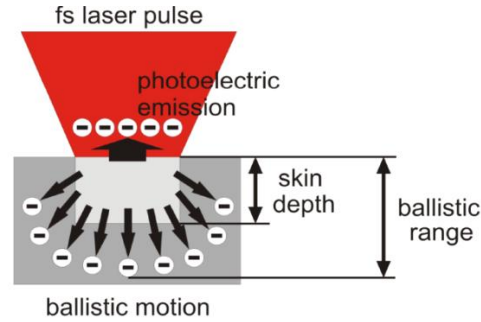


Figure 2-11: Ballistic energy transport following femtosecond laser irradiation as presented in [64], skin depth and ballistic range can be related to the optical and effective penetration depth.

For transition metals such as Iron, by contrast, it has been mentioned already in *Section 2.3.3* that the ballistic range of energy transport is less important. Thus for this kind of material, i.e. Stainless steel, the depth of energy deposition is mainly determined by the optical penetration depth.

In another approach, *BYSKOV-NIELSEN et al.* take up the proposal made by *VESTENTOFT and BALLING* [65] to include the ballistic energy transport in the simulation of ultrashort pulse laser ablation [43, 44, 62]. For noble metals processed in the “low-fluence” regime a good agreement between experimental and theoretical ablation rates was obtained by taking into account ballistic energy transport instead of optical penetration. Moreover it was mentioned that propagation of heat in deeper regions cannot be fully neglected.

For the “high-fluence regime”, by contrast, a linear increase of the ablation rate d_z has been detected. For this, a good approximation between theory and experiment has been found according to the following relation

$$d_z = \sqrt{\frac{2}{\pi e}} \cdot \frac{(1 - R)H_0}{\rho \Omega_{vap}} \quad \text{Equation 2-9,}$$

where \mathbf{R} is the reflectivity, ρ is the density and Ω_{vap} is the mass specific enthalpy of evaporation. This is in contrast to the half-logarithmical correlation presented in previous works, i.e. **Figure 2-10**.

2.4 Laser induced surface structures

2.4.1 LIPSS

LIPSS is an acronym for **L**aser **I**nduced **P**eriodical **S**urface **S**tructures, also often referred to as ripple structures, known as a general phenomenon occurring in laser processing. First mentioned in 1965, *BIRNBAUM et al.* [66] reported the formation of straight lines during surface damaging of semiconductor surfaces using a ruby laser. Since this first publication, ripples have been observed on a wide variety of metals, semiconductors and dielectrics. The self-organising ripple structures appear with dimensions in the order of tens of nanometers to some micrometers. In particular for ultrashort pulse laser irradiation intense ripple formations have been reported due to the high spatial coherence of this type of laser radiation [67].

In general models, specified more in detail in the next paragraphs, the ripple periodicity is related to the wavelength of the incident laser beam. In addition ripple with sub-wavelength period spacing have been achieved under certain irradiation conditions [68-71]. Thus ripples have been distinguished in low-spatial-frequency-LIPSS with periods in the range of the wavelength of the incident laser beam as well as high-spatial-frequency-LIPSS where the period is in the submicrometer / nanometer range [72].

Up to now the appearance of the ripple pattern is not completely understood and the formation mechanism is still under discussion. In the literature, different hypotheses have been identified which attribute ripple formation to laser excited interference phenomena and self-organising mechanisms. Widely accepted models include interference patterns between the incident and the refracted / scattered laser beam due to surface roughness [67, 73], interference phenomena between the incident beam and laser-excited surface electromagnetic waves [74, 75], field enhancement induced by effective coupling of laser radiation with surface plasmons / polaritons [76-79], as well as self-organised formation of ripple structures due to laser induced surface instabilities [80, 81].

SIPE et al. [75] reported three common ripple types, the $s_{(+)}$ -type, $s_{(-)}$ -type and the c-type ripple distinguished depending on the ripple periodicity Λ . Therein the ripple periodicity is related to the laser wavelength and the angle of incidence θ of the incident wave front to the normal of the surface, the positive / negative sign corresponds to the

backward / forward scattering direction of the electromagnetic waves, as

$$\Lambda_s = \frac{\lambda}{1 \pm \sin \theta} , \quad \Lambda_c = \frac{\lambda}{\cos \theta} \quad \text{Equation 2-10.}$$

According to **Equation 2-10**, laser irradiation perpendicular to the surface normal results in ripple spacing almost equal to the wavelength of the laser beam. In case of an inclined beam incidence, s-type ripples emerge with either a smaller ($s_{(+)}$ -type) or larger spacing ($s_{(-)}$ -type), corresponding to the velocity component of the scattered radiation towards or away from the incident laser beam. C-type ripples mostly occur in case of high-order modulation due to the irradiation of higher laser intensities [67]. Further, as a result of nonlinear laser substrate interaction induced by the high intensities, the primordial ripple modulation can be tilted 90° [82], whilst s-type ripples form mostly perpendicular to the polarisation direction of the incident laser beam.

In addition it has been found that the ripple period appears to depend primarily on the laser fluence rather than on the pulse number [70]. With increasing pulse numbers, the modulation depths increase and the ripples become more uniform and consistent, but the distance between the ripples was observed as constant.

2.4.2 Cone-like micro structures

The literature review reveals that origin of cone-like micro structures has attracted research interest in laser processing using nanosecond pulses [83-85], but up to now it is insufficiently investigated for ultrashort laser pulses. Thus a summary about the relevant cone formation mechanisms as proposed by *OLIVIERA et al.* [84] for the nanosecond laser pulse regime is given:

- (I) ***Shadowing mechanism*** is related to vaporisation-resistant areas on the surface to shield the underlying regions from the incident laser beam,
- (II) ***Spatial modulation of absorbed energy mechanism*** is caused by non-uniform laser intensity distribution due to surface tilting, local variations in the optical reflectivity of the surface, or multiple reflections or scattering of the laser beam on topographical artefacts,

- (III) *Vapour phase deposition mechanism* occurs in the vapour phase and causes mass transport from the bottom to the top of the columns, and finally
- (IV) *Hydrodynamic mechanism* leads to growth of cone-like shaped structures due to the upwards flow and re-solidification of melting, the melt flow is driven by surface tension gradients or by the recoil pressure induced by the expanding ablation plume and results in surface melt instabilities on the surface of the molten layer.

Hydrodynamic melt instabilities will be addressed in greater detail next due to their relevance to micro-cone formation. Later on, in *Section 7.3* of this thesis, cone formation induced by high-PRF femtosecond laser pulses will be discussed with regard to hydrodynamic mechanisms.

BRAILOVSKY et al. [86] indicates three different types of hydrodynamic instabilities leading to the formation of large-scale surface structures with characteristic periods ranging between 20 μm to 30 μm . The first one, *capillary wave instabilities* in the field of plume pressure, induces the formation of large-scale surface structures due to instabilities of the plane front of liquid evaporation. In the near-surface plasma layer the pressure undergoes a spatial modulation followed by the outflow of the melting from pits to humps and subsequent re-solidification. *Rayleigh Taylor instabilities* as the second type were formed by irradiation with multiple laser pulses at the liquid vapour interface. The flow of the molten material from pits to humps induced by centrifugal forces increases the corrugation of the surface. Shear flow instabilities, also referred to as *Kelvin Helmholtz instabilities* are denoted as the third mechanism. At this nonlinear stage of the relief formation, the vapour velocity is considerably higher than the velocity of a liquid layer. Moreover the lateral expansion of the plasma/vapour plume causes the excitation of capillary waves tangentially in the melting and the humps transform into vertical columns.

However, the growth of the large-scale surface structures is accompanied by the ejection of droplets and macroscopic particles. Droplet formation occurs due to condensation by cooling of the oversaturated expanding ablated particle/plasma plume in case of the collision with the substrate or other particles [86]. The radius of the droplets and macro-particles has been observed ranging between 10 nm and 100 nm and up to 10 μm , respectively.

A detailed description of the growth of micro cones in steel under multiple raster-scan laser irradiation using a nanosecond Nd:YAG laser is given by *DOLGAEV et al.* [87]. As presented in **Figure 2-12**, the initial protruded micro-hillocks evolve on the sample surface, originated by capillary waves with a period ranging between 10 μm to 20 μm . The micro cones increase in size and number with increasing number of irradiated laser pulses, and heights of up to 100 μm above the original surface were obtained. According to that **Figure 2-12** (left and centre) illustrate micro cone-covered surfaces, obtained in air at atmospheric pressure with 10^4 and 10^5 incident laser pulses, respectively. On the other hand, laser irradiation under a low-pressure air atmosphere formed micro structures with a reduced height and smaller period. Furthermore the tips seem to be rounded and the conical shape is not well developed, as shown in the figure at right. Complementary studies done by *LLOYD et al.* [88] revealed, that under irradiation of a constant number of laser pulses with higher fluence the height of the cones increased whilst the cone number decreased.

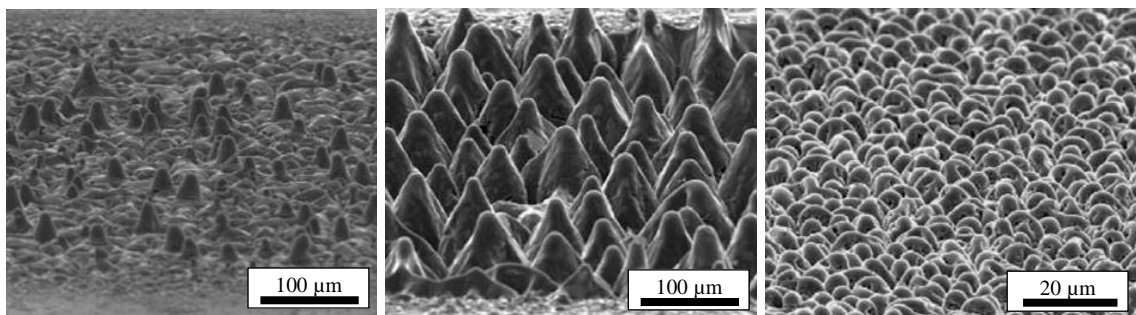


Figure 2-12: SEM images of micro structures grown in Stainless steel under different irradiation conditions, captured at a tilt of view of 75° : 10^4 pulses (left) and 10^5 pulses (centre) irradiated at atmospheric air pressure, and 10^5 (right) pulses irradiated in air at a lower pressure of 10^{-3} Pa, (taken from reference [87]).

However, *BÄUERLE* points out that the origin of conical structures is not necessarily caused by surface melting [7]. Non-coherent structure formation is related to changes in absorptivity, the release of latent heat, and spatial inhomogeneities as a result of spatio-temporal disordering or instabilities in laser ablation, i.e. caused by laser-induced oxidation, explosive crystallisation, exothermal reactions, or temperature gradients due to a heat flux generated by surface deformations, respectively.

Indication about micro-scaled voluminous surface morphologies appearing on Stainless steel as a result of ultrashort pulse laser irradiation is given in [89]. It is reported that mountain-like pillars grew out of the laser processed surface induced by multiple laser

pulse irradiations with repetition rates of 250 kHz and the fluence ten times higher than the ablation threshold. The formation of the mountain-like surface has been suggested by the authors to be due to re-deposition of vapour.

On the other hand, little work has been done recently to fabricate cone-like shaped micro structures utilising ultrashort laser pulses and ambient atmospheric conditions [90-92]. Super-hydrophobic and/or anti-reflective surface characteristics of cone-like micro structured steel surfaces are presented. As a result a great potential of this technology can be hypothesised particularly for the fields of surface texturing and functionalization. However, formation mechanism of cone-like shaped structures induced by femtosecond laser irradiation is not sufficiently studied and understood up to now.

2.5 High-PRF laser processing

2.5.1 Introduction

The following sections discuss heat accumulation and particle shielding because of their relevance as the main ablation process influencing mechanisms. Furthermore the actual state, prospects and limitations of the high-PRF ultrashort pulse laser technology are presented. Until now, little research has been undertaken to investigate and describe the phenomena occurring in high-PRF ultrashort pulse laser processing.

In the studies carried out on metals [1, 2, 19, 93], dielectrics [94, 95] and silicon [4] heat accumulation has been identified as a dominant laser ablation influencing effect. It is reported that this ratio of absorbed laser energy which does not contribute to plasma formation, bond breaking and/or is carried away by ablated particles will be deposited in the laser-irradiated area, inducing a rise of the near-surface temperature.

Furthermore it was found particularly in high-PRF laser processing that particle shielding considerably affects the ablation process. This is due to the short temporal pulse-to-pulse distances and subsequent irradiated laser pulses interact with the ablated plasma/particle plume.

2.5.2 Heat accumulation

In ultrashort pulse laser processing, heat accumulation effects have been initially described in laser irradiation of dielectrics using laser pulses with repetition rates in the range of some MHz. *LUTHER-DAVIES et al.* [94] point out that the time between successive pulses with small temporal distances is too short for complete material cooling in the area encircling the focal spot. Particularly, in the case of poor heat-conducting materials, the surface temperature rises gradually because the following laser pulses irradiate the area already heated by the previous ones.

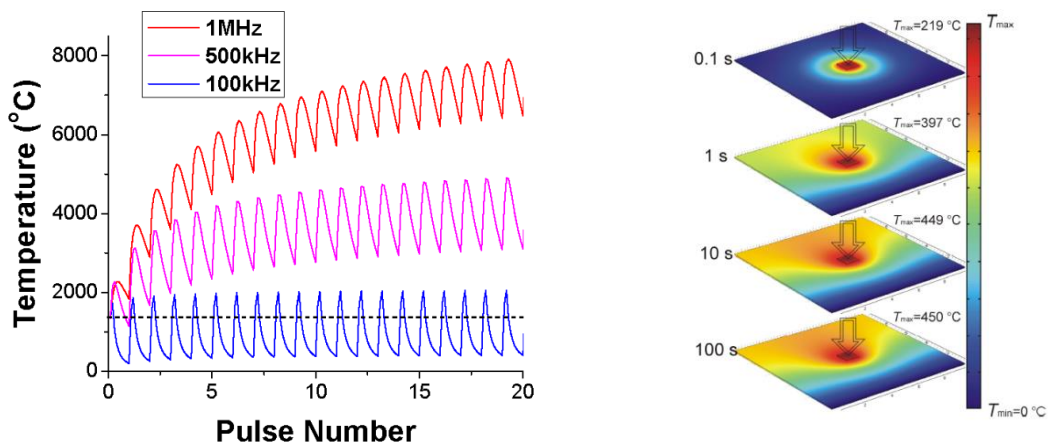


Figure 2-13 left: Glass temperature versus exposure, calculated at a radial position of $2\ \mu\text{m}$ from the centre of the laser beam, taken from [95], **right:** heating of Aluminium foil by remaining energy left in the material under consideration that 10 % of the in-coupled 10 W laser power is converted to heat, modelled in [93].

Figure 2-13 (left) illustrates the temperature rise as a function of the repetition rate, calculated by *EATON et al.* [95] in AF45 glass. With increasing number of incident laser pulses, considerably higher temperatures were calculated for higher repetition rates, induced by accumulation of heat. It is demonstrated that high-PRF laser processing leads to surface temperatures considerably higher than the melting point of the irradiated material, indicated in the figure by the dashed line. This is in contrast to ultrashort pulse laser processing using repetition rates in the kilohertz range, where the low thermal impact has been considered as a main advantage.

Analogously to dielectrics, in the case of high-PRF laser processing of metals, the remaining laser energy accumulates in the focal spot area causing a surface temperature rise. As a result both lowered ablation thresholds and higher ablation efficiency caused by high temperatures near the melting point have been anticipated by the authors. One

explanation of these phenomena might be the increase of the absorptivity of the laser radiation on metals at higher temperatures. Furthermore, in the case of Aluminium as a material with a low melting temperature, the absorptivity increases strongly in states close to solid-melting phase transition.

Heat accumulation in Aluminium has been studied theoretically by *RACIUKAITIS et al.* [93] using ten picosecond long laser pulses. Cumulative heating of a 100 μm thick Aluminium foil was modelled considering a remaining energy of 10 % of 10 W continuous laser output power, irradiated onto the sample surface. After a few seconds, a temperature as high as 450° C was achieved encircled the focal spot area, **Figure 2-13** right.

DOERING et al. [2] studied the influence of the heat conductivity in high-PRF laser drilling of Stainless steel and Copper, materials with divergent heat conductivities. In the case of Stainless steel, the authors found a significant decrease of the pulse number to drill through at higher repetition rates. For this, heat accumulation was suggested as a material ablation enhancing effect, mainly induced by the low heat conductivity. On the other hand, significant material melting as another result of heat accumulation leads to reduced processing qualities, such as shown in **Figure 2-14** left.

By contrast, the repetition rate has only a marginal effect for laser drilling of Copper. Due to the high heat conductivity the drilling process does not suffer from heat accumulative effects with respect to drilling efficiency and quality (**Figure 2-14** right).

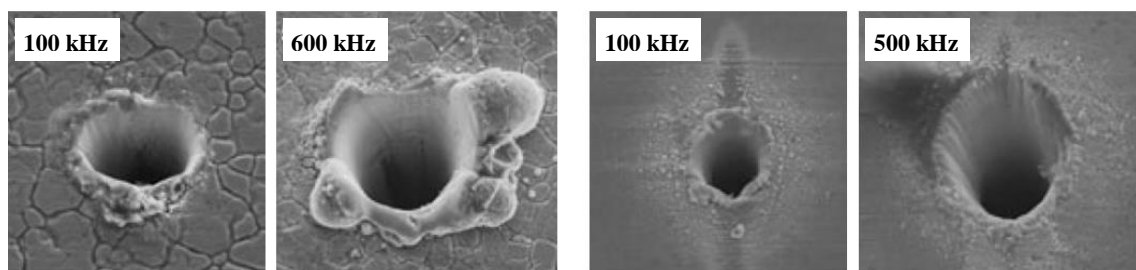


Figure 2-14: Results achieved in high-repetition rate laser drilling of Stainless steel (left) and Copper (right) using constant pulse energy (30 μJ) and wavelength (515 nm) but different repetition rates, taken from reference [2].

2.5.3 Particle shielding

KOENIG et al. [96] studied the impact of plasma/particle plumes induced by ultrashort laser pulses on beam transmission in pump-probe experiments. Aluminium, Copper and Steel have been studied. As shown in **Figure 2-15** for all investigated materials, a first transmission minimum appeared in the range of a few nanoseconds after pulse irradiation. This minimum is induced by the arising plasma plume. Furthermore, in high-intense laser irradiation, another transmission minimum has been detected in timescales of 10^{-7} s after the onset of the laser pulse. For this second transmission minimum ejection of ablated particles and clusters has been suggested.

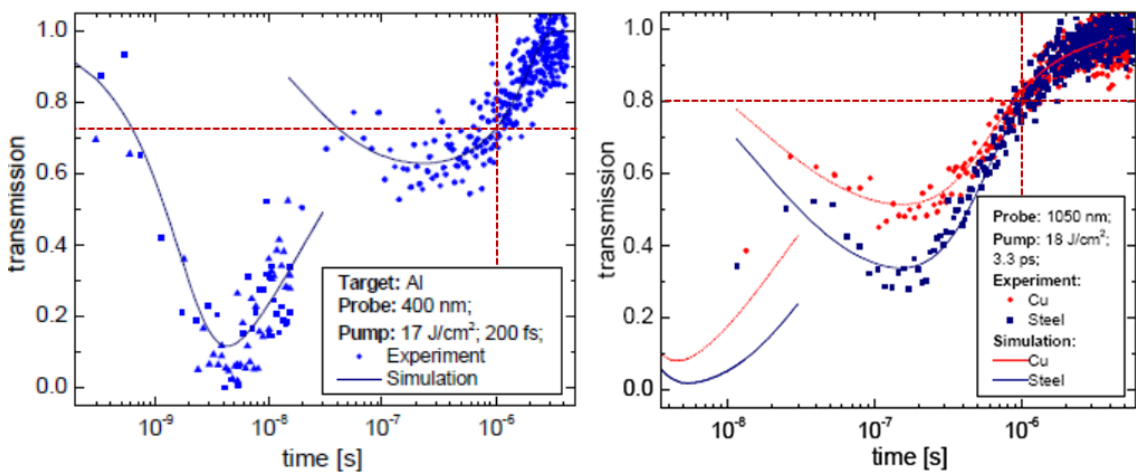


Figure 2-15: Beam transmission through a laser induced plasma/particle plume, obtained in pump-probe beam experiments on Aluminium (left), Copper and Steel (right) [96], in addition reduced laser beam transmission at 1 MHz repetition rate is indicated by red dotted lines.

In the figure the reduced laser beam transmission between 70 % and 80 % at 1 microsecond is indicated by red dotted lines. This time interval correlates to 1 MHz repetition rate that will be investigated in this thesis. As a result, in studying high-PRF laser processing, shielding of consecutive incident laser pulses might be occurring, inducing laser beam energy losses accompanied by reduced ablation rates.

Laser beam shielding has been reported previously [1, 19] using high-energetic ultrashort pulses and repetition rates in the range of some hundreds kilohertz. In this time regime the next incoming laser pulses interact with ablation products (ejected particles, clusters) which are induced by the preceded pulses. The next laser pulse will potentially be reflected, scattered or/and absorbed by the ablation plume of preceding irradiated pulses, and thus a lower amount of energy irradiates the sample surface.

ANCONA et al. [1] report the phenomena of particle shielding in high speed laser drilling of 0.5 mm thick Stainless steel metal sheets using femtosecond laser pulses. In the case of the lower pulse energy of 20 μJ and repetition rates distinctly higher than 500 kHz, a considerably higher number of pulses was needed to drill through (**Figure 2-16**, left). The authors attribute the perturbation of the drilling efficiency to particle shielding effects.

For the higher irradiated laser energies of 30 μJ they found, the number of pulses to drill through decreased with increasing repetition rates (**Figure 2-16**, right). In this case heat accumulation counterbalances energy losses, and thus the ablation efficiency increased, but detrimental effects on the processing quality due to material melting were observed.

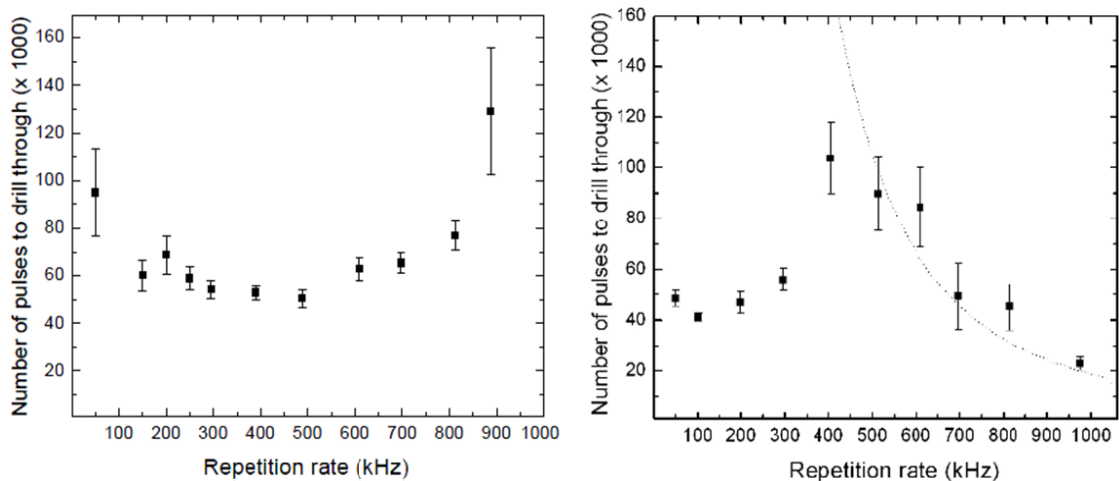


Figure 2-16: Repetition rate versus number of laser pulses to drill through 0.5 mm thick Stainless steel, the pulse energy was 20 μJ (left) and 30 μJ (right), taken from reference [1].

2.5.4 Actual state, prospects and limitations in three-dimensional micro structuring using high-PRF ultrashort laser pulses

Only little research has been done so far using high-PRF ultrashort pulse laser systems in micromachining. The feasibility of the technology in three-dimensional micro structuring is demonstrated by initial machining examples, such as micrometer-sized pyramids and embossing tools [97-100].

NEUENSCHWANDER et al. studied the volume ablation rate and the process efficiency as a function of both laser fluence and repetition rate [97, 100] by using high-PRF picosecond laser pulses. Based on simple models, the authors determined optimised processing conditions to achieve maximum removal rates and highest ablation efficiency with respect to average laser power, repetition rate and fluence. In the study Copper was irradiated with 3 W average laser powers. As shown in **Figure 2-17** (left), the highest removal rate of 0.16 mm³/min was obtained with a pulse repetition rate between 50 kHz and 100 kHz, and decreased with higher repetition rates. However, the author did not explain that the lower ablation rates might be caused by the decrease of the irradiated energy. The decrease of the irradiated laser energy must be taken into discussion, due to the relation between average laser power, the repetition rate and the pulse energy. The pulse energy decreases with higher repetition rates, when the average laser power is constant.

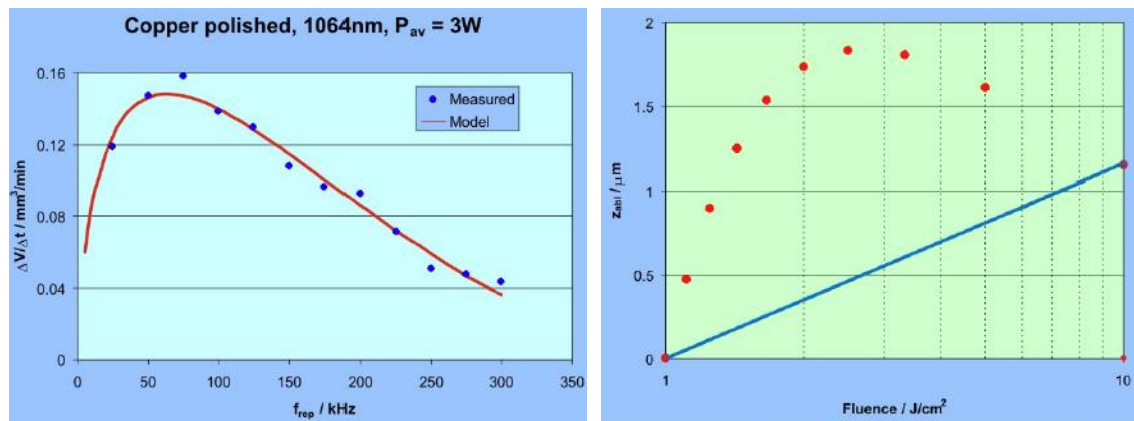


Figure 2-17 left: Experimental and calculated ablation rates as a function of the repetition rate using an average laser power of 3 W; **right:** Ablation depths calculated for single pulse ablation (blue line) and multiple pulse irradiations, red dots represent ablation depths achieved with a total amount of irradiated laser fluence of 10 J/cm², taken from reference [100].

Furthermore, the results presented indicate that a higher ablation depth can be obtained by multiple irradiations using low-fluence laser pulses. Accordingly **Figure 2-17** (right) shows a considerably higher ablation depth obtained with 4 pulses of 2.5 J/cm² (red dots,) compared to a single irradiated laser pulse of 10 J/cm² (blue line). In both cases the total incident laser fluence was constant of 10 J/cm².

The authors conclude that picosecond laser pulses are well-suited to micro processing. In addition they point out that novel control concepts and beam guiding systems with marking speeds of several 100 m/s must be developed to leverage the high-PRF laser

2.6 Summary

technology in the industrial fields. Thus in a first approach [98], fast laser beam deflection has been realised. As shown in **Figure 2-18** (left), a fast rotating cylinder engraving system of 40 m/s scan speed has been used in combination with an even faster acousto-optical deflector (AOD). With the “cross-scan” pulse separation technique, ablation rates as high as 3 mm³/min were obtained (**Figure 2-18**, right).

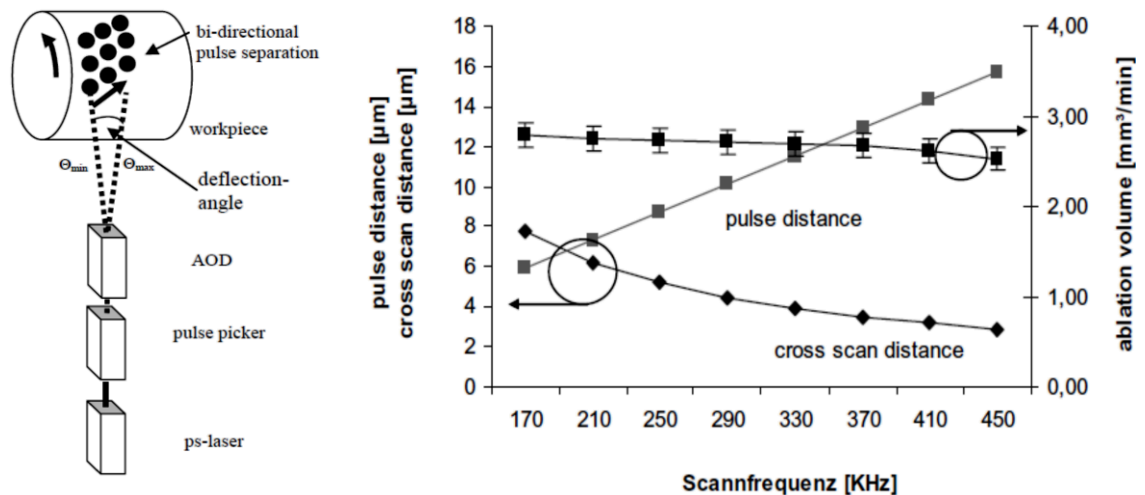


Figure 2-18 left: Machining setup presented in reference [98] for fast laser beam deflection consisting of a fast rotating cylinder engraving system in combination with an acousto-optical deflector (AOD), right: pulse distance and ablation volumes as a function of the scan frequency, obtained using the presented “cross-scan” technique.

2.6 Summary

In this chapter the fundamentals of ultrashort pulse laser processing were discussed to highlight the advantages and critical aspects of this technology in micromachining. The actual state of the art of the ultrashort pulse laser technology in micro processing was presented, followed by the phenomena and effects occurring in laser matter interaction. For ultrashort pulse laser irradiation, the literature research identified phase explosion and critical point phase separation rather than evaporation as the most dominant material removal mechanism. This knowledge will be included in energy balance calculations carried out in *Section 6.5*, helping to clarify the nature of high-PRF laser ablation.

The high-PRF laser drilling experiments reported to date in the literature examined the

impact of the repetition rate on material removal. Heat accumulation and particle shielding were identified as novel phenomena affecting laser matter interaction for ultrashort pulses. Beside these results achieved in fundamental investigations, the application of high-PRF femtosecond lasers to three-dimensional micro structuring has not been published in the recent research literature. Furthermore, in particular for metals, the interplay between heat accumulation and particle shielding, as well as their impact on the machining process has not been sufficiently investigated and understood. Thus a detailed study is required in order to overcome the knowledge gap in terms of complex interaction processes, induced upon high-PRF femtosecond laser irradiation.

Furthermore, the literature research gained a greater insight into energy transport following ultrashort pulse laser irradiation. For fluence levels between the “low-fluence” and the “high-fluence” regime, a gap between experimental and modelled ablation rates was identified. In addition, a few studies considered ballistic energy transport instead of optical penetration for material ablation. Thus more study is needed to contribute to clarify the nature of material ablation. Furthermore, the different energy transport mechanisms recognised in the literature review will be included in a volume ablation rate calculation model. This model will be introduced in *Section 4.3* to evaluate material removal in high-PRF femtosecond laser ablation.

In addition, the currently most accepted mechanisms for laser-induced ripple and cone-like shaped micro structure formation were presented. Recent studies indicate a super-hydrophobic surface behaviour of cone-covered surfaces, processed by using ultrashort laser pulses. The formation mechanism of these cone-like shaped structures is insufficiently understood up to now. In *Section 7.3* the appearance of cone-like microstructures induced by high-PRF laser pulses will be compared to cone formation mechanisms as presented here for laser irradiation using nanosecond laser pulses.

Finally, the actual state as well as the prospects and limitations of the ultrashort pulse laser technology were discussed. The literature review revealed that a detailed study of the interplay between the distinctive mechanisms and processes occurring in high-PRF femtosecond laser processing is required to overcome the current limitations of knowledge. Also it has become evident that only the development of innovative machining concepts can facilitate the successful transfer of the high-PRF femtosecond laser technology to high-precision micromachining.

3 Materials and methodology

3.1 Materials

3.1.1 Investigated materials

The experiments presented in this thesis were conducted using three different industrial grade materials with differing thermo-physical properties: 0.5 mm thick Stainless steel metal sheet X5CrNi18-10 (1.4301, AISI 304), an Aluminium alloy metal bar (Aluminium 6082-T6), and a polished 99 % pure Copper metal sheet of 0.4 mm thickness. Both optical and thermo-physical properties of the investigated materials are discussed. In this thesis, the different investigated metals are designated as follows: Stainless steel denotes the X5CrNi18-10 metal sheet, Copper the 99 % pure Copper metal sheet, and Aluminium the Aluminium 6082-T6 metal bar.

3.1.2 Optical material properties

Material ablation strongly depends on the absorptivity, but optical properties of either industrial grade or laser-treated surfaces differ considerably from the values of virgin materials. Thus for Aluminium, Copper, and Stainless steel the absorptivity of both industrial grade and laser treated surfaces was evaluated by reflectivity measurements. In the later *Section 6.3*, the surface reflectivity values will be used in surface temperature calculations to estimate the amount of remaining laser energy.

The measurements were carried out using an integrating sphere assembly, schematically shown in **Figure 3-1**. It consisted of a hollow spherical standard integrating sphere cavity (K-200G; LOT-Oriel [101]) with small holes for entrance and exit ports, a continuous wave pump laser, a photodiode as optical detector and an oscilloscope for signal recording. The sphere was covered with a high-diffuse reflective gold coating. The wavelength of the unpolarised pump beam of 1070 nm was close to the wavelength of the femtosecond laser beam of 1030 nm, used in this thesis. The pump beam of about 5 W average power was directed through the entry hole of the sphere to the sample surface. The sample was mounted on the exit port of the cavity. The amount of

3.1 Materials

radiation, scattered or reflected by the sample surface was detected by a photodiode through a 90° off-axis port.

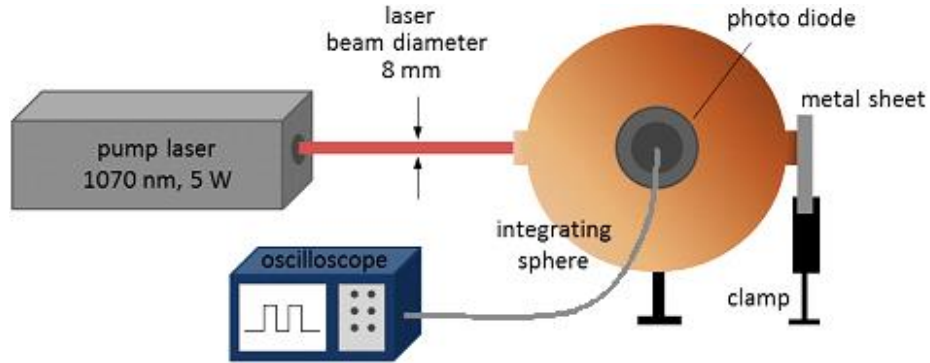


Figure 3-1 top: Schematic of the integrating sphere assembly used in reflectivity measurements on both virgin and laser-treated metal sheet surfaces.

The surface reflectivity of the studied metal samples was varied by surface laser ablation using high-PRF femtosecond laser radiation. The applied laser processing conditions are described in **Table 3-1**. Pump laser irradiations and photodiode measurements were carried out at room temperature and atmospheric air pressure.

In this thesis, the reflectivity \mathbf{R} of the different investigated metals was calculated by the ratio of photodiode signal levels, recorded in reflectivity measurement arrangement [102] accordingly

$$R = \frac{U_M - U'_M}{U_S - U'_S} R_S \quad \text{Equation 3-1,}$$

where \mathbf{U}_M is the voltage from the photodiode of the metal surface during pump laser beam irradiation, \mathbf{U}'_M is the dark signal of the metal surface, \mathbf{U}_S is the voltage from the photodiode of the calibration standard during irradiation, \mathbf{U}'_S is the dark signal of the calibration standard, and \mathbf{R}_S is the reflectivity of the calibration standard, which was $\mathbf{R}_S = 0.99$.

The metal samples were irradiated by a number of one millisecond long pump laser irradiations; the duty cycle was 50 %. For reflectivity calculation, the height of the photodiode voltage signal has been determined as mean value, averaged over nine individual measurements. The signal height correlates to the reflective characteristic of the sample surfaces. As an example, the calculated surface reflectivity obtained for three

3.1 Materials

individual pump laser irradiations on differently reflective Stainless steel samples is shown in **Figure 3-2**. The averaged photodiode voltage levels for all investigated metal samples as well as the respective reflectivity plots calculated for Aluminium and Copper can be seen in *Annex 1*. In addition to these signal levels, the measurement uncertainties are presented, obtained based on standard deviation calculations. For voltage levels measured ranging up to 13.95 V, the standard deviation was equal or smaller than 0.32 V.

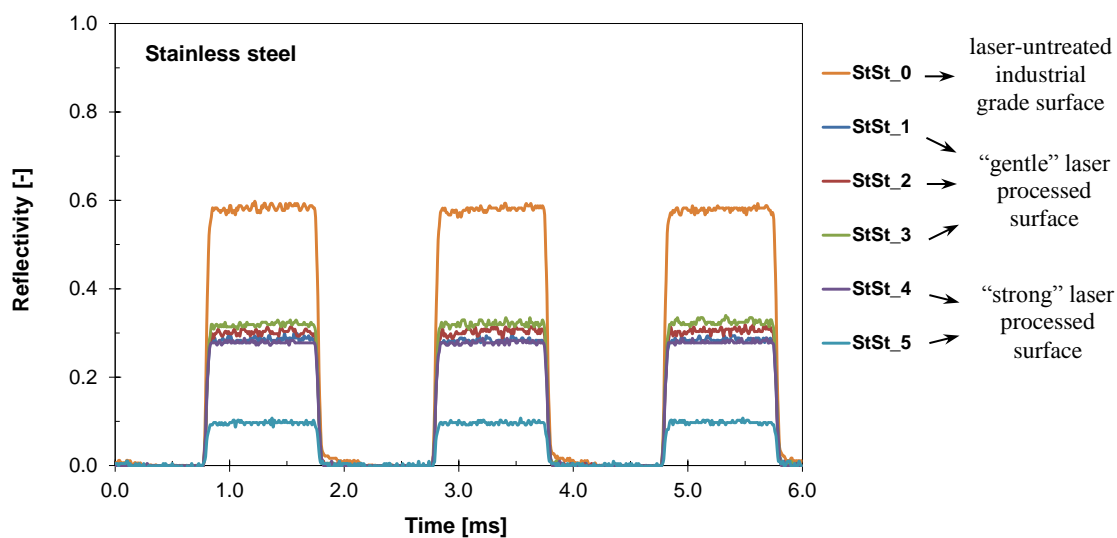


Figure 3-2: Reflectivity calculated from photodiode signals recorded for pump laser irradiations of Stainless steel; StSt_0 to StSt_5 represent differently reflective surface characteristics as described in **Table 3-1**.

The curve **StSt_0**, given in the plot above, represents the reflectivity of the untreated technical metal surface. The curves **StSt_1** to **StSt_5** correspond to the reflectivity obtained on metal sheets machined applying either the “gentle” or “strong” ablation regime. The “gentle” ablation regime indicates processing conditions, which lead to a smooth and almost melt-free surface; in the “strong” ablation regime rough and dark-coloured surfaces were obtained. The number of scan passes and the hatch distance were varied.

Table 3-1 lists the reflectivity **R** and the absorptivity **A** for the studied Aluminium, Copper and Stainless steel metal samples, calculated accordingly

$$A = 1 - R \quad \text{Equation 3-2.}$$

3.1 Materials

Table 3-1: Reflectivity and absorptivity calculated from voltage levels obtained in integrating sphere measurements on differently reflective Aluminium, Copper, and Stainless steel surfaces.

	Sample name	Process regime	Reflectivity R	Absorptivity A
Aluminium	Al_0	laser untreated technical surface	0.72	0.28
	Al_1	“gentle” ablation regime 1 scan	0.51	0.49
	Al_2	“gentle” ablation regime 10 scans	0.54	0.46
	Al_3	“gentle” ablation regime 25 scans	0.57	0.43
	Al_4	“strong” ablation regime wide hatch distance - 10 scans	0.54	0.46
	Al_5	“strong” ablation regime small hatch distance - 5 scans	0.21	0.79
Copper	Cu_0	laser untreated technical surface (polished)	0.97	0.03
	Cu_1	“gentle” ablation regime 1 scan	0.90	0.10
	Cu_2	“gentle” ablation regime 10 scans	0.87	0.13
	Cu_3	“gentle” ablation regime 25 scans	0.87	0.13
	Cu_4	“strong” ablation regime wide hatch distance - 10 scans	0.83	0.17
	Cu_5	“strong” ablation regime small hatch distance - 5 scans	0.28	0.72
Stainless steel	StSt_0	laser untreated technical surface	0.57	0.43
	StSt_1	“gentle” ablation regime 1 scan	0.28	0.72
	StSt_2	“gentle” ablation regime 10 scans	0.30	0.70
	StSt_3	“gentle” ablation regime 25 scans	0.32	0.68
	StSt_4	“strong” ablation regime wide hatch distance - 10 scans	0.28	0.72
	StSt_5	“strong” ablation regime small hatch distance - 5 scans	0.10	0.90

It can be seen that the absorptivity of the laser-treated surfaces is significantly higher, compared to the untreated metal surfaces. The absorptivity changes slightly with the higher number of scan passes in the “gentle” processing regime. The highest absorptivity was obtained in “strong” laser processing. The absorptivity \mathbf{A} of metal surfaces processed in the “gentle” regime can be estimated to be approximately $\mathbf{A} = 0.46$ for Aluminium, $\mathbf{A} = 0.13$ for Copper, and $\mathbf{A} = 0.70$ for Stainless steel, respectively.

The absorptivity/reflectivity values obtained in own measurements, i.e. $\mathbf{R} = 0.97$ for untreated Copper (see **Table 3-1**), seem to be representative due to the good agreement to $\mathbf{R} = 0.97$, presented in [34] for Copper. Furthermore, the reflectivity of laser processed Copper of $\mathbf{R} = 0.87$ agrees to the literature value of $\mathbf{R} = 0.85$, determined in vacuum by using hemi-ellipsoidal metallic reflector technique [36]. However, the comparison of the absorptivity/reflectivity determined in this thesis on laser treated metal sheets with values presented in the literature for untreated technical metal surfaces reveals significant differences. The absorptivity of $\mathbf{A} = 0.15$ for Aluminium [26], $\mathbf{A} = 0.05$ for Copper [26], and $\mathbf{A} = 0.3$ for Steel [29] has been estimated from the reflectivity curves presented in **Figure 3-3** (top) for near-infrared laser radiation at room temperature. These absorptivity values are considerably lower than experimentally determined values presented in **Table 3-1**.

Moreover it can be observed in **Figure 3-3** that the absorptivity increases with increasing surface temperatures. The increase of the surface temperature induced by heat accumulation has been already mentioned in *Section 2.5.2*. As a result, enhancement of laser beam absorption at higher surface temperatures has to be considered in high-PRF laser processing.

The percentage increase of the absorptivity with increasing metal surface temperature is shown in **Figure 3-3** bottom. The data have been derived from the plots given in this figure above. Compared to the absorptivity at room temperature, the highest growth of absorptivity was found for Copper with a percentage increase of 450 % at 1,100 °C, followed by Aluminium with 100 % at 580 °C and Steel with almost 9 % at 1,000 °C.

3.1 Materials

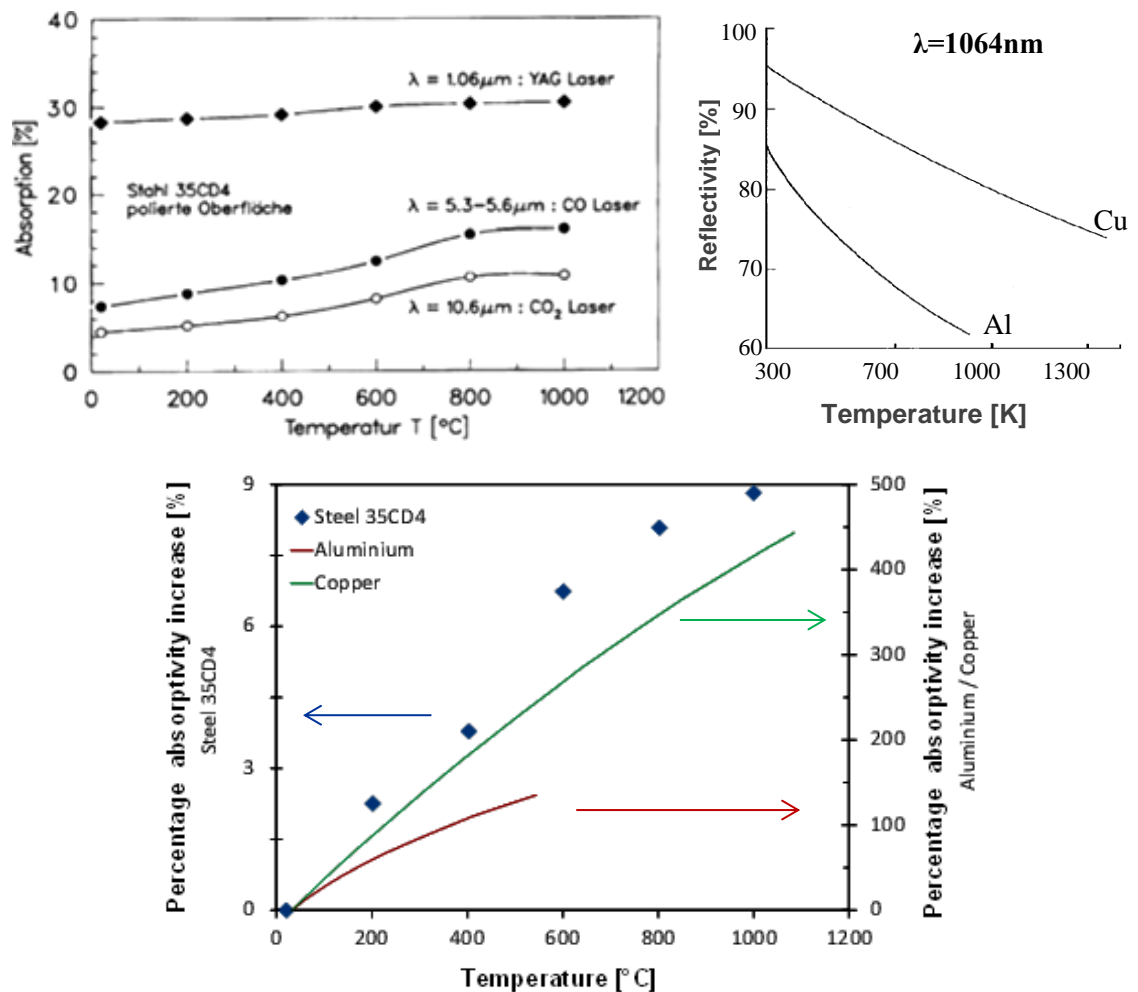


Figure 3-3: Absorptivity and reflectivity versus temperature; **top:** literature data presented for Steel 35CD4 (left) [29] as well as Aluminium and Copper (right) [26], **bottom:** percentage increase of the absorptivity for near-infrared laser radiation versus the temperature, derived from the literature data given above.

YAHNG et al. [30] studied the impact of the substrate temperature on the ablation depth by irradiating Stainless steel at two different substrate temperatures (300 K, 900 K). As shown in **Figure 3-4**, in the fluence regime below 1 J/cm^2 material ablation was almost unaffected by the temperature in laser processing. With higher fluence, by contrast, the ablation depth increased remarkably at the higher substrate temperature of 900 K. Furthermore it was found, that the surface roughness decreased with the higher temperature. The authors explained the results by the more effective laser beam absorption induced by the higher substrate temperatures.

3.1 Materials

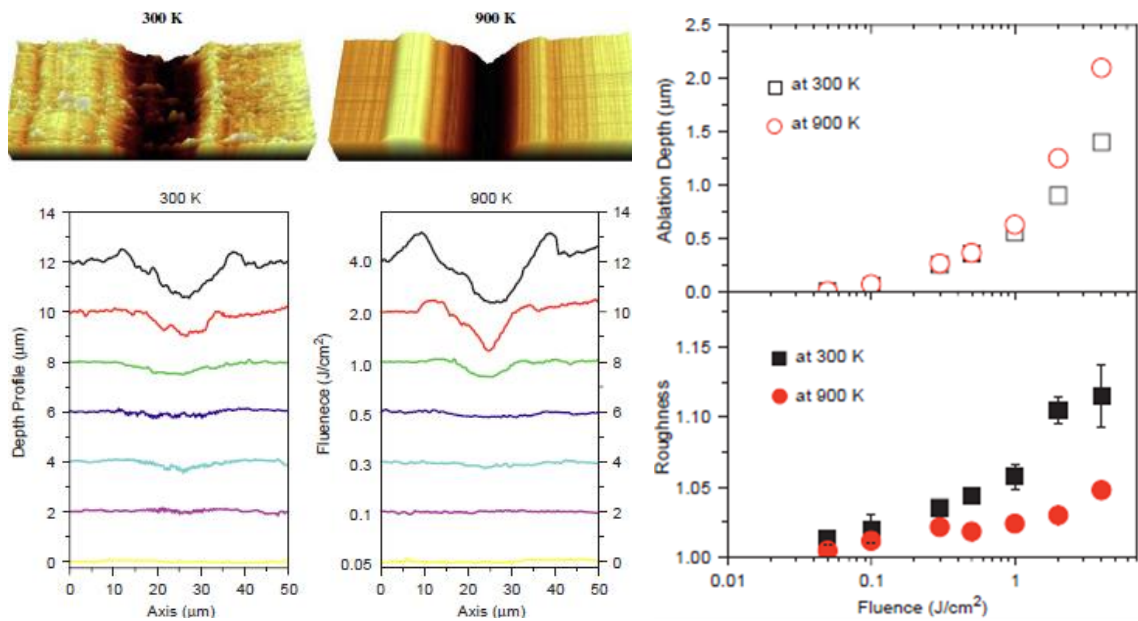


Figure 3-4: Impact of the substrate temperature on ablation depth and roughness, presented for Stainless steel by *YAHNG et al.* [30].

The transfer of the absorbed laser energy into the solid, and thus also the amount of laser removed material, is determined by the absorption coefficient and the respective optical penetration depth. Absorption coefficients and optical penetration depths of pure Aluminium, Copper and Iron as the main constituents of the investigated metal alloys are presented in **Table 3-2**. These data were calculated accordingly **Equation 2-4** and **Equation 2-6** by taking into account the wavelength of the incident laser beam (1,030 nm) as well as the extinction coefficients, given in [34] and [103] for Aluminium and Iron, and Copper, respectively.

Table 3-2: Optical penetration depths for near-infrared laser irradiation of Aluminium, Copper and Iron, calculated by using **Equation 2-4** and **Equation 2-6**.

Parameter		Aluminium	Copper	Iron
Wavelength λ	nm	1,030	1,030	1,030
Extinction coefficient k	-	10.01	6.79	4.26
Absorption coefficient α	1/m	$1.2 \cdot 10^8$	$0.8 \cdot 10^8$	$0.5 \cdot 10^8$
Optical penetration depth δ_{opt} (calculated)	nm	8.2	12.1	19.0

3.1.3 Thermo-physical material properties

The thermo-physical properties of the investigated materials are listed in **Table 3-3**. Because of the lack of available data for the industrial grade metal alloys, data of both pure Aluminium and Copper have been included. In addition comparative values are presented for missing data, taken from materials with comparable alloy compositions.

Table 3-3: Thermo-physical properties of industrial grade metal alloys and both pure Aluminium and Copper; ^[1] [104], ^[2] [105], ^[3] [106], ^[4] [107], ^[5] [108], ^[6] calculated according to **Equation 6-5**; missing values for Aluminium 6083-T6 are supplemented by data achieved for Aluminium alloy 6061-T as a material with comparable alloy composition, indicated by *).

Parameter		Aluminium 6082-T6	Aluminium	Copper	Stainless steel
Thermal conductivity λ	$\text{W m}^{-1} \text{K}^{-1}$	165-185 ^[1]	273 ^[4]	390 ^[4]	14.5 ^[5]
Specific heat capacity c_p	$\text{J kg}^{-1} \text{K}^{-1}$	*) 869 ^[2]	900 ^[4]	390 ^[4]	472 ^[5]
Thermal diffusivity D	$10^{-6} \text{m}^2/\text{s}$	*) 64 ^[3]	97 ^[3]	115 ^[3]	3.9 ^[6]
Melting temperature T_{melt}	$^{\circ}\text{C}$	585 – 650 ^[1]	660 ^[4]	1,083 ^[4]	1,398 - 1,454 ^[5]
Evaporation temperature T_{evap}	$^{\circ}\text{C}$	n.a.	2,467 ^[4]	2,567 ^[4]	2,945 ^[5]
Density ρ	kg/m^3	2,700 ^[1]	2,702 ^[4]	8,960 ^[4]	7,920 ^[5]

The presented data for the thermal conductivity λ , specific heat capacity c_p , and thermal diffusivity D are given at 300 K, but thermo-physical properties strongly depend on the temperature. Moreover, with the change of the state of aggregation from solid to liquid the thermo-physical material constants will change significantly. Thus **Figure 3-5** presents the thermal conductivity of the main alloy constituents versus the temperature [29]. The thermal conductivity of both Copper and Iron decreases slightly with increasing temperature; on molten Aluminium, by contrast, a drastic drop is recognised.

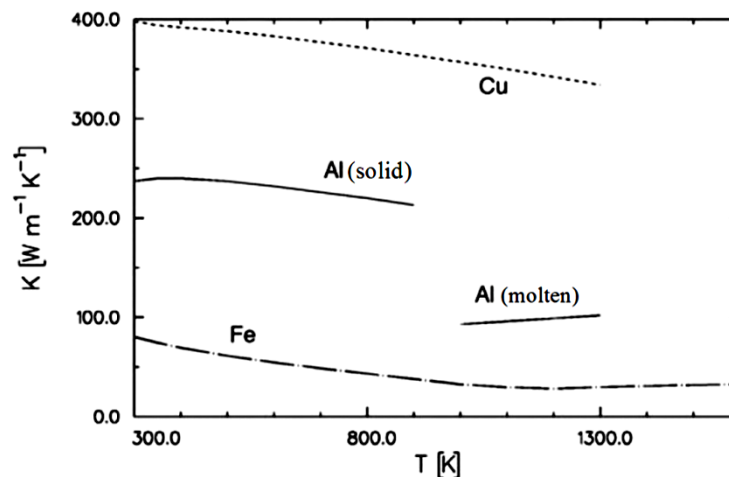


Figure 3-5: Thermal conductivity versus temperature, presented for the main alloy constituents of the investigated metal sheets, taken from reference [29].

3.2 Experimental setup

3.2.1 Micromachining work station

The experiments were conducted using a laser micromachining work station [109, 110], located at the University of Applied Sciences Mittweida (Germany). The work station was designed and constructed by the “*Rapid Micro Tooling*” research group with the “*Laser Institute at the University Mittweida*” [111], launched within the framework of the project “*INNPROFILE – Rapid Micro Tooling with Laser Based Methods*”. A schematic drawing of the work station is presented in **Figure 3-6**.

Central part of the work station was a commercially available high-PRF femtosecond laser system *IMPULSE™* (Clark-MXR Corp., USA) consisting of a diode direct pumped Yb-doped oscillator / amplifier configuration. The laser pulses were generated in a passive mode-locked fibre ring oscillator, where laser modes with fixed phase relationships interfere periodically constructively. Power scaling of the seed pulses utilising a regenerative amplifier fibre setup provided emission of high-intense ultrashort laser pulses. In contrast to the standard *IMPULSE™* model, the laser system used in this work was equipped with another acousto optical modulator (AOM). This special inboard feature was required for user-defined fast laser beam switching.

3.2 Experimental setup

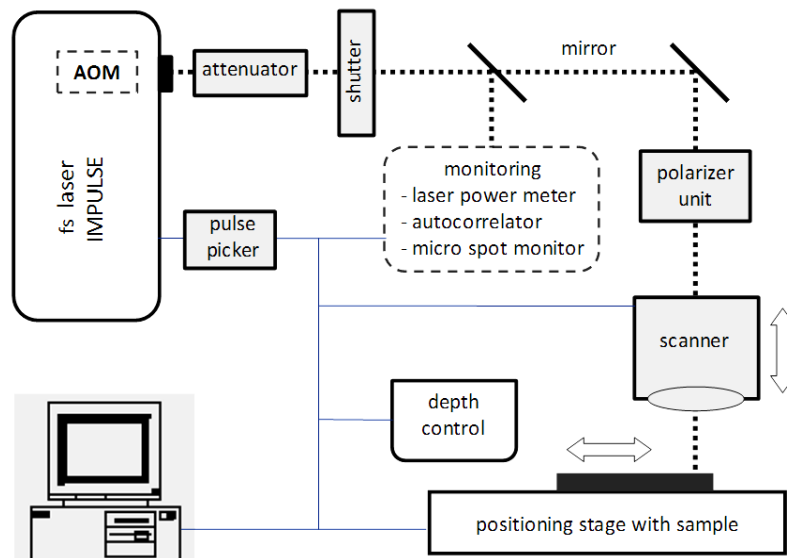


Figure 3-6: Schematic of the laser micromachining work station.

Significant laser parameters, i.e. laser output power, laser pulse duration, and pulse repetition rate were user-adjustable via computer. The machining setup was located in an environmentally controlled room to ensure constant ambient conditions.

The power of the laser beam was controlled by an external half-wave plate polariser attenuator. Turning the half-wave plate's fast axis rotated the angle of the polarisation plane twice, and the beam was attenuated by a polarised beam splitter. Another external polariser stage was implemented to set either user-defined polarisation direction or circular polarisation of the laser beam. This stage consisted of a half-wave plate retarder, quarter-wave plate and bi-prism.

In addition, a number of measuring instruments were included in the setup, a power meter (Gentec), autocorrelator (*MINI*, APE) and focus spot monitor (*MicroSpotMonitor*, Primes). By using this equipment, the laser output power, laser pulse duration, as well as beam waist in the focal region, and focus spot size were monitored, respectively.

The laser beam was deflected by different scan technologies (galvanometer scanner, resonant scanner), synchronised with the laser beam by an external pulse picker. With this external pulse picker, the pulse repetition rate could be set to discrete values ranging between single pulses and 1.4 MHz. The upper limit of the pulse repetition rate was determined by the rise time of the acousto optical modulator being used. In addition, individual pulse sequences could be designed, varying between single shots

3.2 Experimental setup

and bursts consisting of any number of pulses up to the maximum pulse repetition rate. The use of the pulse picker module offered more flexibility in the study of material removal upon high-PRF laser processing.

Relative movement between galvanometer scanner and the sample was carried out by using a high-precision three-axis positioning stage (Foehrenbach), applied in combination with *Automation 3200* multi-axis motion controller (Aerotech). The setup was completed by a confocal single point displacement sensor (CF4; nanoFocus) for “in situ” measurements of the ablation depth and surface roughness.

A view into the laboratory provides **Figure 3-7**.

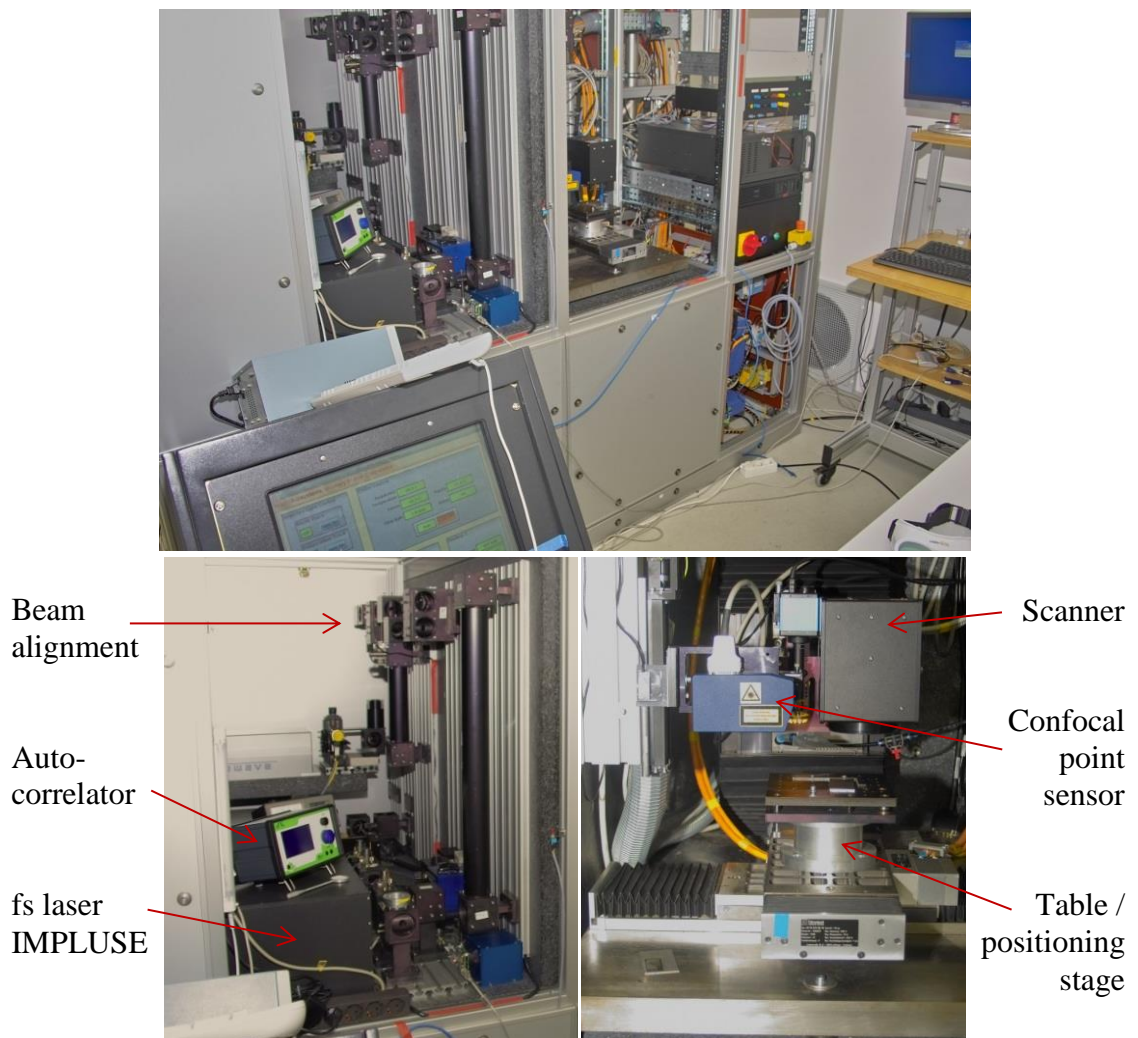


Figure 3-7: A view into the laboratory, micromachining work station (top), laser system / laser beam alignment / measurement equipment (bottom left), and processing chamber (bottom right).

3.2.2 Laser system

The *IMPULSE*TM system emitted a horizontally polarised laser beam with central laser wavelength λ_0 of 1,030 nm, beam propagation factor M^2 of 1.2, and variable repetition rate f_R ranging between 205 kHz and 24.8 MHz. A maximum pulse energy Q_P of 8.2 μ J was provided by the laser system for pulse repetition rates ranging between 200 kHz and 1.78 MHz. With the higher pulse repetition rates, the pulse energy decreased according to the relation

$$P_{av} = Q_P \cdot f_R \quad \text{Equation 3-3,}$$

where P_{av} is the average laser power. The maximum average laser output power P_{av} of 13.8 W was measured at repetition rates higher than 1.78 MHz, as shown in **Figure 3-8**.

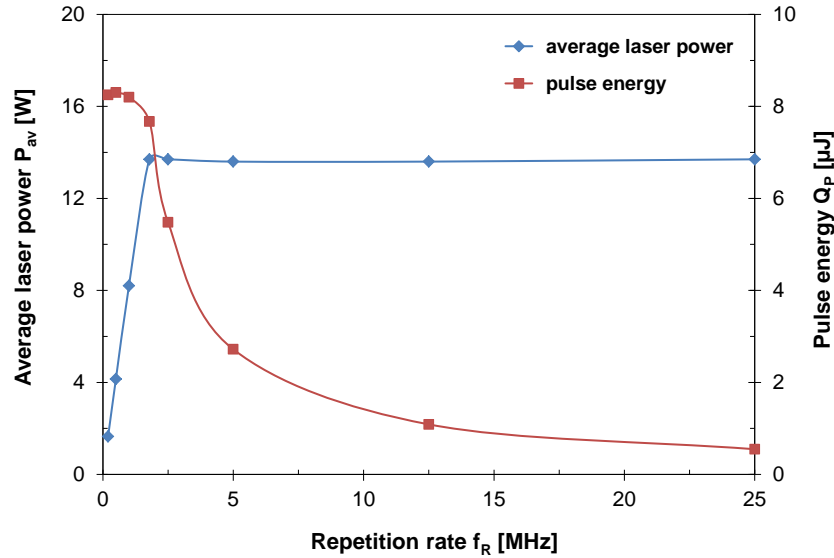


Figure 3-8: Average laser output power and pulse energy versus pulse repetition rate.

The temporal shape of an ultrashort laser pulse depends on the amplitude and phase relationship of the longitudinal laser modes. Theoretically the minimum pulse duration as the full width at half-maximum (FWHM) value of optical power versus time can be estimated from the *time-bandwidth product*. This measure relates to the product of the temporal pulse duration $\Delta\tau$ and the spectral width of the laser pulse in the frequency space $\Delta\nu$ accordingly

$$\Delta\tau \cdot \Delta\nu \geq const \quad \text{Equation 3-4.}$$

3.2 Experimental setup

The temporal pulse shape of the *IMPULSE*TM laser pulse is characterised by the hyperbolic-secant-squared distribution (sech^2), and the time-bandwidth product is 0.315. A minimal pulse duration of 100 fs can be calculated theoretically by taking into account the spectral bandwidth of the laser beam of $\Delta\lambda = 10$ nm. In reality, the pulse duration increases when high-intense ultrashort laser pulses propagate through optical elements i.e. the power amplifier fibre. Nonlinearities and higher order chromatic dispersions temporally stretch the laser pulse while leaving its spectral width constant. This chirp of the ultrashort pulse cannot be fully compensated by the pulse compressor.

The shortest pulse duration of the *IMPULSE*TM laser beam was measured as 176 fs, calculated from the autocorrelation trace recorded with the *MINI* autocorrelator. A typical autocorrelation trace including analysis data is given in **Figure 3-9** (left). The measured symmetric autocorrelation trace (white line) fits very well to a hyperbolic-secant-squared pulse shape (sech^2 ; green line). The wings existing on both sides of the autocorrelation function indicate the residual frequency shift (chirp) after pulse compression as a result of the higher order dispersion.

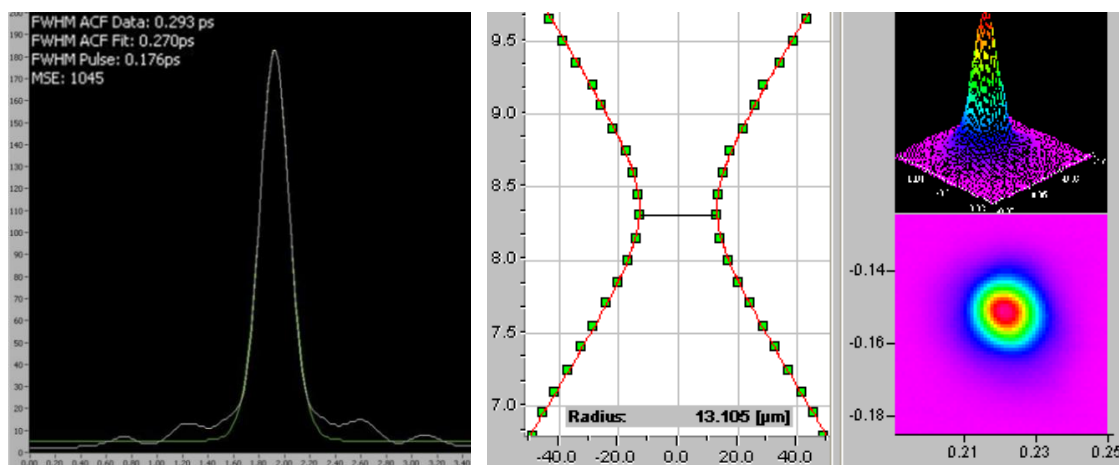


Figure 3-9 left: Autocorrelation trace of a laser pulse with a pulse duration of 176 fs (sech^2); **centre:** beam caustic measurement of the focused laser beam using 56 mm f-theta objective, obtained utilising the *MicroSpotMonitor*, **right:** intensity distribution (top) and size (bottom) of the laser pulse in the focal plane.

The laser beam was focussed onto the sample surface by using a 56 mm telecentric f-theta objective. The spatial laser beam parameters were determined based on *MSM MicrospotMonitor* beam waist measurements, presented in **Figure 3-9** (centre). The intensity distribution as well as the laser spot size in the focal plane can be seen in **Figure 3-9** (right).

3.2 Experimental setup

At the beginning of this work, the focus spot diameter was measured of $w_0 = 26.2 \mu\text{m}$, but this diameter enlarged to $30 \mu\text{m}$ during the experiments. The parameters were specified by the variable aperture method in accordance to the **ISO 11146-3** standard for Gaussian laser beams [112]. This method allows laser beam transmission of 86.5 %, which is equal to the $1/e^2$ value of the total laser beam power.

The maximum laser peak power P_{\max} and the maximum intensity I_0 of the laser pulse have been calculated as follows

$$P_{\max} = \frac{1}{1.135} \cdot \frac{Q_P}{\tau_H} \quad \text{Equation 3-5,}$$

where 1.135 is the correction factor for sech^2 temporal pulse shape, and

$$I_0 = \frac{2 P_{\max}}{\pi w_0^2} \quad \text{Equation 3-6.}$$

According to **Equation 3-5** and **Equation 3-6**, femtosecond laser pulses with a maximum laser power of $4.1 \cdot 10^7 \text{ W}$ and a maximum intensity of $1.5 \cdot 10^{13} \text{ W/cm}^2$ were applied in this work. The values were calculated by taking into account the shortest pulse duration of 176 fs, the maximum available pulse energy of 8.2 μJ , and the focal spot radius of 13.1 μm . The maximum laser peak fluence H_0 of a single laser pulse was 3.0 J/cm^2 , calculated according to

$$H_0 = \frac{2 Q_P}{\pi w_0^2} \quad \text{Equation 3-7.}$$

Figure 3-10 plots the maximum achievable peak fluence versus the pulse energy, calculated by using **Equation 3-7** and the focal spot radius of 13.1 μm . The fluence irradiating the sample surface is slightly decreased, compared to the fluence available at the beam exit of the laser system.

This lower fluence occurred due to energy losses caused by the limited reflectivity of optical beam guidance elements. The energy losses were measured of approximately 3 %, between the beam exit at the laser source and the sample surface. In addition, the maximum available laser pulse energy decreased from 8.2 μJ to 7.1 μJ during the experiments that was mainly attributed to internal laser system re-adjustments. Furthermore the diameter of the emitted laser raw beam reduced during the

3.2 Experimental setup

experimental period. This caused the enlargement of the minimum achievable focus spot diameter from 26 μm to 30 μm . As a result, the maximum of the effective peak fluence irradiating the work piece surface decreased to 1.9 J/cm^2 at the end of the experimental period.

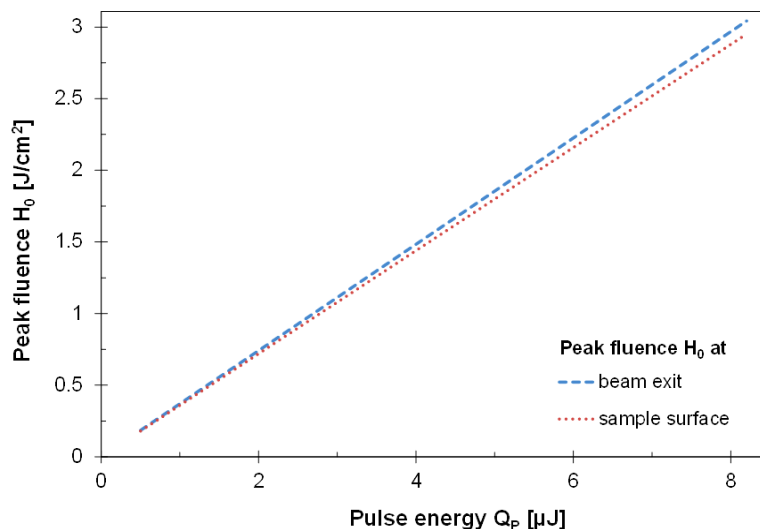


Figure 3-10: Laser peak fluence available at laser source beam exit and impinging on the work piece surface versus single pulse energy.

The values obtained for the most important laser parameters are presented in **Table 3-4**.

Table 3-4: Laser parameters.

Parameter		Value
Wavelength λ (centre)	nm	1030
Pulse duration τ_H (sech ²)	fs	> 176 fs
Max. average laser power P_{av}	W	13.8 W
Repetition rate f_R	MHz	0.2 ... 24.8 (single pulse)
Max. pulse energy Q_P	μJ	8.2
Beam propagation factor M^2	-	1.2
Focus spot radius w_0 (56mm f-theta objective)	μm	13.1
Max. peak power P_{max}	W	4.1×10^7
Max. peak intensity I_0	W/cm^2	1.5×10^{13}
Max. peak fluence H_0	J/cm^2	3.0

3.2.3 Scan systems

In the experiments the laser beam was deflected across the work piece surface by applying two different scan technologies. In most of the experiments two galvanometer scan systems were applied, providing supplementary machining characteristic. These were the *hurrySCAN II 14* (Scanlab AG) with a higher scan speed to increase the machining speed, and the *intelliSCAN 14* (Scanlab AG) with higher resolution to increase the machining precision. In addition a one-dimensional deflecting resonant scan system of our own design was used in initial studies to investigate high speed laser processing. An operation scheme of the galvanometer scan technique is given in **Figure 3-11**.

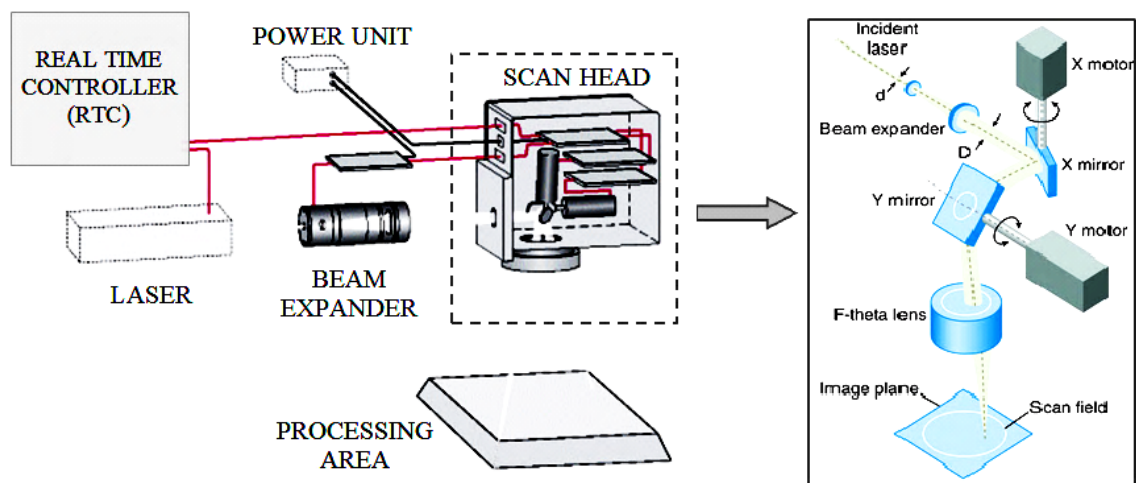


Figure 3-11 left: Operation scheme of laser beam deflection using galvanometer scan systems, taken from website of Scanlab AG; **right:** detail view of laser scan technology, taken from reference [113].

The laser beam is deflected by two different mirrors in both X and Y direction, driven by galvanometer motors respectively. Synchronised and real time controlled interplay between the laser and scan mirrors is guaranteed via the real time interface board **RTC 5** (Scanlab AG).

The other laser beam deflection technology, a self-constructed resonant scan system developed by the *Rapid Micro Tooling* group (SCHILLE / HARTWIG / KLOETZER [111]) is shown in **Figure 3-12 a**. The resonant scan system consisted of a high speed resonant optical scanner *SC-30* (EOPC) and a fixed beam deflection mirror. The scanner oscillated in sinusoidal motion with a fixed frequency of 3.4 kHz. The laser system, resonant scanner and control software were synchronised via the pulse picker

3.2 Experimental setup

module. This setup was used for fast laser beam deflection in initial high speed laser ablation experiments. The highest scan speed was reached at the zero-crossing point, and dropped to zero at the mirror turning points. As a result the laser beam irradiated the sample surface with constantly changing scan speeds and respective varying lateral pulse spacing, in spite of the constant laser pulse repetition rate. As such, **Figure 3-12 b** exemplifies the varying lateral pulse spacing between consecutively incident laser pulses along a line-scan at a repetition rate of 502 kHz. In the figure the widest lateral pulse spacing can be estimated to be 190 μm , representing a scan speed of about 95 m/s. The maximum achieved scan speed was higher than 130 m/s, and a lateral pulse spacing of 32 μm was obtained at 4.1 MHz pulse repetition rate.

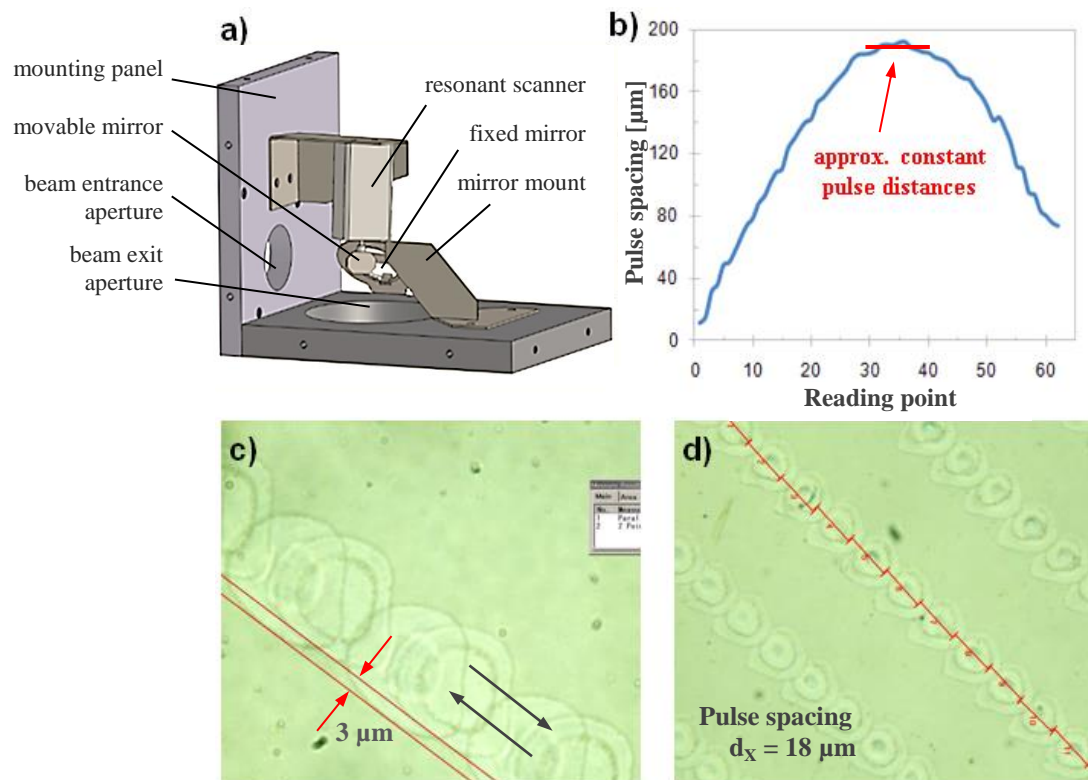


Figure 3-12: Resonant scan technology: (a) schematic of the resonant scanner assembly consisting of a movable mirror driven by resonant scanner and a fixed reflection mirror; (b) lateral pulse spacing along a single line-scan; (c) lateral mismatch between two laser processed lines of one oscillation period; (d) constant lateral pulse spacing enclose the zero-crossing position of the scan mirror.

However, high precision micromachining requires constant processing conditions. As a result the usable processing range for the resonant scan system was determined by a line-scan area of almost constant scan speed and constant lateral pulse spacing. This specific processing area is located close to the zero crossing position of the scan mirror.

3.2 Experimental setup

This area is illustrated in **Figure 3-12 d** for 1.02 MHz repetition rate, 18 μm pulse spacing and 18 m/s scan speed, respectively. Modulation of the scan amplitude enabled the adjustment of the lateral pulse spacing. The longest processing length of approximately 2 mm was reached at the maximal scan amplitude. The decrease of the scan amplitude, in turn, caused a reduced length of the processing path.

Further, as shown in **Figure 3-12 c** a lateral mismatch of approximately 3 μm was detected between two laser processed lines of a single scan mirror oscillation period. As a result, in line-scan laser ablation experiments only one scan direction was used.

The main advantage of the self-constructed resonant scan system was a considerably faster scan speed up to 130 m/s against 4.5 m/s using the galvanometer scanner. On the other hand, the galvanometer scanner covered a scan field of 25 x 25 mm². This is considerably larger than the processing area provided by the resonant scanner system.

By using the resonant scan system, overlapping laser pulses with constant lateral pulse spacing in scan direction of 4 μm were supplied only within a scan range of approximately 0.75 mm. A further disadvantage was that no beam deflection was available in the second orthogonal direction, which is clearly required for fast two-dimensional plane laser processing.

Using the 56mm f-theta focusing objective the focal spot radius was 16 μm , which is slightly larger than the focus spot obtained with the galvanometer scan system. This may occur either due to the incorrect position of the resonant scan mirror to the focussing lens or misalignments of laser beam travelling through the resonant scan system. As a result imaging artefacts may occur, i.e. optical distortions and coma error, induced by the applied sensitive aspherical f-theta objective.

A summary of the significant scanner parameters is given in **Table 3-5**.

3.3 Machining process

Table 3-5: Scanner parameter; ¹⁾ scan speed with a constant lateral pulse spacing of $d_x = 32 \mu\text{m}$ @ 4.1 MHz, ²⁾ scan speed with constant lateral pulse spacing $d_x = 4 \mu\text{m}$ @ 4.1 MHz, ³⁾ irradiating the work piece surface.

Parameter	Galvanometer scanner		Resonant scanner
	hurrySCAN II 14	intelliSCAN 14	
Max. scan speed v_s	10.0 m/s	4.5 m/s	130 m/s
Scan field	25 x 25 mm ²	25 x 25 mm ²	2 mm ¹⁾ 0.75 mm ²⁾
Focal length f	56 mm	56 mm	56 mm
Focus radius w_0	13.1 μm	15.0 μm	16.0 μm
Irradiated average laser power P_{av}	8.2 W	7.3 W	13.0 W
Appropriate repetition rate f_R	1.02 MHz	1.02 MHz	4.1 MHz
Pulse energy Q_P ³⁾	8.2 μJ	7.1 μJ	3.1 μJ
Peak fluence H_0 ³⁾	3.0 J/cm ²	1.9 J/cm ²	0.7 J/cm ²

3.3 Machining process

3.3.1 Laser processing regimes

In this thesis, laser micromachining was studied by utilising different processing strategies. In all cases the laser beam was deflected across the sample surface by scanner systems. **Figure 3-13** gives a first impression about the main differences of the distinct processing regimes by means of machining results obtained in the experimental work.

In the first process regime, either a single laser pulse or a burst consisting of a defined number of pulses was irradiated on the work piece. This method was primarily used in fundamental investigations. As an example, the figure top left shows single pulse laser ablation of a thin Copper layer on glass substrate.

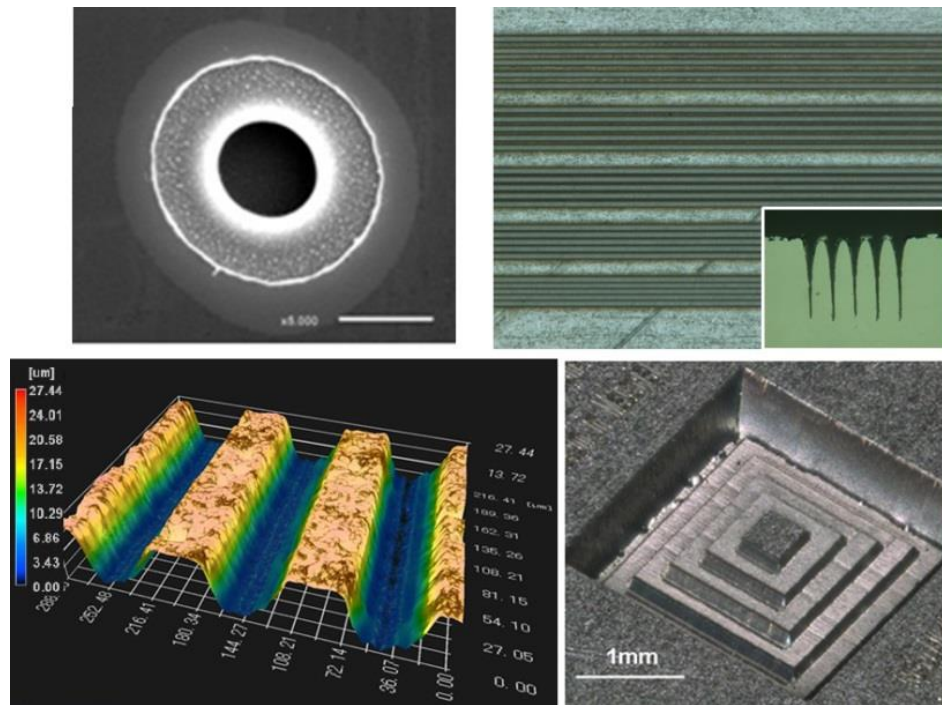


Figure 3-13: Machining results obtained by utilising different machining regimes; top left: single pulse laser ablation of a thin Copper layer on glass substrate; top right: repetitive line-scan laser ablation on Stainless steel; bottom left: 2.5D laser ablation on Stainless steel; and bottom right: step pyramid in Stainless steel obtained by 3D laser micro structuring.

By contrast, trenches with a depth larger than hundred micro meters have been fabricated in Stainless steel by using the line-scan laser ablation strategy. In this case, a certain number of lines of overlapping laser pulses was irradiated (top right). Next, the figure bottom left shows a trench-like micro structure laser fabricated in Stainless steel using the 2.5 D laser processing regime. For this, several numbers of repetitive area scans (scan passes) fulfilled with overlapping single line scans were irradiated.

The last applied machining regime, three-dimensional laser micro structuring, enabled laser fabrication of complex micro-featured devices by using a subtractive layer-wise structuring method. A step pyramid processed in Stainless steel is shown on bottom right as machining example. This machining method can be drawn up by distinct processing steps, as fitted in the process chain illustrated in **Figure 3-14**.

The first step included drawing of the inverse 3D model of the ablation structure to be processed in CAD software. Next the CAD model was triangulated to STL-file format and cut into layers of uniform thickness. This was carried out by using direct slicing methods, provided by the commercially available software *SKM DCAM 2009 (Vers. 5.2.1.0 Unicode)* [114]. As a result each single layer contained the outline of the

ablation area, depending on the actual height of the 3D model. The outline was fulfilled with numerous single line-scans with a predefined geometrical spacing and filling angle. The following post processor step included adding of acceleration and deceleration sections to the laser processing path to avoid pulse accumulation. The overall processing strategy was to fabricate the micro structures layer-wise, “line by line” and “layer by layer”. In this case, the number of the layers to be processed depended on both the model height and the material removal rate.

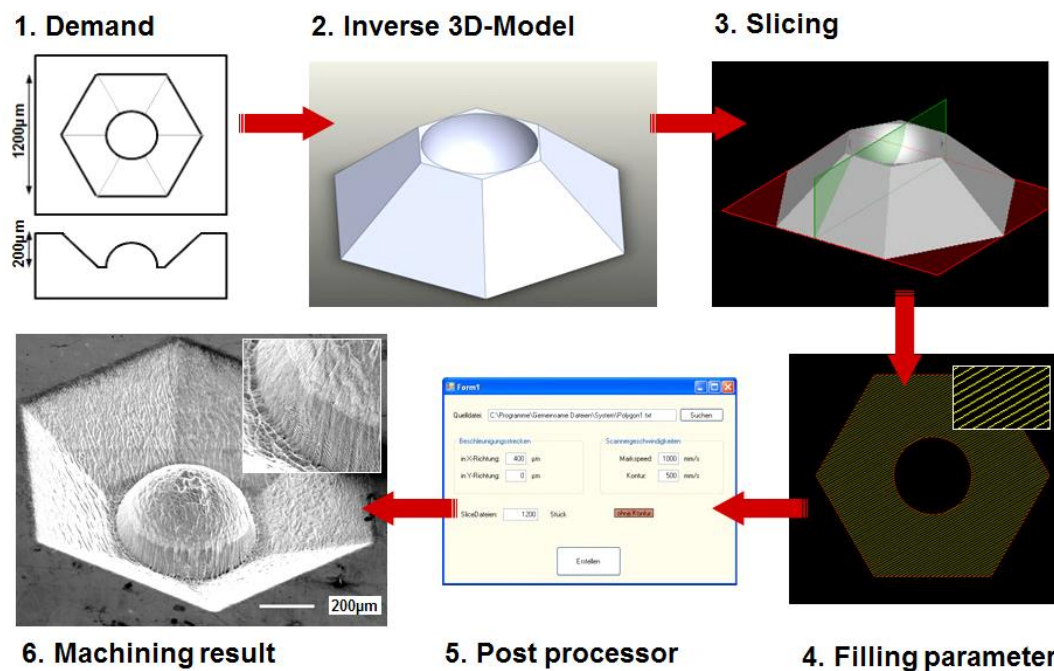


Figure 3-14: Process chain illustrating distinct processing steps in 3D laser micro structuring.

However, the combination of high-PRF laser pulses and galvanometer scan systems affected the accumulation of a high number of laser pulses at the start and the end of laser processed lines. As schematically shown in **Figure 3-15** (top left), the highest number of laser pulses irradiates at the onset of the line scan. On-going, a steadily decreasing energy input due to increasing pulse spacing takes place, until a constant scan speed was reached. The lower scan speeds which have been detected during the acceleration / deceleration movement of the scan mirror were caused by mass inertia effects. The resultant ablation profile obtained is shown in **Figure 3-15** (top right), indicating the highest ablation depth at the beginning of the laser scan.

In addition the **Figure 3-15** (bottom) illustrates the empirical method used to determine the lengths of the sections with non-uniform pulse overlap. These sections have been denoted as acceleration path and deceleration path, for the onset and the end of the laser

3.3 Machining process

scanned line, respectively. The section lengths were considerably affected by the design of the galvanometer scan system (mirror mass, tuning) and the focal distance of the focusing objective. Further it was found, that the scan speed influenced the lengths of the acceleration path and deceleration path considerably.

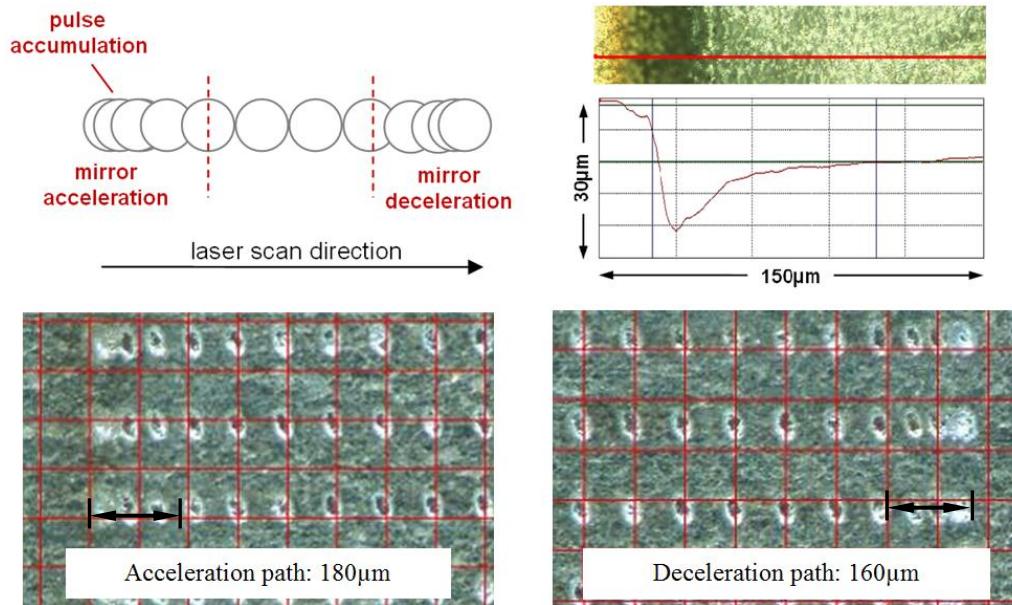


Figure 3-15: Definition of acceleration and deceleration paths; **top left:** schematic of non-uniform overlapping pulses due to low scan speeds; **top right:** ablation profile obtained in the start area in top view (above) and cross section profile; **bottom:** empirical determination of the length of both acceleration path (left) and deceleration path (right) using digital microscope images.

The effective scan speed, obtained for nominal scan speeds ranging between 0.5 m/s and 4.0 m/s versus the laser travelling distance, is plotted in **Figure 3-16**. For the case of the low scan speed of 0.5 m/s, the nominal scan speed was reached after a scan distance of less than 100 µm. The scan distance increased with faster scan speeds, and with the highest scan speed of 4.0 m/s the minimum required scan distance was 0.8 mm. A similar behaviour was observed for the deceleration movement of the scanned laser beam. In total, the lengths of the deceleration paths were shorter than the lengths of the respective acceleration paths.

Moreover, **Figure 3-16** indicates a linear correlation between the effective scan speed and the minimum scan distance, which the laser beam travels to reach the nominal scan speed for the first time. The wobble in the effective scan speed is mainly induced by the applied evaluation method. The effective scan speed was determined by the product of the distance between spatially separated single pulse ablation craters and the applied

repetition rate. The distances between the ablation craters were measured with the digital optical microscopy with the measurement accuracy better than 1 μm . A little measurement error, however, resulted in a significant error of the reached effective scan speed. In addition to this, the poisoning error of the galvanometer scan system becomes more important with the higher scan speeds.

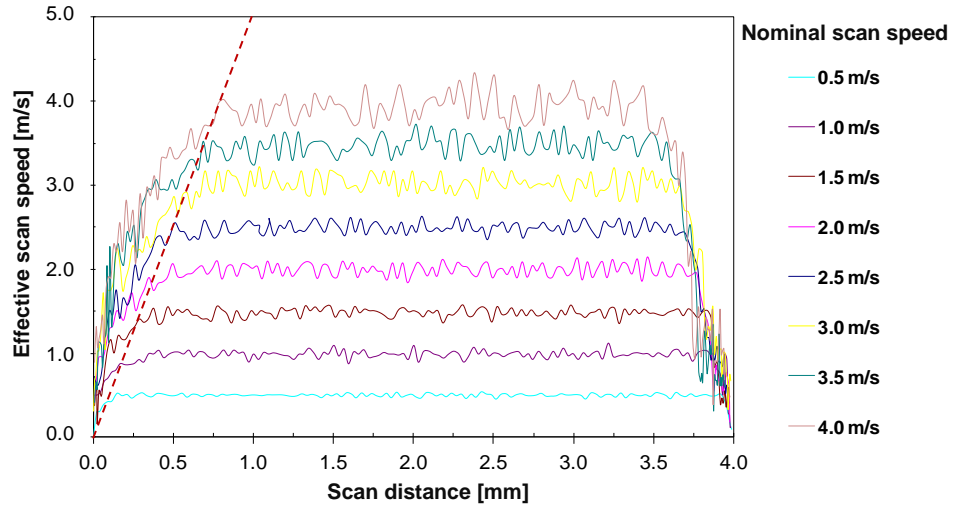


Figure 3-16: Effective scan speed versus travelling distance obtained for various nominal scan speeds; the linear relation between the travelling distance, where the maximum scan speed was reached first time, and nominal scan speed is fitted by a red line.

A linear approximation between the effective scan speed and the minimum required scan distance is fitted in the plot by a red scattered line. The slope m of this linear approximation yields the length of the acceleration path l_{acc} for any scan speed v_s . It calculates approximately equal to $m = 5000 \text{ s}^{-1}$ and, as a result, the acceleration length can be estimated as a function of the scan speed as

$$m = \frac{dy}{dx} = 5000 \frac{1}{s}, \quad l_{acc} = \frac{v_s}{m} \quad \text{Equation 3-8.}$$

However, non-uniform laser pulse accumulation, appearing in laser processing using high-PRF lasers together with galvanometer scanning systems, is a limiting aspect for the implementation of the technology in high-precision micromachining. A simple but useful machining strategy, considering the acceleration and deceleration movement of the laser beam was developed in this thesis, schematically demonstrated in **Figure 3-17** left.

After starting a line-scan by scan mirror movement, the laser beam will be switched on

3.3 Machining process

when the nominal scan speed is reached. At the end, the laser beam is switched off, when the scanner position has reached the target position, which is determined by the ablation structure. To ensure the initial geometric structural dimensions, extra acceleration and deceleration paths are added to the laser processing path, over-scanning the area to be processed. The path lengths correlate to the laser switch-on and switch-off sections, calculated accordingly **Equation 3-8**.

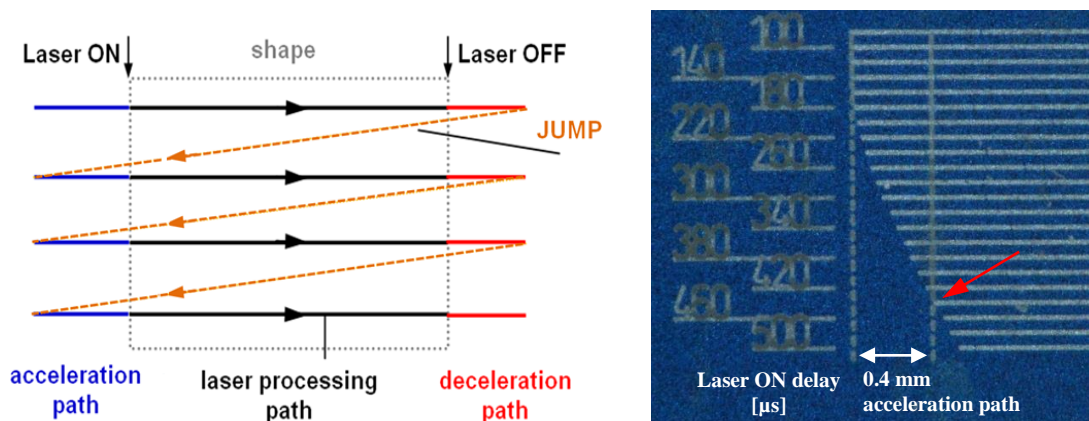


Figure 3-17: Machining strategy developed to avoid non-uniform pulse overlap in high-PRF laser processing at the start and the end of laser processed lines; **left:** schematic of the process regime, acceleration and deceleration paths are added to the laser processing path; **right:** determination of the **Laser ON** delay.

On the right, determination of the **Laser ON** delay time for a scan speed of 2.0 m/s is shown. According to **Figure 3-16** and **Equation 3-8**, an acceleration path of 0.4 mm is required at this scan speed. For this length the **Laser ON** delay time is 440 μs .

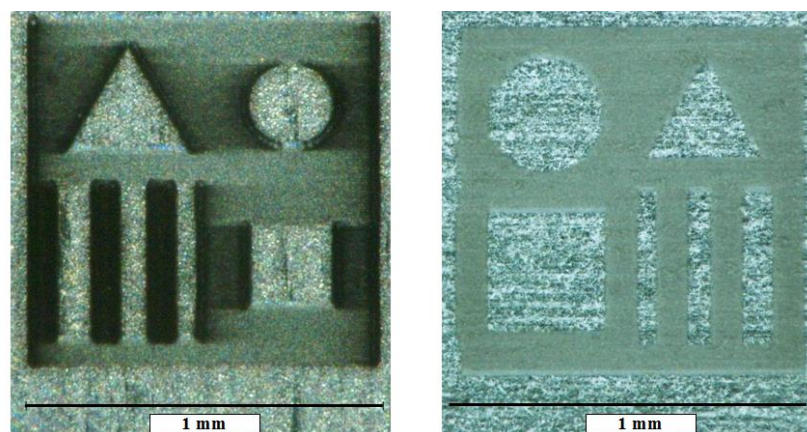


Figure 3-18: Effect of different machining strategies, illustrated by means of one processed layer of a 3D test structure; **left:** dark coloured areas indicate deep and inhomogeneous ablation zones due to spatially undefined laser pulse irradiations; **right:** well-defined laser ablation structure, obtained by using acceleration and deceleration paths.

The advantage of the introduced machining regime is highlighted in **Figure 3-18**, illustrating the different machining quality obtained by either using or not using extra acceleration/deceleration paths. Viewing from above, a single layer of a three-dimensional test structure processed across the Stainless steel sample surface is shown. In the left-sided figure dark coloured areas are visible at the edges of the micro scaled features, obtained due to massive material ablation as the result of the high number of impinging laser pulses. To prevent such adverse ablation formations, acceleration and deceleration sections have been added to the processing path, and thus laser processing resulted in adequate ablation structures (**Figure 3-18**, right).

3.3.2 Definition of raster-scan parameter

In the experiments the laser beam was deflected across the machining sample using a raster-scan processing regime. Thereby the structure to be processed was subdivided into layers consisting of single lines. These lines have been processed layer-wise by alternating scanning of the laser beam. Initially the laser beam was deflected horizontally forward, followed by vertically side-shifting of the scan mirror with constant spacing, and starting from that point the laser beam moved backwards. A schematic of the raster-scan processing regime is illustrated in **Figure 3-19**.

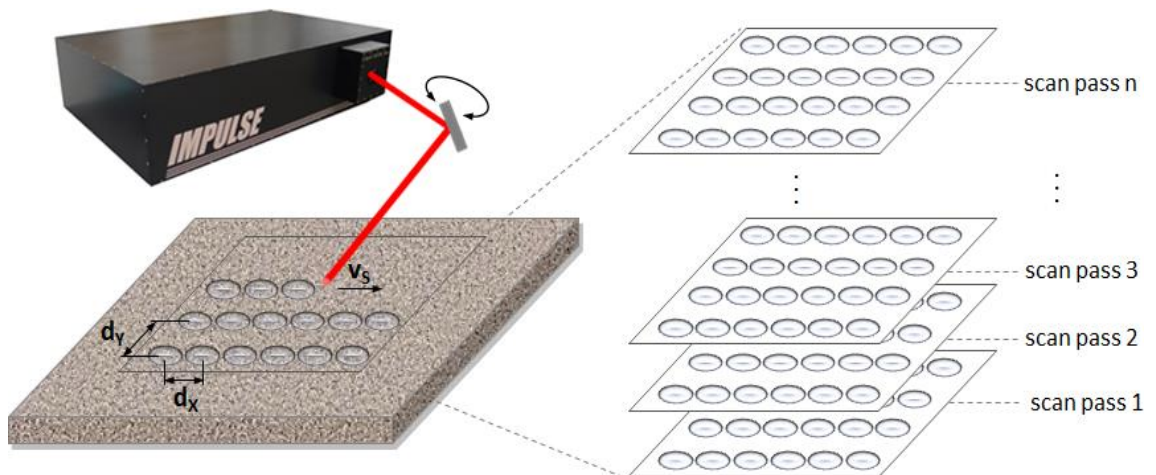


Figure 3-19: Schematic of raster-scan regime.

In scan direction, the lateral spacing between two consecutive irradiated laser pulses is given by the lateral pulse spacing d_x . The lateral pulse spacing can be varied by either the scan speed v_s or the repetition rate f_R , according to the relation

$$v_s = d_x \cdot f_R \quad \text{Equation 3-9.}$$

In two-dimensional processing, the spacing between two adjacent single laser scanned lines is indicated by the hatch distance d_y . The total number of (overlapping) laser scans in one plane was represented by a layer, in this thesis denoted as scan pass. Multiple processing of such scan passes yield deep ablation structures, whereby the number of scan passes n_s denotes the number of consecutive processed layers.

In this work, the effective number of laser pulses n_p is determined as the average quantity of laser pulses impinging on one place of the sample surface. In **Equation 3-12** the effective pulse number is averaged by the ratio of the total number of impinging laser pulses per irradiated area n_t , and the pulse number n_A , which is given by the laser irradiated area divided by the focal spot area, respectively.

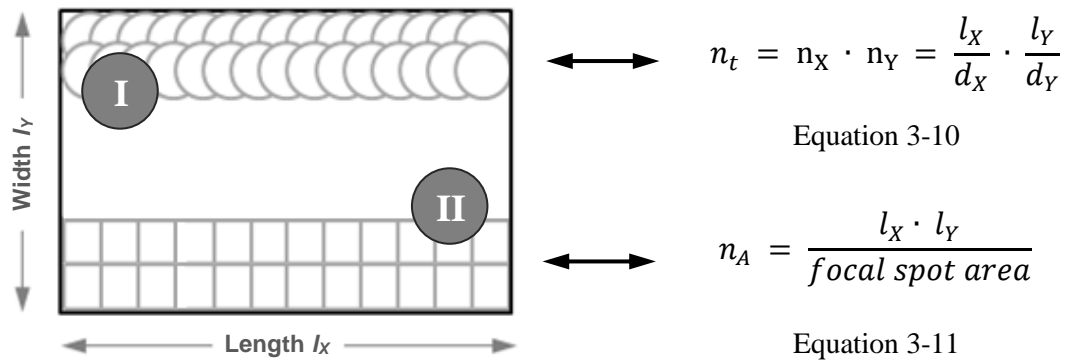


Figure 3-20 (I): Schematic of overlapping laser pulses to visualise the total number of incident laser pulses n_t ; **(II):** schematic of laser pulses string together to visualise a scan pattern which is completely filled with single laser pulses; in this view a rectangular instead of a circular pulse shape is shown; the equations used to calculate the quantity of incident laser pulses in one distinct layer are presented.

In **Figure 3-20**, by assuming a rectangular scan pattern, the total number of incident laser pulses n_t is given by the product of the number of pulses irradiated in both X and Y direction. The number of pulses n_x irradiating in the lateral direction is obtained by dividing the structure length l_x by the lateral pulse spacing d_x . The pulse number n_y impinging in orthogonal direction is calculated by dividing the structure width l_y by the hatch distance d_y . By contrast, the ratio of the scan pattern area and the focal spot area yields the number of laser pulses n_A which are required to fill the scan pattern area.

The effective number of laser pulses n_p describes the average number of laser pulses irradiating a surface increment. It is calculated n_s as follows:

$$n_p = n_s \frac{n_t}{n_A} = n_s \frac{\frac{l_x \cdot l_y}{d_x \cdot d_y}}{\frac{l_x \cdot l_y}{\pi \cdot w_0^2}} = n_s \frac{\pi \cdot w_0^2}{d_x \cdot d_y} \quad \text{Equation 3-12.}$$

The effective number of laser pulses n_p will be used later-on in *Section 4.3.2* to calculate the ablation rate.

3.4 Measurement systems

3.4.1 Introduction

The experimental results achieved in this thesis have been evaluated by means of the structural width, the ablation depth, the surface roughness, and visual impressions. Moreover, depth-measurement data have been included in model-based analyses to compare experimentally and theoretically determined material removal rates.

Both optical digital microscopy and scanning electron microscopy (SEM) were used. In addition, two confocal topography sensors were used for topography measurements, and a tactile surface profiler provided surface roughness measurements. A more detailed technical specification of the measurement systems is given below.

3.4.2 Measurements in X-Y-plane

The linear measurement of the lateral dimensions of the ablation structures were carried out using two different measurement devices. Highly-resolved photographs were obtained using the low vacuum scanning electron microscope SEM (JSM-6510LV, Jeol) and the optical digital microscope (VHX 100, Keyence). The maximum magnifications were 300,000 X for the SEM and 5,000 X for the digital microscope, respectively. Further, the microscopy photographs were taken into account to evaluate the machining quality of the ablation structures.

3.4.3 Topography measurement

Two different confocal topography sensors were applied, in order to evaluate the geometric surface characteristics of laser processed structures. A confocal point sensor (CF4, nanofocus) was implemented in the laser machining work station. This setup facilitates quasi “in-situ” measurements of the laser processed areas with a resolution better than 1.5 μm in lateral direction, and better than 25 nm in vertical direction. The movement of the sample between the galvanometer scanner and the confocal sensor was enabled by using a highly-precise positioning stage (Fohrenbach).

In addition, three-dimensional analysis of laser processed structures was done by using the optical 3D measurement system *$\mu\text{surf Explorer}$* (nanoFocus AG). The measurement system was available for a limited time during the experiments, kindly provided by *nanoFocus AG* as a loan.

3.4.4 Roughness measurement

The quality of laser processed surfaces was evaluated by means of the arithmetical mean roughness R_a . The R_a value is one of the most commonly used and widely accepted profile roughness parameters for industrial products. The arithmetical mean roughness is defined in DIN EN ISO 4287, representing the arithmetic average of the deviations of the roughness profile from the mean-line along the defined measurement section l_m . The value is given in the micrometer range, and can be obtained accordingly

$$R_a = \frac{1}{l_m} \int_0^{l_m} |y| dx \quad \text{Equation 3-13}$$

The surface roughness was determined by using the tactile surface profiler DEKTAK 3030 (VEECO / SLOAN) with a vertical resolution of 0.5 nm. The lateral resolution of the measurement was limited by the provided diamond stylus, having a tip radius of 2 μm . All the measurements were performed with a load of 10 mg and a measurement speed of 1 mm/s.

4 Ablation results and discussion

4.1 Introduction

An initial approach is presented to evaluate high-PRF ultrashort pulse laser ablation of metals. As previously mentioned in *Chapter 2*, laser ablation was of interest in numerous investigations up to now. However, a large number of these studies were focussed either on the “low-fluence” or the “high-fluence” regime rather than the “transition-fluence” area. In this chapter, the “transition-fluence” regime is of particular interest, to potentially overcome the existing lack of knowledge in this parameter range. Furthermore, determination of optimal processing conditions requires good knowledge of both the individual effects of the laser parameters on material ablation and how they interact together. According to this, the chapter contributes further to determine optimised laser processing conditions for micromachining.

After this introductory section, in *Section 4.2* the impact of the repetition rate on the ablation threshold is investigated for Aluminium, Copper and Stainless steel.

After this, in *Section 4.3* both the ablation rate and the volume ablation rate are evaluated as the key parameters for material removal, obtained by measuring the depths of standardised cavities. The empirically obtained results are compared to the values achieved in theoretical considerations. For this, a material removal calculation model is established in *Section 4.3.1* to calculate the ablation volume per incident laser pulse. In addition, the impact of the pulse energy, the lateral pulse spacing, and temporal pulse-to-pulse distance are discussed.

The subsections *4.4* and *4.5* deal with the material removal efficiency as well as the roughness of laser processed surfaces. The chapter concludes with a short summary, presented in *Section 4.6*.

4.2 Ablation threshold

4.2.1 Introduction

Material ablation takes place when the amount of absorbed laser energy exceeds the damage threshold of the material. This material specific parameter is referred to as either the ablation threshold or the threshold fluence \mathbf{H}_{th} . It has been demonstrated already that the ablation threshold is strongly influenced by the laser processing conditions. However, previous research in this field has been mostly limited in studying the impact of the laser pulse duration and the number of incident laser pulses. For laser processing of metals it has been demonstrated that the ablation threshold decreased with lower pulse durations, but it was almost constant for ultrashort laser pulses in the range of a few hundred femtoseconds [115]. Moreover, it was found that the threshold fluence decreased with increasing numbers of incident laser pulses, and thus the literature supposed incubation and defect accumulation as most influencing effects [57, 116].

In addition, a thermal impact on the ablation threshold can be expected in particular in high-PRF laser processing of low thermally conductive materials. Accumulation of heat has been reported already in *Section 2.5.2* and it was concluded, that increasing substrate temperatures enhance laser beam absorption. However, up to now there is insufficient research in this topic. In order to overcome this, the impact of the temporal laser pulse-to-pulse distance on the ablation threshold is subject to more detailed investigations in this work.

The ablation threshold can be determined by using a scientifically accepted method [57, 62, 117-120], introduced by *LIU* [121]. For Gaussian beams with focus spot radius w_0 and a radial fluence distribution $\mathbf{H}(\mathbf{r})$ following

$$H(r) = H_0 \cdot e^{-2\left(\frac{w(r)}{w_0}\right)^2} \quad \text{Equation 4-1,}$$

the square of the ablation crater diameter \mathbf{D}^2 correlates to

$$D^2 = 2w_0^2 \ln \frac{H_0}{H_{th}} \quad \text{Equation 4-2,}$$

where \mathbf{H}_0 is the irradiated laser fluence and \mathbf{H}_{th} is the ablation threshold.

4.2 Ablation threshold

Semi-logarithmical plotting of the squared ablation crater diameters versus the irradiated laser peak fluence expresses a linear dependence, comparable to the graph shown in **Figure 4-1**. In the figure, the laser focal spot radius is plotted versus the laser fluence, referred to as E_0 and ρ respectively.

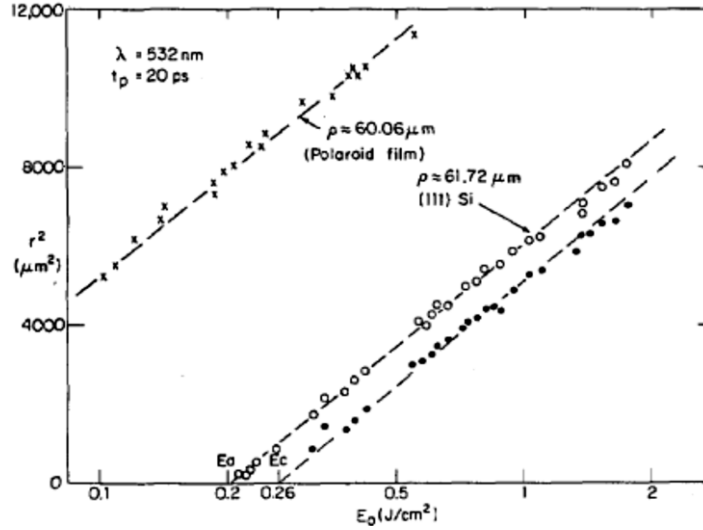


Figure 4-1 left: Semi-logarithmical plot of irradiated laser fluence versus the outer radii (○) and the inner radii (●) of amorphous ring patterns, obtained on (111) silicon surface as well as radii of burn spots on polaroid films (■), induced by 20 ps pulses at 532 nm; taken from reference [121]; in the figure the laser fluence and the focal spot radius are referred to as E_0 and ρ .

The ablation threshold can thus be calculated by extrapolation of the regression curve to the X – axis intercept point. Thus, under consideration of the linear equation of the regression curve, given as

$$y = f(x) = m \cdot \ln(x) + n \quad \text{Equation 4-3,}$$

recalculation of **Equation 4-2** to

$$D^2(H_0) = 2 w_0^2 \cdot \ln H_0 - 2 w_0^2 \cdot \ln H_{th} \quad \text{Equation 4-4}$$

yields the slope \mathbf{m} and the y-intercept \mathbf{n} as

$$m = 2 w_0^2 \quad \text{Equation 4-5 and}$$

$$n = -2 w_0^2 \cdot \ln H_{th} \quad \text{Equation 4-6.}$$

By recalculation of these equations, ablation thresholds for laser pulses of varied repetition rates have been calculated from the regression curves presented in **Figure 4-2** and **Figure 4-3** as

$$H_{th} = e^{-\frac{n}{m}} \quad \text{Equation 4-7.}$$

Furthermore the focal spot radius w_0 can be calculated from the slope m of the regression curve

$$w_0 = \sqrt{\frac{m}{2}} \quad \text{Equation 4-8.}$$

In this thesis, the impact of the temporal distance on the ablation threshold was evaluated by means of the relation between the irradiated laser fluence and the ablation crater diameter. The ablation craters were processed with laser pulses of different repetition rate in air at atmospheric pressure, at constant temperature and humidity. A single ablation crater was obtained by stationary irradiations of bursts consisting of 50 single laser pulses. Accordingly the incubation effect to the ablation threshold, mentioned above, was suggested as almost constant.

In this experimental approach studying the ablation threshold, ablation craters were fabricated with different laser fluence and varied temporal distances between the individual laser pulses. For statistical analysis, ten single ablation craters were processed for each individual parameter set. The diameters of these ablation craters were measured using the digital optical microscopy and 2,000x magnification. In these measurements, the ablation crater profile was estimated as circular. The little deviation of the crater profile from a circular shape was mainly due the spatial laser beam profile.

4.2.2 Results and discussion

At the beginning of this study the threshold fluence has been determined at the lower repetition rate of 20 kHz. In this time regime the ablation threshold can be assumed as almost unaffected by heat because of the long times of 50 μ s between the laser pulses.

The increase of the ablation crater diameter with higher laser fluence is shown for the example of Aluminium, **Figure 4-2** top. In addition, in the lower figure the square of the measured ablation crater diameter is plotted as a function of fluence for Aluminium, Copper and Stainless steel. The plot is derived from the experimentally determined

4.2 Ablation threshold

crater diameters, presented as mean values averaged over the ten ablation craters processed for each individual processing parameter set. The averaged crater diameter values, the measurement uncertainty provided in the form of standard deviation, as well as the calculated squares of the crater diameters are summarised in *Annex 2*.

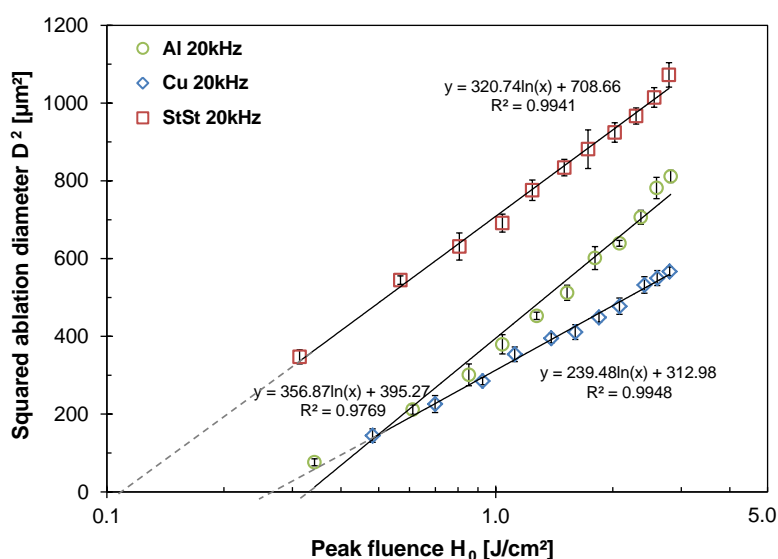
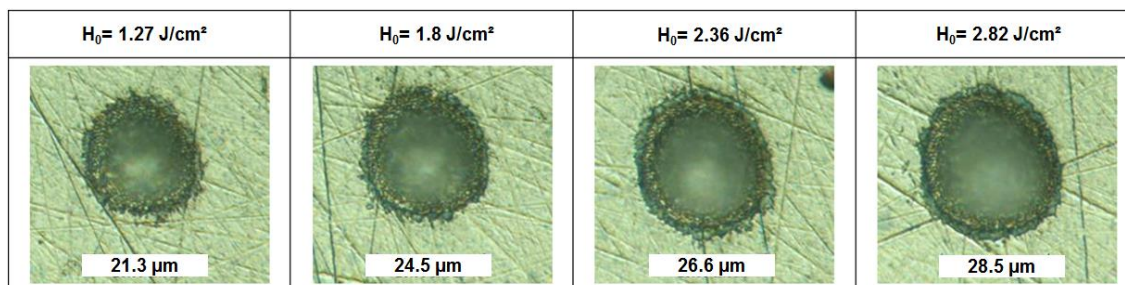


Figure 4-2: Semi-logarithmic plot of the squared ablation crater diameter D^2 versus the laser peak fluence H_0 , obtained for stationary irradiated bursts consisting of 50 individual laser pulses; the temporal distance between the pulses was $50 \mu\text{s}$ (20 kHz); in this study the focal spot diameter was $26.2 \mu\text{m}$.

As expected for the semi-logarithmic scaling, there is a linear correlation between the fluence and the square of the ablation crater diameters. The ablation thresholds are pointed out by the extrapolated intercept of the regression curve on the X - axis ($D^2 \rightarrow 0$). The high R-square-values of the regression lines given in the plot indicate good fit between the fluence and the square of the ablation crater diameters. By using **Equation 4-13**, the ablation thresholds have been calculated to be 0.33 J/cm^2 for Aluminium, 0.27 J/cm^2 for Copper, and 0.11 J/cm^2 for Stainless steel, respectively. Moreover, the focal spot radii, estimated as mean values from the slopes of the graphs, fit very well to the laser focus spot radius of $13.1 \mu\text{m}$, measured using the *MicroSpotMonitor*.

According to **Equation 4-8**, the calculated focal spot radii are 13.5 μm and 12.7 μm for Aluminium and Stainless steel, respectively. By contrast, the radius of 11.0 μm calculated for Copper seems to be a little low, compared to the *MicroSpotMonitor* measurement.

In **Figure 4-3** mean values of ablation crater diameters obtained with various repetition rates are plotted as a function of the laser fluence. The measurement values of these diameters and measurement uncertainties are given in *Annex 2*. From the plot it becomes clear that the temporal pulse-to-pulse distance has significant impact on the ablation crater diameter and the ablation threshold. A summary of the slopes, Y-intercepts, as well as the resultant ablation thresholds and focus radii derived from this figure is given in *Annex 3*.

Considering the same impinging laser fluence, the ablation craters have been greatly enlarged with higher repetition rates in case of Aluminium. On Copper by contrast, the ablation diameters are not significantly different. On the other hand, in Stainless steel the crater diameters increased only at the higher repetition rates. According to these experimental results, for Aluminium and Stainless steel lower ablation thresholds are expected for higher repetition rates, whereas for Copper the ablation threshold seems to be almost unaffected by the repetition rate.

The impact of the temporal pulse-to-pulse distance on the ablation threshold of the investigated metals can be mainly explained by thermal effects, primarily induced by heat accumulation. It has been previously reported in *Chapter 2*, that both the surface temperature and state of matter affect significantly the laser beam absorption behaviour of the laser processed surfaces.

The significant decrease of the ablation threshold recognised for Aluminium can be assumed to be due to material melting. In Aluminium, a high amount of laser energy is deposited close to the surface as a result of the high heat capacity. Thus, in spite of the high heat conductivity, the low melting temperature of Aluminium will be easily exceeded. For ultrashort pulse laser irradiation of Aluminium targets, a maximum melt depth up to 400 nm has been reported [9]. The depth was calculated for an absorbed laser fluence of 0.2 J/cm². According to this, it can be concluded, that in high-PRF laser processing the next irradiating laser pulse will interact with a thin molten Aluminium layer.

4.2 Ablation threshold

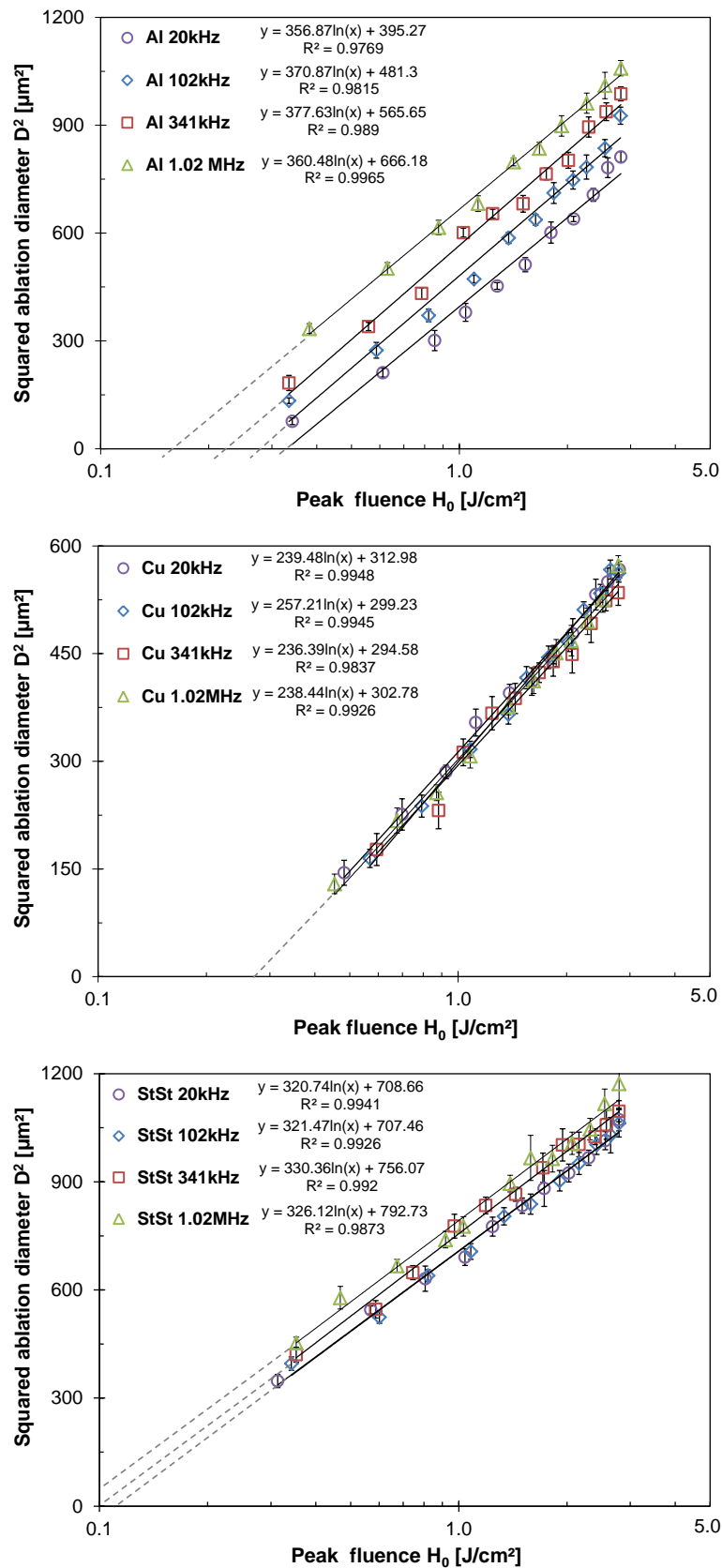


Figure 4-3: Laser fluence H_0 versus the squared ablation diameter D^2 to emphasize the impact of the repetition rate on the ablation diameter, stationary irradiated bursts consisting of 50 individual laser pulses have been irradiated on Aluminium (top), Copper (centre) and Stainless steel (bottom) metal sheets.

Moreover, it can be assumed that the change of the state of matter of the irradiated surface will potentially enhance laser beam absorption. As a result, a higher amount of energy will be deposited in the bulk, causing enlarged material ablation. This is demonstrated in **Figure 4-3** by the enlarged ablation crater diameters, obtained with similar processing parameters and shorter temporal pulse-to-pulse distances. The enlarged ablation crater diameters indicate the decrease of the ablation threshold with increasing repetition rates, summarised in **Table 4-1**.

On Stainless steel the ablation crater diameters appeared almost constant for laser processing with repetition rates in the range up to hundreds kilohertz. In contrast, evaluation of the ablation craters, obtained with laser pulses of similar pulse energy and high repetition rate, showed the enlargement of the diameters. The enlarged ablation crater diameters, detected in this study, reveal a reduced ablation threshold for Stainless steel at the higher repetition rates.

The explanation can be found in the low heat conductivity of Stainless steel, which can be considered as heat accumulation initiating effect. As a result, a significant surface temperature rise can be supposed particularly for high-PRF laser processing. According to the relation between temperature and absorptivity as given in *Section 3.1.2*, it can be concluded, that the higher surface temperatures enhance absorption of the laser beam. Thus the detected enlarged ablation crater diameter, obtained in this study at the higher repetition rates, give strong evidence of reduced ablation threshold due to enhanced laser beam absorption.

However, on Copper no significant impact of the repetition rate on the ablation crater diameter can be observed in **Figure 4-3** (centre). The ablation crater diameters obtained scatter within a statistical uncertainty area within the investigated parameter range. Only the slope of the 102 kHz regression curve seems to be little high. As a result, a higher ablation threshold will be calculated for this repetition rate. However, comparison of the crater diameters and regression lines obtained indicates similar ablation behaviour for Copper. This suggests that the ablation process is almost unaffected by heat accumulation and melting, which might be due both a high heat conductivity and high melting temperature of Copper.

Table 4-1 summarises the ablation thresholds obtained with various repetition rates. The threshold values were calculated by using **Equation 4-13**. For this, the slopes and

4.2 Ablation threshold

Y-intercepts derived from the plots in **Figure 4-3** were taken into calculation. It can be seen that the ablation thresholds obtained at 20 kHz repetition rate are in good agreement to literature data presented elsewhere. Little differences existing between literature and threshold values determined in this thesis can be explained by the various experimental conditions applied in each individual study.

Table 4-1: Ablation thresholds H_{th} depending on the repetition rates, calculated from the plots presented in **Figure 4-3**, ablation threshold values achieved elsewhere are presented.

Material	H_{th} (20 kHz) J/cm ²	H_{th} (102 kHz) J/cm ²	H_{th} (341 kHz) J/cm ²	H_{th} (1.02 MHz) J/cm ²	Literature J/cm ²
Aluminium	0.33	0.27	0.22	0.16	0.37 [120]
Copper	0.27	0.31	0.29	0.28	0.14 [60] 0.35 [56]
Stainless steel	0.11	0.11	0.10	0.088	0.13 [56] 0.21 [57]

The dependence of the ablation threshold on the temporal laser pulse-to-pulse distance is presented in **Figure 4-4** using a standardised display format. For this, the ablation thresholds obtained at the higher repetition rates are normalised to the threshold values obtained at the lowest repetition rate of 20 kHz by taking into account the data given in **Table 4-1**. In addition, the uncertainty of the threshold fluence is presented, estimated from the averaged standard deviations of the ablation crater diameters.

For the low thermally conductive Stainless steel substrate, about 20 percentage lower threshold fluence has been obtained at the repetition rate of 1.02 MHz, compared to the 20 kHz value. For Copper, by contrast, the ablation threshold was almost independent from the repetition rate, except the 102 kHz value. The statistical outlier at 102 kHz might be mainly due the evaluation method used in this thesis. As mentioned above, the ablation threshold was calculated by interpolation of the regression line to the fluence axis. Thus a small difference in the slope of the regression line will lead to a larger variance in terms of the threshold fluence. However, an effect of the repetition rate cannot be ruled out entirely, and further experimental work is needed.

The highest impact of the temporal distance between consecutive incident laser pulses on the ablation threshold can be clearly seen for Aluminium. In this case the ablation

4.3 Material removal

threshold decreased more than 50 percentages at the highest repetition rate of 1.024 MHz, compared to the lowest rate of 20 kHz.

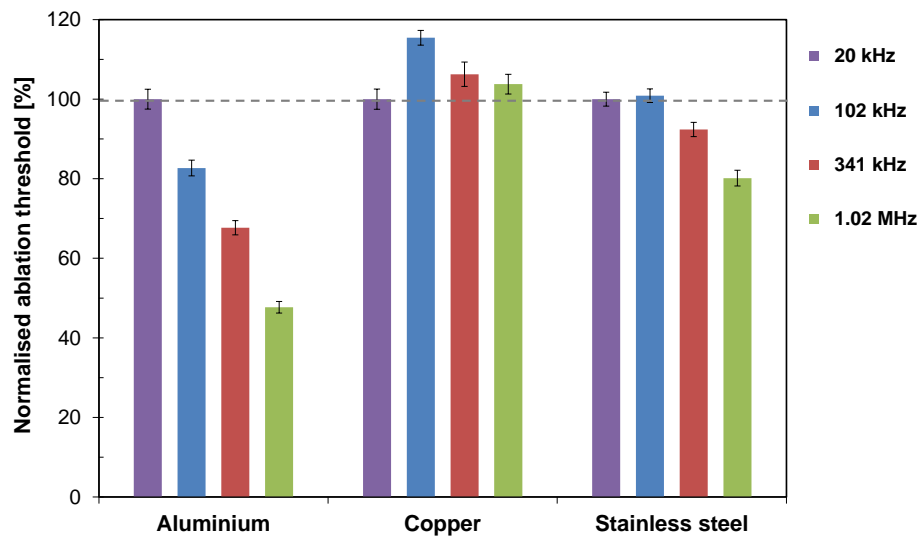


Figure 4-4: Impact of the temporal laser pulse-to-pulse distance on the ablation threshold in a standardised display format, the ablation threshold values are normalised to the 20 kHz value, measurement uncertainties are derived from the standard deviations of the averaged ablation crater diameters.

The impact of the repetition rate on the ablation threshold will be considered in the material removal calculation model, introduced in *Section 4.3* below. Further, the change of the ablation threshold with the repetition rate will be included in the model calculating the material removal rate, presented in *Section 5.4*.

4.3 Material removal

4.3.1 Determination of the material removal parameter and design of the material removal calculation model

One of the key parameters used to evaluate the impact of the laser fluence on material removal is the ablation rate \mathbf{d}_z , defining the ablation depth per incident laser pulse. According to a scientifically recognised method, the ablation rate is calculated from the maximum depth of the ablation crater, processed in stationary single-shot or multi-shot laser irradiations, divided by the number of impinging laser pulses.

4.3 Material removal

In this work, the ablation depth per pulse is determined as an average value from the depth measured on standardised laser processed cavities. The cavities were produced in multi-shot laser processing using the “line-by-line” and ”layer-by-layer” scan regime. The depth of the cavity l_z is defined by the distance from the surface to the bottom of the laser processed cavity, schematically shown in **Figure 4-5** (right).

In **Figure 4-5** (left), the red-coloured area indicates that area wherein the depth was averaged over a series of profile measurements across a number of laser fabricated cavities. Furthermore, profile irregularities appearing at the wall edges and/or the beginning or the end of the ablated structure were not included in the cavity depth calculation. The resulting cavity profile is shown in 3D cross section view on bottom right.

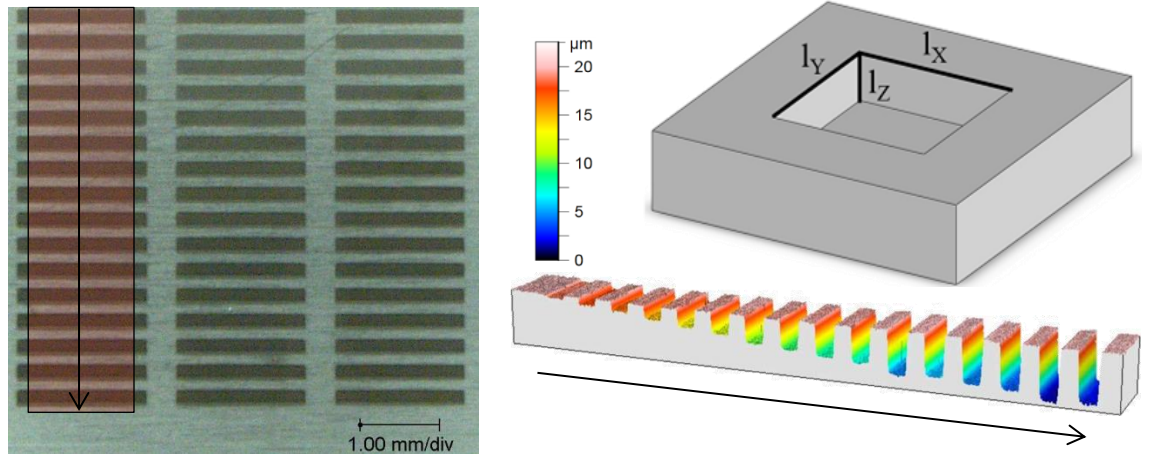


Figure 4-5 left: Digital microscopy photograph of cavities laser processed in Stainless steel for depth evaluation, three columns with constant processing parameter sets but increasing laser fluence from top to bottom were made; **top right:** schematic of the standardised laser processed cavity where l_x is the cavity length, l_y is the cavity width, and l_z is the cavity depth, **bottom right:** *µsurf Explorer* profilometer measurements showing the profile view of cavities obtained with increasing laser fluence.

The ablation rate d_z is given by the ratio of the cavity depth l_z and the number of irradiated laser pulses according to

$$d_z = \frac{l_z}{n_p} = \frac{l_z \cdot d_x \cdot d_y}{n_s \cdot \pi \cdot w_0^2} \quad \text{Equation 4-9,}$$

where n_p is the effective number of impinging laser pulses, d_x is the lateral pulse spacing, d_y is the hatch distance, and n_s is the number of scan passes. In this equation, the effective number of impinging laser pulses per area given in **Equation 3-12** is used

in order to specify material removal with overlapping laser pulses. In this way, the calculated ablation rate represents the mean ablation depth removed with a single laser pulse, averaged across the cavity surface area.

However, this method differs somewhat from the usual evaluation methods, where using stationary laser irradiations the ablation crater depth is divided by the pulse number. As a result, the maximum ablation rate in the centre of the laser spot size area will be obtained.

Figure 4-6 illustrates the difference between both evaluation methods in a schematic view. For the pulse overlapping process regime (right) it can be seen that local averaging of the ablation depth results in smaller ablation depths per pulse, compared to the higher ablation depth obtained in the stationary regime (left). In total, the removed material volume per laser pulse seems to be almost similar for both processing regimes.

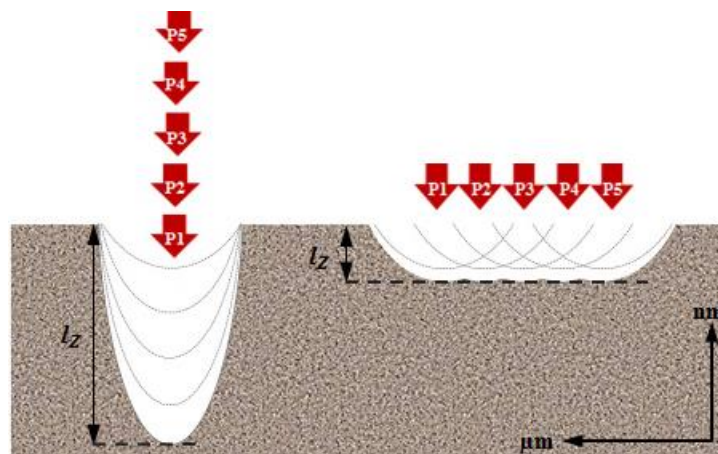


Figure 4-6: Schematic view of ablation structures applying stationary (**left**) and overlapping (**right**) laser processing, in any case 5 laser pulses (P1 ... P5) irradiate the sample surface, different orders of magnitude in depth and width dimension are displayed by the black arrow.

In this thesis, a model is introduced for femtosecond laser irradiation, to estimate the achievable ablation volume per incident laser pulse. The model is inspired by the work done by *NEUENSCHWANDER et al.* [97], who calculated the ablation volume for UV laser pulses with a pulse duration of 10 picoseconds. In volume calculation, the authors considered the experimentally observed energy penetration depth of 500 nm for Copper and 5.5 nm for Stainless steel. Both values differ considerably from the optical penetration depths presented in **Table 3-2** for Copper (12 nm), and Stainless steel (19 nm). These differences might be induced by the thermal nature of energy distribution following picosecond laser irradiations [122].

As shown in **Figure 4-7**, material ablation takes place when the intensity of the incident laser beam exceeds the material specific threshold value. Further it can be seen, the ablation crater profile strongly depends on both the intensity profile of the incident laser beam as well as the propagation of the photon energy in **Z** - direction. Therefore, by assuming “low-fluence” ultrashort laser pulses, optical penetration of photons but neither electron diffusion nor heat diffusion are initially considered in the material removal calculation.

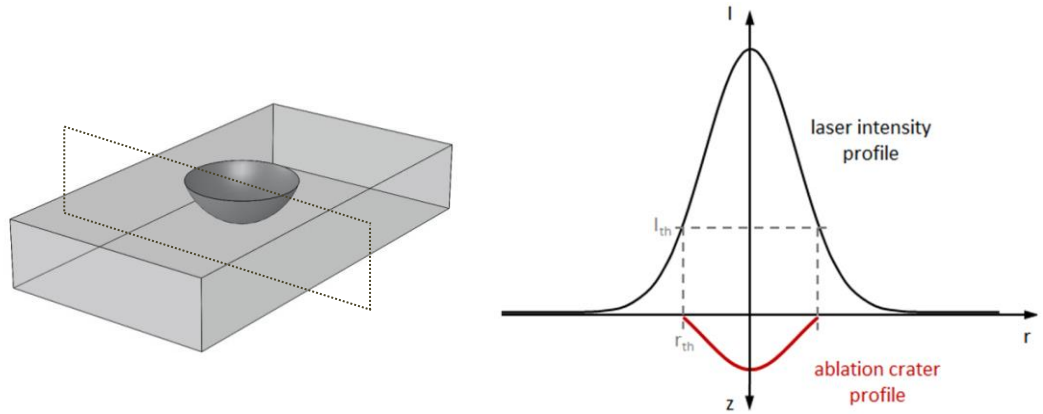


Figure 4-7 left: Schematic of the ablation crater obtained following single pulse laser irradiation with cross section plane; **right:** cross section view of irradiated laser intensity profile (black line) and resulting ablation crater profile (red line), I_{th} and r_{th} denote the ablation threshold and the threshold radius, respectively.

For the incident laser beam, a Gaussian intensity profile in radial direction as well as propagation losses following *Beer’s law* in depth direction can be assumed. As a result the intensity distribution $\mathbf{I}(\mathbf{r},\mathbf{z})$ within the bulk material is given by

$$I(r, z) = I(r) \cdot I(z) = I_0 e^{-\frac{2r^2}{w_0^2} - \alpha z} \quad \text{Equation 4-10,}$$

where $\mathbf{I}(\mathbf{r})$ is the intensity in radial direction, $\mathbf{I}(\mathbf{z})$ is the intensity in depth direction, \mathbf{I}_0 is the maximum irradiated intensity, \mathbf{w}_0 is the focal radius, and α is the absorption coefficient.

The maximum radial dimension of the ablation crater at the solid surface $z = 0$ is determined by the threshold radius r_{th} . Outside this position, the intensity decreases below the ablation threshold and no material removal takes place. The threshold radius can be obtained by transformation of **Equation 4-1**. By assuming that the intensity $\mathbf{I}(\mathbf{r}, \mathbf{z}=0)$ is equal to the threshold intensity \mathbf{I}_{th} , it calculates to

$$r_{th} = w_0 \sqrt{\frac{1}{2} \ln \left(\frac{I_0}{I_{th}} \right)} \quad \text{Equation 4-11.}$$

Further it is considered, intensity distribution in Z - direction of the irradiated solid follows *Beer's law* as given in **Equation 2-1**, and the incident intensity $I(\mathbf{r},z)$ is greater than /equal to the ablation threshold I_{th} . As a result, recalculation of **Equation 4-10** yield the ablation depth $d_z(\mathbf{r})$ as

$$d_z(r) = -\frac{1}{\alpha} \left[\ln \left(\frac{I_{th}}{I_0} \right) + \frac{2r^2}{w_0^2} \right] \quad \text{Equation 4-12.}$$

Figure 4-8 hence presents an example of the intensity distribution in solids in both radial direction (left) and depth direction (centre). The intensity profiles were calculated assuming a Gaussian laser pulse with pulse energy of 5 μJ , pulse duration of 176 fs (sech^2), and focal spot radius of 15 μm .

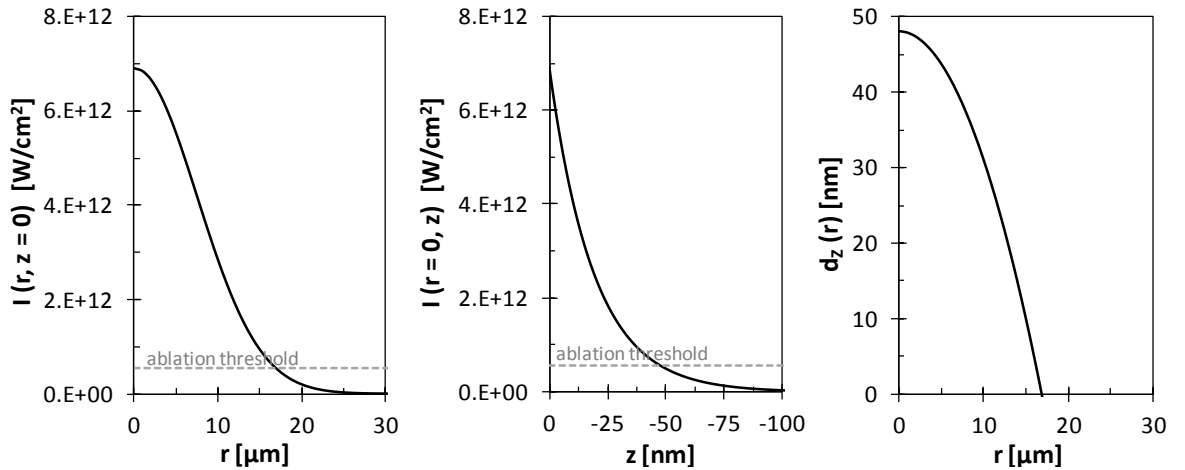


Figure 4-8: Intensity distribution $I(r, z = 0)$ and $I(r = 0, z)$ calculated in both radial (left) and depth (centre) direction, Gaussian laser pulse irradiation on Stainless steel with 5 μJ pulse energy, a pulse duration of 176 fs (sech^2) and 15 μm focal spot radius, the optical penetration depth of 15 nm was taken into calculation; the ablation crater profile $d_z(r)$ shown on the right was obtained by taking the ablation threshold of 0.55 TW/cm^2 (0.11 J/cm^2) into account.

The optical penetration depth of the laser beam into the solid was estimated to be 19 nm, taken from **Table 3-2**. The resulting ablation crater depth profile is shown in **Figure 4-8** (right) for an ablation threshold of 0.55 TW/cm^2 , which correlates to the previously determined threshold fluence of 0.11 J/cm^2 .

The volume of the ablation crater can be estimated by the assumption of a solid of the

4.3 Material removal

revolution, by rotating the ablation depth profile $\mathbf{d}_Z(\mathbf{r})$ as given in **Figure 4-8** around the central axis $r = 0$

$$V = 2\pi \int_0^{r_{th}} (r \cdot d_Z(r)) dr \quad \text{Equation 4-13}$$

Integration of **Equation 4-13** within the integration limits $0 \leq r \leq r_{th}$ yield the crater volume which can be removed with a single laser pulse. This is determined by the ablation rate \mathbf{V}_{SP} as

$$V_{SP} = \frac{\pi r_{th}^2}{\alpha} \left(\ln \left(\frac{I_0}{I_{th}} \right) - \frac{r_{th}^2}{w_0^2} \right) \quad \text{Equation 4-14.}$$

Using the effective penetration depth δ_{eff} instead of the reciprocal of the absorption coefficient, and further substituting the threshold radius by using **Equation 4-11** leads to the final expression below. In the equation the intensity is replaced by the fluence due to the correlation of the values over the pulse duration.

$$V_{SP} = \frac{\delta_{eff}}{4} \pi w_0^2 \ln^2 \left(\frac{H_0}{H_{th}} \right) \quad \text{Equation 4-15.}$$

In addition to the modelled volume ablation rate, in this work the empirically achieved material removal rate is included for discussion. Material removal of a single laser pulse \mathbf{V}_{SP_exp} is given by the ratio of the laser removed volume \mathbf{V}_{tot} of a standardised volume body, against the total number of incident laser pulses \mathbf{n}_t . The body volume is determined by the geometrical dimensions length, width and depth, given by \mathbf{l}_X , \mathbf{l}_Y and \mathbf{l}_Z . The number of incident laser pulses can be obtained using **Equation 3-11**. As a result the volume ablation rate is calculated very easily from the product of the depth of the laser processed cavity \mathbf{l}_Z , the lateral pulse spacing \mathbf{d}_X and the hatch distance \mathbf{d}_Y , divided by the number scan passes \mathbf{n}_S , as

$$V_{SP_exp} = \frac{V_{tot}}{n_t} = \frac{l_X \cdot l_Y \cdot l_Z}{n_t} = \frac{d_X \cdot d_Y \cdot l_Z}{n_S} \quad \text{Equation 4-16.}$$

4.3.2 Ablation rate

Initially the impact of the laser fluence on material removal is evaluated by means of the ablation rate d_z , which refers to the averaged ablation depth per incident laser pulse. It is calculated using **Equation 4-9** by taking into account the depths of the laser processed cavities. In this study, the cavities were fabricated using 25 scan passes. The laser fluence was varied in the range between the onset of voluminous material ablation and the maximum provided laser fluence of 1.9 J/cm². To minimise the thermal impact of the ablation rate on the material removal, the lower repetition rate of 205 kHz and a lateral pulse spacing of 5 μm have been applied. A series of three individual cavities were produced with each parameter set, in order to evaluate material ablation with a reasonable statistical certainty. The depths of these cavities, the calculated ablation rates d_z as well as the measurement uncertainties are given in *Annex 4*.

As shown in **Figure 4-9**, for all three investigated metals the ablation rate increases with increasing fluence. The maximum ablation rate was achieved with the highest irradiated laser fluence. For Stainless steel the largest ablation rate was reached, whilst in the case of Aluminium and Copper the depths have been on similar level.

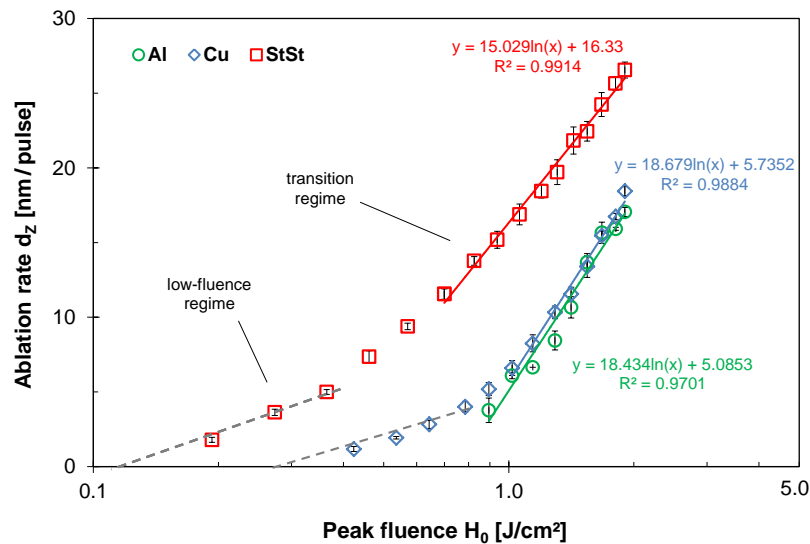


Figure 4-9: Ablation rate versus laser fluence obtained on Aluminium, Copper and Stainless steel by applying multi pulse processing with 25 scan passes, 5 μm lateral pulse spacing and 205 kHz repetition rate, measurement values and standard deviations are given in *Annex 4*.

In addition, trend lines are plotted emphasising the semi-logarithmical correlation between laser fluence and ablation rate. In the plots two characteristic regions can be distinguished, the “low-fluence” regime and the “transition” regime. The slopes of the

regression lines represent the effective penetration depth. Accordingly, the effective penetration depth of Stainless steel was estimated to be 15.0 nm. This is little smaller than the optical penetration depth for iron, calculated previously in the *Section 3.1.2* of 19 nm.

By contrast, the effective penetration depths, determined for Aluminium and Copper of 18.4 nm and 18.7 nm, are significantly higher than the calculated optical penetration depths presented in **Table 3-2**. In accordance to this findings, *SALLE et al.* [123] reported overheated surface layers in the depth significantly greater than optical laser beam penetration. The absorbed laser energy is transmitted into deep matter zones by electron diffusion, taking place as a result of the laser-induced high electron temperature gradients. Other studies on this subject conclude that the energy transport is largely affected by electron interaction with other electrons or/and the lattice. This is expected to be much stronger in amorphous and polycrystalline samples rather than in single-crystalline materials [44, 124]. Thus the specific characteristic of the laser irradiated metal in terms of thickness, crystallinity and grain boundaries may influence the laser energy distribution into the material considerably. As a consequence, the larger effective energy penetration will be considered in the ablation volume rate calculation model depth instead of the optical penetration depth.

However, the curve progression in the “low-fluence” regime confirms the ablation thresholds of Stainless steel and Copper, determined in the previous *Section 4.2* using the method of squared ablation crater diameters. The ablation thresholds presented there for Stainless steel (0.11 J/cm²) and Copper (0.27 J/cm²) are in good agreement to the ablation thresholds given in **Figure 4-9**, obtained by the intersection of the ablation rate regression line (grey-dashed) and the fluence axis.

Laser irradiation of Aluminium using “low-fluence” laser pulses, meanwhile caused only a little material ablation. The ablation threshold for Aluminium cannot be detected from these values because of the very high level of measurement uncertainty. Reliable cavity depths were however obtained on Aluminium by irradiating pulses with a fluence ranging between 0.9 J/cm² and 1.9 J/cm², which relates to the “transition” fluence regime.

4.3.3 Process parameter optimisation

The impact of the laser fluence and the lateral pulse-to-pulse distance on material removal was studied, aiming to optimise the laser processing parameters with respect to ablation rate, process efficiency and surface roughness.

In laser processing using overlapping laser pulses, the accumulated irradiated laser fluence H_{acc} defines the total amount of irradiated energy per area. The local energy input is influenced by both the spatial laser pulse profile and the lateral pulse spacing. According to this, **Figure 4-10** (top) presents a graphical view of the energy distribution across the laser processed area. Therefore the accumulated fluence was calculated by using a method introduced in *Annex 5*. Calculation input values have been as follows: a single processed layer of $200 \times 200 \mu\text{m}^2$ in length and width, single pulse energy of $Q_P = 3.88 \mu\text{J}$, focus spot diameter of $30 \mu\text{m}$, and the resulting peak fluence of $H_0 = 1.07 \text{ J/cm}^2$. The lateral pulse spacing was varied between $5 \mu\text{m}$, $10 \mu\text{m}$ and $15 \mu\text{m}$.

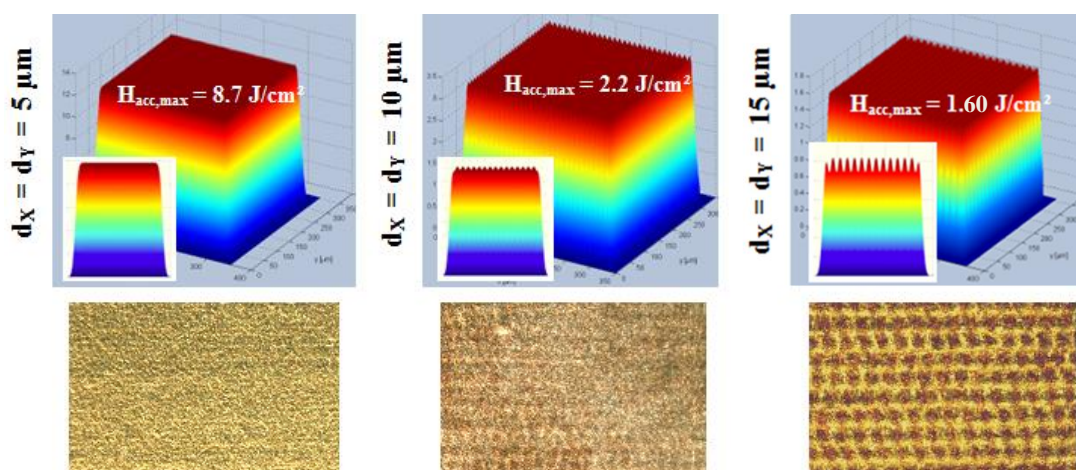


Figure 4-10: Graphical view of both accumulated laser energy input per area (top) and laser processed Copper surface (bottom); results were achieved considering a constant laser pulse energy of $3.88 \mu\text{J}$, focus spot diameter of $30 \mu\text{m}$ and peak fluence of $H_0 = 1.07 \text{ J/cm}^2$; the lateral pulse spacing was varied between $5 \mu\text{m}$, $10 \mu\text{m}$ and $15 \mu\text{m}$.

The highest accumulated fluence of 8.7 J/cm^2 was calculated for the minimum spatial pulse spacing of $5 \mu\text{m}$. By contrast, considering the widest pulse spacing of $15 \mu\text{m}$, the accumulated fluence was only 1.60 J/cm^2 . These results suggest that the largest ablation depth will be obtained by using the smallest lateral pulse spacing, due to the high amount of irradiated energy.

In addition, the graphical analysis distinguishes different processing regimes. With the

4.3 Material removal

smaller spatial pulse spacing, the energy input is uniformly distributed across the sample surface. Laser irradiation with wider pulse spacing, by contrast, will initiate non-uniform energy input including pronounced energy maximums.

In accordance with these findings, digital-microscopic photographs of laser processed Copper surfaces reflect the different processing regimes, observable in the **Figure 4-10** (bottom). On one hand, a uniform and smooth laser processed surface was achieved by using the small lateral distance of 5 μm (left). On the other hand, laser processing using wider pulse spacing caused irregular rough ablation surfaces accompanied by deep crater formations. The figures emphasise that the applied laser processing parameters affect significantly the machining results. A more detailed study was hence carried out in order to determine the optimised processing parameter with respect to ablation rate, efficiency, surface quality and throughput.

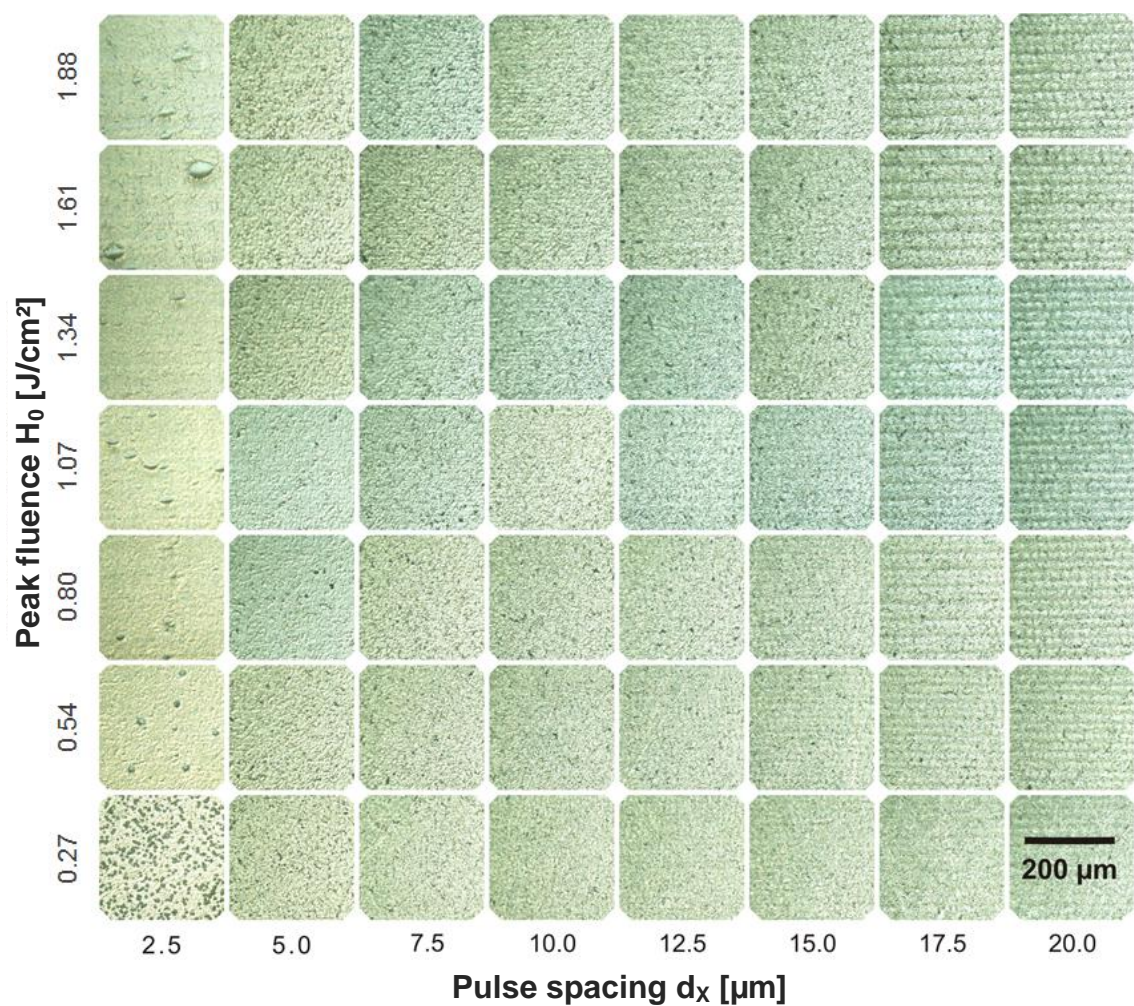


Figure 4-11: Digital optical photographs of laser processed Aluminium surfaces, obtained with 10 scan passes; the laser peak fluence and the lateral pulse spacing were varied, ranging between 0.27 J/cm² and 1.88 J/cm², and 2.5 μm and 20 μm , respectively.

4.3 Material removal

Figure 4-11 summarises digital-optical microscope photographs of ablation structures, obtained on Aluminium upon laser processing of 10 scan passes. The processing parameter fluence and lateral pulse spacing were varied, ranging between 0.27 J/cm^2 and 1.88 J/cm^2 , and $2.5 \text{ }\mu\text{m}$ and $20.0 \text{ }\mu\text{m}$, respectively. Irregular bulges of molten material can be seen on Aluminium surface for the small pulse spacing of $2.5 \text{ }\mu\text{m}$. In spite of irradiation of ultrashort laser pulses, local melting took place, induced by the high amount of deposited energy. On the other hand, with pulse spacing wider than $12.5 \text{ }\mu\text{m}$, rough surfaces covered by wavy structures were obtained.

A similar machining behaviour was observed on Stainless steel and Copper. Representative photographs of the laser processed surfaces, obtained with various processing parameter and 10 scan passes are presented in the figures below. These surfaces were captured with the digital optical digital microscopy and 500x magnification.

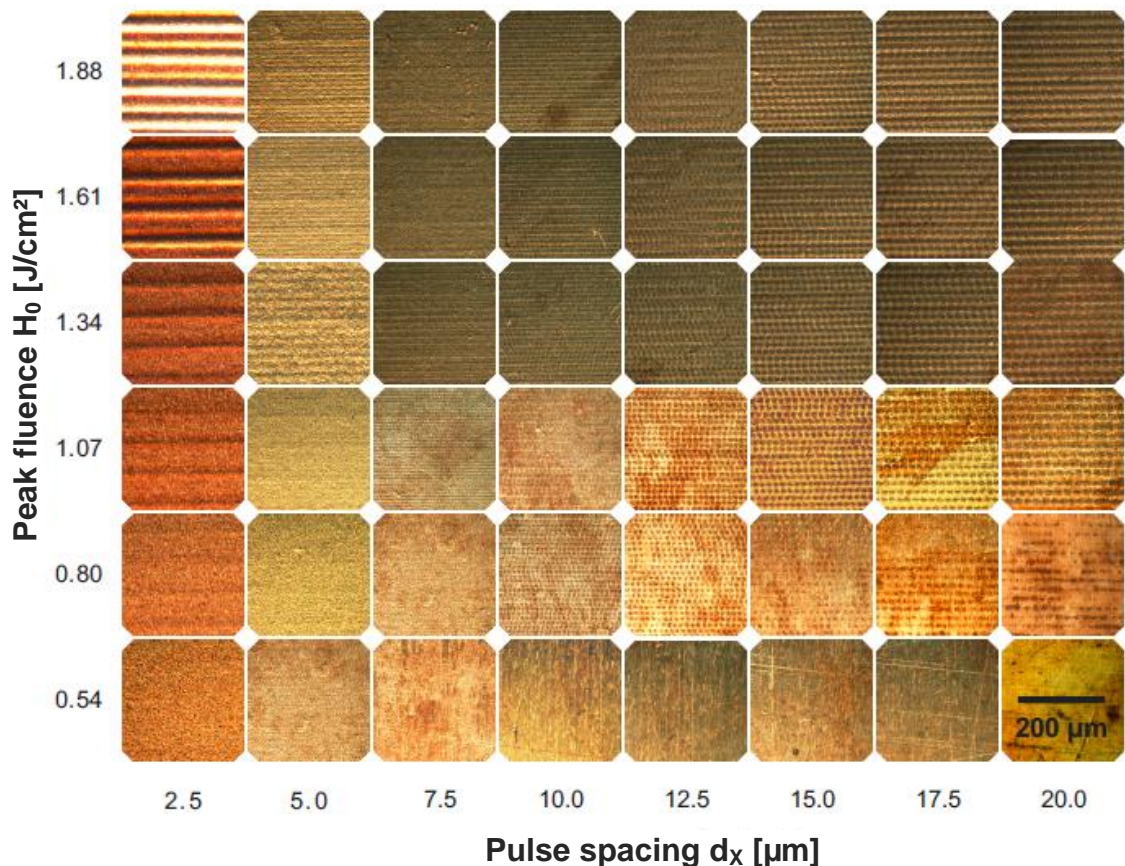


Figure 4-12: Digital optical photographs of laser processed Copper surfaces, obtained with 10 scan passes; the laser peak fluence and the lateral pulse spacing were varied, ranging between 0.27 J/cm^2 and 1.88 J/cm^2 , and $2.5 \text{ }\mu\text{m}$ and $20 \text{ }\mu\text{m}$, respectively.

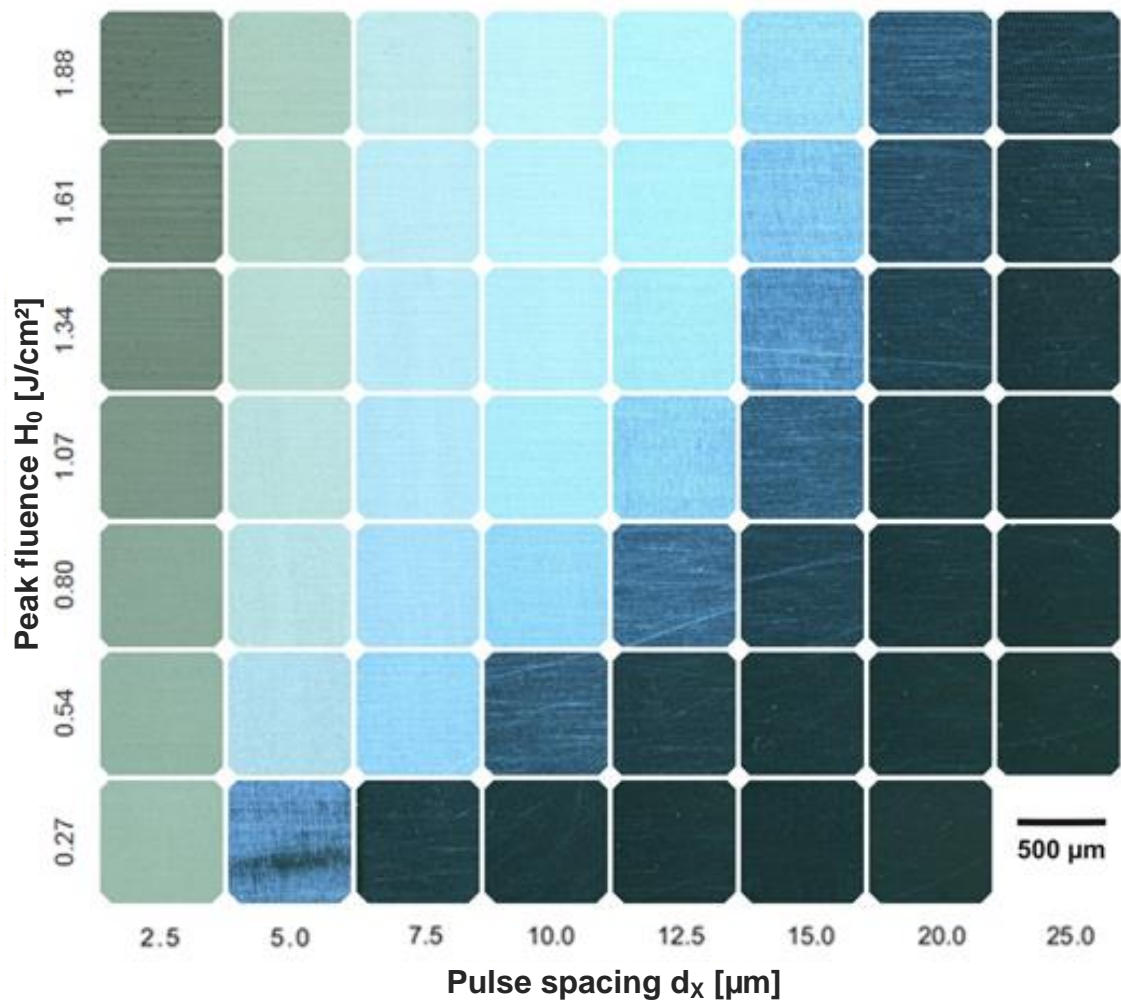


Figure 4-13: Digital optical photographs of laser processed Copper surfaces, obtained with 10 scan passes; the laser peak fluence and the lateral pulse spacing were varied, ranging between 0.27 J/cm² and 1.88 J/cm², and 2.5 μm and 20 μm, respectively.

Based on the results of this initial parameter study, appropriate processing conditions are selected in terms of both high ablation rate and smooth surface roughness. Following, these preselected processing parameters have been included in a more in-depth analysis of material removal. Thus high-PRF femtosecond laser processing of Aluminium and Copper was studied by using different lateral pulse spacing ranging between 5.0 μm and 12.5 μm. The investigated laser fluence range was between 0.8 J/cm² and 1.88 J/cm². Stainless steel was investigated between 2.5 μm and 12.5 μm, and 0.54 J/cm² and 1.34 J/cm², respectively. Standardised cavities as introduced in *Section 4.2.2* were fabricated with a depth of approximately 30 μm and a repetition rate of 205 kHz. By this way, influencing effects on material removal due to both defocusing of the laser beam and heat accumulation could be prevented. The focal

position was on the material surface. The focal spot size enlarged only marginal in the depth of 30 μm , and thus the irradiated fluence can be assumed as almost constant during the experiments. The impact of the processing parameters on material removal was evaluated by means of the ablation rate \mathbf{d}_z . The ablation rate was calculated accordingly **Equation 4-9** by taking into account experimentally determined depths of laser processed cavities. The cavity depths used in the calculations are given in *Annex 6*.

Figure 4-14 identifies the relationship between the lateral pulse spacing and the fluence versus the ablation rate for Aluminium, Copper and Stainless steel. The change in the ablation characteristics of the materials seems to be mainly induced by the different thermo-physical and optical properties of the investigated metals. Therefore heat conductivity, latent heat, and melting and/or evaporation temperatures, as well as the absorptivity have to be considered.

For Aluminium the highest ablation rate was obtained by applying the highest fluence and the smallest pulse spacing. The ablation rate decreased dramatically with wider lateral pulse spacing. This result is consistent with the explanation given above in *Section 4.2.2*, where a molten Aluminium surface layer was proposed as the material ablation enhancing effect.

It can be assumed, that Aluminium melting occurs primarily due to heat accumulation, caused by high energy inputs. In case of low energy deposition, the molten layer can be expected as less developed. In the latter case most of the irradiated energy has been used for material removal, and thus only a little amount of remaining energy contributed to material heating. Supporting these assumptions, the decrease of the ablation rate obtained with the lower laser fluence is less pronounced than with the higher fluence.

4.3 Material removal

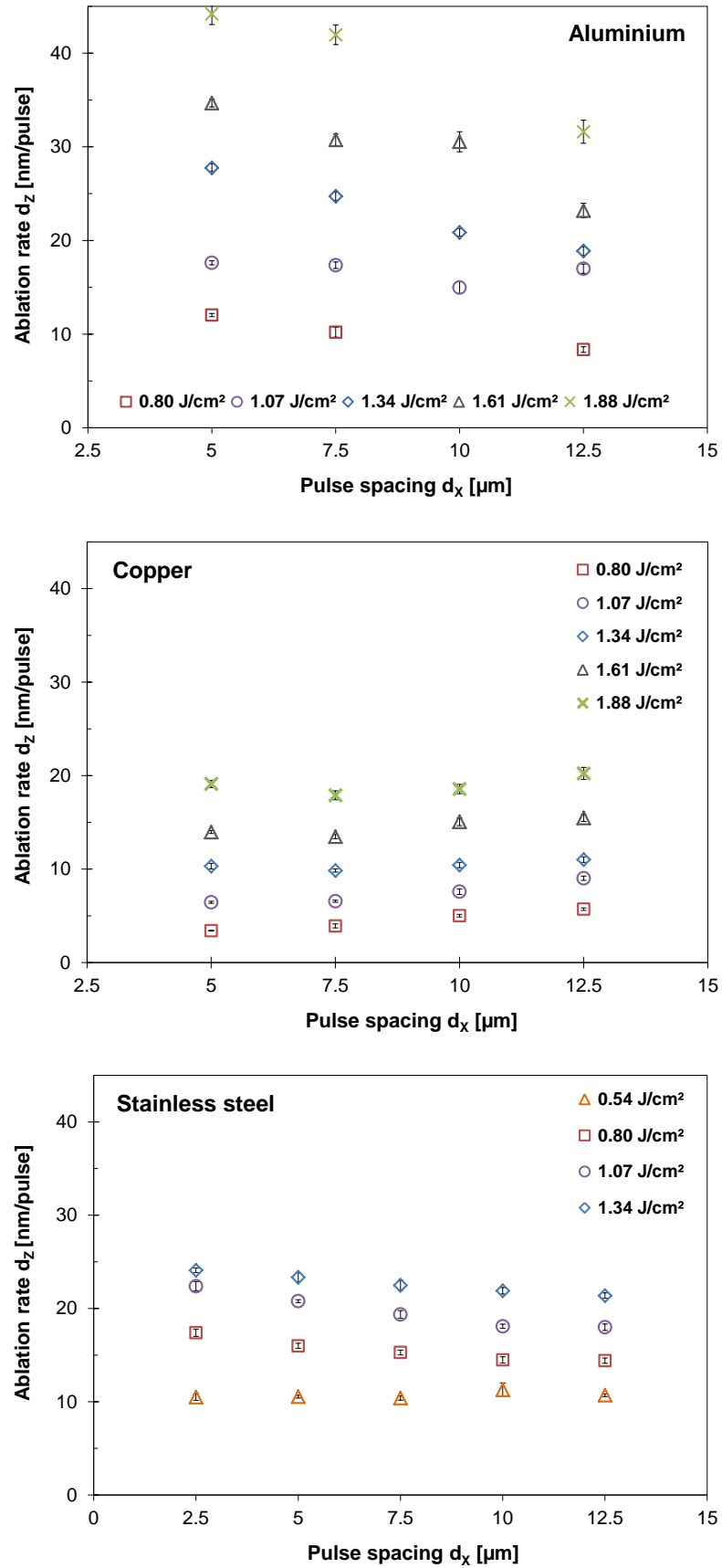


Figure 4-14: Ablation rate depending on both the lateral pulse spacing and irradiated fluence, illustrated for Aluminium (top), Copper (centre), and Stainless steel (bottom).

By studying Copper metal sheets, **Figure 4-14** identifies a noticeable increase of the ablation rate with the higher fluence. Furthermore it can be observed that the ablation rate increased with wider pulse spacing, which is in contrast to the other investigated materials. This increase of the ablation rate is also inconsistent with the results shown for Copper in the previous chapters, where laser ablation enhancing effects induced by heat accumulation were largely ruled out. The recognised increase of the ablation rate with wider pulse spacing might be induced by the considerably higher laser beam absorption. It is worth noting that **Figure 4-10** revealed an increase of surface roughness with wider pulse spacing. In addition, as already shown in *Section 3.1.2*, a considerably higher absorptivity value of 19 % was detected on laser processed Copper surfaces by irradiating “high-fluence” laser pulses and wider hatch distance. In contrast, the absorptivity level of Copper surfaces processed in the “low-fluence” regime was found to be only 15 %.

However, on Copper the surface roughness might become of growing importance because the roughness is one of the major laser beam absorption affecting parameters. As demonstrated in *Section 4.5*, the roughness of laser processed Copper surfaces will increase with wider lateral pulse spacing. For these rough laser processed surfaces, in turn, enhanced laser beam absorption can be suggested, causing the increase of the volume ablation rate.

With Stainless steel metal sheets, the ablation rate decreased with increasing pulse spacing, except for the low fluence of 0.54 J/cm^2 , where the ablation rate is constant. Therefore heat accumulation can be assumed to be the main influencing effect. Due to the low heat conductivity of Stainless steel, the surface temperature will potentially rise closely around the laser processed area, inducing the enhancement of laser beam absorption. As a result, laser processing using small lateral pulse spacing can be supposed as more efficient than laser processing applying wider lateral pulse spacing. In the latter case, the following laser pulses hit a colder area, and laser beam absorption is not enhanced.

On the other hand, no effect of the lateral pulse spacing on material ablation was detected by the irradiation of low-fluence laser pulses ($H = 0.54 \text{ J/cm}^2$). In this case it can be assumed that heat accumulation is almost negligible. The little remaining energy may not induce significant material heating.

4.3.4 Volume ablation rate

In this section ultrashort pulse laser processing is evaluated by comparison of theoretically predictable and experimentally determined volume ablation rates. The experimental volume ablation rates of Aluminium, Copper and Stainless have been determined using **Equation 4-16**. In these calculations, the depths of the standardised laser processed cavities as well as the lateral pulse spacing used in cavity fabrication were taken into account. The cavity depths have been used already in the ablation rate calculation, discussed in the previous *Section 4.3.3*. The calculated volume ablation rates are presented in *Annex 7*.

On the other hand, **Equation 4-15** yields the theoretical volume ablation rate, introduced in the material removal calculation model in *Section 4.3.1*. For direct comparison between theoretical predictions and experimental measurements, real processing conditions were considered in modelling. In theoretical calculations the laser fluence was varied between 0.4 J/cm² and 2.1 J/cm². This is slightly larger than the experimentally investigated fluence interval, ranging between 0.54 J/cm² and 1.88 J/cm². In addition, material specific ablation thresholds have been included into the calculation, determined in *Section 4.1.2* for the higher repetition rate of 102 kHz.

However, the results presented in *Section 4.2.3*, provide evidence that the effective penetration depth instead of the optical penetration depth determines the laser energy distribution into the bulk. In addition to this, the literature review indicated different points of views in terms of energy distribution during ultrashort pulse laser irradiation.

A large number of studies have identified either optical penetration in the “low-fluence” regime, or thermally driven electron diffusion in the “high-fluence regime” as the main energy transfer mechanisms. By contrast, recent studies revealed that the energy transfer in noble metals is mainly caused by ballistic electron transport. In Copper, for instance, the depth of energy penetration is assumed by the mean-free path length of electrons, which is considerably larger than the optical penetration depth.

On the other hand, as previously mentioned in *Section 2.3.5*, for ignoble metals such as Iron, ballistic energy transport is negligibly small due to strong electron-phonon coupling. As a result for Stainless steel the mean-free path of electrons can be assumed to be in the range of the optical penetration depth.

4.3 Material removal

This section contributes to overcome this identified discrepancy in terms of the laser energy transport mechanism. Experimentally determined ablation volume rates are compared to theoretical predicted ablation volumes. Therefore different energy transport mechanisms are taken into discussion.

Figure 4-15 compares experimentally determined and theoretically calculated volume ablation rates for Aluminium.

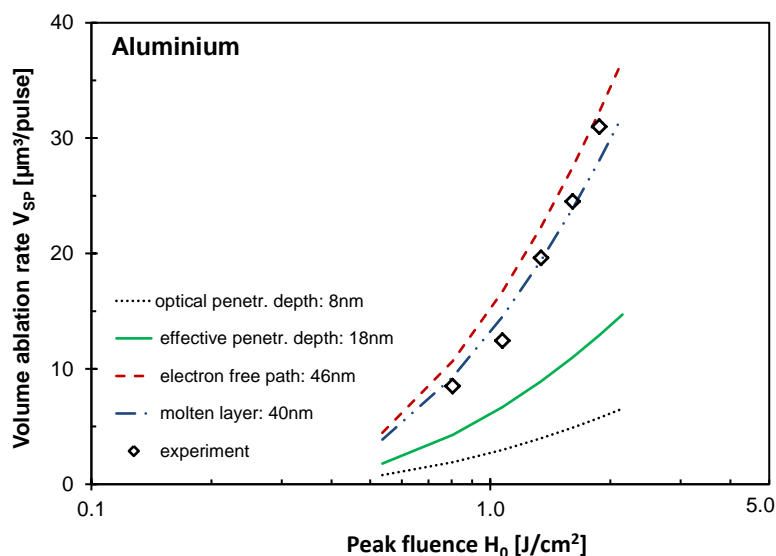


Figure 4-15: Theoretically predicted and experimentally determined volume ablation rates versus fluence on Aluminium; theoretical values were calculated considering different energy transport mechanism, such as optical penetration (dotted line), effective penetration depth (solid line), mean-free path length of electrons (dashed), and molten layer (rough-dashed line); the experimentally obtained data are indicated by the black rhombus (\diamond).

The theoretically achievable volume ablation rates are calculated considering the ablation threshold of 0.27 J/cm^2 , determined in *Section 4.2.2* with 102 kHz repetition rate. Furthermore the volume ablation rate calculations were carried out by taking into account different energy transport mechanisms, such as optical penetration, the effective penetration depth as derived from the regression line given in **Figure 4-9**, and the mean-free path of electrons. The distinct energy penetration depth values included in the model are summarised in the following table.

4.3 Material removal

Table 4-2: A summary of different depth of energy transport, used in volume ablation rate calculations on Aluminium.

Aluminium		
Mechanism	Depth value	Verification
Optical penetration depth	8.2 nm	Table 3-2
Effective penetration depth	18.4 nm	Figure 4-9
Mean-free path of electrons	46 nm	[46]
Thickness of molten Aluminium layer	40 nm	[125]

A good agreement between theoretical and experimental data has been obtained by taking into account the laser energy penetration depth of 40 nm. On one hand, this depth correlates closely to the mean-free path of electrons, reported for pure Aluminium of 46 nm. On the other hand, it is considerably larger than both the optical penetration depth and the effective penetration depth determined in *Section 4.3.2*.

However, a study presented by *COLOMBIER et al.* [125] might be help to clarify the mechanisms taking place. In this paper a remaining liquid layer with a thickness in the range of 40 nm is reported. This liquid layer originated on the Aluminium surface upon ultrashort pulses laser irradiation using 1 J/cm² fluence, which is similar to the laser fluence investigated in this thesis. Transferring these observations to high-PRF laser processing it can be assumed, that this layer may be molten when the next laser pulse irradiates. The molten Aluminium potentially enhances laser beam absorption, and thus the increase of material removal can be assumed. As a result, a mixture of both ballistic energy transport and material melting seems to be more preferable rather than energy distribution only driven by the mean-free path of electrons.

Moreover, with the assumption of a higher surface temperature, the mean-free path of electrons will be reduced due to the higher probability of collisions of the electrons with the more oscillating lattice [107]. As a result, the lower mean-free path of electrons would suggest lower volume ablation rates, in contrast to the experimental outcomes. For Aluminium it has been shown that the ablation threshold decreases and the amount of material removed increases with the higher repetition rates. This might be induced by

the higher thermal load of the work piece as a result of high-PRF irradiated laser pulses. Thus the increase of the surface temperature can be suggested for increasing repetition rates, causing a thicker melting layer accompanied by higher material removal.

However, a mismatch exists in terms of energy transfer mechanism. **Figure 4-9** shows an effective penetration depth of 18.4 nm, determined on cavities produced with 25 scan passes. In **Figure 4-15**, by contrast, the energy penetration depth of 40 nm was estimated as “best fit” parameter. This might be explainable by a higher thermal impact on the work piece in the latter case. The volume ablation rate was determined on 30 μm deep cavities, fabricated with a varying number of scan passes ranging between 25 and 900 passes. The number of passes was varied depending on the fluence, to ensure the constant cavity depth. As a result of the significant higher number of scan passes in comparison to the 25 scan passes applied before, a considerably higher thermal load of the work piece can be assumed. This will affect both the heat transfer mechanism and the ablation rate.

For Copper, experimentally and theoretically obtained volume ablation rates versus the impinging laser fluence are presented in **Figure 4-16**. The theoretically achievable volume ablation rates were calculated based on different energy transport mechanisms. The optical energy penetration, the effective penetration as determined in *Section 4.2.3* by studying the ablation rates and the penetration depth in the range of the electron mean-free path were taken into account. Further, the ablation threshold of 0.29 J/cm^2 was considered in the model. This is the averaged ablation threshold, estimated from distinct threshold values determined for Copper in *Section 4.2.2*.

A good agreement between the experimental ablation volumes and calculated values has been obtained by taking into account the experimentally determined effective penetration depth of 19 nm. The theoretical volume ablation rates calculated with the optical penetration depth are definitively too small. On the other hand, putting the mean-free path of electrons into the volume ablation rate calculation model does not fit to the experimentally determined values at all.

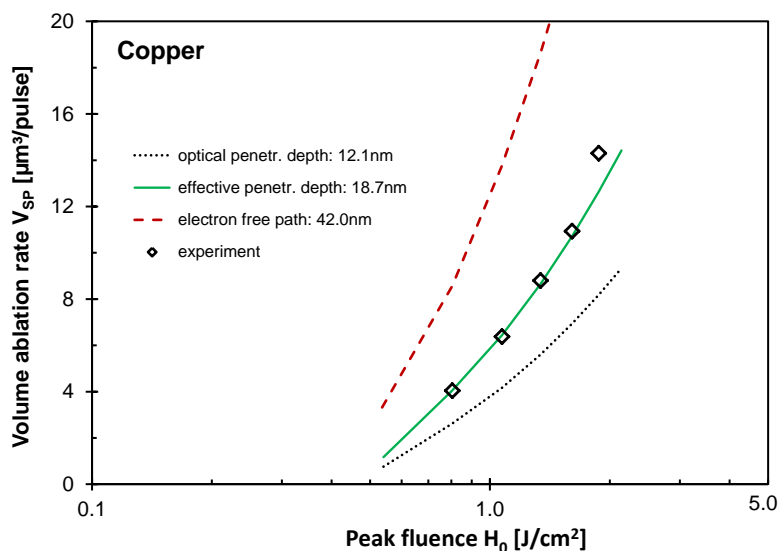


Figure 4-16: Theoretically predicted and experimentally determined volume ablation rates versus fluence on Copper; theoretical values were calculated considering different energy transport mechanism, such as optical penetration (dotted line), effective penetration depth (solid line), and mean-free path length of electrons (dashed line); the experimentally obtained data are indicated by the black rhombus (\diamond).

The distinct energy penetration depths considered in the volume ablation rate calculation model are summarised in **Table 4-3**.

Table 4-3: A summary of different depths of energy transport, used in volume ablation rate calculations on Copper.

Copper		
Mechanism	Depth value	Verification
Optical penetration depth	12.1 nm	Table 3-2
Effective penetration depth	18.7 nm	Figure 4-9
Mean-free path of electrons	42.0 nm	[43]

Figure 4-17 presents the comparison of both the experimentally and theoretically determined volume ablation rate versus the impinging laser fluence for Stainless steel. The experimentally determined ablation threshold of 0.11 J/cm² was used in the volume ablation rate calculation, derived from the threshold values presented in *Section 4.2.2*. Within the parameter range investigated, the experimentally achieved volume ablation rates correlate very well to the theoretical calculations, obtained based on 15 nm energy

penetration depths. This depth corresponds exactly to the effective penetration depth of Stainless steel, estimated as 15 nm from the slope of the ablation rate regression line in **Figure 4-9**.

In addition, the volume ablation rate based on the optical energy penetration depth of 18 nm is plotted in **Figure 4-17**. At the lower fluence, the calculated ablation volume is little above the experimentally determined values, but differs slightly more with higher fluence.

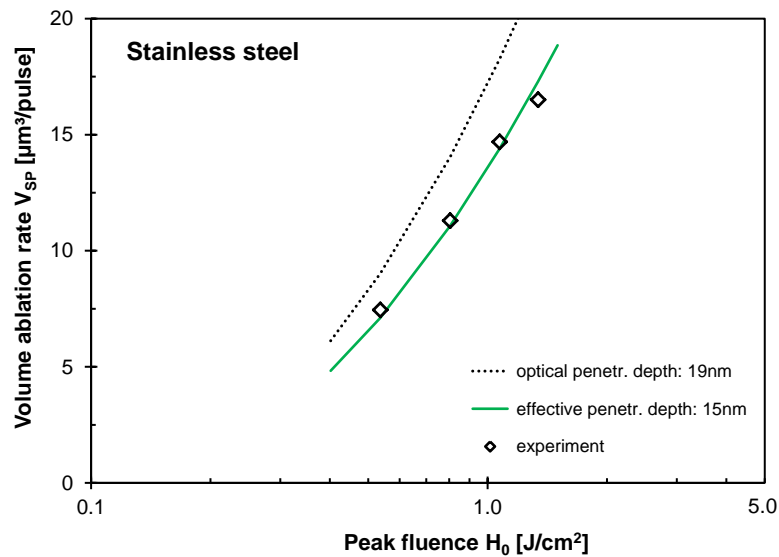


Figure 4-17: Volume ablation rate versus peak fluence obtained on Stainless steel; theoretically values were calculated considering two different energy transport mechanisms: optical penetration depth (dashed line), and the effective penetration depth (solid line); experimentally determined ablation rates are indicated by the black rhombus.

For Stainless steel it can be concluded, that material ablation upon high-PRF femtosecond laser irradiation is determined by the effective penetration depth of 15 nm. Thus the depth of energy transition is a little lower than the optical penetration depth, supposed as relevant mechanism elsewhere. Apart from differing experimental conditions, another explanation for the detected variance in energy penetration might be given by the reduced mean-free path of electrons. The depth of energy transfer will be limited as a result of the higher number of collisions between electrons and lattice ions, affected by the more heated bulk material due to high-PRF laser irradiation.

As before, **Table 4-4** lists the relevant penetration depths that have been included in volume ablation rate calculation. In case of the ignoble metal alloy Stainless steel, the mean-free path of electrons is in the length scale of optical penetration. This is in

4.4 Material removal efficiency

contrast to the noble metals Aluminium and Copper, where the mean-free path of electrons considerably differ from the optical penetration depth [46].

Table 4-4: A summary of different depths of energy transport used in volume ablation rate calculations on Stainless steel.

Stainless steel		
Mechanism	Depth value	Verification
Optical penetration depth	18.0 nm 19.0 nm (Iron)	[126] Table 3-2
Effective penetration depth	15.0 nm	Figure 4-9
Mean-free path of electrons	for ignoble metals in the range of the optical penetration depth	[46]

4.4 Material removal efficiency

Material removal efficiency is chosen as another material removal evaluation criterion providing a measure of volumetric material removal per irradiated laser energy. The material removal efficiency R_{eff} calculates by the ratio of the empirically determined material removal rate V_{SP_exp} divided by the irradiated laser energy Q_P

$$R_{eff} = \frac{V_{SP_exp}}{Q_P} \quad \text{Equation 4-17.}$$

The higher the material removal efficiency, the more material can be removed with the irradiated laser energy. Thus the value can be used to determine optimised processing parameters for practical applications.

In this analysis, material removal rates have been calculated from the volume ablation rate of laser processed cavities accordingly **Equation 4-17**. The cavities were fabricated by using different machining parameters. Both, the pulse energy Q_P and the lateral pulse

4.4 Material removal efficiency

spacing d_x were varied, ranging between 2 μJ and 7 μJ as well as 2.5 μm and 12.5 μm , respectively. The pulse repetition rate was kept constant at 205 kHz. The volume ablation rates are presented in *Annex 7*, and have been discussed already in the previous *Section 4.3.3*.

Figure 4-18 summarises the material removal efficiency, calculated for Aluminium, Copper, and Stainless steel. Therein the material removal efficiency is presented colour-coded. The bright green colour represents the highest removal efficiency whilst the red colour highlights the lowest level of material removal per energy.

Material removal efficiency R_{eff} [$\mu\text{m}^3/\mu\text{J}$]							
		Lateral pulse spacing d_x [μm]					
		2.5	5	7.5	10	12.5	
Pulse energy Q_P [μJ]	Aluminium						
	3	X	2.83	2.40	X	1.97	
	4	X	3.11	3.07	2.65	3.00	
	5	X	3.93	3.49	2.95	2.67	
	6	X	4.08	3.62	3.60	2.73	
	7	X	4.43	4.24	X	3.19	
	Copper						
	3	X	0.80	0.95	1.18	1.35	
	4	X	1.14	1.16	1.34	1.59	
	5	X	1.46	1.39	1.47	1.56	
	6	X	1.64	1.59	1.77	1.82	
	7	X	1.93	1.81	1.89	2.04	
	Stainless Steel						
	2		3.71	3.73	3.67	3.65	3.78
	3		4.10	3.77	3.60	3.41	3.39
4		3.96	3.67	3.42	3.20	3.18	
5		3.41	3.30	3.18	3.10	3.02	

Figure 4-18: Material removal efficiency calculated for Aluminium, Copper, and Stainless steel; the green coloured fields represent the highest efficiency, the red coloured fields highlight the lowest level of energy efficiency.

For Aluminium the highest material removal efficiency of 4.43 $\mu\text{m}^3/\mu\text{J}$ was obtained by irradiating pulses with the highest investigated energy of 7 μJ and a small spacing of 2.5 μm . By using these parameters, a maximum thermal load of the Aluminium work piece can be suggested. Thus the results obtained are conclusive to the previous assumptions. In *Section 4.3.4* it was reported that a molten Aluminium layer, potentially originated due to high thermal load of the work piece, caused the enhancement of both laser beam absorption and material removal.

By contrast, on Copper the highest fluence of 7 μJ and the largest lateral pulse spacing of 12.5 μm provided the highest material removal efficiency of 2.04 $\mu\text{m}^3/\mu\text{J}$. The high pulse energy seems to be beneficial for material removal because of the high evaporation temperature of Copper. Further it was demonstrated already that high surface roughness will enhance laser beam absorption. According to this, a high surface roughness will be indicated in the next subchapter for the detected parameter set.

In Stainless steel the largest amount of 4.10 $\mu\text{m}^3/\mu\text{J}$ removed volume per irradiated laser energy was obtained by irradiating laser pulses of 3 μJ energy and the smallest lateral pulse spacing of 2.5 μm . Thus laser ablation of Stainless steel might have benefitted from the temperature rise induced by heat accumulation that can be expected to be greatest in areas close to the laser processing zone.

However, in practical application not only the material removal efficiency is important, but also the processing quality plays a major role. Thus the surface roughness of high-PRF laser processed surfaces is evaluated.

4.5 Surface roughness

The surface quality of the laser fabricated 30 μm deep standardised cavities is evaluated by means of the surface roughness. The roughness was determined by using the tactile surface profiler DEKTAK 3030, described in the previous *Chapter 3.4.3*. The values presented in **Figure 4-19** are given as mean surface roughness R_a , averaged over three distinct surfaces fabricated with the same parameter set. The surface roughness of each surface was determined by three individual, one millimeter long measuring lines, obtained by moving the DEKTAK stylus along the laser processed surface.

In the figures a clear dependency between the roughness and both the fluence and the lateral pulse spacing is recognisable. For all kinds of investigated materials, high-quality surfaces with small roughness have been fabricated by using moderate laser fluence and the lateral pulse spacing of 5 μm . On the other hand, the surface roughness increased with increasing laser fluence and wider lateral pulse spacing. The increase of the

roughness can be explained by two different mechanisms. The first one is related to crater formations across the laser processed surface, fabricated due to insufficiently overlapping laser pulses due to wider lateral pulse spacing. By contrast, irradiation high-fluence laser pulses with small pulse spacing induce heat accumulative effects. This causes either material melting or formation of self-organising micro structures, appearing on Aluminium and Stainless steel, respectively.

After laser treatment the minimum surface roughness of 0.1 μm was obtained on the polished Copper metal sheet. The smallest roughness value obtained for Aluminium and Stainless steel were 0.16 μm and 0.32 μm , respectively.

Furthermore it was observed that the roughness of the untreated sample surface influences significantly the roughness of the laser processed structure. Thus it can be concluded the lower the roughness of the untreated surface, the lower the achievable roughness of the laser processed surface. In addition, laser processing in defocused surface plane position did not improve the surface roughness.

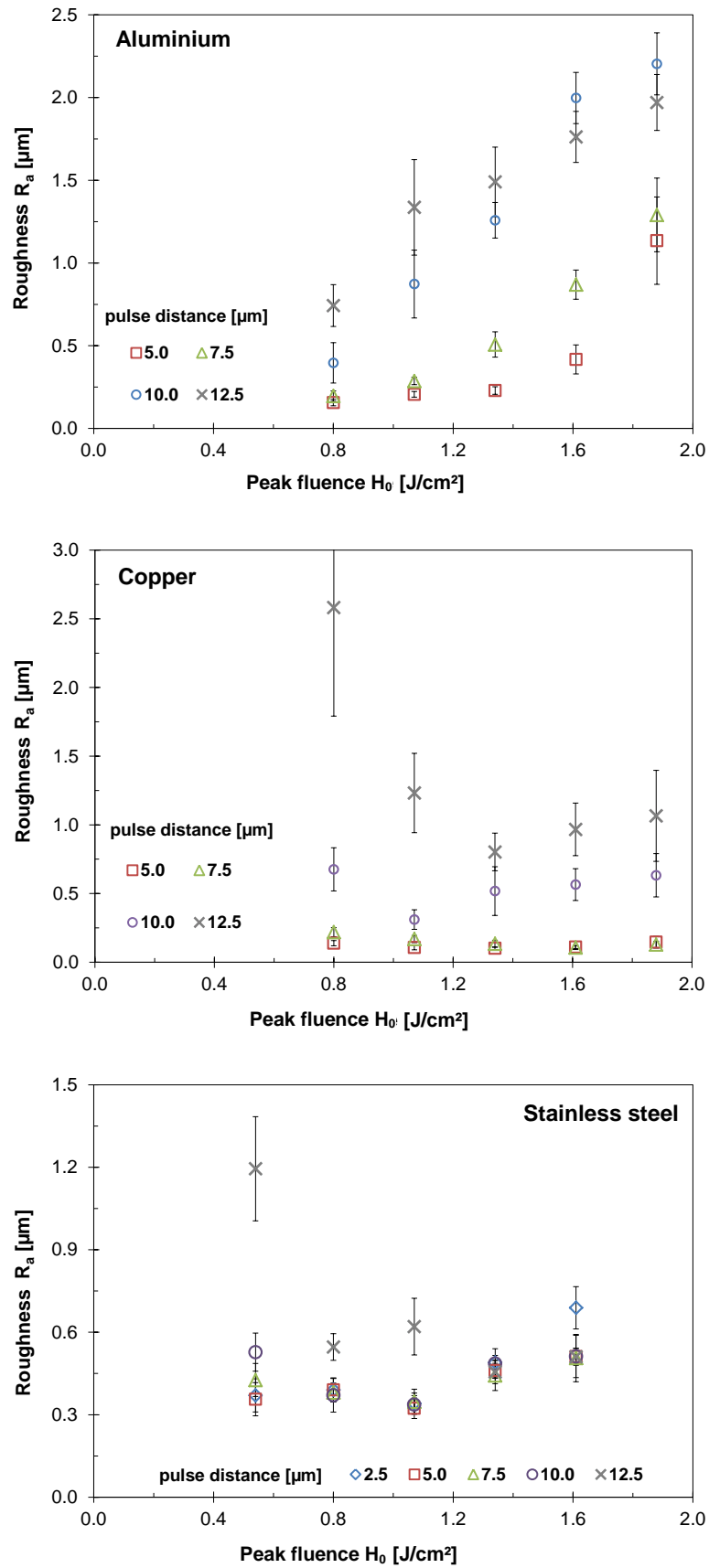


Figure 4-19: Surface roughness R_a measured on laser processed cavities utilising the DEKTAK surface profiler; laser fluence and lateral pulse spacing were varied.

4.6 Summary

High-PRF femtosecond laser ablation of metals was investigated in order to clarify the impact of the temporal pulse-to-pulse distance on material ablation. Initially it has been found for the low thermally conductive Stainless steel that the ablation threshold decreased at the higher repetition rates. Comparison of the ablation thresholds obtained with 20 kHz ($H_{th} = 0.11 \text{ J/cm}^2$) and 1.02 MHz ($H_{th} = 0.088 \text{ J/cm}^2$) showed an almost 25 % lowered ablation threshold for the highest repetition rate. Therefore enhanced laser beam absorption due to the surface temperature rise caused by heat accumulation was supposed as mainly influencing mechanism. The highest impact of the repetition rate on the ablation threshold was found for Aluminium. For this metal the ablation threshold was lowered more than 50 %.

It is suggested that material melting takes place due to heat accumulation and the low melting temperature, inducing enhanced laser beam absorption. Finally no significant impact of the repetition rate on the ablation behaviour on Copper was observed. Because of the high heat conductivity and the high melting point, heat accumulative effects can be largely ruled out in the investigated parameter range.

Further a model was designed to calculate the volume ablation rates. Good agreements between modelled and experimental values were obtained by taking into account the effective penetration depth instead of the optical penetration depth for laser energy transport.

Further, optimised laser process parameters can be derived from the results achieved in this study with regard to volume ablation rate, material removal efficiency and roughness. To obtain a surface roughness R_a less than $0.5 \mu\text{m}$, optimised pulse spacing and pulse energy can be summarised as follows:

Aluminium: $5.0 \mu\text{m}$ pulse spacing and $5.0 \mu\text{J}$ pulse energy,

Copper: $7.5 \mu\text{m}$ pulse spacing and $7.0 \mu\text{J}$ pulse energy,

Stainless steel: $5.0 \mu\text{m}$ pulse spacing and $3.0 \mu\text{J}$ pulse energy.

5 Enhanced study of high-PRF laser ablation

5.1 Introduction

The chapter is divided into six sections presenting the enhanced study of high-PRF ultrashort pulse laser processing. After a brief introduction, insights into material ablation following high-PRF ultrashort pulse laser processing are presented in *Section 5.2*. Time-resolved photographs of the ablation plume are shown, captured on Aluminium, Copper and Stainless steel by using an intensified high speed camera.

Section 5.3 discusses the interplay between the significant interaction phenomena heat accumulation and particle shielding, observed in high-PRF laser processing. For this, laser irradiations of Stainless steel and Copper are evaluated with respect to the volume ablation rate by using different lateral pulse spacing, pulse energy and repetition rates.

Section 5.4 presents further work on material removal. It is reasonable to expect that the increase of the repetition rate potentially increase the material removal rate as a result of feasible higher processing speed. The good knowledge about the achievable material removal rates is supportive to evaluate machining throughput and productivity. This is highly essential for potential industrial applications.

SEM photographs of both laser processed trench-like structures and ablation products deposited around the processing area are presented in *Section 5.5* to underline the impact of the temporal pulse-to-pulse distance on the machining outcome.

Section 5.6 comprises the conclusions based on results achieved in this chapter.

5.2 High speed camera imaging of material ablation

5.2.1 Camera trigger scheme

The impact of the temporal distance between consecutively irradiated laser pulses on material ablation was investigated by high speed camera imaging. In the study a four camera channel MCP-image intensifier (micro channel plate) high speed camera (hsfc pro, PCO) was utilised. The camera was triggered in double shutter exposure mode, supplying two recorded sequences consisting of four individual snapshots each. The minimum temporal distance provided by the camera was either 3 ns between four distinct snapshots of a single captured sequence, or longer than 500 ns between two possible sequences.

In this thesis, the progress of ablation plume origin was recorded within a time frame of two micro seconds. Because of only eight snapshots can be captured in a single double shutter record, two separate camera recordings consisting of each two double shutter sequences and 16 individual snapshots in total were included in the evaluation process. As a result ablation plume origin could be evaluated with a sufficiently high temporal resolution.

The camera trigger scheme applied in this study is described in **Figure 5-1** (top). Exposure to the four camera channels is termed C1-A to C4-A for the first double shutter exposure sequence, and C1-B to C4-B for the second double shutter exposure sequence. In addition a further double shutter recording immediately captured following the first record is included in the schematic, labelled by *. The exposure time of each camera channel was 240 ns throughout the study. The individual snapshots were captured between 20 ns and 1,740 ns after a single laser pulse irradiated the sample surface, illustrated by the rectangle of 240 ns length.

The lower part of **Figure 5-1** indicates the sequence of laser pulses irradiated within the time frame of two microseconds. Depending on the repetition rate, a various number of pulses irradiate the samples. Each impinging laser pulse is highlighted by a black bar. To guarantee comparable laser irradiation conditions during the recording of material ablation, the laser system and the high speed camera were synchronised via the pulse picker.

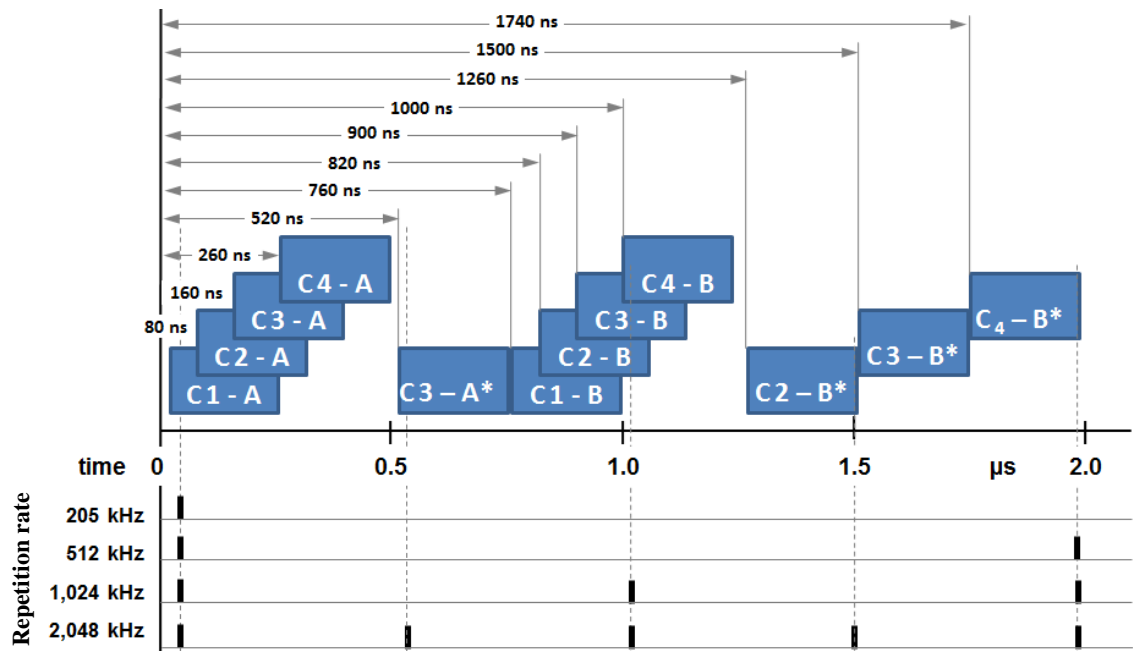


Figure 5-1: Trigger scheme applied in double shutter high speed camera imaging (top) and sequence of impinging laser pulses indicated by the black bars (bottom); exposure time of each record was 240 ns, indicated by the blue rectangles.

5.2.2 High speed camera photographs and discussion

Figure 5-2 illustrates the expansion of laser ablated particle plumes within the time frame of two micro seconds in a chronological view. All three metals on interest have been irradiated with laser pulses of $6 \mu\text{J}$ energy and fluence of 1.6 J/cm^2 . At the lower repetition rate of 205 kHz only a single pulse event was recorded in the time frame chosen for this study. For laser irradiations using higher repetition rates, by contrast, a higher number of pulse impacts can be seen in the figure. This is due the shorter temporal pulse-to-pulse distance for laser pulses of higher repetition rates.

It is worth mentioning that the arising ablation plumes, presented in the first photograph of each rows in **Figure 5-2**, are not induced by the very first irradiated laser pulse. Rather the camera recordings have been started randomly during steady laser processing, thus the metal surfaces had already been hit by an uncertain higher number of laser pulses when the recording has started.

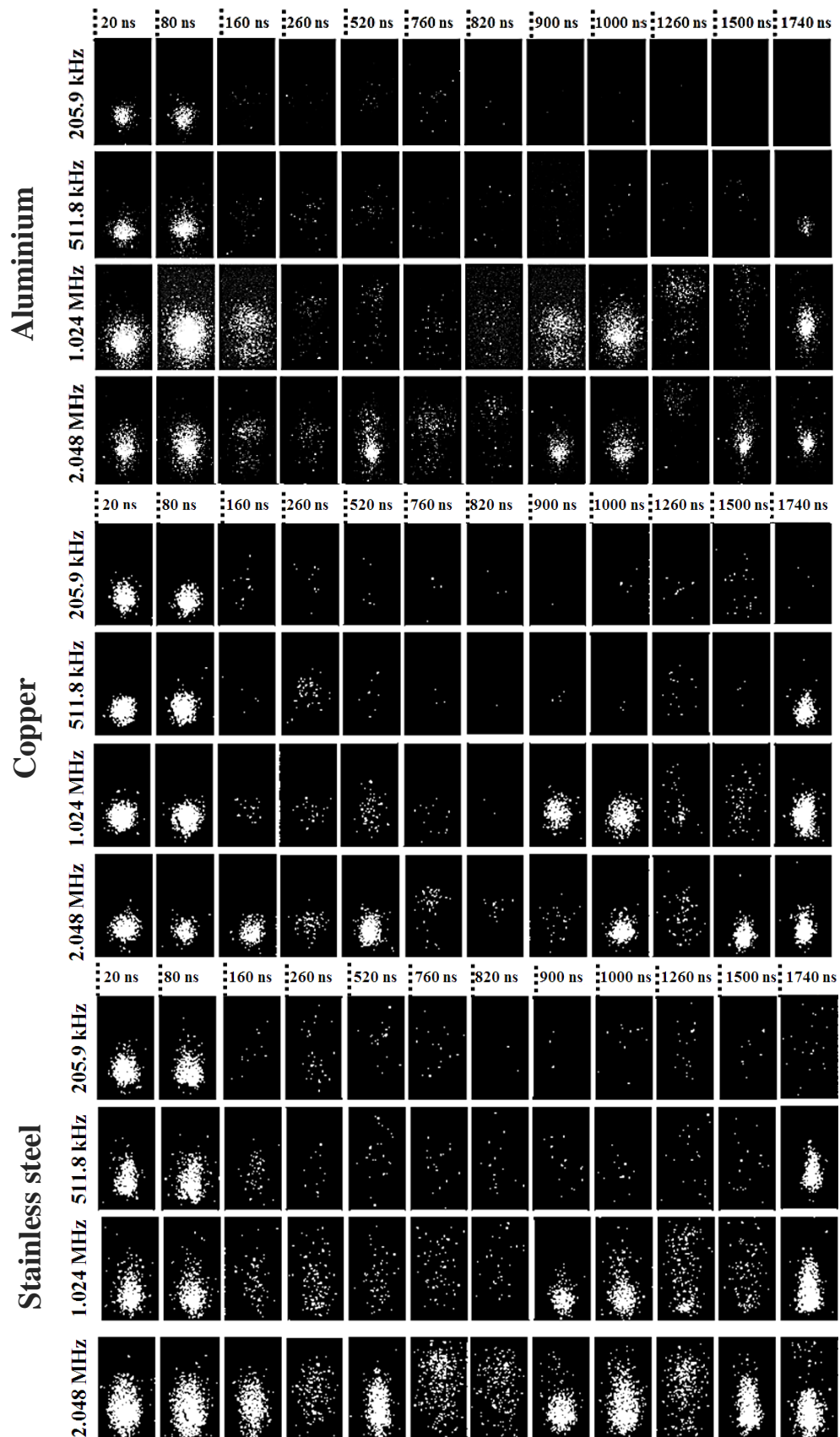


Figure 5-2: Ablation particle/plasma plumes arising in high-PRF femtosecond laser irradiation of Aluminium (top), Copper (entre), and Stainless steel (bottom); different repetition rates were applied; exposure time of each camera record was 240 ns.

Bright ablation particle/plasma plumes can be seen in **Figure 5-2** for all investigated metals shortly after the laser pulse irradiated the sample surface. In Aluminium and Copper the ablation plume expanded almost half-spherically that is conclusive to observations made by *SALLÈ et al.* [123] on Copper. The authors reported almost similar plume expansion rates in both longitudinal ($4.6 \cdot 10^5$ cm/s) and transverse ($3.0 \cdot 10^5$ cm/s) directions, which is in the range of the speed of sound of Copper.

In Stainless steel the ablation plume is largely directed towards the incoming laser beam. The ablation plumes expand progressively, but it can be seen that particles and clusters are still flying nearby the laser processing area even for times greater than one micro second after laser pulse irradiations. These remaining particles potentially induce absorption, scattering or/and spatially distortion of the next following laser pulses. As a result, material removal is detrimentally affected by these shielding effects, particularly in case of high-PRF laser irradiation when a higher number of laser-ablated particles is apparent enclose the processing zone.

Further, the snapshots presented in **Figure 5-2** for Stainless steel, reveal enlarged and brighter ablation plumes obtained at the higher repetition rates. From this it can be suggested that in high-PRF laser processing the next following laser pulses irradiate a molten/overheated surface area, causing enhanced material ablation. This assumption is supported by the results obtained in temperature calculations, which will be presented in the later *Chapter 6*. In this chapter it is shown that high-PRF laser irradiation will lead to surface temperatures above the melting temperature of Stainless steel.

For Aluminium and repetition rates greater than 1 MHz, the captured photographs show considerably enlarged ablation plumes, giving evidence of increased material removal. For this, material melting can be suggested potentially induced by accumulation of heat due to the short temporal distances of high-PRF laser pulses. A molten Aluminium layer, in turn, might be beneficial for laser beam absorption and material ablation, suggested already in the previous *Section 4.3.4*. In addition, it can be assumed that laser irradiation of a molten layer instead of solid material may potentially cause a more explosive material ablation that is accompanied by higher material removal rates.

The ablation plumes recorded on Copper, by contrast, seems to be almost unaffected by the repetition rates. Only with the highest investigated repetition rate of 2.048 MHz both a higher number of particles and slightly enlarged ablation plumes can be recognised.

As a result, it can be concluded for Copper that particle shielding and heat accumulation may have an effect on laser matter interaction only at the higher repetition rates in the range of a few mega Hertz, but further investigations are required.

5.3 Interplay between heat accumulation and particle shielding

The impact of the lateral pulse spacing on material ablation was investigated on the example of Copper and Stainless steel. The study contributes to clarify the interplay between heat accumulation and particle shielding in high-PRF laser processing. On one hand, particle shielding might be reduced with wider spatial distance between incoming laser pulses. This is due a smaller surface area may be partially shielded from the laser beam. As a result a higher amount of laser energy irradiates the sample causing stronger material removal. On the other hand, the already mentioned enhancement of laser beam absorption induced by heat accumulation may be diminished with wider lateral pulse spacing. In this case, the next incoming laser pulses irradiate a less thermally affected area. This is due distribution of heat is limited by the thermal diffusion length.

In the following, the interplay between heat accumulation and particle shielding as well as the effect on material removal is discussed. For this, the volume ablation rates have been calculated from the depths of standardised cavities by using **Equation 4-16**. The cavities were produced with different repetition rates (102 kHz, 1.024 MHz) and pulse energies (3.3 μJ , 6.6 μJ). Furthermore, the lateral pulse spacing \mathbf{d}_x was varied in the range between 2 μm and 16 μm . The hatch distance \mathbf{d}_y was kept constant at 5 μm during the experiments.

Because of the relation between the lateral pulse spacing and the repetition rate a maximum scan speed of 16 m/s was applied. To supply such high scan speed with the available galvanometer scan system, the 56 mm f-theta focusing objective was replaced by the 80 mm f-theta objective. By using this experimental setup the focus spot diameter enlarged to 42 μm due to the longer focal distance. As a result the maximum fluence decreased to 0.48 J/cm² and 0.95 J/cm² for the irradiated laser pulses of 3.3 μJ

5.3 Interplay between heat accumulation and particle shielding

and 6.6 μJ , respectively. This fluence was sufficiently high for Stainless steel ablation. Copper, by contrast, was only investigated with the higher pulse energy of 6.6 μJ due to the higher ablation threshold.

Three cavities were processed with each individual processing parameter set for statistical analysis. Using the non-contact surface profiler *$\mu\text{surf Explorer}$* , the depth of each cavity was measured as mean depth value averaged across the ablated surface.

As shown in the **Figure 5-3**, laser irradiation of Stainless steel with the low pulse energy of 3.3 μJ and the low repetition rate of 102 kHz yielded more or less constant ablation volumes, almost independent from pulse spacing. Thus the material ablation seems to be unaffected by particle shielding and heat accumulation.

Moreover, with the widest pulse spacing and twice of the irradiated pulse energy of 6.6 μJ the ablation rate is nearly doubled. For high-energy laser pulses but small pulse spacing, by contrast, the volume ablation rates increased disproportionately more than twice. For this a more efficient material removal can be suggested, potentially induced by a higher surface temperature closely around the laser processing area, which might be caused by the higher laser energy input.

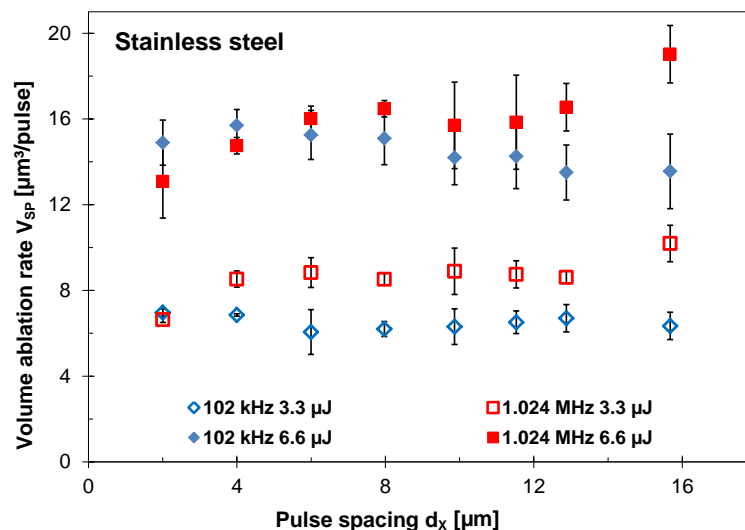


Figure 5-3: Volume ablation rate versus lateral pulse spacing on Stainless steel; the pulse energy and the repetition rate were varied.

On the other hand, the ablation rates obtained by using the high repetition rate (1.024 MHz) low energy (3.3 μJ) laser pulses are considerably larger than ablation rates achieved with the same pulse energy but lower repetition rate (102 kHz). In this case,

material ablation seems to be enhanced by heat accumulation as a result of less energy distribution at the higher repetition rates. The ablation rates are almost unaffected by the lateral pulse spacing, exceptionally the pulse spacing of 2 μm .

The interplay between particle shielding and heat accumulation becomes more evident by comparison with the volume ablation rates obtained with the high pulse energy of 6.6 μJ and both different repetition rates and pulse spacing. By irradiating low repetition rate high energy laser pulses, the volume ablation rate decreased with wider pulse spacing. Because the laser induced temperature field distributes by thermal diffusion, a reduced long-distance effect of heat to material ablation can be assumed with wider pulse spacing. A further drop of the volume ablation rate can be observed for pulse spacing in the range between 8 μm and 10 μm . This is close to the heat diffusion length of 12 μm , calculated based on 10 μs time interval between two consecutively irradiated laser pulses of 102 kHz repetition rate.

Irradiation of high-energy high-fluence laser pulses induced strong particle ejection and thus particle shielding becomes dominant when laser pulses of short temporal distances irradiate the ablation area. As a result for the pulse spacing of 2 μm , a lower ablation rate has been achieved with 1.024 MHz, compared to 102 kHz. However, with the wider lateral pulse spacing, the removal rates achieved with 1.024 MHz increased considerably, although laser beam shielding is still apparent. The results obtained in high-PRF laser processing of low thermally conductive materials give evidence that energy losses caused by particle shielding can be counterbalanced by heat accumulation effects.

For Copper, by contrast, neither significant effects of heat accumulation nor particle shielding on material removal can be observed in **Figure 5-4**. Only the wider pulse spacing caused a slight increase of the volume ablation rate, which might be induced by the rough surface. As a result, a negligible impact of the repetition rate on the volume ablation rate can be suggested for the investigated parameter range.

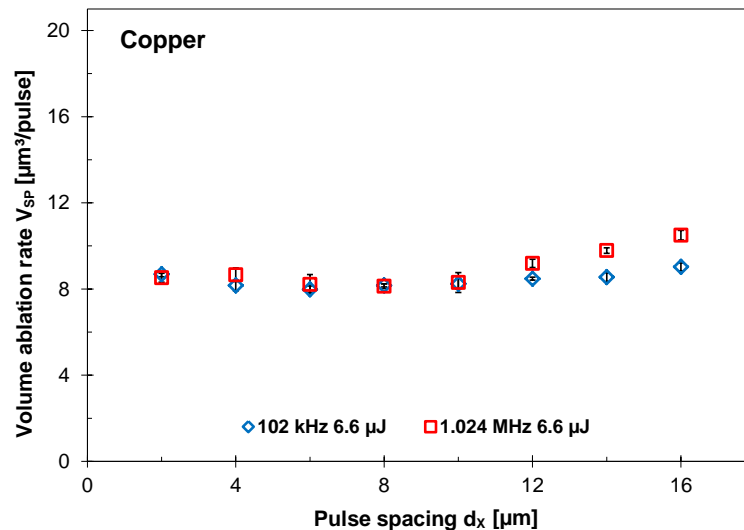


Figure 5-4: Volume ablation rate versus lateral pulse spacing on Copper; the repetition rate was varied.

5.4 Material removal in high-PRF laser ablation

5.4.1 Evaluation criterion

The material removal rate **MRR** defines the laser-removed material volume divided by the laser processing time and rate has been used in this thesis in order to evaluate the laser processing speed. Furthermore, experimentally determined material removal rates are compared with theoretically achievable values.

The experimental material removal rate MRR_{exp} has been determined by taking into account the depths of laser processed standardised cavities. The cavities were fabricated by applying appropriate machining parameters, derived from the results presented in *Chapter 4* with respect to the ablation efficiency, machining quality, and roughness. During cavity laser fabrication, the machining parameters were kept constant with the exception of the repetition rate. Further, to provide constant lateral spacing between consecutively irradiated laser pulses, the scan speed increased with the repetition rate. A maximum scan speed of 4.1 m/s was applied at 1.02 MHz and 4 μm pulse spacing. This was little below the maximum scan speed of the used galvanometer scanner of 4.5 m/s.

The experimental material removal rate was calculated by the product of the volume

ablation rate and the repetition rate. It was achieved by taking into account the depth of the laser fabricated standardised cavities accordingly

$$MRR_{exp} = V_{SP_{exp}} \cdot f_R = \frac{d_P \cdot d_H \cdot l_Z}{n_S} \cdot f_R \quad \text{Equation 5-1.}$$

In addition, the theoretically achievable material removal rate MRR_{th} has been determined. It calculates by the quantity of the volume ablation rate V_{SP} and the laser repetition rate f_R to as

$$MRR_{th} = V_{SP} \cdot f_R = \frac{\delta_{eff}}{4} \pi w_0^2 \ln^2 \left(\frac{H_0}{H_{th}} \right) \cdot f_R \quad \text{Equation 5-2.}$$

In these calculations the dependence of the ablation threshold from the repetition rate has been considered. Therefore the ablation threshold values presented in the **Table 4-1** were taken into calculation.

5.4.2 Cavity depth and material removal rate - results and discussion

Figure 5-5 presents the relation between the depths of laser processed cavities obtained on Aluminium, Copper and Stainless steel versus the repetition rate. The given depths values represent mean values averaged over three individual cavities, processed with the same laser processing parameter set. By using the confocal point sensor, the averaged depth of each individual cavity was determined from three individual scan measurements across the laser processed cavity. The processing parameters applied in this study are given in **Table 5-1**.

In addition, **Figure 5-5** presents the percentage increase of the cavity depth depending on the repetition rate to point out the impact of heat accumulation and particle shielding on material removal. In this analysis, the mean values of the cavity depths achieved with the higher repetition rates are related to the depth values obtained with the lowest investigated repetition rate of 26 kHz. For this low repetition rate it was assumed that material ablation is almost unaffected by heat accumulation and particle shielding. The measurement values of the cavity depths as well as measurement uncertainties are presented in *Annex 8*.

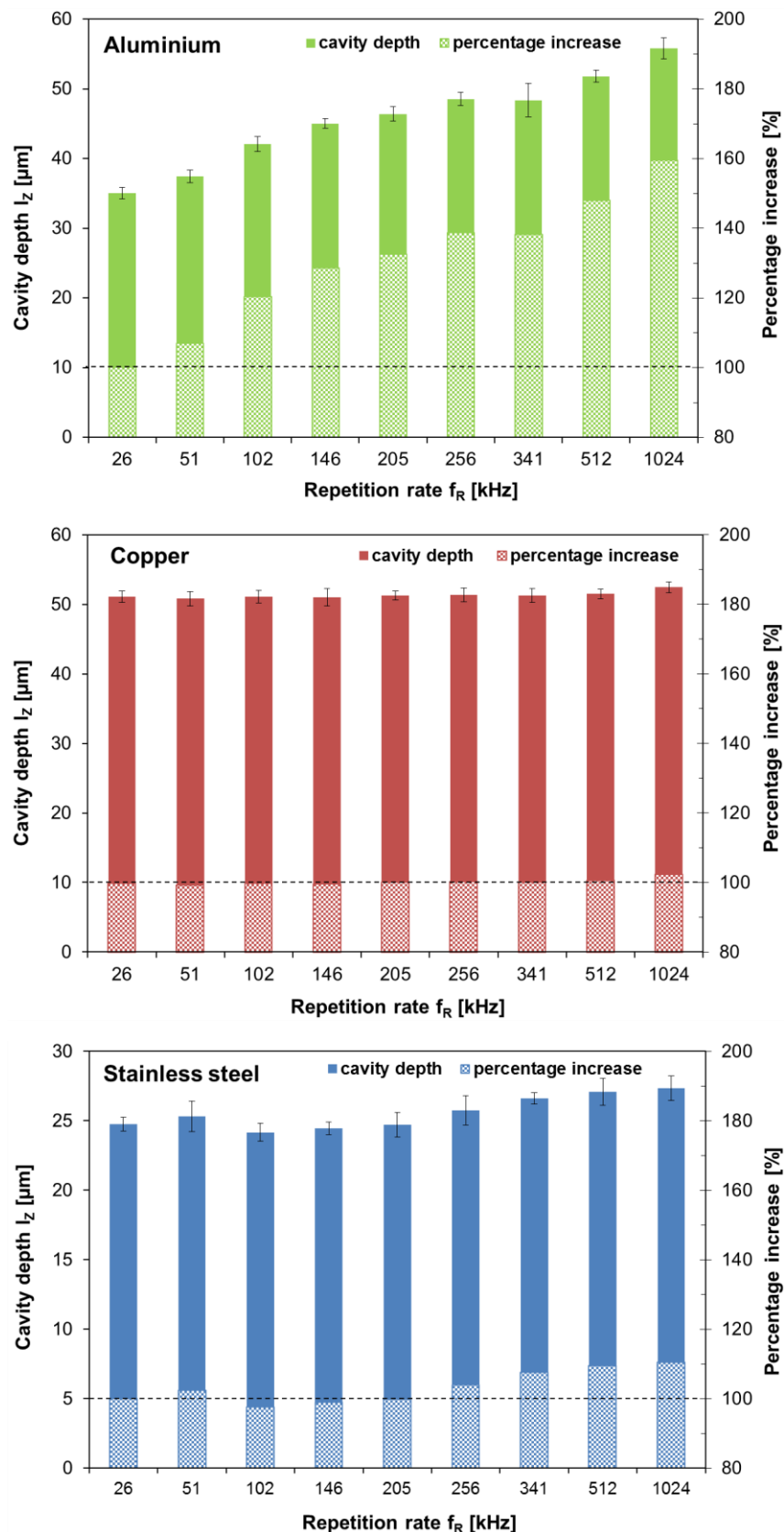


Figure 5-5: Cavity depth versus repetition rate obtained on Aluminium (top), Copper (centre), and Stainless steel (bottom) by using constant processing parameters except the repetition rate; in addition the percentage increase of the cavity depth obtained with various repetition rates in relation to the 26 kHz cavity depth measurement are presented.

5.4 Material removal in high-PRF laser ablation

In the case of Aluminium, the cavity depths strongly increase with the higher repetition rates. Thus a more developed molten Aluminium surface layer can be expected at higher repetition rates, mainly increased due to the shorter cooling cycles between high-PRF laser pulses. It has been already mentioned in the previous *Section 4.3.3* that Aluminium melt enhances considerably the material removal process. For Aluminium, comparison of the cavity depths obtained with the highest and the lowest repetition rate yield a maximum percentage increase of almost 60 % (**Table 5-1**).

On Copper, there is only marginal impact of the repetition rate on the cavity depth. This result emphasizes the assumptions made in *Section 5.3*, that laser processing of Copper is almost unaffected by heat accumulation and particle shielding. Both, high heat conductivity and high ablation threshold have been mentioned already as the most influencing effects. In **Table 5-1** it can be seen that the depths of the cavities processed with the highest investigated repetition rate increased as little as 2.6 %, compared to the cavity depths obtained with the lowest repetition rate.

Table 5-1: Processing parameters and maximal percentage increase of the cavity depths obtained experimentally at 1,024 kHz, related to the 26 kHz value.

Parameter		ALUMINIUM	COPPER	STAINLESS STEEL
Pulse energy Q_P	[μJ]	3	6	3
Lateral pulse spacing $d_x = d_y$	[μm]	4	4	4
Scan number n_s	-	65	65	35
Percentage increase of cavity depth (1,024 kHz depth value related to 26 kHz depth value)	[%]	59.5	2.6	10.4

On Stainless steel, by contrast, the cavity depths achieved with repetition rates ranging between 102 kHz and 205 kHz are slightly lower than cavity depths processed with a repetition rate lower than 100 kHz, potentially induced by particle shielding. With increasing repetition rates, the material removal rates increased. This suggests that laser energy losses affected by particle shielding may be counterbalanced by heat accumulation. The maximum percentage increase of the cavity depth was 10.4 %, obtained by comparing the cavity depths processed with the highest repetition rate to the lowest repetition rate. These findings are conclusive to results presented in the previous

sections, identifying heat accumulation and particle shielding as significant material removal influencing effects in high-PRF laser processing of Stainless steel.

The impact of the repetition rate on the material removal rate is shown in **Figure 5-6**. The material removal rate has been calculated accordingly **Equation 5-1** by taking into account the experimentally determined cavity depths given in **Figure 5-5**. For all investigated metals, the highest material removal rate was achieved with the highest repetition rate of 1,024 kHz. The maximum material removal rates are summarised in **Table 5-2**, calculated for Aluminium of 0.84 mm³/min, for Copper of 0.79 mm³/min, and for Stainless steel of 0.77 mm³/min.

In addition, up-scaled material removal rates are plotted in the figure below by scattered lines. The up-scaled material removal rate MRR_{scal} was calculated by the product of the value of the material removal rate achieved at 26 kHz and the repetition rate. It is obvious for Aluminium and Stainless steel that the experimentally determined material removal rates increased disproportional, whilst the up-scaled values grow linearly. Therefore it can be assumed that material removal benefits from heat accumulative effects, induced by the short temporal pulse-to-pulse distances at the higher repetition rates.

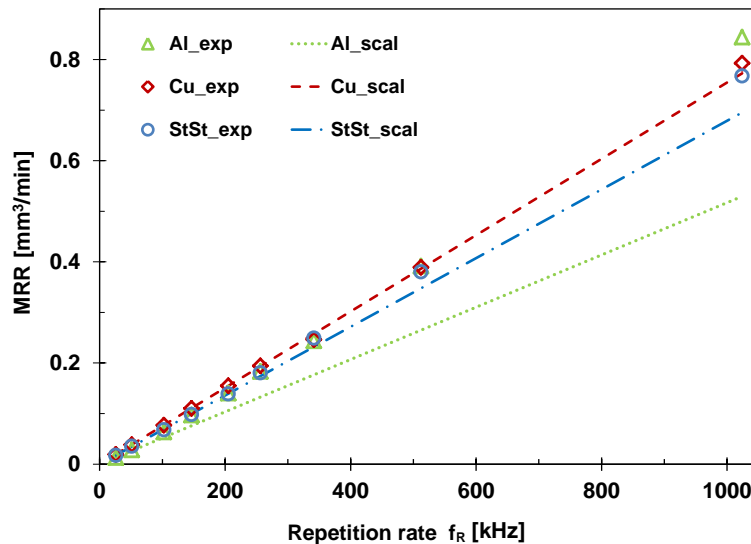


Figure 5-6: Experimentally determined material removal rates (indicated by *exp*) obtained on Aluminium, Copper and Stainless steel versus the repetition rate, the scattered lines reveal the up-scaled material removal rates considering the 26 kHz ablation volume rate (indicated by *_scal*).

5.4 Material removal in high-PRF laser ablation

On **Copper**, by contrast, material removal differed only marginally with higher repetition rates and the material removal rate increased linearly. Thus for the high thermally conductive material, ablation influencing effects as previously reported for Aluminium and Stainless steel can be neglected.

Table 5-2: Material removal rates MRR determined for different repetition rates: MRR_{theo} is the theoretically calculated material removal rate by taking into account the ablation threshold H_{th} ; MRR_{exp} is the experimentally determined material removal rate calculated from the cavity depth; MRR_{scal} is the up-scaled material removal rate calculated by the product of the material removal rate obtained with 26 kHz and the repetition rate.

Material Removal Rate MRR [mm ³ /min]		26 kHz	341 kHz	1,024 kHz
Aluminium	H_{th}	0.33 J/cm ²	0.22 J/cm ²	0.16 J/cm ²
	MRR_{theo}	0.01	0.26	1.20
	MRR_{exp}	0.01	0.24	0.84
	MRR_{scal}	0.01	0.18	0.53
Copper	H_{th}	0.28 J/cm ²	0.28 J/cm ²	0.28 J/cm ²
	MRR_{theo}	0.02	0.23	0.68
	MRR_{exp}	0.02	0.24	0.79
	MRR_{scal}	0.02	0.18	0.77
Stainless steel	H_{th}	0.11 J/cm ²	0.10 J/cm ²	0.09 J/cm ²
	MRR_{theo}	0.02	0.24	0.84
	MRR_{exp}	0.02	0.25	0.77
	MRR_{scal}	0.02	0.23	0.70

Furthermore, **Table 5-2** compares the experimental material removal rate MRR_{exp} , obtained with the theoretically calculated material removal rate MRR_{theo} . In addition, up-scaled material removal rates MRR_{scal} are presented. The material removal rates have been determined for three different repetition rates (26 kHz, 341 kHz, 1,024 kHz). The theoretical material removal rates MRR_{theo} were calculated by using **Equation 5-2**.

In this calculation the decrease of the ablation threshold with the higher repetition rates was taken into account. Ablation threshold values determined in *Section 4.2* have been included into these calculations.

However, the variance of the presented material removal rates points out that material ablation occurring in high-PRF laser processing is much more complex than laser processing using low pulse repetition rates. Moreover, the findings suggest that the material removal rate obtained with the lower repetition rate is not simply scalable with the repetition rate. For all investigated materials it has been found that the up-scaled values are lower than the experimentally determined removal rates. This is mainly due to the fact that material ablation enhancing effects driven by heat accumulation are not included in the calculation of the up-scaled values.

On the other hand, for the highest investigated repetition rate of 1,024 kHz, the theoretical material ablation rates estimated for Aluminium and Stainless steel are greater than experimentally determined removal rates. Explanation therefore can be found in the calculation model. In this model the impact of heat accumulation is included by the lowered ablation threshold, but energy losses due to particle shielding are ignored. Furthermore it can be seen in the next section that the temporal pulse-to-pulse distance influences the roughness of laser processed surfaces. The surface roughness, in turn, affects laser beam absorption. Thus, the change of the absorption conditions might be the dominant effect for Copper, where the theoretically calculated material removal rate is smaller than the experimental material removal rate.

5.5 Material ablation and repetition rate

In this section, high-PRF laser ablation of Aluminium, Copper, and Stainless steel is inspected by SEM analysis. **Figure 5-7** shows SEM photographs of laser processed trench-like structures with a closer view on re-solidified particles deposited around the processing area. The trenches were produced using the line-scan laser processing method. In each case, 10 line-scans with pulses of 5.5 μJ energy, lateral pulse spacing of 2 μm , and repetition rates ranging between 32 kHz and 2,048 kHz were irradiated.

5.5 Material ablation and repetition rate

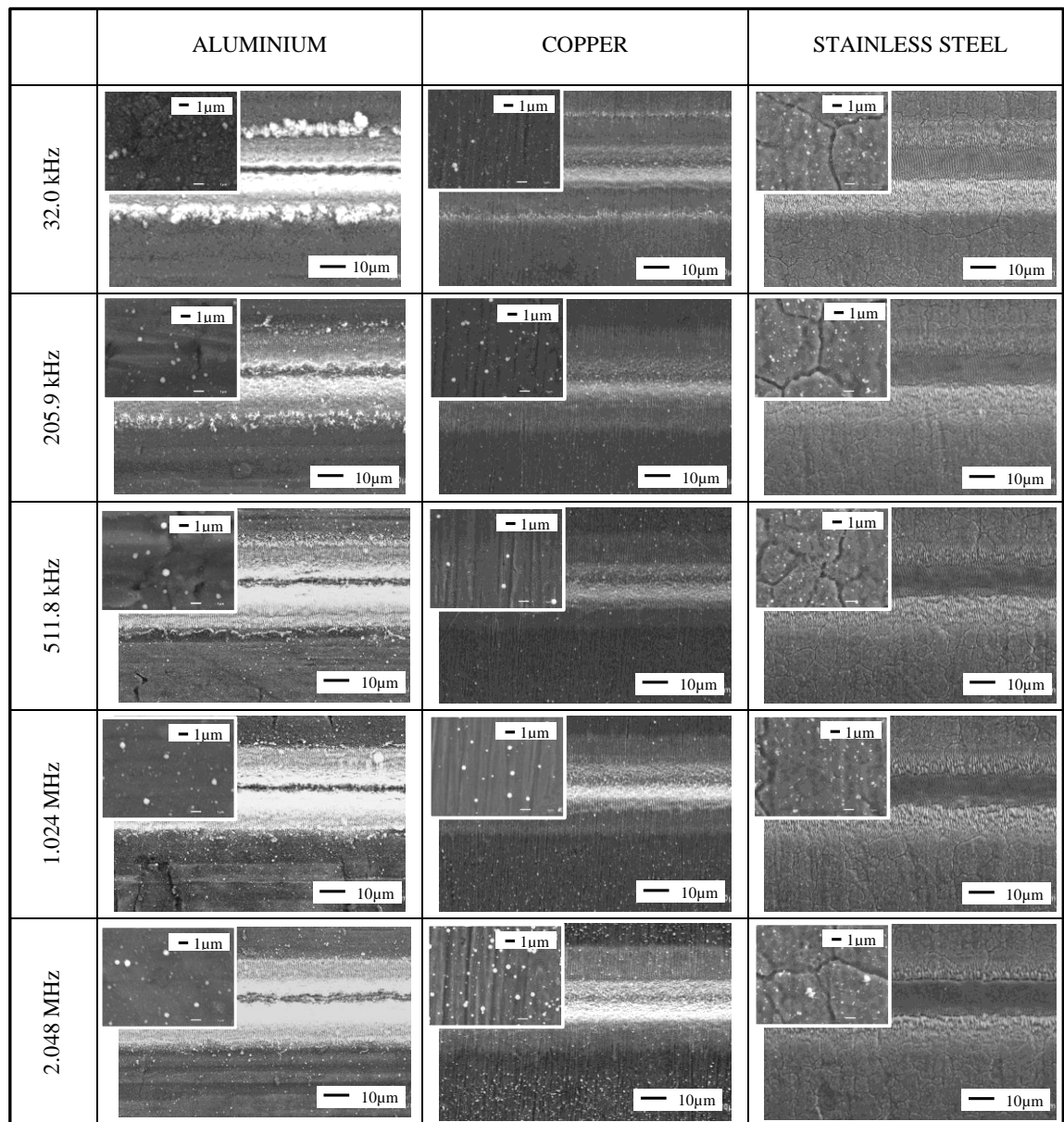


Figure 5-7: SEM images of trench-like structures processed on Aluminium, Copper and Stainless steel in order to evaluate the quantity and size of re-solidified particles deposited close to the processing areas; the structures were achieved with 10 scans, 5.5 μJ pulse energy and 2 μm pulse spacing, the temporal pulse-to-pulse distances were varied.

Laser processing of Aluminium at lower repetition rates showed voluminous material bulging along the trench edges. Only a little number of re-deposited nanometer sized particles can be seen around the processing area. With the higher repetition rates, both the number and the size of the particles increased, but material bulging disappeared. Further the width of the trenches enlarged with higher repetition rates. These results suggest a more efficient material removal process by using high-PRF laser pulses.

For Copper the characteristics of the ablated particles seem to be almost similar over the

broad range of the investigated temporal pulse-to-pulse distances. Only at the highest repetition rate of 2,048 kHz a significant increase of the particle quantity is observable. Furthermore the width of the trenches increased only marginally with the higher repetition rate, but qualitatively the trench structures seems to be much more pronounced.

In case of Stainless steel re-solidified particles formed much smaller compared to those deposited on Copper and Aluminium. Both, the size and the number of the ablation particles are almost similar in the range between 32 kHz and 1,024 kHz, but the particle size increased with 2,048 kHz. Furthermore, the trench width enlarged and, moreover, the ripple structures originated by using low repetition rates at the trench bottom disappeared at the higher repetition rates.

5.6 Summary

In this chapter the impact of the temporal pulse-to-pulse distance on ultrashort pulse laser ablation was studied to clarify the interplay between heat accumulation and particle shielding in high-PRF laser processing.

Initially the expansion of the ablation plume induced by ultrashort laser pulses was recorded by using an intensified high speed camera. The temporal distance between the laser pulses was varied ranging between 0.5 μs and 5 μs . It was shown for all three investigated materials that in time scales of one micro second after laser pulse irradiation a significant amount of ablated particles is still moving above the laser processed surface. As a result, it was concluded for high-PRF laser irradiation that even in case of ultrashort pulse laser processing, particle shielding may have significant impact on laser material interaction. On the other hand, by irradiating laser pulses with a temporal pulse-to-pulse distance shorter than one micro second, considerably brighter ablation plumes were recognised on Stainless steel and Aluminium. This suggested stronger material removal which might be induced by heat accumulative effects.

Furthermore, a closer insight to the interplay between heat accumulation and particle shielding was presented with particular focus on the volume ablation rate achieved with

both varied repetition rate and lateral pulse spacing. For the low thermally conductive Stainless steel it was demonstrated that particle shielding losses may be counterbalanced by heat accumulation. On Copper, by contrast, the volume ablation rates were almost constant at varied temporal pulse-to-pulse distances and lateral pulse spacing.

In addition, the maximum achievable material removal rates were determined for the repetition rate of 1.024 MHz: Aluminium 0.84 mm³/min, Copper 0.79 mm³/min, and Stainless steel 0.77 mm³/min. The comparison of these values with up-scaled material removal rates indicated a disproportion for Aluminium and Stainless steel. It was suggested that material removal has benefitted from heat accumulation, which is not included in the up-scaled calculation model.

Moreover it was demonstrated that material ablation by using high-PRF laser pulses is much more complex. The theoretically calculated removal rates vary widely from experimentally determined values. It was found that the impact of heat accumulation and particle shielding on material ablation is insufficiently taken into consideration in the material removal rate calculation model.

Finally, SEM photographs of laser processed trenches were presented, giving a closer view to the re-deposited ablation particles. For all the investigated materials a larger amount of re-deposited particles was observed. Furthermore the width of the trenches enlarged slightly with higher repetition, indicating a more efficient material removal at the higher repetition rates.

6 Heat accumulation and energy balance – a phenomenological consideration

6.1 Introduction

In this phenomenological study, heat storage and near-surface temperature change are investigated by means of Aluminium, Copper and Stainless steel. Three distinct temporal pulse-to-pulse distances as 20 μs , 5 μs , and 1 μs are taken into discussion. The chosen timescales correlate to repetition rates of 51 kHz, 205 kHz, and 1.024 MHz as experimentally investigated in material ablation.

A simplified temperature calculation model is introduced in *Section 6.2* to evaluate high-PRF laser processing with regard to energy distribution, accumulation of heat, and surface temperature rise.

In a first approach presented in *Section 6.3*, the fraction of remaining energy below the ablation threshold is considered as minimum energy input for heat. By this way, heat accumulation could be proven qualitatively as influencing effect in high-PRF laser processing, but quantitatively the calculated temperatures seemed to be too low.

As a result, the temperature calculation model is enhanced in *Section 6.4* by taking a higher amount of remaining energy into account. Further the computed temperature values are compared to experimentally observations.

Section 6.5 presents results obtained in energy balance calculations. This subchapter contributes to enhance the understanding of material removal mechanisms in ultrashort pulse laser processing.

The chapter concludes with a brief summary in *Section 6.6*.

6.2 Temperature calculation model

A temperature calculation model is designed to investigate the change of the near-surface temperature on metals that may induced by high-PRF ultrashort pulse laser irradiation. In general, the two temperature model introduced by *ANISIMOV et al.* [127] is applied to discuss energy transport and temperature change following ultrashort pulse laser irradiations. By contrast, the approach presented here outlines energy transfer using macroscopic descriptions instead of the two temperature model.

The two temperature model seems not to be appropriate to evaluate the surface temperature changes induced by heat accumulation. The model distinguishes the energy distribution in the electron subsystem and the lattice in time scales which are significantly shorter compared to temporal pulse-to-pulse distances investigated in this thesis.

However, temperature modelling carried out in other works, i.e. [1], seems to be not transferrable to high-PRF laser processing. The thermal impact of the foregone incident laser pulses, the deposited fractions of remaining laser energy, both spatial and temporal energy distribution in radial and depth directions, as well as the temporal distance between the laser pulses failed or have been insufficiently taken into account. These weaknesses will be corrected in this thesis by the introduction of a simplified temperature calculation model.

Based on the assumption that the laser irradiated zone appears as surface heat source, it can be suggested that distribution of heat into the bulk material is potentially driven by the thermal diffusion length. In addition, it is assumed that thermal energy expands uniformly within the heat affected volume. The initial approximation of the model implies that only the fraction of absorbed laser energy, which does not contribute to material ablation, accumulates in the near-surface area surrounding the laser processing zone [128]. Hereinafter, this minimum possible quantity of deposited laser energy is referred to as the remaining energy Q_{rem} .

On the other hand, thermal losses as a result of heat convection and heat radiation are not included in this temperature calculation model. This method is conform to other work [129], which neglect these very low thermal losses. According to this, a rough estimate of energy losses caused by either heat radiation or convective heat transfer has been calculated in *Annex 9*. By taking into account *Stephan-Boltzmann law*, heat

radiation energy losses have been estimated of $0.2 \cdot 10^{-8}$ J. The considered timescale was 20 μ s, corresponding to 50 kHz pulse repetition rate. In addition, thermal convection losses were calculated of $1.4 \cdot 10^{-10}$ J. These little amounts of energy losses are significantly lower than the energy of laser pulses investigated in this study, ranging between 1 μ J to 7 μ J. As a result, energy losses caused by heat radiation or/and convection heat transfer have been neglected in the model.

Moreover, the temperature dependency of thermo-physical material properties is excluded in this simplified model to reduce the high level of complexity. The surface temperature calculation model includes the following key assumptions:

- The heat distribution is considered macroscopically; the two temperature model is not taken into account,
- The first approximation calculates the temperature rise based on the fraction of remaining energy which does not contribute to material ablation,
- In further improvements of temperature modelling enhanced thermal energy coupling with residual energy input greater than 70 % is taken into account,
- The heat affected volume arising locally around the laser processing zone in both radial and depth direction is determined by the thermal diffusion length,
- All energy losses other than those caused by thermal diffusion are neglected (such as heat convection, heat radiation, plasma/particle shielding, kinetic energy of ablated particles, overheated particles, etc.),
- The temperature dependency of the thermo-physical material properties are excluded (heat conductivity, heat capacity, beam absorption, etc.),
- The spatial thermal energy distribution within the heat affected volume is assumed uniform.

A basic approach to estimate the fraction of remaining energy which does not contribute to material ablation is schematically shown in **Figure 6-1**. For a Gaussian shaped laser pulse, the energy distribution in Z-direction is determined by optical penetration according to *Beer's law*. Material ablation takes place in this area, where the isophote is greater than or equal to the ablation threshold. This is indicated in the figure by the ablation depth profile. In the deeper volume, the laser fluence is lower than the ablation threshold. The model considers the amount of energy transferred in this depth as transferred into heat.

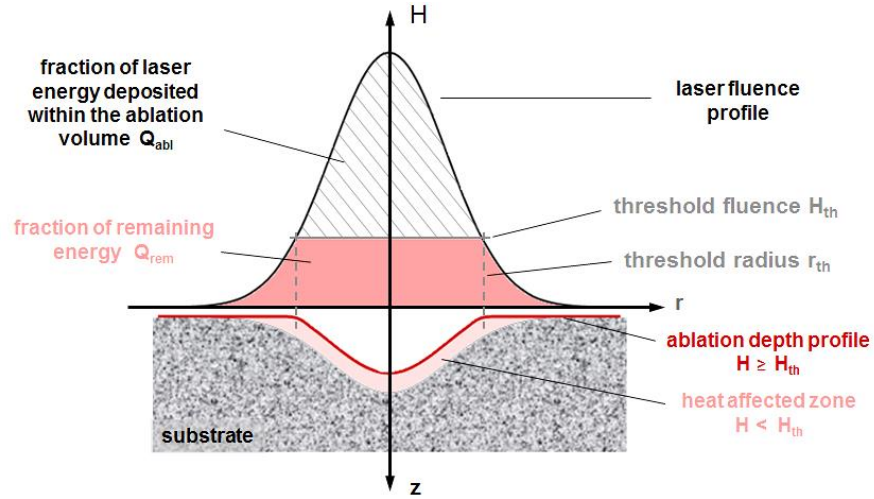


Figure 6-1: Laser fluence profile and ablation depth profile for a Gaussian laser pulse; fraction of optical energy below the ablation threshold represents the amount of remaining energy; fraction of optical energy greater than the ablation threshold is deposited in the ablation volume.

The amount of energy deposited in the ablation volume Q_{abl} correlates to the fraction of laser energy, which is greater than the threshold fluence. By taking into account a solid of revolution, it calculates by integration of the laser fluence profile minus the ablation threshold within the integration limits $0 \leq r \leq r_{th}$ as

$$Q_{abl} = \int_0^{2\pi} \int_0^{r_{th}} \left(H_0 e^{-\frac{2r^2}{w_0^2}} - H_{th} \right) \cdot r \cdot dr \cdot d\varphi \quad \text{Equation 6-1}$$

$$Q_{abl} = \frac{1}{2} \cdot \pi \cdot H_0 \cdot w_0^2 \cdot \left(1 - e^{-\frac{2r_{th}^2}{w_0^2}} \right) - \pi \cdot H_{th} \cdot r_{th}^2 \quad \text{Equation 6-2.}$$

The fraction of remaining energy Q_{rem} is given by the difference of the optical energy of one single laser pulse Q_P minus the fraction of energy deposited within the ablation volume Q_{abl} as

$$Q_{rem} = (1 - R) \cdot (Q_P - Q_{abl}) \quad \text{Equation 6-3.}$$

The reflectivity R of the material surface was taken into the calculation.

The thermally affected volume, caused by remaining thermal energy distribution locally around the laser irradiation zone, can be estimated as schematically shown in **Figure 6-2** (left). The laser irradiation zone is highlighted by a red line. The optical penetration depth of laser radiation is considerably smaller than thermal heat diffusion.

6.2 Temperature calculation model

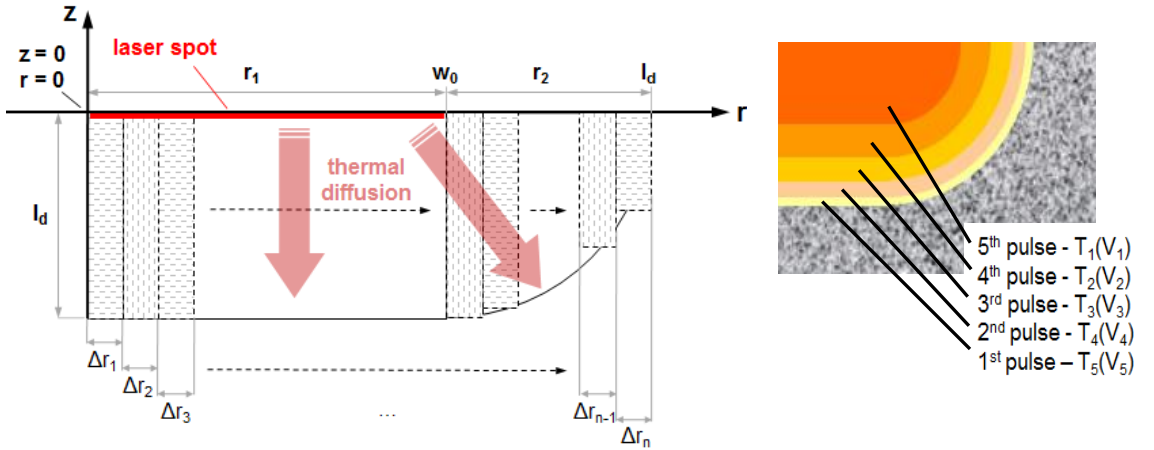


Figure 6-2: **left:** Schematic view to approximate the thermally affected volume, the laser spot area is indicated by a red line; **right:** heat affected volume and colour-coded temperature as a result of 5 consecutive incident laser pulses.

Shortly after laser irradiation, the optical energy is transferred into heat and material ablation takes place. The remaining fraction of laser energy, by contrast, induces a strong temperature rise within a thin surface layer. As a result, the arising large temperature gradient initiates conductive heat transfer, and thus the deposited thermal energy spread out over a large volume.

In the model, the spatial distribution of the thermal energy into the bulk is estimated based on the thermal diffusion length l_d . The thermal diffusion length defines the isotherms for the $1/e$ decrease of the surface temperature [7]. It calculates accordingly

$$l_d = 2\sqrt{D \cdot t} \quad \text{Equation 6-4}$$

where \mathbf{D} is the thermal diffusivity and \mathbf{t} is the time between two consecutive impinging laser pulses, determined by the pulse repetition rate. The thermal diffusivity is given by the thermal conductivity λ divided by the density ρ and the specific heat capacity c_p as

$$D = \frac{\lambda}{\rho \cdot c_p} \quad \text{Equation 6-5.}$$

The thermally affected volume \mathbf{V} can be approximated by numerical integration

$$V = \int_0^{2\pi} \int_0^{w_0} (r \cdot l_d) dr d\varphi + \int_0^{2\pi} \int_{w_0}^{w_0+l_d} (r \cdot f(r)) dr d\varphi \quad \text{Equation 6-6.}$$

In this equation, thermal energy distribution is regarded by the thermal diffusion length

in both depth and radial direction, schematically shown in **Figure 6-2** (left). Using this specific numerical integrating method, the heat affected volume calculates by adding infinitesimally small volume elements Δr_n . Two distinct types of volume profiles are given, determined within the integration limits $0 \leq r \leq w_0$ and $w_0 \leq r \leq w_0 + l_d$. The first area correlates to the laser spot in the centre, and the latter is related to the thermally affected area. By using this method, heat affected volumes arising from the different irradiation conditions investigated in this study are summarised in *Annex 10*.

Figure 6-2 (right) illustrates the thermally affected volume, induced by five consecutive incident laser pulses. It is clearly observable that the energy induced by the first irradiated laser pulse continues to have an effect on the surface, even on time scales when the fifth laser pulse arrives. Expansion of heat is a function of time, and thus the temporal distance between two consecutive laser pulses affects thermal distribution.

The schematic view given in **Figure 6-3** illustrates the expansion of the isotherms with increasing number of pulses and different repetition rates exemplarily by means of low thermally conductive Stainless steel. For short times between consecutive incident laser pulses, due to high repetition rates, the absorbed laser energy dissipates into a considerably smaller area.

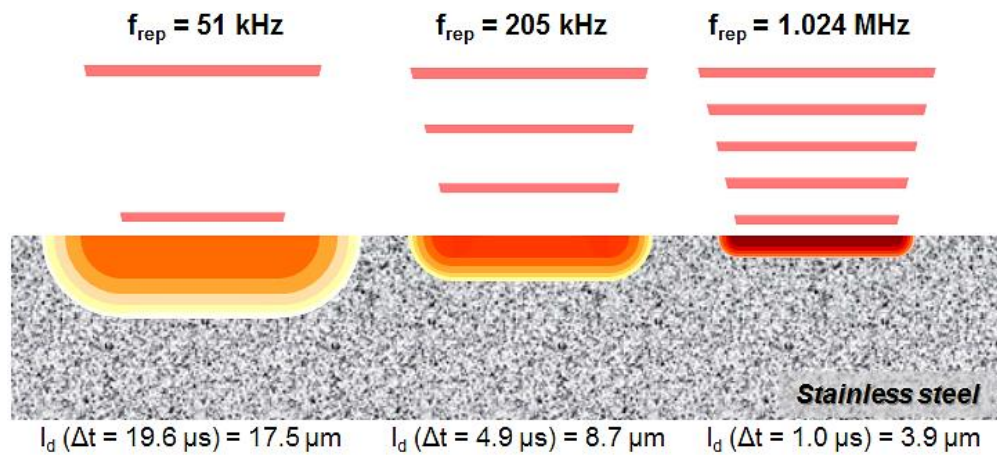


Figure 6-3: Expansion of isotherms in Stainless steel, induced by 5 consecutive incident laser pulses; the thermal diffusion length calculates to 17.6 μm at 20 μs , 8.8 μm at 5 μs and 3.9 μm at 1 μs temporal pulse-to-pulse distance, which correspond to repetition rates of 51 kHz, 205 kHz, and 1.024 MHz, respectively.

For example, at the lower repetition rates of 51 kHz and 205 kHz, which correspond to the temporal pulse-to-pulse distance of 19.6 μs and 4.9 μs , the thermal diffusion length calculates to 17.5 μm and 8.7 μm , respectively.

6.2 Temperature calculation model

By contrast, the thermal diffusion length amounts to just 3.9 μm at the higher repetition rate of 1.024 MHz, corresponding to 1 μs pulse-to-pulse distance. For high-PRF laser pulses it becomes clear that the next following pulse (irradiated in shorter time scales due to the high repetition rate) will potentially irradiate a warmer surface, compared to laser pulses of low repetition rates.

In addition, the thermo-physical material properties affect significantly the expansion of thermal energy. **Figure 6-4** presents results obtained in thermal diffusion length calculations by using **Equation 6-4** and 100 laser pulses. Significant variances in distribution of heat have been recognised for the three metals. The thermal diffusion lengths calculated for the high thermally conductive materials Aluminium and Copper can be seen approximately by half an order of magnitude larger, compared to the low thermally conductive Stainless steel.

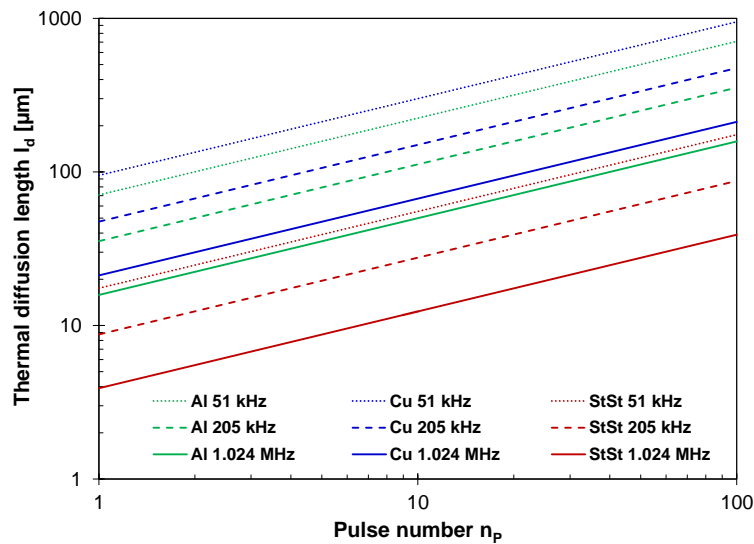


Figure 6-4: Logarithmical plot of the heat diffusion length l_d versus pulse number, calculated on industrial grade Aluminium, Copper and Stainless steel for 100 pulses and three repetition rates (51 kHz, 205 kHz, 1.024 MHz).

However, in case of the minor thermal diffusion length the absorbed laser energy is deposited in small volume. As a result, the higher energy density induces the increase of the surface temperature. Under consideration of the fundamental thermodynamic equation

$$dQ = m \int_{T_1}^{T_2} c(T) dT = m \cdot c_p \cdot (T_2 - T_1) \quad \text{Equation 6-7,}$$

6.2 Temperature calculation model

and the basic model key assumption, that the heat capacity c_p is independent from the temperature, the surface temperature rise ΔT induced by a laser pulse calculates to

$$\Delta T = \frac{Q_{rem}}{m \cdot c_p} = \frac{Q_{rem}}{\rho \cdot V} \cdot \frac{1}{c_p} \quad \text{Equation 6-8.}$$

This formula can be rearranged by replacing the mass with the product of the heat affected volume V and the density ρ .

In addition, the temporal distance between consecutive incident laser pulses becomes into play a primary role. In case of the short pulse-to-pulse distance the deposited remaining energy is not completely diffused away. The energy input of the foregone incident laser pulses continues to have an effect on the material surface when the next laser pulse irradiates. As a result, this laser pulse will potentially hit a heated area of higher surface temperature. The rise of the surface temperature T_{surf} can be calculated as following

$$T_{surf} = T_0 + \sum_{n=1}^{n_p} \Delta T_n = T_0 + \Delta T_1 + \Delta T_2 + \Delta T_3 + \dots + \Delta T_{n_p} \quad \text{Equation 6-9,}$$

where T_0 is the ambient temperature (300 K), n_p is the number of laser pulses and ΔT_n is the temperature rise induced by a single laser pulse. By this way, each temperature rise, which continues to have an effect on the surface temperature when the last laser pulse irradiates, is taken into calculation.

Rearrangement of **Equation 6-9**, by substituting ΔT_n with **Equation 6-8**. yield the final expression

$$T_{surf} = T_0 + \frac{Q_{rem}}{\rho \cdot c} \sum_{n=1}^{n_p} \frac{1}{V_n} = T_0 + \frac{Q_R}{\rho \cdot c} \left(\frac{1}{V_1} + \frac{1}{V_2} + \frac{1}{V_3} + \dots + \frac{1}{V_{n_p}} \right) \quad \text{Equation 6-10.}$$

In this equation the heat affected volume V_n induced by each irradiated pulse is considered. The heat affected volumes V_1, V_2, V_3 , etc. are determined by the heat diffusion length based on the passed time between the actually considered pulse event $n = 1, 2, 3$, etc. and the last incident laser pulse n_p .

The next subsections present the rise of surface temperatures calculated by using **Equation 6-10**. The processing conditions used in this thesis were included into

calculation in order to make theoretical results reliable and comparable to the experimental work. The surface temperature has been calculated for 100 consecutively incident laser pulses. This number of pulses fits very well to real laser processing conditions in practice. A lateral pulse spacing of 5 μm is taken into account because this spacing was determined as appropriate lateral pulse spacing previously. As a result, by irradiating 100 pulses, a scan length of 500 μm can be processed. This processing length corresponds to standard machining paths in laser micro processing.

By using this way, the results obtained in the temperature calculation seem to be transferrable to the scanned laser processing regime applied in this work. Further it can be assumed for line scans of pulses of small lateral pulse spacing, the temperature field is moving along with the laser beam across the sample surface.

However, the surface temperature calculation model disregards the temperature dependence of the thermo-physical material specific input values. Thus the thermal conductivity, heat capacity, thermal diffusivity, as well as the reflectance will be assumed constant. Only the lowering of the ablation threshold with higher repetition rates is considered because of this value influences significantly the amount of remaining energy. Ablation thresholds as experimentally determined in *Section 4.2* for the distinct investigated repetition rates are included into calculation. The heat affected volumes used in temperature calculations are presented in *Annex 10*.

6.3 Temperature calculation under consideration of the remaining energy

6.3.1 Aluminium

The temperature rise induced by high-PRF laser processing of Aluminium is calculated for 100 consecutive irradiated laser pulses of 7 μJ pulse energy. The numerical values are given in *Annex 11*. It has been mentioned already, that the ablation threshold decreases with shorter temporal pulse-to-pulse distance. Thus, a minor fraction of remaining energy was taken into calculation at the higher repetition rates, which is conclusive to **Equation 6-1** and **Equation 6-3**.

6.3 Temperature calculation under consideration of the remaining energy

The input values for temperature calculation on Aluminium are summarised in **Table 6-1**. The ambient temperature was 20 °C.

Table 6-1: Input values for surface temperature calculations on Aluminium.

Repetition rate f_R	51 kHz	205 kHz	1024 kHz
Pulse energy Q_P	7.0	7.0 μJ	7.0 μJ
Ablation threshold H_{th}	0.33 J/cm ²	0.25 J/cm ²	0.16 J/cm ²
Surface reflectivity R	0.54	0.54	0.54
Remaining energy Q_{rem}	1.50 μJ	1.25 μJ	0.91 μJ
Ambient temperature T_0	20.0 °C	20.0 °C	20.0 °C
Surface temperature T_{surf} (calculated for 100 pulse irradiations)	21.4 °C	27.4 °C	58.2 °C

For Aluminium, the rise of the surface temperature is presented in **Figure 6-5** as a function of the pulse number and different repetition rates. The results indicate a little temperature rise of 58.2 °C, achieved at the highest repetition rate of 1.024 MHz. At the lower repetition rates, the temperature increased only marginally either up to 21.4 °C at 51 kHz or 27.4 °C at 205 kHz. Because of the high thermal diffusivity of Aluminium, the deposited thermal energy distributes into a large volume, even in short time scales between high-PRF incident laser pulses.

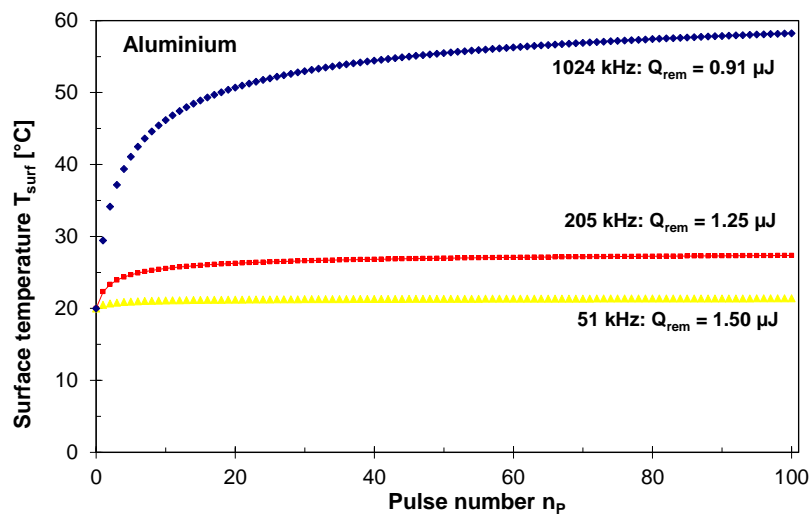


Figure 6-5: Surface temperature versus pulse number, calculated for Aluminium and 100 incident laser pulses, three different repetition rates, and irradiated pulse energy of 7 μJ .

The calculation outcomes do not reflect the experimental results, which show the highest impact of the temporal pulse-to-pulse distance on the ablation behaviour of the investigated materials. In the experimental study, Aluminium melt caused by heat accumulative effects was pointed out as most influencing effect at the higher repetition rates. In contrast, the melting temperature failed to be reached by using this simplified temperature model.

However, Aluminium is a material with a low melting point, and further the thermo-physical melt characteristic differs considerably from solid state properties. According to this, enhanced temperature modelling includes the assumption that material melting takes place in the initial stage of laser matter interaction. As a result, lower thermal diffusivity has to be taken into account, suggesting the deposited thermal energy diffuses in a considerably smaller volume.

6.3.2 Copper

For Copper, the surface temperature rise versus the pulse number is calculated for 100 pulses and 7 μJ single pulse energy, given in *Annex 11*. However, the experimental study of Copper concluded, that the ablation threshold is almost unaffected by the repetition rate. Thus a constant fraction of remaining energy of 0.45 μJ was taken into temperature calculation. The input values for surface temperature calculation on Copper are summarised in **Table 6-2**.

Table 6-2: Input values for surface temperature calculations on Copper.

Repetition rate f_R	51 kHz	205 kHz	1024 kHz
Pulse energy Q_P	7.0 μJ	7.0 μJ	7.0 μJ
Ablation threshold H_{th}	0.29 J/cm^2	0.29 J/cm^2	0.29 J/cm^2
Surface reflectivity R	0.85	0.85	0.85
Remaining energy Q_{rem}	0.45 μJ	0.45 μJ	0.45 μJ
Ambient temperature T_0	20.0 $^\circ\text{C}$	20.0 $^\circ\text{C}$	20.0 $^\circ\text{C}$
Surface temperature T_{surf} (calculated for 100 pulse irradiations)	20.1 $^\circ\text{C}$	20.9 $^\circ\text{C}$	26.9 $^\circ\text{C}$

6.3 Temperature calculation under consideration of the remaining energy

The calculation results presented in **Figure 6-6** confirm the main findings of the experimental study, that material ablation on Copper is mainly unaffected by heat. The maximum temperature was calculated of 26.9 °C by taking into account the highest investigated repetition rate of 1.024 kHz. This outcome sustains the experimental finding that high-PRF laser processing of Copper is almost unaffected by accumulation of heat.

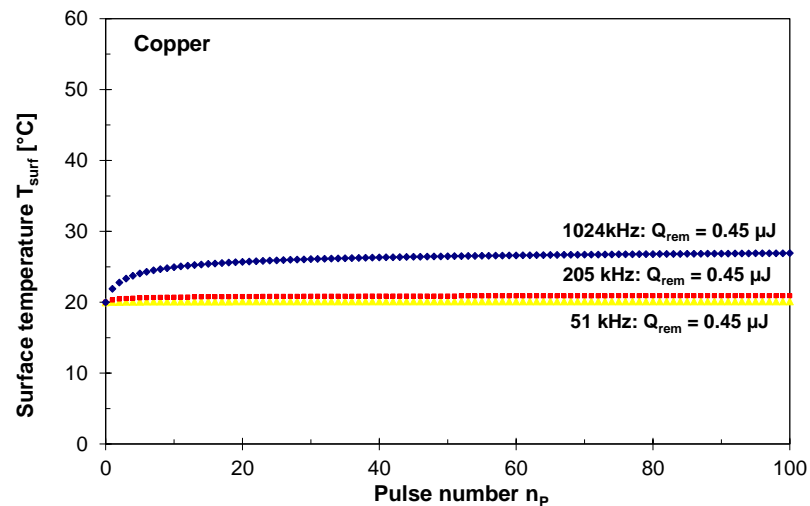


Figure 6-6: Surface temperature versus pulse number, calculated for Copper and 100 incident laser pulses, three different repetition rates, and irradiated pulse energy of 7 μJ .

The micrographs presented in **Figure 6-7** (left) support these results. Ablation craters obtained by studying the impact of the repetition rate on material ablation on Copper are shown. Laser induced surface structures appeared at the crater bottom encircled a modified zone, but neither heat accumulation induced structures nor heat affected zones (HAZ) can be recognised with higher energy or/and the higher repetition rates.

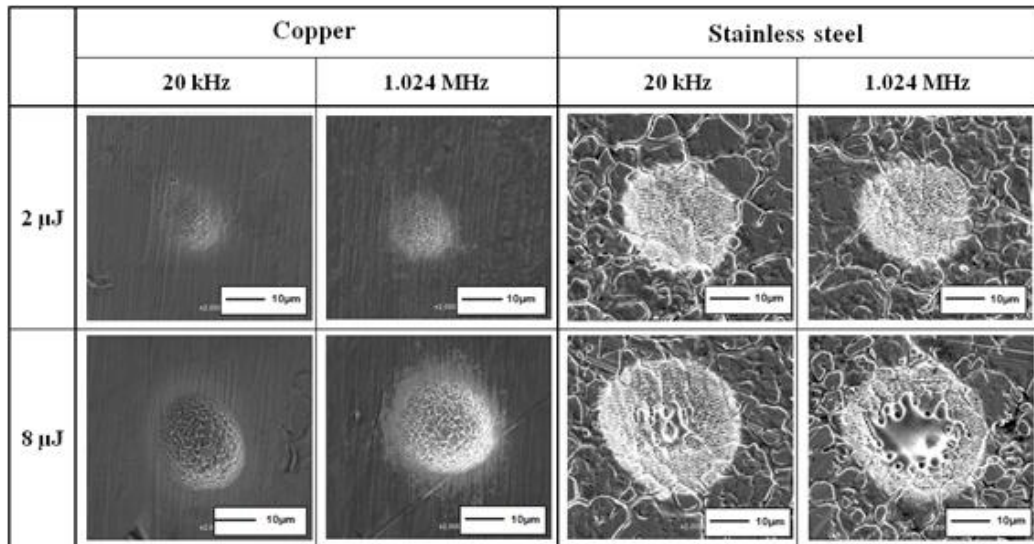


Figure 6-7: Ablation craters in Copper (left) and Stainless steel (right), each crater was obtained by irradiating a burst of 50 single laser pulses, both temporal pulse-to-pulse distance and single pulse energy are varied.

6.3.3 Stainless steel

The input values used in temperature calculation on Stainless steel are given in **Table 6-3**. The single pulse energy of $5 \mu\text{J}$ was taken into calculation, determined in *Chapter 4* as optimised parameter for laser micro processing of Stainless steel. Furthermore the impact of the repetition rate on the ablation threshold was considered.

Table 6-3: Input values for temperature calculations on Stainless steel.

Repetition rate f_R	51 kHz	205 kHz	1024 kHz
Pulse energy Q_P	5.0 μJ	5.0 μJ	5.0 μJ
Ablation threshold H_{th}	0.110 J/cm ²	0.108 J/cm ²	0.088 J/cm ²
Surface reflectivity R	0.3	0.3	0.3
Remaining energy Q_{rem}	0.97 μJ	0.95 μJ	0.82 μJ
Ambient temperature T_0	20.0 °C	20.0 °C	20.0 °C
Surface temperature T_{surf} (calculated for 100 pulse irradiations)	42.0 °C	119.7 °C	435.9 °C

6.3 Temperature calculation under consideration of the remaining energy

According to this the amount of deposited remaining energy differed with the repetition rate in the range between $0.97 \mu\text{J}$ and $0.82 \mu\text{J}$. The deposited energy distributes only within a small volume due to the low thermal diffusivity of Stainless steel. As a result, a considerably high temperature increase can be expected, which is in contrast to Copper and Aluminium.

The calculation results given in *Annex 11* are plotted in **Figure 6-8**, indicating considerable temperature rise with maximum surface temperature of 437°C . The temperature was reached after 100 incident laser pulses and $1 \mu\text{s}$ temporal pulse-to-pulse distance at the highest studied repetition rate of 1.024 MHz . At the lower repetition rates, the time between incident laser pulses is being too long, so a considerable amount of thermal energy diffuses into the bulk. As a result the temperature increase is on a low level with a maximum surface temperature of 47°C and 120°C , calculated for 51 kHz and 205 kHz , respectively.

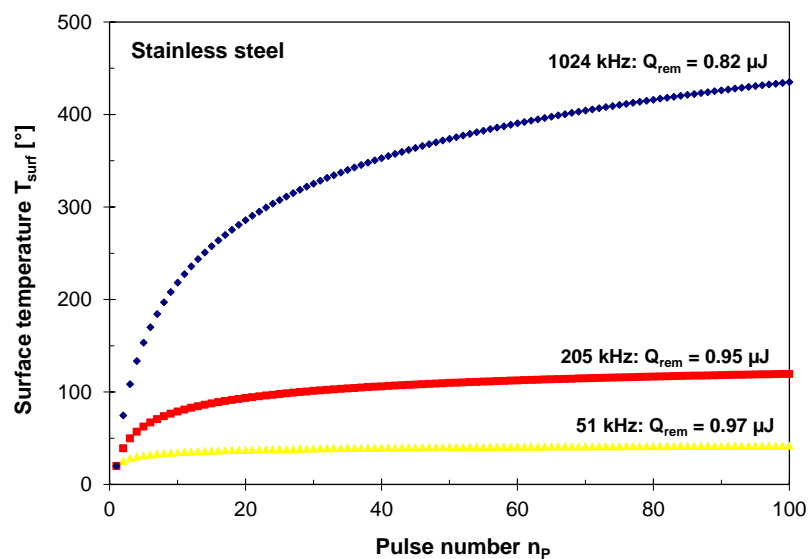


Figure 6-8: Surface temperature versus pulse number, calculated for Stainless steel and 100 consecutive incident laser pulses, three different repetition rates, and irradiated pulse energy of $7 \mu\text{J}$.

However, in spite of the comparably low quantity of deposited energy of $0.82 \mu\text{J}$, particularly the temperature rise calculated for 1.024 MHz repetition rate seems to be high. It can be concluded that thermally driven effects induced by heat accumulation will affect laser matter interaction, particularly in high-PRF femtosecond laser processing.

In accordance to this, micrographs shown in **Figure 6-7** (right) indicate material melting

at the higher pulse energy and the high repetition rate. In addition, depths measurements of the ablation craters reveal a discontinuation of the curve progression at the higher repetition rate. **Figure 6-9** plots the averaged maximum ablation depth per single pulse, measured on ablation craters obtained with a burst consisting of 50 single laser pulses, versus the laser fluence. At the lower repetition rate, the crater depth increased steadily with the fluence, but a drop of the ablation depth was found for the higher repetition rate and the fluence between 1.39 J/cm² and 1.58 J/cm². At this fluence the growth of a larger pool of molten and re-solidified Stainless steel can be observed. The melt pool is shown in **Figure 6-7** (right), obtained by laser processing with 8 μJ pulse energy and 1.024 MHz repetition rate.

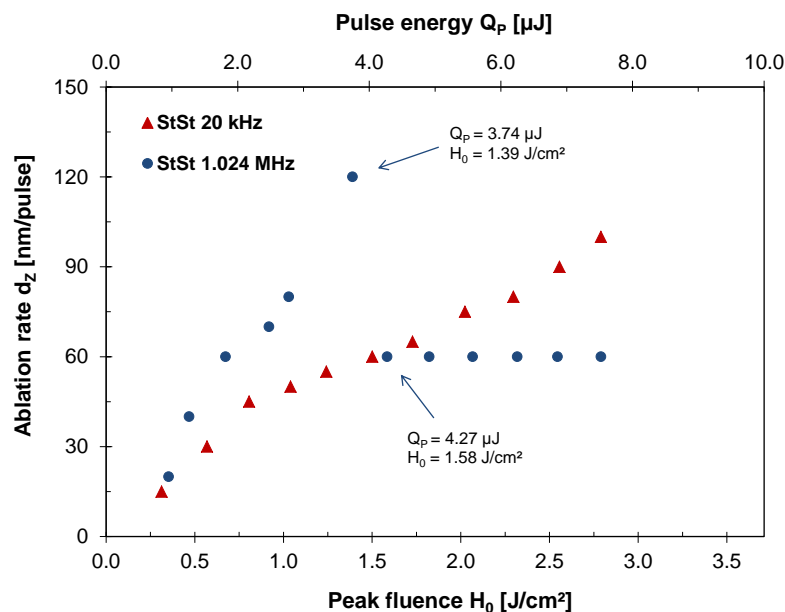


Figure 6-9: Ablation depth per pulse versus laser fluence, obtained on ablation craters on Stainless steel by using the digital microscope VHX-100 for depth measurement.

The observed molten material at the crater bottom gives evidence that under real laser processing conditions the melting temperature may potentially be reached. In comparison to the calculated surface temperature of 437 °C, the considerably higher melting temperature might be induced by a considerably higher thermal load of the work piece.

In accordance with this conclusion, the literature attributed enhanced thermal coupling as a significant material ablation influencing effect in ultrashort pulse laser processing. *KONONENKO et al.* [17] pointed out that plasma induced by sub-picosecond pulses screens the laser beam and act as secondary low-intensity long-lived heat source. In

addition, *VOROBYEV et al.* identified plasma induced energy re-deposition [130-132] as main mechanisms for enhanced energy coupling. Furthermore the authors report a significant enhancement of the absorptivity of metals [35, 133]. Therefore plasmonic absorption mechanisms at ablated and re-deposited nanoparticles, or/and structural surface modification in the nano / micro / macro range are suggested. Further, for metals with periodic sub-wavelength structural surfaces, an almost 100 % laser beam absorption was demonstrated [134].

However, both the amounts of re-deposited thermal energy, as well as enhanced laser beam absorption have not been considered in the first stage of the temperature calculation model.

6.4 Temperature calculation considering thermal energy coupling

Up to now, only a little research has been done in the field of enhanced thermal energy coupling. A couple of publications indicate a high level of energy that is transferred into heat, even by using ultrashort laser pulse. As mentioned above in the previous subchapter, residual energy deposition on metals has been evaluated by *VOROBYEV et al.* using calorimetric measurement methods. The authors defined the residual energy coefficient **K** as the ratio of laser deposited residual energy transferred into heat, divided by the amount of irradiated single pulse energy. With the assumption of moderate femtosecond laser processing, the following residual energy coefficients can be estimated from the published results: Aluminium: **K** = 0.8 ... 0.9 [130], and Copper: **K** = 0.4 ... 0.5 [131].

These high thermal energy couplings are conclusive to the work published by *TRAN et al.* [135, 136], presenting thermo camera in-situ direct measurements of temperature fields during multiple femtosecond laser pulse ablation of metals. According to these, for the laser fluence greater than the ablation threshold, the percentage of heat flow into the bulk metal can be averaged to 70 % for Steel and 50 % for Copper, related to the average incident laser power.

From this point of view, enhanced thermal energy coupling can be supposed as a significant femtosecond laser ablation affecting mechanism. As a result, the temperature calculation model has been improved by taking into account a higher ratio of thermally deposited energy instead of the little fraction of remaining energy below the ablation threshold. Calculated temperatures by taking enhanced energy coupling into account are presented in *Annex 12*.

Although by using the enhanced temperature calculation model considering thermal energy coupling, an insignificant increase of the surface temperature was calculated for Aluminium and Copper. For Copper, the residual energy coefficient was found of $K = 0.5$, suggesting that 50 % of the irradiated single pulse energy of $7.0 \mu\text{J}$ was transferred into heat. Surface temperature calculations were carried out with residual energy input of $3.5 \mu\text{J}$ and the repetition rate of 1.024 MHz . A temperature maximum of $74 \text{ }^\circ\text{C}$ was obtained, indicating that heat accumulation is not taking place on Copper within the investigated parameter range. This finding is conclusive to the results achieved in the experimental study of Copper, where no impact of heat on material ablation was identified.

For Aluminium, surface temperature calculations using the enhanced model yield a maximum of $234 \text{ }^\circ\text{C}$. The pulse energy of $7.0 \mu\text{J}$, repetition rate of 1.024 MHz , and the residual energy coefficient of 0.8 were included into calculation. Comparing this result to experimental observations, it seems that this little temperature increase can neither explain the decrease of the ablation threshold nor the significant increase of the removal rate, detected at higher repetition rates. Indeed the temperature dependence of the calculation input values has not been considered yet, but for the resulting temperature increase up to 234° , a minor effect can be assumed, as shown in **Figure 3-5**.

However, Aluminium is a metal with a low melting temperature and it was supposed in the experimental chapters that in high-PRF laser irradiation a molten Aluminium layer can originate. By postulating that the next incident laser pulse hits a molten Aluminium surface, the thermal diffusivity is determined by both the heat capacity and the thermal conductivity of the Aluminium melt. The thermal conductivity of the Aluminium melt is considerably lower than for the solid material, as presented in **Figure 3-5**. In addition, a work published by *TAKAHASHI et al.* [137] reports the increase of the heat capacity of Aluminium depending on the temperature in the range from $c_{\text{mol}} = 24.08 \text{ J mol}^{-1} \text{ K}^{-1}$ at

6.4 Temperature calculation considering thermal energy coupling

300 K to $c_{\text{mol}} = 32.0 \text{ J mol}^{-1} \text{ K}^{-1}$ at 880 K.

The molar heat capacity c_{mol} and the specific heat capacity c_p correlate by the molar mass of Aluminium of $M = 26.98 \text{ g/mol}$. Thus the heat capacity of the Aluminium melt compared to the solid increases by a factor of 1.33, obtained by dividing the solid and melt molar heat capacities. In addition, the thermal conductivity of the melt is lowered by a factor of almost 2.38, estimated from data presented in **Figure 3-5**. Thus, according to **Equation 6-5** by taking into account heat capacity and thermal conductivity for the Aluminium melt, the thermal diffusivity reduces from $D_{\text{solid}} = 64.0 \text{ m}^2/\text{s}$ (solid) to approximately $D_{\text{melt}} = 20.2 \text{ m}^2/\text{s}$ (melt). As a result of the lower thermal diffusivity, a significant smaller heat affected area can be expected. This, in turn, may induce a significant higher surface temperature, compared to the solid state Aluminium.

Figure 6-10 illustrates the surface temperature rise on Aluminium with increasing pulse number. In total, 100 pulses with different laser pulse energies ranging between $3 \mu\text{J}$ and $7 \mu\text{J}$, the repetition rate of 1.024 MHz, a residual energy coefficient of 0.8 (that means 80 % of the incident laser energy is transferred into heat), and the heat diffusivity estimated for Aluminium melt ($D_{\text{melt}} = 20.2 \text{ m}^2/\text{s}$) were taken into calculation.

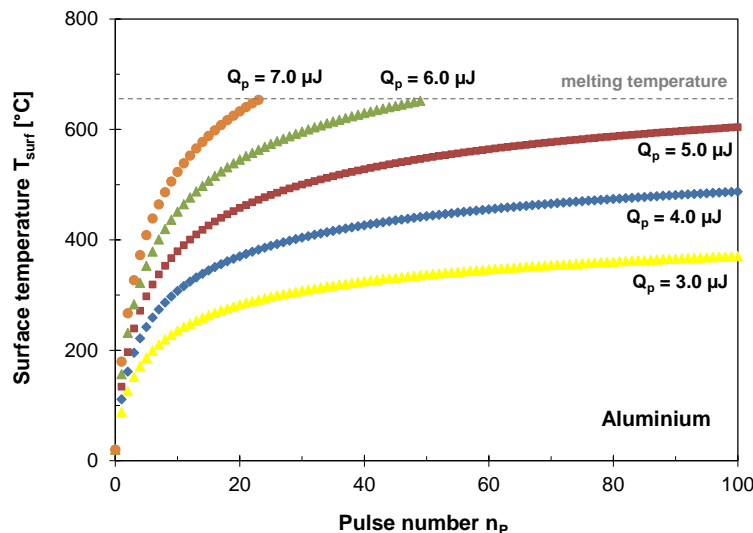


Figure 6-10: Enhanced surface temperature calculation on Aluminium, according to reference [130] 80 % of the plot depicted incident single pulse laser energy Q_P was taken into calculation, the repetition rate was 1.024 MHz.

In the figure it can be seen that the melting temperature of the Aluminium alloy ($650 \text{ }^\circ\text{C}$) has not been exceeded with laser pulses of the lower energy ranging between

3.0 μJ and 5.0 μJ . By using pulses of higher energy, the melting temperature was reached after 50 pulses of 6 μJ and 23 pulses of 7 μJ . The calculation results are in good agreement with experimental observations. The experimental study of high-PRF laser ablation of Aluminium revealed a considerably higher amount of molten and re-solidified material / debris for the higher pulse energies. In this experimental study, the pulse energy of 5 μJ was estimated as appropriate laser processing parameter to fabricate melt-free and accurately outlined micro-featured structures.

Figure 6-11 presents results achieved in enhanced surface temperature calculation on low thermally conductive Stainless steel. With regard to reference [136], 70 % of the irradiated single pulse laser energy was taken into account in the calculation. The irradiated laser pulse energy was varied between 2.0 μJ and 5.0 μJ , the repetition rate was kept constant of 1.024 MHz. It is shown that the melting temperature (1,400 $^{\circ}\text{C}$) can be reached with either 65 pulses of 4.27 μJ or only 35 pulses of 5.0 μJ . The temperature curve plotted for the lower pulse energy of 3.74 μJ , by contrast, indicates that the melting temperature may not be reached. The melting threshold identified here between 3.74 μJ and 4.27 μJ is in good agreement to **Figure 6-9** which pointed out a drop of the ablation rate between these energy values at 1.024 MHz repetition rate.

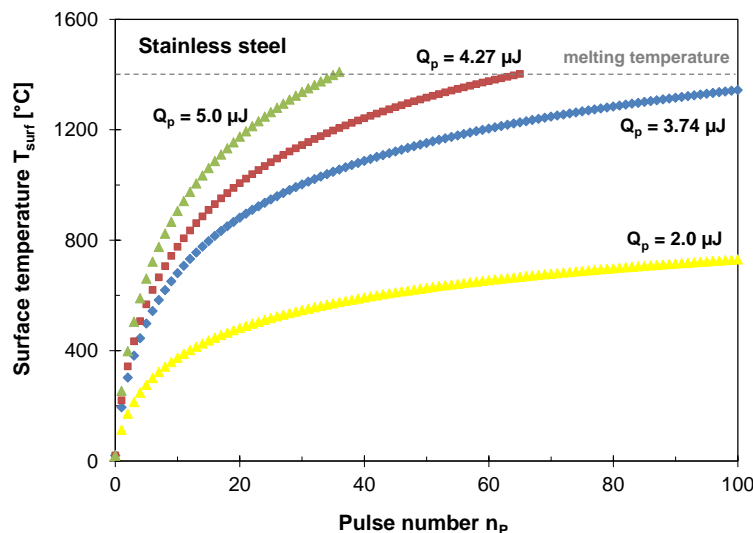


Figure 6-11: Enhanced surface temperature calculation on Stainless steel, according to reference [136] 70 % of in the plot depicted incident single pulse laser energy was taken into in calculation, the repetition rate was 1.024 MHz.

However, for all three investigated materials the results obtained in enhanced temperature calculation reflect the observations made in the experimental chapters in a proper manner. In the experimental study of high-PRF laser processing of Aluminium,

the pulse energy of 5 μJ was determined as appropriate processing parameter, in order to avoid material melting. In temperature calculation, this amount of energy constitutes the border value for material melting. For Copper no evidence of heat accumulation was detected within the investigated parameter range, neither in the experimental study nor temperature calculation. Finally, for Stainless steel the start of melting as experimentally detected for pulse energies between 3.74 μJ and 4.27 μJ was proven by enhanced temperature calculations. As a result the designed surface temperature calculation model calculation model seems to be appropriate in high-PRF femtosecond laser processing of metals.

6.5 Energy balance

The subchapter discusses the energy balance of material removal exemplarily by means of Stainless steel. This energetic analysis is further required in order to avoid having mismatch in the enhanced surface calculation model. A possible problem might be occur, because of residual thermal energy on steel was estimated of approximately 70 % of the irradiated laser beam. In addition to this, the reflectivity on laser treated steel surfaces was averaged of 30 % in own measurements. In summary, the total amount of irradiated laser energy divided in two fractions, the reflected beam ratio and thermal energy due to thermal energy coupling. As a result, none energy seems to left for any other energy losses, which are physically existent during laser ablation. Among others this can be kinetic energy for material ejection, plasma, thermal energy carried away by ablated particles/clusters, shock / pressure waves or the little energy losses caused by heat radiation and convection.

The energy balance model calculates the difference between the total amounts of energy Q_t , required to remove a distinct material volume, minus the irradiated laser pulse energy Q_p . The amount of energy required for material removal Q_t is determined by the sum of residual thermal energy Q_R , added by the heat of material evaporation Q_{vap} .

Since the energy balance is positive, the irradiated laser energy seems to be high enough for material removal. A negative energy balance, by contrast, identifies inaccurateness

of the underlying physical mechanisms which have been regarded in the material removal model. The basic physical mechanisms considered in this model were: partially reflection of the irradiated laser beam, material melting as the result of thermal coupling, material removal based on evaporation.

In the analysis, a laser pulse of $Q_P = 5 \mu\text{J}$ energy was regarded, irradiating the Stainless steel metal plate surface. With the resulting laser fluence of $H_0 = 1.34 \text{ J/cm}^2$, a material volume of $17.3 \mu\text{m}^3$ can be theoretically removed, calculated according to **Equation 4-15**. This material volume corresponds to a mass of $m = 1.37 \cdot 10^{-10} \text{ g}$. To evaporate this amount of material the energy of $1.01 \mu\text{J}$ is required, calculated in *Annex 13* by taking into account **Equation 6-11**.

This equation calculates the heat of evaporation required for material removal by assuming that the surface temperature is already heated up to the melting point, when the laser pulse irradiates. This assumption is based on both thermal coupling and heat accumulation effects, taking place in high-PRF laser processing, and has been proved by temperature calculations in *Chapter 6.4*. As a result, for material removal there is no extra energy required to heat up the system from the ambient temperature to the melting point. Thus the heat of evaporation Q_{vap} calculates to

$$Q_{vap} = m \cdot c_p \cdot (T_{vap} - T_{melt}) + m \cdot L_{melt} + m \cdot L_{vap} \quad \text{Equation 6-11,}$$

where m is the mass of the evaporated volume, c_p is the specific heat capacity, and L_{melt} and L_{vap} are the latent heat for melting and evaporation, respectively.

Figure 6-12 presents results obtained in energy balance calculations by taking into account four fictive processing states representing various material removal mechanisms. The left column indicates evaporation as dominant material removal mechanism. In the right column evaporation is completely neglected and explosive material removal as discussed in *Section 2.3.4*, such as phase separation, nucleation or fragmentation, are regarded as the main mechanism. In the centre of the table a minor percentage of evaporation in material removal was hypothetically assumed, either 60 % or 40 %, respectively. As a result, a lower amount of energy is required for material removal, due to the decreased energy need in latent heat absorption for evaporation.

Further, in reality laser beam absorption is less than 100 %, caused by laser beam reflection. Thus in **Figure 6-12**, the reflectivity was varied in the range between 10 %

6.5 Energy balance

and 30 %, representing real laser processing conditions. This can be suggested from a work done by *KAAKKUNEN et al.* [37], presenting absorptivity values for Stainless steel in the range between 70 % and 90 %. In addition, a further increase of laser beam absorption might be induced by the high surface temperatures, arising due to heat accumulation.

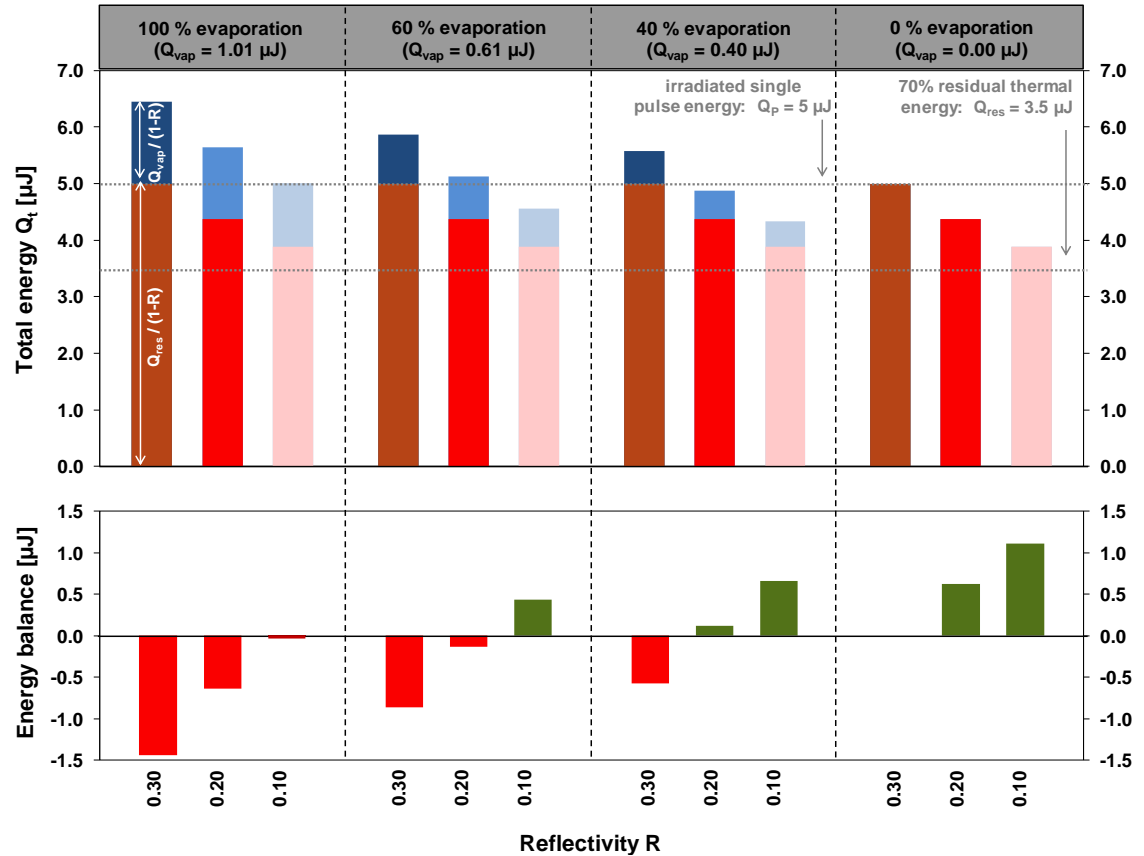


Figure 6-12: Energy balance calculated to remove a volume of $16.5 \mu\text{m}^3$ Stainless steel with the mass of $1.37 \cdot 10^{-10}$ g; **top:** required energy for material evaporation including thermal coupling (70 %) are plotted by taking into account different levels of surface reflectivity and fractions of evaporation, **bottom:** energy balance as the difference between the total required energy for material removal and the irradiated pulse energy of $5 \mu\text{J}$.

Figure 6-12 (top) plots the total amount of energy required to laser ablate $17.3 \mu\text{m}^3$ of Stainless steel. In the first case, under consideration of 100 % evaporation, the total energy of $4.51 \mu\text{J}$ is required, which has to be spend due to $1.01 \mu\text{J}$ evaporation energy and $3.5 \mu\text{J}$ thermal energy. To deposit this energy in the material, a higher amount of laser pulse energy is needed. A considerably amount of energy will be lost due to the reflection of the incident laser beam. Thus, by assuming a reflectivity of 30 %, laser pulses of $6.44 \mu\text{J}$ energy have to irradiate the material. This energy was obtained by dividing the amount of required evaporation energy and the absorptivity $\mathbf{A} = 1 - \mathbf{R}$.

With the lower reflectivity **R**, considered in this analysis of 20 % and 10 %, the required irradiation energies decrease to 5.64 μJ and 5.01 μJ , respectively. In addition to the assumption of a reduced reflectivity, the energy need was also calculated for a lower evaporation ratio in material removal (60 %, 40 %, 0 %). The computed values can be seen in *Annex 13*.

The lower scheme in **Figure 6-12** illustrates the energy balance. The energy balance is calculated by difference between the irradiated energy, required to remove the specified material volume, minus the incident laser pulse energy, which was 5 μJ . In some of the modelled cases the energy balance is negative. This indicates that a higher energy is needed for material removal compared to the irradiated pulse energy.

In general, two material removal mechanisms can be identified as improperly for material removal in the femtosecond laser regime: material removal induced by 100 % material evaporation, modelled in the left column, and 70 % laser beam absorption. In this cases the energy, which has to spend for evaporation and thermal heat coupling is about one third higher than the irradiated laser pulse energy. Even in case of the low reflectivity of only 10 %, the energy balance calculates slightly negative. As a result it can be assumed that evaporation may not be the dominant ablation mechanism. With this in mind, in the next following columns explosive material ejection mechanisms have been considered. By taking into account significant lower evaporation ratio for material removal, minor amount of latent heat for evaporation was included in the calculations. However, also in this case the energy balance remains still negative, and thus the reflectivity of 30 % seems to be too high.

The energy balance turns positive with a reflectivity lower than 20 % and the evaporation ratio in the range of 40 % or less. From this point of view it can be concluded that material removal in femtosecond laser processing is not dominated by evaporation. Material ablation may potentially be forced by mechanisms inducing a voluminous ejection of particles and clusters. This is conclusive to *Section 2.3.4*, where phase explosion and fragmentation have been indicated as relevant removal mechanisms for ultrashort laser pulses. Supporting this conclusion, a high amount of ablated particles and clusters have been detected in the high speed camera images presented in *Section 5.2.2* as well as the analysis of ablated and re-solidified particles in *Section 5.5*.

6.6 Summary

A simplified temperature calculation model was introduced to investigate heat accumulation and surface temperature rise. In a first approach, the little amount of remaining energy was taken into calculation, which does not contribute to material ablation. For the low-heat conductive Stainless steel, a surface temperature increase up to 435.9 °C was obtained, although on Aluminium and Copper the surface temperature increased only marginally.

A good agreement between calculated surface temperatures and experimental observations was obtained by the enhancement of the temperature calculation model. Considerably higher surface temperatures were calculated by taking into account residual thermal energy coupling. As a result, the surface temperatures modelled for the highest investigated repetition rate of 1.024 MHz exceeded the melting temperature on Stainless steel and Aluminium. By contrast, on Copper no significant temperature rise was calculated, potentially affected by the high heat conductivity of the material.

The energy balance in material removal has been evaluated exemplarily by means of Stainless steel. The energy amount required for material removal, including evaporation energy and remaining thermal energy, was compared to the irradiated laser energy. The positive energy balance was obtained by assuming, the reflectivity of the irradiated laser beam is less than 20 % and the evaporation ratio is lower than 40 %. It was concluded that material ablation might be forced by other mechanism, i.e. phase explosion and fragmentation. This is supportive to results obtained in molecular dynamic simulations, presented in the literature review.

These presented results contribute to the main goal of this thesis to enhance the fundamental understanding of the complex laser material interaction in high-PRF femtosecond laser ablation. It was verified for high-PRF laser irradiation, that thermal energy coupling is one of the dominant interaction mechanism. Further it was shown that material melting potentially occurs in high-PRF femtosecond processing, which is in contrast to commonly given statements in ultrashort pulse laser processing. Finally, energy balance calculations confirm the assumptions of the high thermal heat load made in the enhanced temperature calculation model.

7 Laser-induced surface structures

7.1 Introduction

In this chapter the formation of self-organised periodical surface structures, induced by high-PRF femtosecond laser irradiation is studied. As an example, in **Figure 7-1** (left), different types of characteristic micrometer / submicrometer-scaled structures can be identified on a laser irradiated Stainless steel surface: (a) ripple structures, (b) micro grooves, (c) deep micro holes and (d) hillocks / cone-like shaped micro structures. In **Figure 7-1** (right) it can be seen that ripple and cone-like micro structures appeared at the same time. The steel surface is not completely covered by the cones and ripples originated at the sample surface and the cone sidewalls.

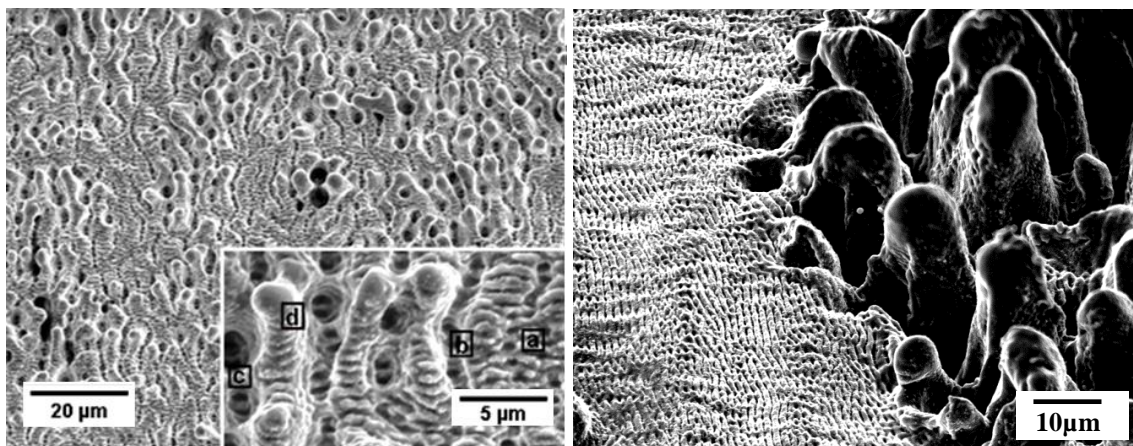


Figure 7-1: Characteristic laser induced surface structures on Stainless steel, **left:** (a) ripple, (b) micro groove, (c) deep micro hole, (d) hillocks / cone-like shaped micro structure; **right:** ripple and cone-like structures originated at the same time.

Ripple structures are a well-known and widely investigated phenomenon in laser processing, but as indicated above in *Section 2.4.1*, the formation mechanism is still not entirely understood and a number of differing theories have been proposed as possible explanations. It has been demonstrated already that ripple formation is a function of laser wavelength, laser beam polarisation and fluence. In addition to ripples, *Section 2.4.2* reported about cone-like shaped micro structures induced by ultrashort pulse lasers and ambient atmospheric conditions [90]. Previous work indicated that the formation mechanism of these structures is not sufficiently studied and understood.

To overcome these knowledge gaps, ripple formation following high-PRF laser irradiations is discussed in *Section 7.2*. The impact of laser beam polarisation, the machining direction and surface irregularities are of special interest. *Section 7.3* presents results obtained in studying the formation of cone-like structures. The impact of the processing parameters repetition rate, pulse energy, as well as spatial pulse spacing was investigated.

The chapter concludes with a short summary in *Section 7.4*.

7.2 Ripple structures

Ripple formation induced by high-PRF laser irradiation of 1 mm thick Stainless steel metal sheets was investigated by means of SEM photographs, shown in **Figure 7-2**. The spatial period of the highly regular ripple structures of about 1 μm correlates very well to the wavelength of the incident laser beam of 1.03 μm . This is conclusive to ripple formation mechanisms discussed above in *Section 2.4.1*. Moreover, it is demonstrated that ripple orientation formed perpendicular to the polarisation direction of electrical field of the laser beam.

As shown in **Figure 7-2**, ripple orientation turns by rotating the laser beam polarisation, which confirms the polarisation dependence of the ripple structures. In addition to the ripples, the figure exhibits deep micro-scaled groove / channel structures, appearing almost perpendicular to the ripples. The spacing between the grooves is about five times larger than the ripple spatial distance. Furthermore, it can be seen that orientation of the micro grooves depended on the laser beam polarisation. Micro-channel orientation turns with the rotation of the laser beam polarisation, shifted by 90 degrees to the orientation of the ripples.

In contrast to regular ripple formation, both ripple appearance and ripple orientation direction are predominated by surface irregularities. As shown in **Figure 7-3** ripple disorientation may be induced by scratches, material distortions, and debris on the surface. In addition, it has been reported that both distinct alloying constituents or/and grain boundaries will affect the origin of ripple structures [138].

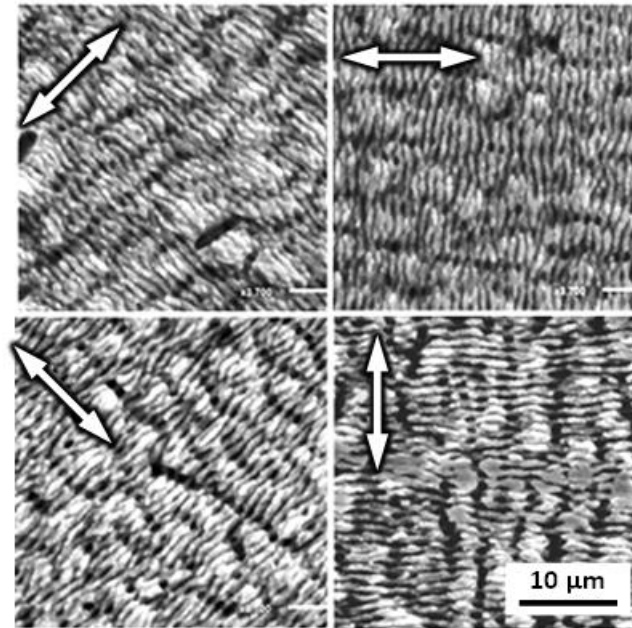


Figure 7-2: SEM photographs taken on Stainless steel to show the dependence of both ripple orientation and superior micro-scaled groove structure on laser beam polarisation; the electrical field vector is highlighted as a white arrow.

A higher-order mechanism for ripple formation can be suggested and the plasmon model already mentioned in *Section 2.4.1* seems to be more relevant for ripple formation. From this point of view it can be assumed that surface irregularities greatly enhance disordering of the surface plasmons that may result in the irregular ripple patterns.

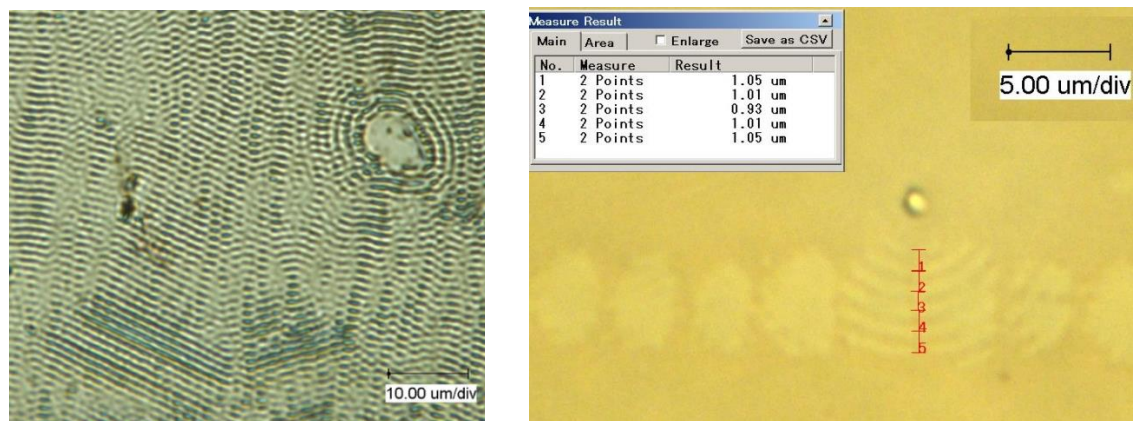


Figure 7-3: Ripple disordering induced by micro-scaled particles, observed on Stainless steel (left) and Copper (right).

Highly-regular ripple structures have been obtained in laser patterning of polished Stainless steel metal plates across large areas, as shown in the **Figure 7-4** upper left. In this case the polarisation direction of the laser beam was aligned exactly perpendicular

to the scan direction of the laser beam. The laser fluence was chosen slightly above the ablation threshold. As a result a high regularity of the ripple pattern was obtained.

White-light illuminations of ripple phase gratings are shown in **Figure 7-4**. The photographs were taken by **M. KOCH** (ThyssenKrupp Steel Europe AG). Distinctive light diffraction patterns can be observed. The ripple orientation is indicated by the arrows.

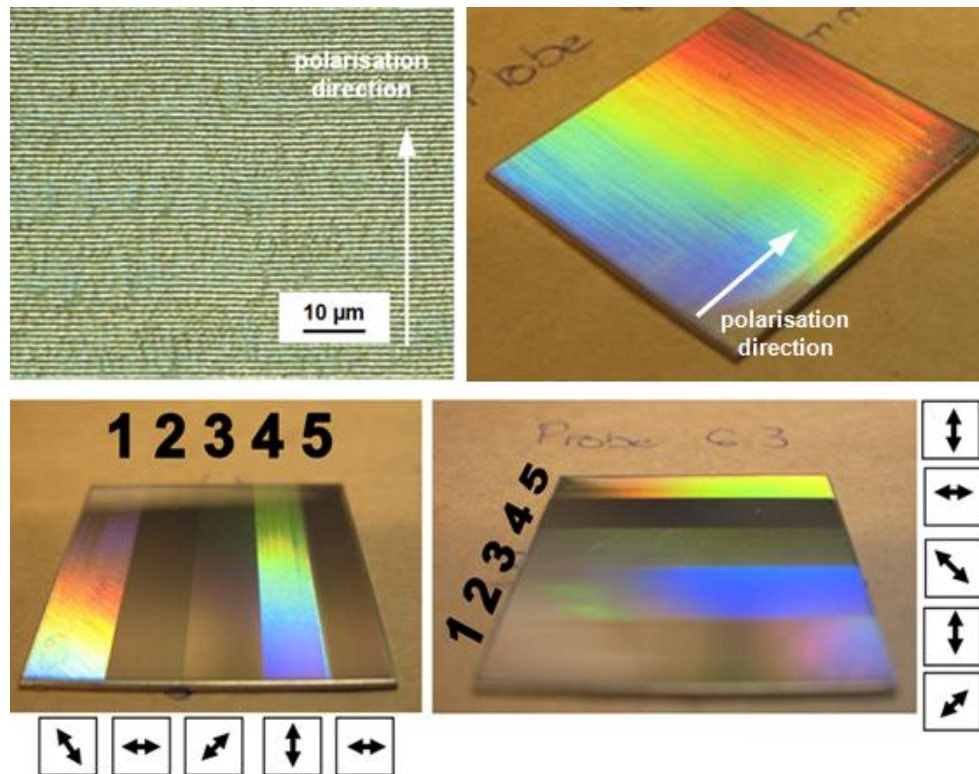


Figure 7-4: Highly-regular ripple formation on Stainless steel surface (top left); light diffraction due to white-light illuminations of ripple phase gratings are shown; the polarisation direction of the laser beam is indicated by the arrow; the photographs showing light diffraction were taken by **M. KOCH** (ThyssenKrupp Steel Europe AG).

7.3 Cone-like structures

In this chapter formation of self-organising cone-like shaped micro structures on Stainless steel is studied utilising high-PRF femtosecond laser pulses. Initial investigations suggest that the properties of the micro cones in terms of size and number can be directly varied by the processing parameters. Thus the impact of the repetition

rate, pulse energy, and lateral pulse spacing on cone formation was investigated in a broader range. The utilised machining parameters are listed in **Table 7-1**; the number of scan passes (100) and the hatch distance (7.5 μm) were kept constant.

Table 7-1: Processing parameter used in studying formation of cone-like micro structures on Stainless steel; number of scan passes and hatch distance were kept constant of 100 and 7.5 μm .

	Repetition rate [kHz]	Pulse energy [μJ]	Lateral pulse spacing [μm]
a	512	2.0	3.75
b	512	6.0	3.75
c	1,024	2.0	3.75
d	1,024	6.0	3.75
e	1,024	2.0	1.9
f	1,024	6.0	1.9
g	2,048	2.0	1.9
h	2,048	6.0	1.9

Figure 7-5 presents SEM photographs of laser processed Stainless steel surfaces, obtained by using the processing parameters given above. The origin of the cone-like shaped micro structures is shown with increasing laser energy input from left to right, and from top to bottom. With the higher accumulated laser energy (higher pulse energy, shorter temporal pulse-to-pulse distances or/and smaller lateral pulse spacing), both the height and volume of the cones increased, whilst the cone number decreased. In addition, with the higher accumulated energy, the conical geometrical structure shape is being lost in irregular voluminous bulge formations.

Figure 7-5 (a) to (d) shows the results obtained with the widest investigated lateral pulse spacing of 3.75 μm . The lower repetition rate of 512 kHz was used in the figures (a) and (b), and no cones originated. In the figure (a), by irradiating laser pulses of 2.0 μJ energy, a high number of singular holes emerged at the smooth surface. Laser pulses with the higher energy of 6.0 μJ , by contrast, caused smooth surfaces without this high number of holes (b).

7.3 Cone-like structures

In the figures (c) and (d), insular occurrence of cone-like shaped micro structures can be observed, obtained with laser pulses of the higher repetition rate of 1,024 kHz. On-going laser irradiation of these areas using multiple scan passes caused the expansion of the micro structures until the laser processed surface is completely covered with cone-like shaped structures.

Moreover, laser irradiation with the small lateral pulse spacing of $1.9\ \mu\text{m}$ caused extensive cone-like micro structure formation, as presented in the figures (e) to (h). It can be qualitatively derived from these photographs that the cone number per area decreased with higher total laser energy input. In addition it can be seen that the height of the cones increased with higher irradiated laser energy.

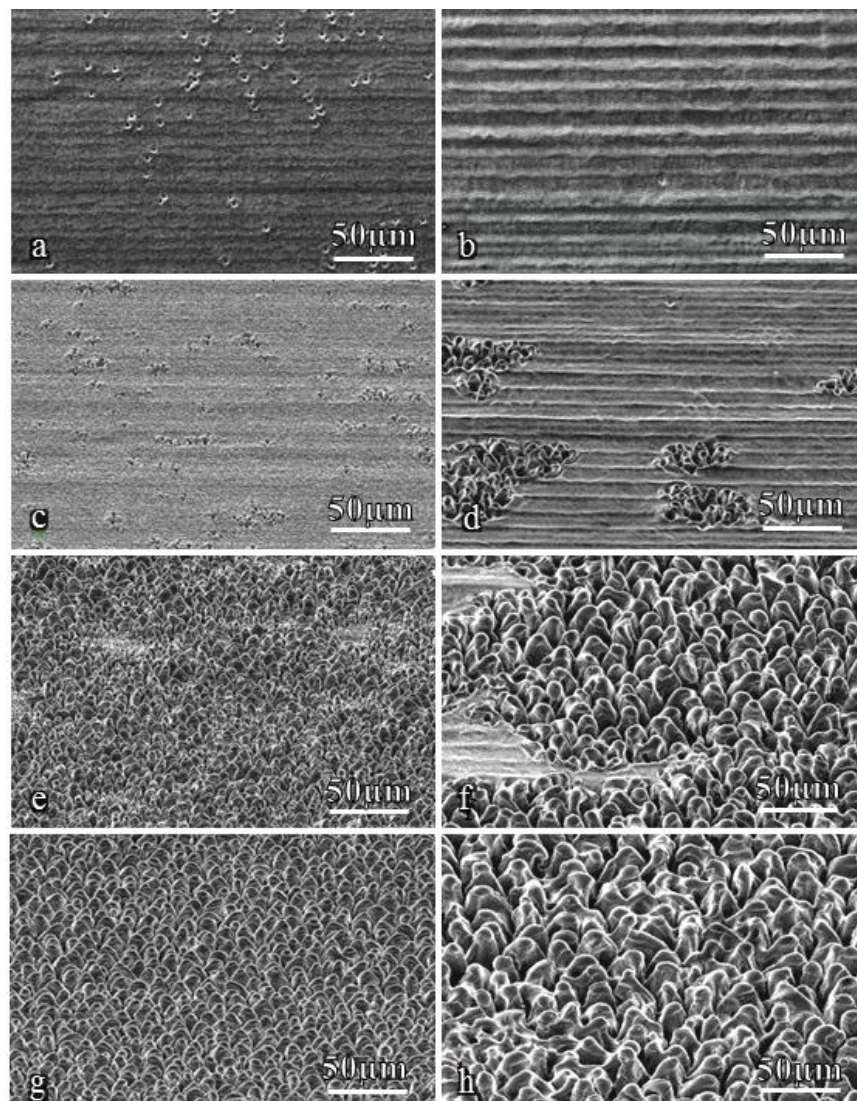


Figure 7-5: Cone-like shaped micro structures obtained on Stainless steel after 100 scans and $7.5\ \mu\text{m}$ hatch distance, the varied processing parameters repetition rate, pulse energy and lateral pulse spacing are given in **Table 7-1**.

However, the experimentally achieved results give evidence that the orientation of the cone-like shaped structures is strongly influenced by the polarisation direction of the irradiated laser beam. Thus micro cone orientation was analysed by using direction-dependent graphical analysis. In **Figure 7-6** it can be seen that micro structure orientation tends to align perpendicular to the laser beam polarisation. The preferential orientation direction of the cone-like shaped structures is given by the largest black bars, indicating cone orientation by an angle with reference to the horizontal zero position. The polarisation direction of the laser beam is highlighted by white arrows.

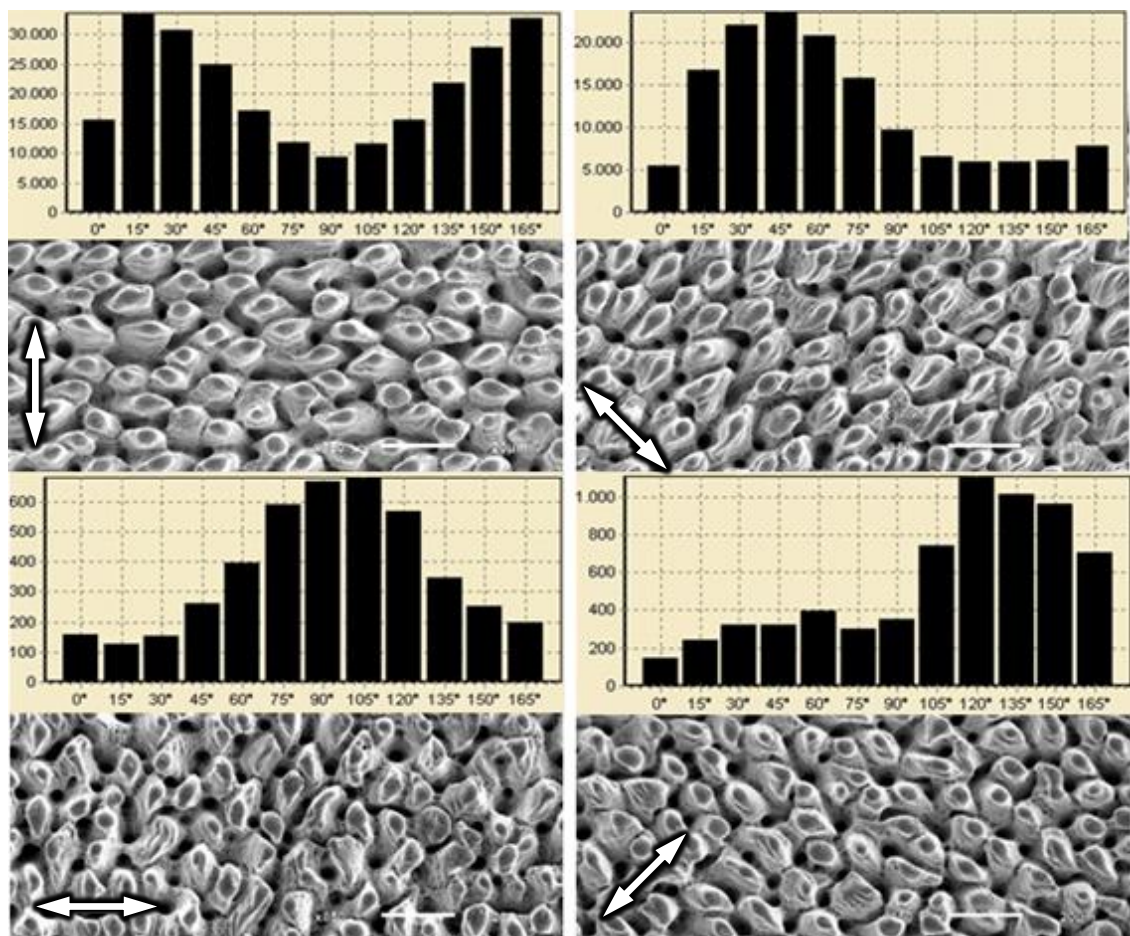


Figure 7-6: Polarisation dependence of micro cones, the preferred direction of cone orientation is illustrated by bar graphs determined in graphical analyses; the electrical field vector of the laser beam is indicated by a white arrow.

In the next subsection a closer view to the formation of cone-like shaped structures originating following high-PRF laser irradiations will be given because of insufficient research has been done in this topic. Overcoming this knowledge gap will provide new laser processing options. This is due cone-like shaped structures may or may not be desirable at laser processed surfaces, depending on the application.

Figure 7-7 distinguishes four characteristic states during micro cone formation: (a) development of deep micro holes, (b) formation of the initial micro cone structure, (c) spreading out of cone-like shaped micro structures across the laser treated surface, which is caused by multiple irradiations of the initial cones until (d) the surface is completely covered with the cone-like shaped pattern.

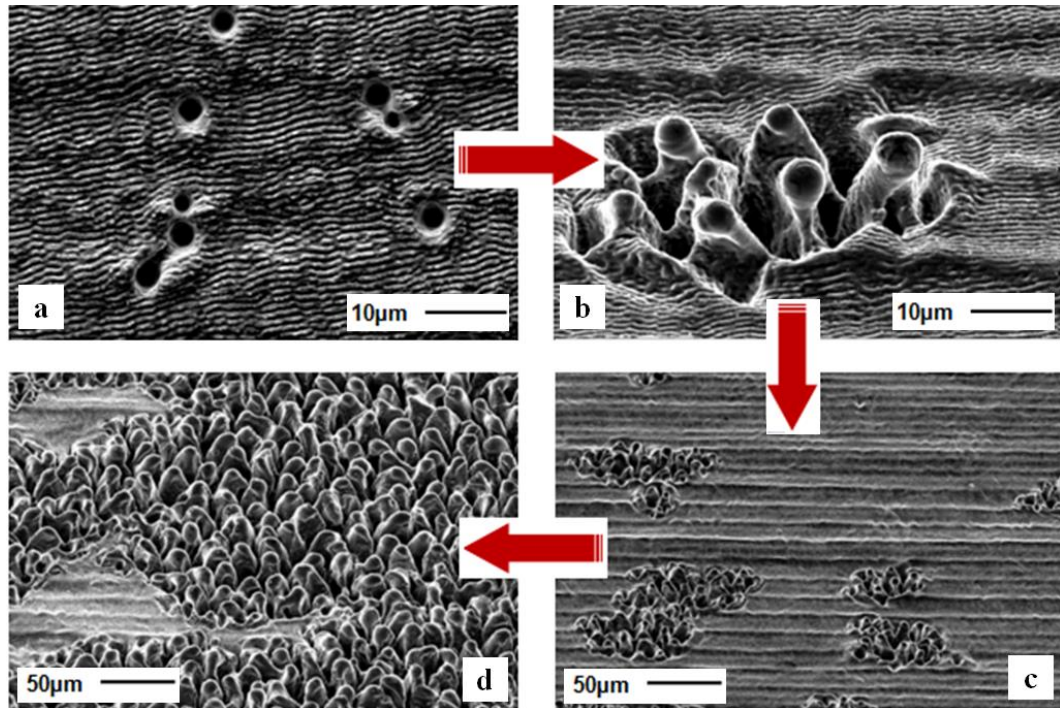


Figure 7-7: Micro cone formation on Stainless steel: (a) micro crater development, (b) initial state of micro structure formation, (c) micro cone spreading, (d) surface covered with cone-like shaped micro structures.

The initial state given in (a) is characterised by deep micro crater formations, randomly developed at the laser processed surface. Therefore ablation centres, i.e. material inhomogeneities, surface defects or grain boundaries, are likely initial sites for micro crater formation. In addition, the near field enhancement model seems to be a possible explanation for micro crater development [7, 139]. According to this, a considerably larger amount of laser intensity irradiates a specific small surface area underneath micro / nano-scaled spheres or particles. The enhancement of the near field is induced by such micro spheres, based on *Mie scattering theory* or shadowing reflectivity. In addition, near field enhancing effects have been proven recently for gold nanorods [140]. It was shown that energy transfer is dominated by the enhanced near-field around the particle, and the directly ionized and heated nanoplasma interacts with the surrounding.

According to this, even in high-PRF femtosecond laser processing, sub-micron scale particles can be assumed as initial point for field enhancement. These re-solidified particles can be found surrounding the laser processing zone, re-deposited after laser ablation. Underneath these particles the fluence of the following irradiated laser pulse might be enhanced due to near-field enhancement mechanisms. As a result, the ablation threshold will be locally exceeded, and ablation of micro craters can occur.

From the micrographs presented in **Figure 7-7 (b)**, the micro craters may be identified as a primary origin for cone-like shaped micro structure formation. Starting from locally insulated cone-covered areas (**Figure 7-7 c**), on-going laser processing by multiple laser passes caused the spread of the conical structures (**Figure 7-7 d**) until the entire processed surface area was completely covered.

In the previous *Section 2.4.2* hydrodynamic mechanisms have been proposed as potential mechanisms of cone-like structure formation. Capillary wave instabilities (*Rayleigh-Taylor* instabilities, *Kelvin-Helmholtz* instabilities) have been identified as initiators of droplet formation during nanosecond laser pulses. The basic prerequisite in terms of these hydrodynamic mechanisms is melt and/or evaporated material. Since the initial micro craters have formed, the following incident laser pulses reflect on the crater side walls, causing enlarged energy deposition due to multiple laser beam absorption. As a result, local overheating of the material may occur and, in addition to material ablation, enhanced material melting can potentially take place.

Material melting, however, has been demonstrated already in this thesis for high-PRF laser processing of Stainless steel. Thus, in the following, micro cone formation induced by high-PRF laser pulses will be compared with different hydrodynamic mechanisms.

The first hydrodynamic mechanism, *capillary wave instabilities in the field of plume pressure*, is induced by heating in the evaporation regime by laser beam absorption in a vapour plume. Furthermore *capillary wave instabilities* imply spatial modulation of pressure in the plasma surface layer. This can be achieved by local focusing and defocusing of the flux of the evaporated substance which is directed along the normal to the target surface [86]. However, heating of the evaporated ablation/vapour plume can only take place by using longer laser pulses. In case of femtosecond laser pulses the pulse has been already finished when the plasma plume arises. Thus *capillary wave instabilities* can most likely neglected for micro cone formation following high-PRF

laser irradiation.

A schematic given in reference [7] supports the proposition that hydrodynamic mechanisms induce micro cone formation during high-PRF femtosecond laser irradiations. In Figure 7-8 left, a schematic of *Kelvin-Helmholtz* instability is related to machining examples, achieved in high-PRF laser processing of Stainless steel. *Kelvin-Helmholtz* instabilities determine the transition from humps into vertical columns because of the vapour velocity is much higher than the velocity of liquid layers. This kind of vertical columns can be observed on high-PRF laser processed surfaces. Explanation therefore might be given by the lateral expansion of the plasma/vapour plume, initiating excitation of capillary waves in the melt that will transform into vertical columns.

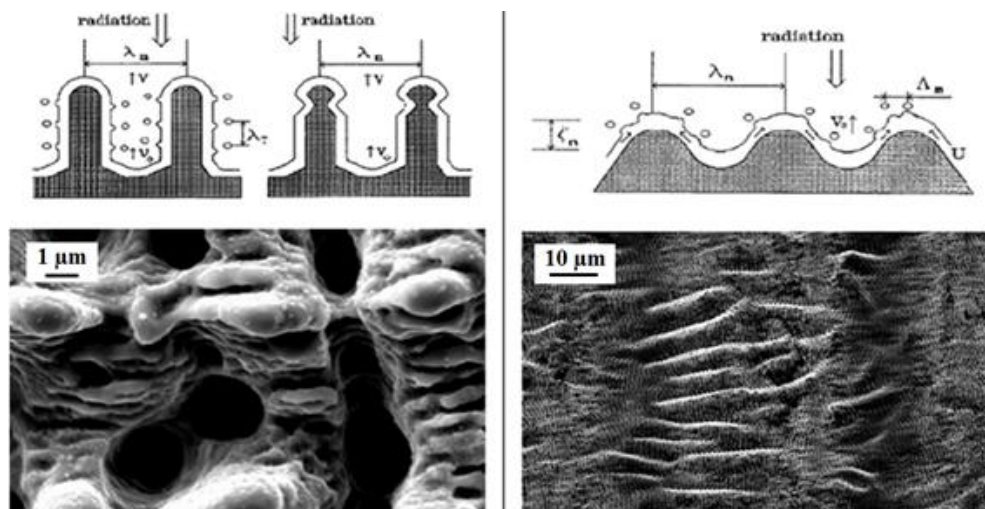


Figure 7-8 top: Schematic of micro droplet formation mechanisms occurring in nanosecond laser irradiation, taken from reference [7], with Kelvin-Helmholtz instabilities (left) and Rayleigh-Taylor instabilities (right); **bottom:** micro structure formation upon high-PRF femtosecond laser processing of Stainless steel.

Rayleigh-Taylor instabilities, in the other hand, describe droplet formation as a result of centrifugal forces, induced by the outflow of the molten material from pits to humps. In relation to this, Figure 7-8 (right) shows the start of cone formation, obtained on femtosecond laser processed Stainless steel metal plates. The droplets might be formed due to the existing liquid vapour interface. In the schematic, the corrugation of the surface is induced by the flow of the molten material from pits to humps, induced by centrifugal forces. According to this, the ripple relief can be assumed as one initiating event for melt corrugation, observable on the laser processed surfaces.

7.4 Potential application of laser-induced surfaces structures

Micro textured / structured surfaces permit novel material properties for innovative industrial applications. In terms of wettability, the enhancement of the hydrophobic characteristic of laser micro structured surfaces has been demonstrated already [141]. In this thesis, surface wettability behaviour of high-PRF femtosecond laser processed surfaces was tested in an initial approach. The wettability was determined by using the contact angle measuring method using water as testing liquid. Three Stainless steel metal sheets with different surface characteristics were evaluated, a laser untreated Stainless steel surface compared to both “gentle” (1 μJ pulse energy) and “strong” (6 μJ pulse energy) laser processed metal sheets.

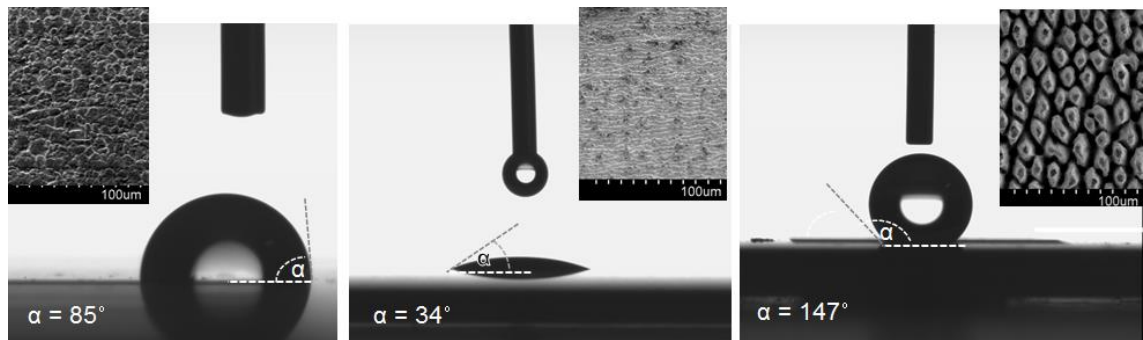


Figure 7-9: Contact angle measurements on Stainless steel surfaces, **left:** laser untreated material surface with a contact angle of 85° , **centre:** low-fluence laser processed surface, the contact angle of 34° indicates a hydrophilic character; **right:** cone-like shaped Stainless steel surface, the contact angle of 147° indicates a super hydrophobic character.

Figure 7-9 illustrates the influence the surface characteristic on the wettability. The contact angle of laser untreated technical Stainless steel surface was 85° . A hydrophilic surface behaviour with a contact angle less than 34° was detected on the low-fluence laser processed surface. This surface was covered with small micro structures. By contrast, for the cone-like shaped surface, fabricated by irradiating high-fluence laser pulses, a super hydrophobic surface characteristic with contact angles up to 147° was obtained.

7.5 Summary

Ripple formation induced by high-PRF laser processing was studied on Stainless steel. The dependence of ripple orientation on the polarisation direction was confirmed, In addition to this, a higher-order mechanism for ripple formation was suggested because of irregularities greatly enhance disordering of the ripple patterns. White-light illumination of the ripple phase grating caused diffraction patterns.

Further, results achieved in studying micro cone formation suggest, that the droplet formation mechanism as presented in the nanosecond pulse regime may be potentially transferrable to high-PRF femtosecond laser processing. Both, formation of cone-like shaped micro structures as well as wave-like structures appear on femtosecond laser processed surfaces. This was explained by hydrodynamic processes, such as *Rayleigh-Taylor* or *Kelvin-Helmholtz* instabilities.

However, in this thesis the formation of cone-like shaped micro structures, appearing during high-PRF laser irradiations are not fully explained due to time constraints. To achieve an overall explanation of the interacting mechanisms and effects occurring, significant complementary studies would be required. Potentially, metallographic analysis might be beneficial to detect potentially assumed melting phases on the micro cone covered surface.

A potential industrial application of this technology can be seen in laser fabrication of metal surfaces with customised wettability characteristics.

8 Machining examples

8.1 Introduction

To demonstrate the feasibility of the high-PRF femtosecond laser technology in micromachining for industrial applications, a number of machining samples were investigated. In this context it is worth noting that only a limited analysis of all aspects and underlying mechanisms is undertaken. The results obtained using two different machining strategies are presented here.

Demonstrator structures fabricated using both line-scan laser ablation and 3D laser micro structuring methods are reviewed in the *Sections 8.2 and 8.3*. Further, an example of micro mould fabrication is shown in *Section 8.4* to demonstrate the feasibility of the technology in rapid manufacturing.

Section 8.5 points out technical limitations of the high-PRF femtosecond laser technology in micromachining, identified during the experimental work. The chapter concludes with a short summary in *Section 8.6*.

8.2 Line-scan laser ablation

Line-scan laser ablation was studied on Stainless steel with particular focus on the influence of pulse energy, pulse repetition rate, and number of line-scan passes on both the width and depth of laser processed kerfs. In addition, the spatial distance between the laser processed lines was varied to evaluate spatial process resolution.

The laser pulse energy was varied in the range between 0.92 μJ and 6.81 μJ , the repetition rate between 102 kHz and 4.1 MHz, and the number of line-scans between 100 and 1000. The lateral pulse spacing in scan direction was kept constant of 4.5 μm ; the distance between ablation lines was ranging from 20 μm to 50 μm . With each individual parameter set 5 individual lines were processed. The width and depth of the resulting kerfs, as well as the minimum achievable distance between the kerfs were

evaluated by means of digital micrographs taken from polished cross sections. A test pattern as well as definition of the kerf width and kerf depth is shown in **Figure 8-1**.

To irradiate a constant energy per unit section at both similar laser pulse energy and varying pulse repetition rates, a faster scan speed was applied at the higher repetition rates. The scan speed was increased linearly with the repetition rates according to the relation $v_S = d_X \cdot f_R$. Thus, for the highest investigated repetition rate of 4.1 MHz, the resonant scan system was utilised to supply the required scan speed of 18 m/s. At the lower repetition rate, the galvanometer scan system was used with maximum scan speed of 4.5 m/s.

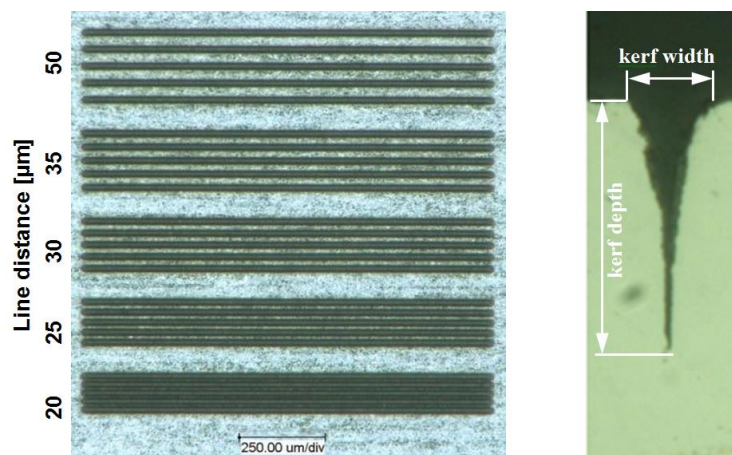


Figure 8-1 left: Machining example in Stainless steel to evaluate laser line-scan ablation, processed with 0.92 μJ pulse energy, 100 scan passes, 102 kHz repetition rate, increasing line distance; **right:** determination of evaluation parameters *kerf width* and *kerf depth*.

The results obtained in kerf width measurement are summarised in **Figure 8-2**. The kerf widths increased with higher number of line-scan passes and laser fluence. At the low pulse energy of 1 μJ , only little widths differences were obtained for repetition rates of either 102 kHz or 1.02 MHz. The smaller kerf width obtained at 4.1 MHz might result from the lower irradiated laser fluence. This is likely caused by the wider focus diameter using the resonant scan system. By contrast, at the higher irradiated pulse energies, the width of the kerfs fabricated with the higher repetition rates are wider than the kerf widths obtained with low pulse repetition rate but similar pulse energy. This may be explained by heat accumulative effects as demonstrated in *Section 4.2*. It was suggested that the ablation crater diameters for Stainless steel increase at higher repetition rates, originating from reduced ablation thresholds due to heat accumulation.

8.2 Line-scan laser ablation

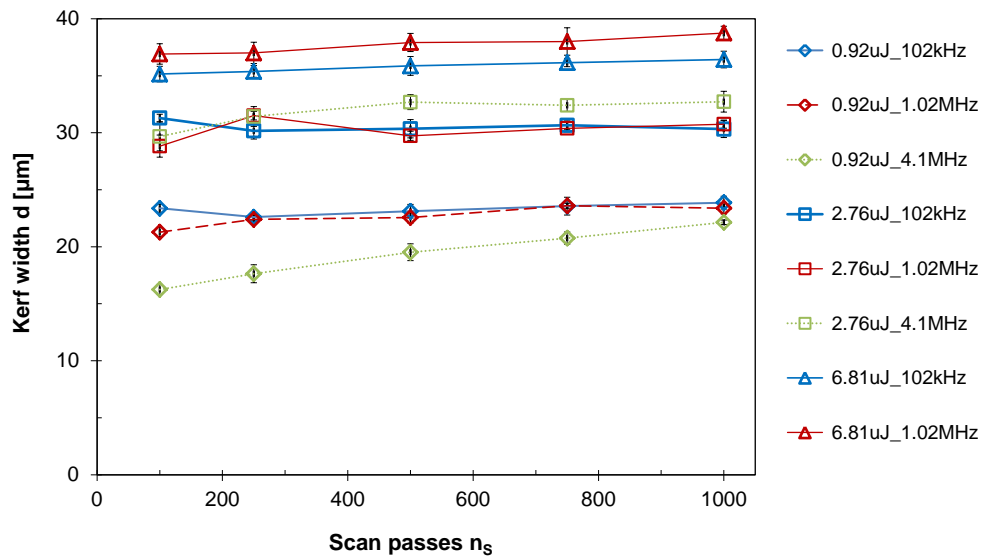


Figure 8-2: Kerf width versus number of line-scan passes at various pulse energies (0.92 μJ , 2.7 μJ , 6.81 μJ) and repetition rates (102 kHz, 1.02 MHz, 4.1 MHz).

Cross section views of kerfs fabricated in Stainless steel with different machining parameters are summarised in **Figure 8-3**. In all cases the initial kerf formed V-shaped, but with increasing number of line-scan passes or/and higher pulse energy the kerf became even smaller with increasing depth.

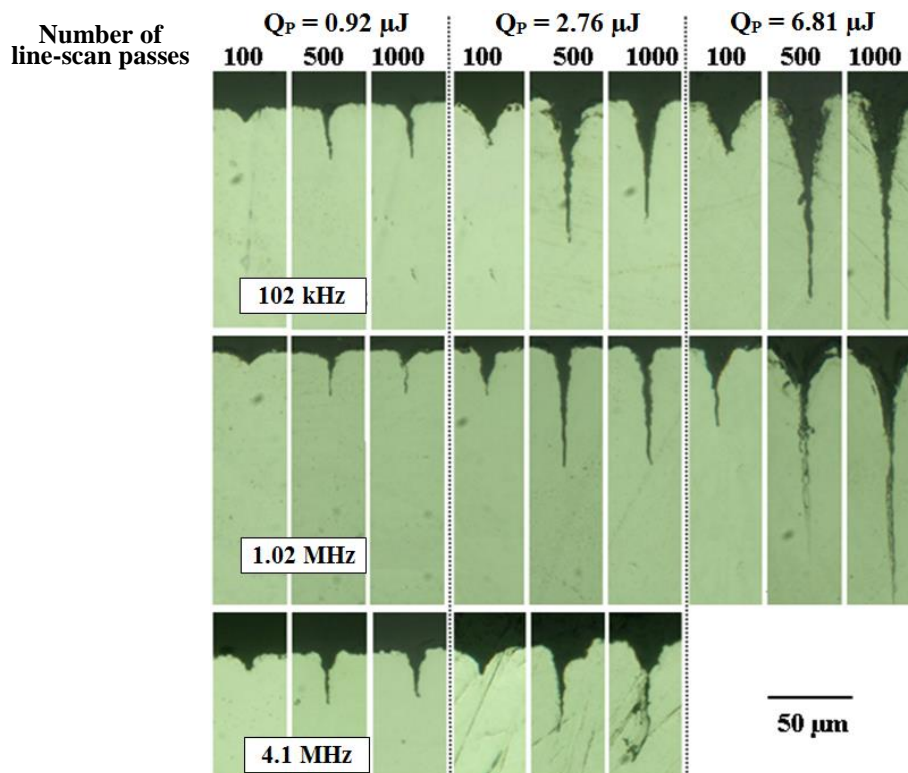


Figure 8-3: Cross section view of laser ablated kerfs processed with different machining parameters in Stainless steel: pulse energy 0.92 μJ , 2.76 μJ , 6.81 μJ ; number of line-scan passes 100, 500, 1000; repetition rate 102 kHz, 1.02 MHz, 4.1 MHz.

Figure 8-4 presents ablation kerf development for the highest investigated repetition rate of 4.1 MHz. Whilst ripple structures emerged following irradiation of the low pulse energy of 0.92 μJ (see figure (a)), deep crater and melt formation can be seen in the figures (b) and (c) for the higher pulse energies of 1.84 μJ and 2.76 μJ , respectively. In figure (d) irregular formation of the ablation kerf is shown. In this case laser processing using 250 line-scans and 2 μJ pulse energy, deep ablation craters and molten wall structures alternates with a distance of approx. 5 μm at the structure bottom. For this heat accumulation accompanied by strong material melting may be assumed as the dominant interaction effect.

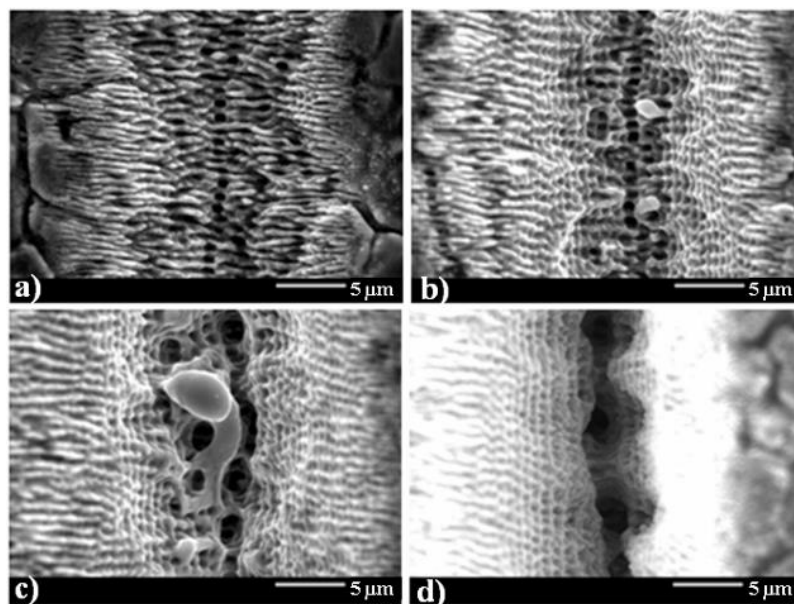


Figure 8-4: Ablation kerf development at the bottom of line-scan laser ablation structures, processed with 100 scan passes, 4.1 MHz repetition rate and different pulse energies; a) 0.92 μJ , b) 1.84 μJ and c) 2.76 μJ ; d) deep micro craters obtained with 250 scans and 1.84 μJ .

The kerf depths achieved in these laser line-scan ablation experiments are summarised in **Figure 8-5**. At the low pulse energies of either 1 μJ or 3 μJ , the kerf depths increased continuously up to 500 line-scans independently from the repetition rates. With higher numbers line-scans the kerf depths did not further increase. The pulse energy seems to be too low to eject the material from deeper regions satisfactorily. This suggests that material removal is saturated by material re-deposition and material melting. By using the higher pulse energy of 6.91 μJ , a sufficient amount of laser energy irradiates the surface to eject the ablated material out of the crater. The kerf depth increases with higher number of line-scans.

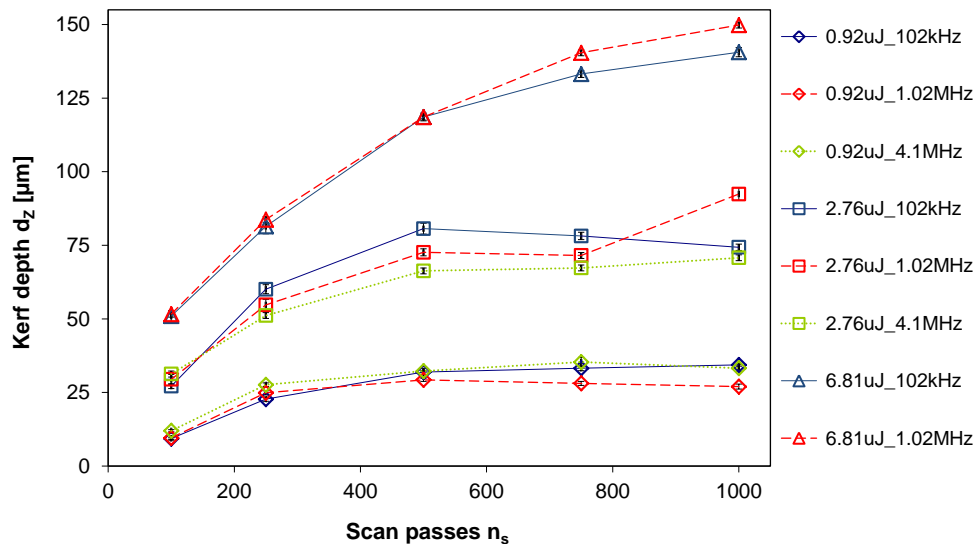


Figure 8-5: Kerf depth versus number of line-scans obtained with different pulse energies (0.92 μJ , 2.76 μJ , 6.81 μJ) and rep. rates (102 kHz, 1.02 MHz, 4.1 MHz).

Laser micro processing using high average laser power resulted in reduced spatial resolution between single ablated line-scans, likely due to heat accumulative effects.

Figure 8-6 illustrates cross sections of the kerfs processed with the line distance ranging between 25 μm and 50 μm . In each case the maximal available pulse energies of either 6.81 μJ at 102 kHz and 1.02 MHz or 2.76 μJ at 4.1 MHz was utilised.

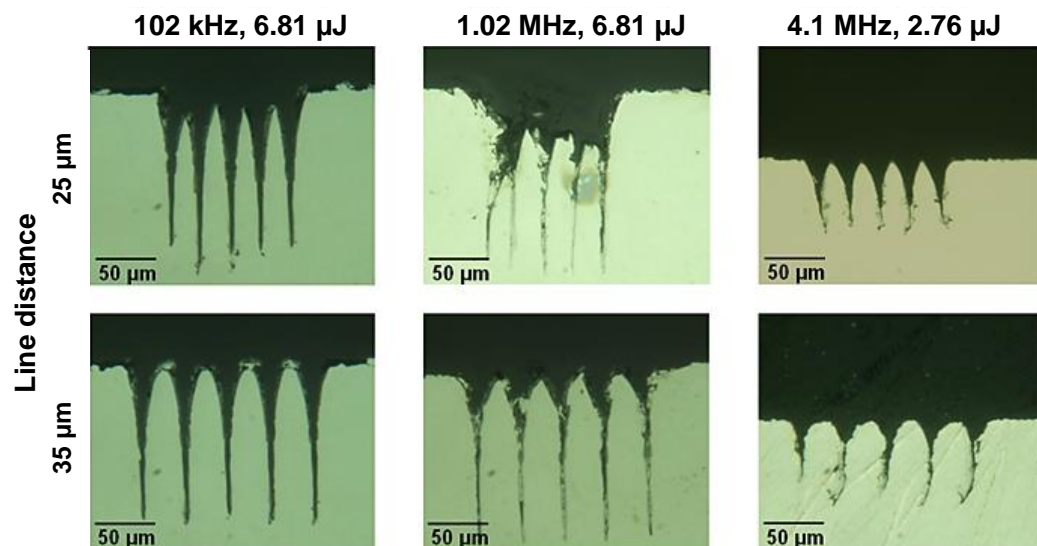


Figure 8-6: Cross section of kerf structures obtained using various laser processing conditions.

The highest processing quality was obtained by using the lowest repetition rate (102 kHz) and maximum pulse energy (6.81 μJ). The highest aspect ratio was 1:10. In the micrographs it can be seen that height defects occurred at the smallest line distance of

25 μm . The crossbars are eroded below the sample surface due to the overlapping line scans. The achievable spatial resolution to reach an alternating kerf-wall formation without any height defects was found to be 35 μm . It can be seen that irradiation of high-PRF laser pulses with repetition rates higher than 1 MHz is negatively affecting the processing quality due to fragmentation and melting.

However, by arranging overlapping line-scans in a distinct processing regime, trench-like ablation structures have been fabricated, shown in **Figure 8-7**. Multiple scan passes were irradiated to erode the material up to a depth of 90 μm . With increasing number of scan passes the numbers of line-scans in a single scan pass decreased. As a result the V-shaped ablation structure could be fabricated.

Furthermore the pulse energy and the numbers of scan passes were varied in a way that a constant amount of laser energy irradiates the sample surface. As such, the number of line-scans decreased at higher pulse energies. In addition, both the impact of the repetition rate and the scan direction was investigated. The unidirectional (scan direction from left to right) and bidirectional (meander) processing regime was applied. The depths of these structures were measured using a confocal displacement sensor.

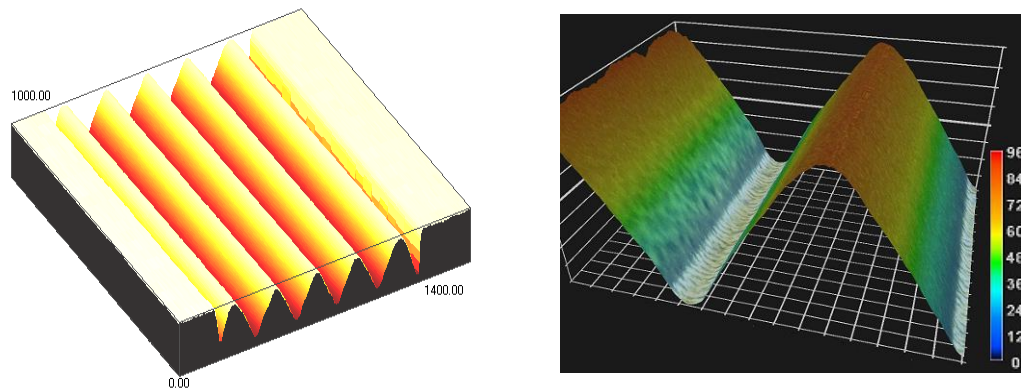


Figure 8-7 left: Trench-like ablation structure obtained by overlapping line-scans; the dimension is 1 mm width, 1 mm length and 90 μm in height; **right**: detailed view.

Table 8-1 summarises the depths of trench-like structures fabricated with different processing regimes. Structure ablation was carried out by irradiating a constant amount of accumulated energy (84.4 J/cm²). The accumulated energy is the product of the energy per unit length and the number of scan passes. The energy per unit length, in turn, calculates by the ratio of average laser power P_{av} divided by the scan speed v_s .

Table 8-1: Depths of trench-like structures obtained with different processing regimes.

Pulse energy [μJ]	Energy per unit length [J/m]	Number of scan passes	Accumulated laser energy [J/m]	Structure depth [μm]		
				Bidirectional 102 kHz	Unidirectional 1.02 MHz	Bidirectional 1.02 MHz
1.9	0.47	180	84.4	76.0	81.9	82.4
2.5	0.63	135	84.4	84.7	85.5	89.4
3.75	0.94	90	84.4	83.8	85.0	86.9

In spite of the constant total (accumulated) laser energy input, laser processing with the lowest single pulse energy of 1.9 μJ yielded the lowest ablation depth. On the other hand, the ablation depth increased by using higher repetition rates. The percentage increase of the structure depth ranges between 4 % at 3.75 μJ irradiated pulse energy and 8 % at 1.9 μJ , respectively. This increase of the structure depth will most likely be related to heat accumulation.

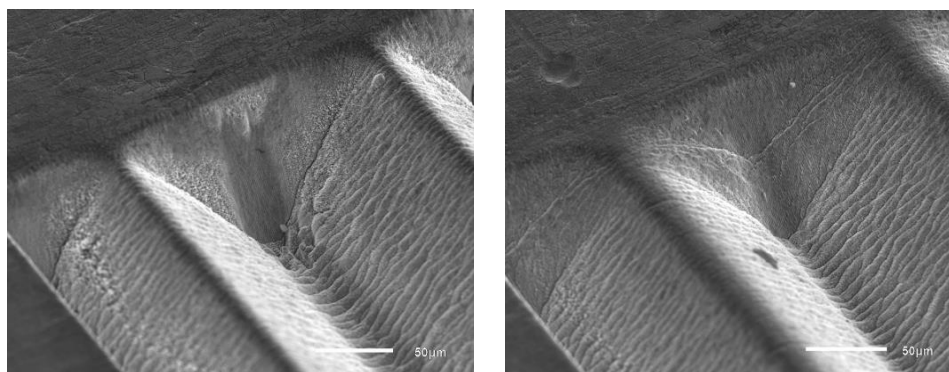


Figure 8-8: SEM photographs showing a detailed view on trench-like ablation structures obtained using unidirectional (left) and bidirectional (right) processing regimes; processing parameters were: pulse energy: 2.5 μJ , repetition rate: 1.02 MHz.

However, the micrographs shown in **Figure 8-8** indicate some impact of the scan regime on the accuracy of the laser process. For this a difference in the thermal field around the laser irradiation zone is proposed. By applying the unidirectional scan regime each single line-scan will start in a cooled down area. By contrast, for bidirectional laser processing it can be assumed that the temperature field is moving with the laser beam across the sample surface. As a result, bidirectional laser processing

(**Figure 8-8**, right) caused rounded shapes at the laser turning point and soft edges. This is likely to be induced by an enlarged ablation zone due to the higher thermal load. In unidirectional laser processing even more detailed and sharp structure features were obtained (**Figure 8-8**, left).

In addition, an influence of the pulse energy on the surface behaviour of the ablation structure can be suggested, indicated by the micrographs presented in **Figure 8-9**. A higher amount of re-deposited debris / ablated material can be observed on the trench sidewalls processed with the higher pulse energy of 3.75 μJ , compared to 2.5 μJ . These material re-deposits are negatively affecting the machining quality.

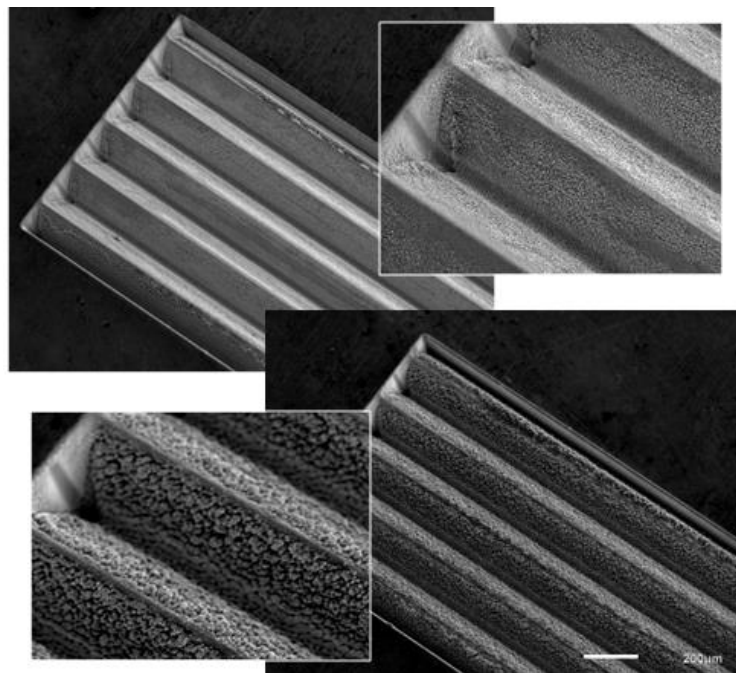


Figure 8-9: Trench-like structures obtained by using different pulse energies of either 2.5 μJ (top) or 3.75 μJ (bottom).

8.3 3D laser micro structuring

A set of complex three-dimensional demonstrator structures were fabricated utilising the high-PRF femtosecond laser and layer-by-layer process regime. Laser beam deflection was carried out by using the galvanometer scanner system. To prevent any defocussing effects due to the limited Rayleigh length of the laser beam, the focus position was realigned to the surface of the ablation structure after each processed layer.

Step pyramid demonstrators such as shown in **Figure 8-10** were fabricated in Stainless steel with 2 μJ pulse energy and 4 μm spatial pulse spacing. Different repetition rates of either 205 kHz or 1.02 MHz were applied. To keep the lateral pulse spacing constant, the scan speed used was 0.8 m/s at the lower repetition rate and 4.1 m/s at the higher ones. The dimension of the pyramid was 2.4 x 2.4 x 0.5 mm^3 (length x width x depth) that corresponds to the total removed volume of 1.7 mm^3 . Acceleration and deceleration paths were used to avoid irregular material removal due to laser pulse accumulation at the pyramid edges. The total processing time was 50 minutes using the higher repetition rate. The material removal rate derived from these values calculates of 0.035 mm^3 / min . This is significantly smaller than the material removal rate presented in the previous *Section 5.5*, which was 0.77 mm^3 / min for Stainless steel. The main reason for this is the increase of the processing time during fabrication of complex structures, primarily due to acceleration / deceleration sections, jumps between the line-scans as well as focus position realignments. In fundamental investigations, by contrast, the maximum achievable material removal rate was determined, regardless of any time delays that may have occurred during laser fabrication of complex three-dimensional structures.

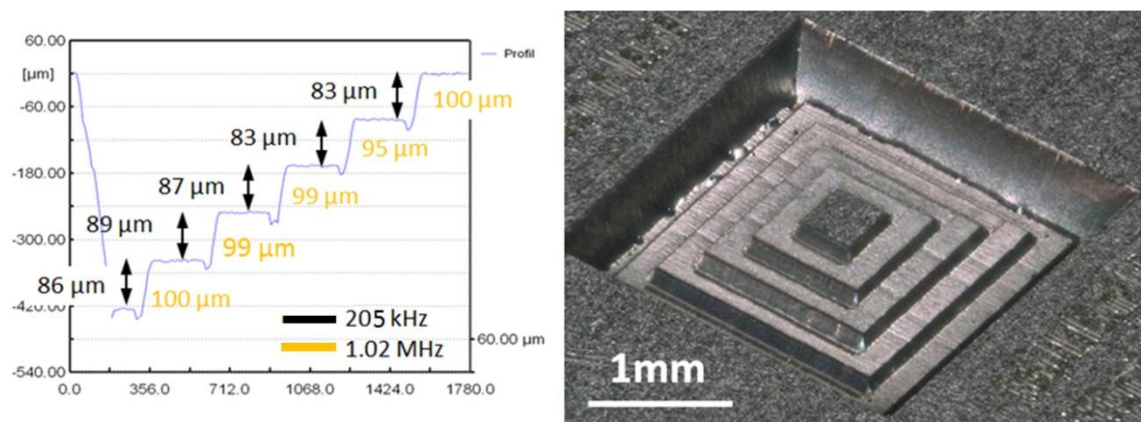


Figure 8-10: A pyramid demonstrator structure made in Stainless steel, different step heights were obtained for the repetition rate of either 205 kHz or 1.02 MHz, respectively.

Pyramid depth measurements utilising the confocal point sensor confirmed the impact of the repetition rate on material removal, already discussed in *Chapter 5*. With the lower repetition rate of 205 kHz the pyramid step height was measured in the range between 83 μm and 87 μm . With the higher repetition rate of 1.02 MHz, by contrast, the step height was almost 100 μm , potentially induced by heat accumulative effects. The study of high-PRF laser processing of Stainless steel presented in *Section 4.2.2* indicated an almost 20 % lower ablation threshold for 1.02 MHz, compared to 102 kHz.

According to this, the percentage increase of the step height of 20 % at the higher repetition rate corresponds to the decrease of the ablation threshold.

In addition, high-PRF laser micro structuring was compared to laser processing using conventional femtosecond laser systems emitting laser pulses with repetition rates in the range of kilo Hertz. **Figure 8-11 (a)** presents a micro-featured demonstrator structure of $1 \times 1 \times 0.1 \text{ mm}^3$ (width x length x depth) made in Stainless steel. This structure is similar to a work done by *ENGEL et al.* [142] using a low average power femtosecond laser (1 W average laser power at 1 kHz repetition rate), presented in **Figure 8-11 d**.

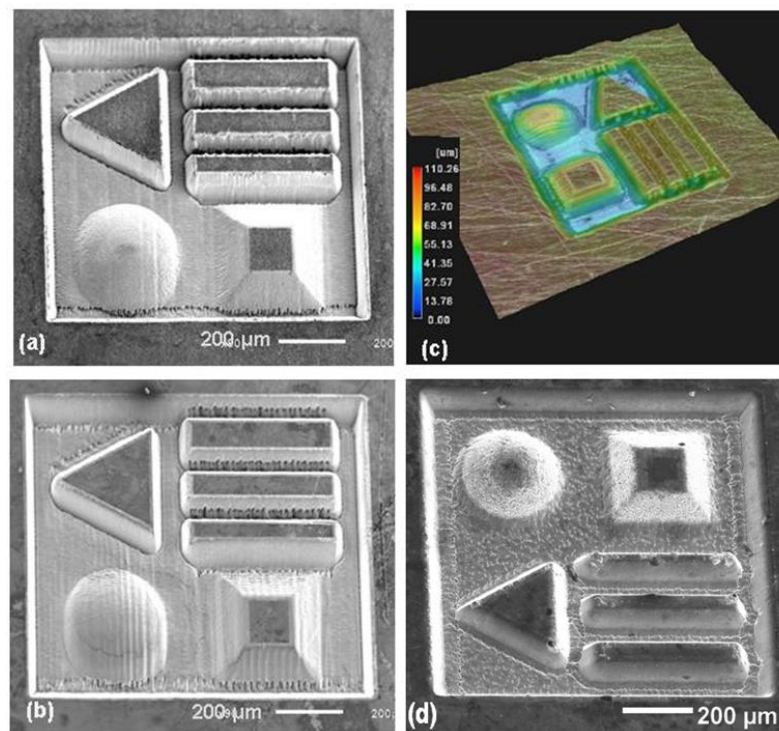


Figure 8-11: High-PRF laser fabricated demonstrator structures made in (a) Stainless steel, (b) Copper, and (c) Aluminium; for comparison a similar structure made in Stainless steel, taken from reference [142].

The high-PRF laser fabricated demonstrator structure was obtained after laser processing of 100 individual layers. Both, acceleration/deceleration path processing regime and focus position tracing of $1 \mu\text{m}$ from layer to layer were applied to avoid pulse accumulation and defocusing effects. Maximum processing speed was 1.4 m/s, obtained with 341 kHz repetition rate and $4 \mu\text{m}$ lateral pulse spacing. Laser processing time was about 6 minutes. The processing speed was limited due to the applied acceleration/deceleration path process regime. A faster scan speed was not applicable by using this method. The real time controller (RTC) used to control the laser in

combination with the galvanometer scanner failed to supply the very short cycles of operation which are required for micro scaled structure manufacturing.

The processing time achieved by using high-PRF laser pulses is about 40 times shorter than laser processing using the 1 kHz femtosecond laser system, mentioned above. In the latter case the laser beam was deflected with a speed of only a few mm/s due to the limited pulse repetition rate in the kHz-range.

The demonstrator structure was also produced in Copper (**Figure 8-11 b**), and Aluminium (**Figure 8-11 c**). For all three high-PRF laser fabricated structures, a considerably higher processing quality can be recognised in the figure, compared to the 1 kHz processing result.

8.4 Micro mould fabrication

The high-PRF laser micromachining technology was applied in micro mould fabrication in order to produce micro-fluidic demonstrators by micro-injection moulding.

A micro patterned Aluminium structure was produced to be used as a mould demonstrator and is shown in **Figure 8-12**. The approximate dimension of this mould was 15 x 11 mm² with a depth of 80 µm. The width of the remaining bridge was 58 µm at the surface and increased with the depth. By using a horizontally polarised beam, the wall angle of the bridge formed differently. This was due the relation between polarisation direction and plane of beam incidence. At the bottom of the ablated structure, the width of the bridge was measured of 110 µm when the plane was parallel to the plane of incidence. In vertical orientation the bridge width was determined of 116 µm, respectively. However, a homogeneous bridge width of 112 µm was obtained by irradiation of circular polarised laser radiation. This can be seen in **Figure 8-12** bottom, right. The processing time of the mould was almost one hour.

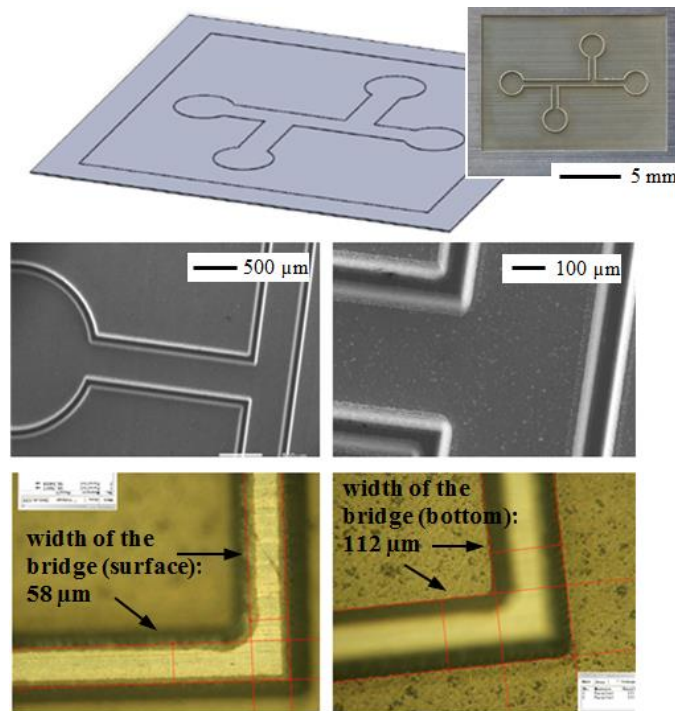


Figure 8-12: Micro featured mould processed in Aluminium; the drawing of the demonstrator and the manufactured Aluminium mould are shown on top, a detailed view of the micro features is given by means of both SEM (centre) and optical microscope photographs (bottom).

A micro-fluidic system as cast from this Aluminium demonstrator mould is shown in **Figure 8-13**. The size of the produced microfluidic channel was $116\ \mu\text{m}$ (surface) respectively $60\ \mu\text{m}$ (bottom) by $80 \times 80\ \mu\text{m}^2$ in width and depth. This size fits very well to the bridge dimension of the mould. The optical microscopy photographs below confirm the highly detailed results from the injection moulding process.

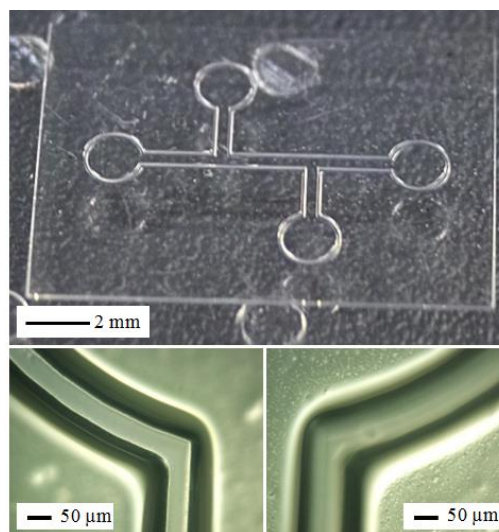


Figure 8-13: Plastic replica of the microfluidic demonstrator mould; the channel was $80\ \mu\text{m}$ deep with a width of $60\ \mu\text{m}$ at the bottom (left) and $116\ \mu\text{m}$ at the surface, respectively.

In another approach, a ripple structured mould processed on Stainless steel was injection moulded in plastic. The ripple structure was replicated, presented in **Figure 8-14**. The photograph shows white-light illumination of the replicated ripple structure. Diffraction of the light is clearly recognisable. In addition, the replicated ripple structure is shown, captured using a digital optical microscopy and 4,000X magnification.

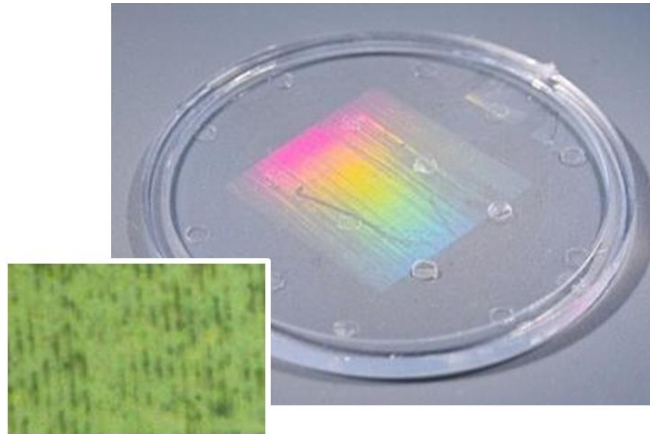


Figure 8-14: Plastic replica of a ripple structured Stainless steel mould; structure size was 20 by 20 mm² with the ripple period of approx. 1 μm ; diffraction of light is clearly recognisable, induced by white light illumination; the replicated ripple pattern is shown (left).

8.5 Technical limitations of the high-PRF laser technology in micromachining

A number of technical limitations have been identified during the experimental work by using the developed high-PRF femtosecond laser processing technology. The limitations are based on the laser system, the galvanometer scanner system and the applied machining strategy.

A major inconvenience of the utilised laser system is the limited available pulse energy, in particular at the higher repetition rates. Adequate laser fluence for metal ablation was only supplied up to a repetition rate of 2.0 MHz, where the maximum pulse energy was ranging between 7 μJ and 8 μJ . This energy was found in this work as sufficiently high enough for Stainless steel and Aluminium processing, but appears to be too low for efficient Copper and hard metal machining.

Another limit of the laser system is the AOM module, used for fast and precise laser beam switching. This module is useful for repetition rates up to 1.3 MHz; at the higher repetition rates the laser pulses cannot be clearly separated.

The galvanometer scan technology is regarded as the restricting element for fast laser processing due to the limited maximum scan speed of 4.5 m/s. However, this scan speed is appropriate to machine with the maximum switchable repetition rate of 1.02 MHz and 4.5 μm lateral pulse spacing. A dithering of the laser beam along the laser scanned line was observed, indicated in **Figure 8-15**. A positioning error up to 3 μm of the individual laser pulses can be observed on Copper in the left figure. This is in the range of the spatial resolution of the scan system. As a result of this positioning faults, imperfect ablation surfaces were obtained, illustrated in **Figure 8-15** right. An alternating wall / ablation formation was achieved with a period twice the hatch distance. This alternating structure is moving in scan direction.

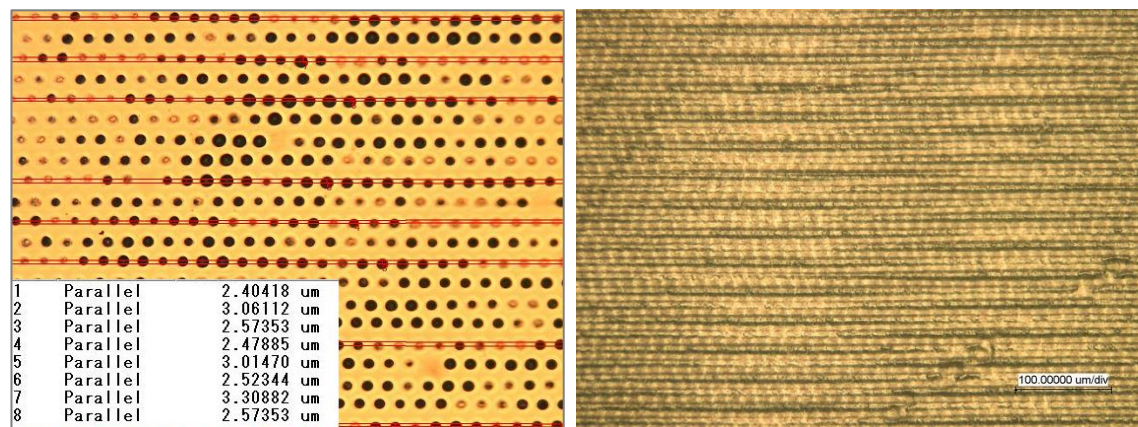


Figure 8-15: Positioning error on Copper caused by the limited spatial resolution of the galvanometer scan technology.

Another technological limitation appears to be caused by the applied machining regime using acceleration and deceleration paths. **Figure 8-16** illustrates processing times, calculated for the galvanometer setup used in this thesis, one scan pass of 1 cm^2 , unidirectional scan regime, and 4 μm spatial pulses spacing in length and width. The length of the processing path and the scan speed are varied. Acceleration and deceleration sections were added to the nominal pass lengths.

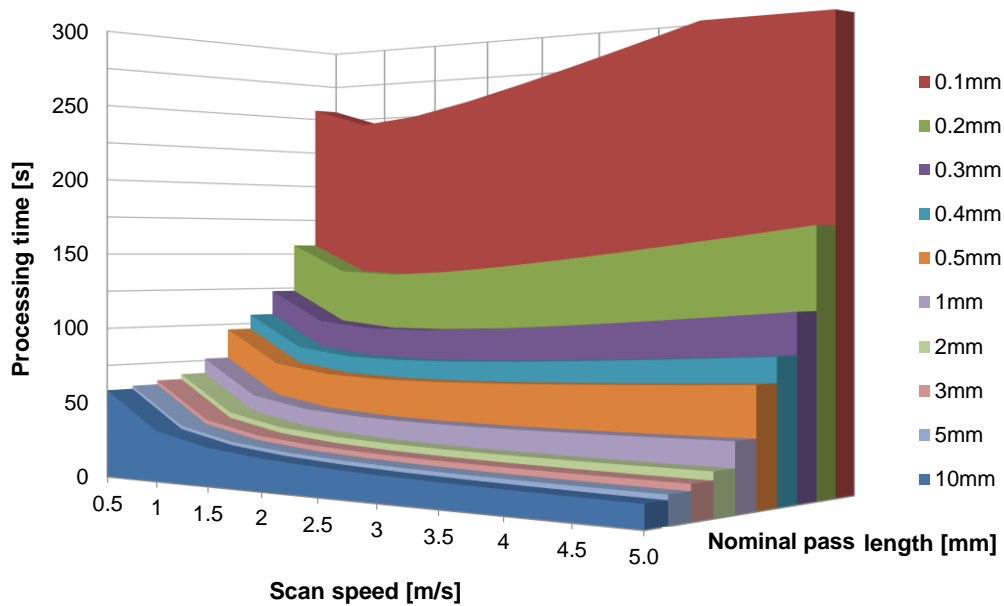


Figure 8-16: Processing time versus scan speed and nominal pass length, calculated for 1 cm² processing area and 4 μm lateral pulse spacing in width and length, the scan direction was unidirectional.

Initially it can be seen that the processing time decreased with faster scan speed. Moreover, shorter processing times are calculated for the longer path length, compared to the smaller scan passes. This is due to the smaller number of large scan lines, required to ablate 1 cm² processing area.

For laser processing of small passes, by contrast, the processing time increased with faster scan speeds, starting from about 1.5 m/s. This is caused by the longer acceleration and deceleration path lengths needed at the higher speeds. For the longer processing paths, the processing time decreases slightly.

As a result, the appropriate scan speed for micromachining using galvanometer scan systems can be suggested to be in the range between 1.5 m/s and 2.5 m/s.

However, there are indications that these technical limitations may be overcome soon. Novel laser systems with sufficient high average laser power up to 1.1 kW have already been demonstrated [143]. In addition, polygon scan technologies for ultrafast laser beam deflection with scan speeds of several hundred meters per second have been developed [144]. As such, the next engineering challenge will be to combine these technologies for effective and rapid micromachining applications.

8.6 Summary

In this chapter, machining examples were presented to demonstrate the feasibility of high-PRF femtosecond technology in micromachining. Almost melt free ablation kerfs with a depth up to 150 μm were fabricated using line-scan laser processing regime. Maximum pulse energy and repetition rates of about 100 kHz were applied for this purpose. In addition, by using a distinct arrangement of overlapping lines, trench-like structures were fabricated. Smooth surfaces and higher structure resolution were achieved with moderate fluence of 2.5 μJ and unidirectional scan regime.

Applying this technology to a practical set of challenges, three-dimensional laser micro structuring was investigated. The impact of heat accumulation on material removal was demonstrated using a step pyramid, processed in Stainless steel. With the repetition rate of 1.02 MHz an about twenty percentage greater pyramid step height was achieved, compared to laser processing using 205 kHz. Moreover, more than 40 times shorter processing times are demonstrated for high-PRF laser ablation, compared to laser machining using kHz femtosecond lasers. For this a micro-featured demonstrator structure was laser processed in Stainless steel.

In addition, the feasibility of the investigated technology in potential industrial application was proven. A micro mould demonstrator was fabricated in Aluminium and utilised to produce a functional micro-fluidic system.

The chapter concludes with a summary of technical limitations of the developed high-PRF micromachining technology. It was pointed out that inconveniences in terms of laser power and scan speed may soon be overcome by recently developed high power femtosecond lasers and ultrafast polygon scan systems.

9 Main conclusions and recommendations for future work

9.1 Conclusion of research work and summary of contribution to the body of knowledge

In this thesis laser micromachining of metals was investigated utilising a high-PRF femtosecond fibre laser, aiming to improve the scientific knowledge about the principle mechanisms in processing regime. Three industrial grade metals with different thermo-physical properties were investigated (Aluminium, Copper, Stainless steel).

In the study, the main ablation process influencing machining parameters were varied, the laser fluence, lateral pulse spacing, laser pulse energy and repetition rate. Machining results obtained were evaluated by means of the ablation depth, ablation rate, volume ablation rate, material removal efficiency, and roughness. From the results optimised laser processing parameters were determined to achieve a minimised surface roughness and high process efficiency.

For Stainless steel it was found that the ablation threshold reduced by almost 25 % when utilising pulses of high repetition rates (1.02 MHz, $H_{th} = 0.088 \text{ J/cm}^2$), compared to lower rates (20 kHz, $H_{th} = 0.11 \text{ J/cm}^2$). To explain this, enhanced laser beam absorption due to the surface temperature rise induced by heat accumulation was proposed as the primary influencing mechanism.

On Aluminium, the highest impact of the repetition rate on the ablation threshold was detected with the ablation threshold lowered by more than 50 % at high repetition rates. A thin molten Aluminium surface layer is suggested as a beam absorption enhancing mechanism. The resulting melting might be induced by heat accumulation and the low melting temperature.

By contrast, heat accumulative effects can be largely ruled out for Copper because of the high heat conductivity and the high melting point. No significant impact of the repetition rate on the ablation threshold was detected for Copper within the investigated parameter range.

From the depth of laser processed cavities, the volume ablation rate (removed volume per incident laser pulse) was assessed. The maximum volume ablation rates were $32.0 \mu\text{m}^3 / \text{pulse}$ on Aluminium, $23.8 \mu\text{m}^3 / \text{pulse}$ on Copper, and $17.3 \mu\text{m}^3 / \text{pulse}$ on Stainless steel. Subsequently, a model was designed to calculate the volume ablation rates. Good agreement between modelled and experimental values was obtained by calculations utilising the effective penetration depth instead of the optical penetration depth for laser energy transport.

From the results achieved in studying material removal, optimised laser process parameters were determined with regard to volume ablation rate, material removal efficiency and roughness as follows: Aluminium: $5.0 \mu\text{m}$ pulse spacing and $5.0 \mu\text{J}$ pulse energy, Copper: $7.5 \mu\text{m}$ pulse spacing and $7.0 \mu\text{J}$ pulse energy, and Stainless steel: $5.0 \mu\text{m}$ pulse spacing and $3.0 \mu\text{J}$ pulse energy.

The maximum material removal rates were achieved by using pulses of 1.024 MHz repetition rate as: Aluminium $0.84 \text{ mm}^3 / \text{min}$, Copper $0.79 \text{ mm}^3 / \text{min}$, and Stainless steel $0.77 \text{ mm}^3 / \text{min}$. For Aluminium and Stainless steel it was shown that material removal benefitted from heat accumulation, material removal obtained on Copper differed only marginally with higher repetition rates.

Novel insights into particle shielding processes were obtained by high speed camera imaging of the ablation plumes at different repetition rates. It was demonstrated for all three investigated materials that in time scales of one micro second after laser pulse irradiation a significant amount of ablated particles is still apparent around the processing zone. As a result it was concluded for high-PRF laser irradiation that even in ultrashort pulse laser processing particle shielding will affect laser material interaction. For Aluminium and Stainless steel, considerably brighter ablation plumes were recorded at higher repetition rates, suggesting stronger material removal which might be caused by heat accumulation effects.

Heat accumulation was also analysed by surface temperature calculations, carried out for various processing parameters. Therefore a temperature calculation model was designed, considering either the remaining energy or enhanced energy coupling as thermal heat load. However, temperature rise induced by heat accumulation was confirmed by this calculation using the minor fraction of remaining energy. A good agreement between the computed temperature values and experimental observations

were obtained by taking into account enhanced energy coupling mechanisms. By this way, a temperature rise exceeding the melting temperature was obtained for Aluminium and Stainless steel at the repetition rate of 1.02 MHz. Due to the significantly higher heat conductivity of Copper the temperature increased only slightly to 74 °C.

The formation of high-PRF laser-induced micro structures, ripples and cone-like shaped microstructures, was evaluated. Ripples formed with a spacing of about 1 µm, which correlates with the wavelength of the incident laser beam. Experimentally it was confirmed that ripple orientation depends on the polarisation of the laser beam. Furthermore it was suggested for high-PRF femtosecond laser irradiation, hydrodynamic mechanisms such as *Rayleigh-Taylor* instabilities and *Kelvin-Helmholtz* instabilities may induce micro cone formations. Structure size and period of the cones varied with the processing parameters.

Machining examples were presented to demonstrate the feasibility of the high-PRF femtosecond laser technology in micromachining. Almost melt free ablation kerfs with a depth up to 150 µm were fabricated using line-scan laser processing regime. By means of a step pyramid processed in Stainless steel, the impact of the repetition rate on the ablation depth was demonstrated. At 1.02 MHz an about twenty percentage greater pyramid step height could be achieved compared to laser processing using 205 kHz. A micro-featured demonstrator structure was processed in Stainless steel. The machining time was over 40 times shorter than laser processing using kHz femtosecond lasers.

Finally, both the restricted average laser power of the available femtosecond laser systems as well as the limited scan speed of galvanometer scan systems were identified as the main technical limitations of the introduced laser micromachining technology. It was pointed out that these inconveniences may be overcome by recently developed high power femtosecond lasers and ultrafast polygon scan systems.

The thesis contributes to the current body of knowledge by characterisation and discussion of the phenomena and interaction effects occurring in high-PRF femtosecond laser processing of metals. An improved explanation of heat accumulation has been derived from results obtained in laser irradiation of metals with different thermo-physical characteristics. In case of the low thermally conductive Stainless steel the ablation thresholds decreased with the shorter temporal distance between consecutive incident laser pulses accompanied by increasing ablation rates. The results obtained in

studying the impact of the lateral pulse spacing on the ablation rate implied that energy losses caused by particle shielding have been counterbalanced by heat accumulation. Conversely no evidence of heat accumulative effects has been detected during high-PRF laser irradiation of high thermally conductive Copper. It has been concluded from the results obtained, that heat accumulation is the likely cause of the increase of the surface temperature on low thermally conductive metals. This in turn suggests higher laser beam absorption and lower ablation thresholds. The assumed increase of the surface temperature following high-PRF laser pulses has been supported by the calculation of the surface temperatures. The surface temperature rise was calculated by using a simplified surface temperature calculation model that was designed in this thesis work. In this model either the little fraction of remaining energy or enhanced energy coupling was considered for thermal heat load.

In another approach, a model was designed to calculate the material removal per laser pulse. Initially the Gaussian energy distribution of the laser beam in lateral direction and the optical penetration depth according to *Beer's law* were taken into calculation. Good agreement between experimental and theoretical values has been obtained by utilising the effective penetration depth instead of the optical penetration depth. With these variations, a number of discrepancies identified in the literature review could be explained.

Furthermore the impact of the temporal laser pulse-to-pulse distance on the ablation plume was evaluated by ultra high speed camera imaging. Increased material ablation rates have been detected for the low thermally conductive Stainless steel, emphasising particle shielding as another dominant interaction effect. In Aluminium and Copper, particle shielding has been identified on almost negligible levels.

Another contribution to knowledge has been the study of laser induced periodical surface structures, originating in high-PRF femtosecond laser processing. Ripple structures are well known and widely investigated phenomenon, a knowledge gap exists in terms of formation of self-organising cone-like shaped structures. In this work, the origin of high-PRF laser generated cone-like shaped micro structures was related to hydrodynamic mechanisms. These mechanisms have been proposed in the literature to explain both formations of cone structures and micro columns induced by irradiation of nanosecond laser pulses.

Finally a machining strategy has been developed to utilise high-PRF femtosecond laser technology in micromachining. From this, the conditions for industrial mass production, the requirements in terms of accessory devices, i.e. beam deflection systems, but also the trend concerning future developments of the high power femtosecond laser technology can be derived.

The developed high-PRF laser machining technology was applied in micro mould fabrication, demonstrating the feasibility of high-PRF laser micromachining in industrial applications. With the results achieved, this work is intended to contribute to establishing *Laser Micromachining* as high-tech and innovative industrial technology, capable of substituting standard methods in numerous micromachining applications

9.2 Recommendations for future work

This thesis has extended the understanding of high-PRF femtosecond laser processing and has provided some insights to the potential industrial relevance. It was shown that heat accumulation and particle shielding can have a significant impact on laser material interaction. However, the investigated parameter range (pulse energy, repetition rate, average laser power) was limited in this work.

The study of high-PRF laser processing using high average power lasers with hundreds of Watts of laser power will supply complementary results. This will provide useful background information for potential developments of the ultrashort pulse laser technology. Moreover, from these results, appropriate laser systems and processing regimes may be defined for specific industrial applications.

Further this work was focussed on metal machining. A knowledge gap still exists in high-PRF laser processing of glass, ceramics, and certain hard metals. Thus there is a need to enlarge the study of high-PRF laser processing to other industry relevant materials.

From industrial point of view, throughput and processing area are on special interest. In this work, the scan field was 25 x 25 mm² that is too small for most of industrial applications. Further it was demonstrated, that processing time will not significantly

decrease in spite of higher scan speeds. For this innovative laser beam deflection technologies, i.e. polygon scan systems, may be combined with high power laser systems.

Control, reduction, or elimination of high-PRF laser induced micro structure formation may be another important goal in micromachining. In this work the appearance of cone-like shaped structures has not completely cleared up and complementary studies seems to be required. For this metallographic analysis might be beneficial to detect potentially assumed melting phases on the micro cone covered surface.

Two models were developed, a temperature model, and a material removal model. For the investigated metals Aluminium, Copper and Stainless steel, good agreements between modelled values and experimental observations were achieved. Thus the models appear applicable to study high-PRF laser processing of other materials.

Finally, a future comparative study of high-PRF laser processing using high power femtosecond and picosecond lasers would contribute to fill the existing knowledge gap in this field. The pulse duration of recent developed ultrashort pulse laser systems is adjustable in a broad range between some hundreds femtoseconds and a few tens of picoseconds.

Annex 1: Determination of reflectivity and absorptivity of laser processed metal surfaces

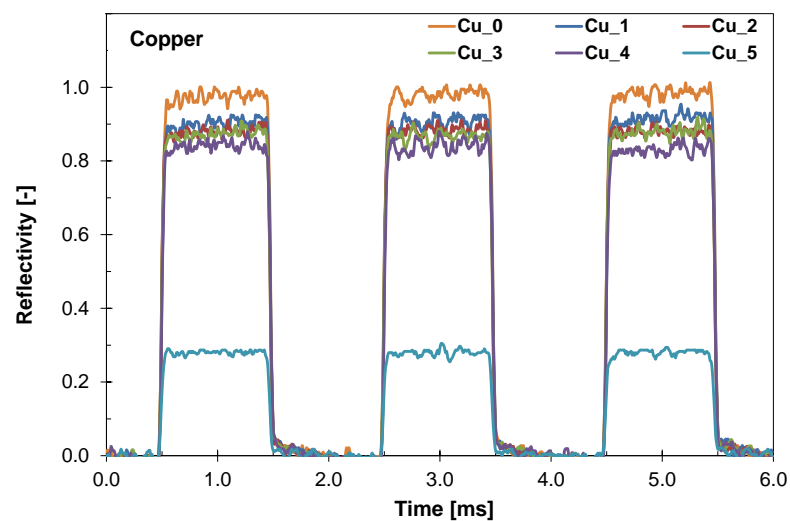
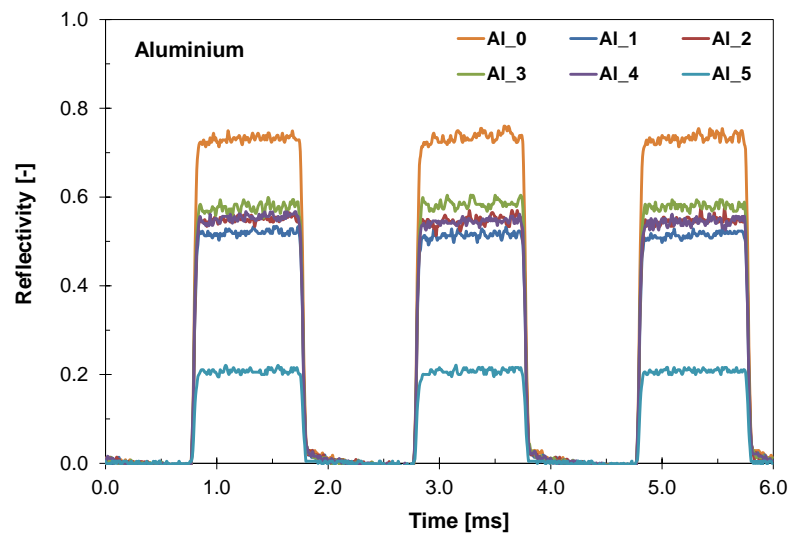
- Voltage levels averaged over nine individual measurements using the integrating sphere assembly in reflectivity measurement arrangement. The height of the voltage levels correlates to the reflectivity characteristic of untreated and laser treated Aluminium and Copper metal sheets. In addition to the averaged voltage levels, the uncertainty of the signal measurement is presented, obtained based on standard deviation calculations.

Aluminium		Al_0	Al_1	Al_2	Al_3	Al_4	Al_5
voltage level (metal sheet / laser irradiation)	U_M [mV]	10.11 ± 0.24	7.03 ± 0.17	7.44 ± 0.17	7.94 ± 0.21	7.47 ± 0.21	2.82 ± 0.13
dark signal (metal sheet)	U'_M [mV]	0.63 ± 0.20	0.36 ± 0.14	0.35 ± 0.15	0.44 ± 0.15	0.39 ± 0.15	0.14 ± 0.09
voltage level (calibration standard)	U_S [mV]	13.95 ± 0.28					
dark signal (calibration standard)	U'_S [mV]	1.00 ± 0.17					
reflectivity	R	0.72	0.51	0.54	0.57	0.54	0.21
absorptivity ($A = 1 - R$)	A	0.28	0.49	0.46	0.43	0.46	0.79

Copper		Cu_0	Cu_1	Cu_2	Cu_3	Cu_4	Cu_5
voltage level (metal sheet / laser irradiation)	U_M [mV]	11.69 ± 0.28	10.73 ± 0.27	10.41 ± 0.24	10.31 ± 0.25	9.85 ± 0.26	3.12 ± 0.14
dark signal (metal sheet)	U'_M [mV]	0.62 ± 0.23	0.49 ± 0.23	0.44 ± 0.22	0.42 ± 0.22	0.39 ± 0.21	-0.04 ± 0.16
voltage level (calibration standard)	U_S [mV]	11.96 ± 0.32					
dark signal (calibration standard)	U'_S [mV]	0.65 ± 0.24					
reflectivity	R	0.97	0.90	0.87	0.87	0.83	0.28
absorptivity ($A = 1 - R$)	A	0.03	0.10	0.13	0.13	0.17	0.72

Stainless steel		StSt_0	StSt_1	StSt_2	StSt_3	StSt_4	StSt_5
voltage level (metal sheet / laser irradiation)	U_M [mV]	7.96 ± 0.18	3.87 ± 0.11	4.12 ± 0.15	4.35 ± 0.13	3.81 ± 0.08	1.33 ± 0.09
dark signal (metal sheet)	U'_M [mV]	0.45 ± 0.15	0.20 ± 0.05	0.20 ± 0.04	0.20 ± 0.06	0.20 ± 0.03	0.07 ± 0.10
voltage level (calibration standard)	U_S [mV]	13.95 ± 0.28					
dark signal (calibration standard)	U'_S [mV]	1.00 ± 0.17					
reflectivity	R	0.57	0.28	0.30	0.32	0.28	0.10
absorptivity ($A = 1 - R$)	A	0.43	0.72	0.70	0.68	0.72	0.90

- Normalised signal curves derived from the voltage levels given above.



Annex 2: Ablation crater diameter used in ablation threshold calculations

- The ablation crater diameter represents a mean value, averaged over a series of 10 individual measurements (*).

ALUMINIUM

Pulse repetition rate f_R : 20 kHz												
Pulse energy Q_P (on target)	μJ	0.92	1.65	2.30	2.80	3.43	4.11	4.85	5.61	6.36	6.98	7.60
Fluence H_0	J/cm^2	0.34	0.61	0.85	1.04	1.27	1.53	1.80	2.08	2.36	2.59	2.82
Crater diameter D (*)	μm	8.7	14.5	17.3	19.5	21.3	22.6	24.5	25.3	26.6	28.0	28.5
Standard deviation δ_D	μm	0.5	0.4	0.8	0.6	0.2	0.4	0.6	0.1	0.3	0.5	0.3
Squared crater diameter D^2	μm^2	76.0	211.6	300.9	379.6	452.6	512.0	601.4	639.2	706.3	781.6	811.4
Standard deviation δ_{D^2}	μm^2	9.1	12.3	28.2	24.9	9.4	19.6	29.4	7.4	17.9	27.4	15.6

Pulse repetition rate f_R : 102 kHz												
Pulse energy Q_P (on target)	μJ	0.90	1.58	2.21	2.96	3.70	4.39	4.94	5.59	6.09	6.86	7.58
Fluence H_0	J/cm^2	0.33	0.59	0.82	1.10	1.37	1.63	1.83	2.07	2.26	2.55	2.81
Crater diameter D (*)	μm	11.6	16.5	19.3	21.7	24.2	25.2	26.7	27.3	28.0	28.9	30.4
Standard deviation δ_D	μm	0.3	0.7	0.5	0.2	0.3	0.3	0.5	0.5	0.6	0.4	0.4
Squared crater diameter D^2	μm^2	133.6	273.8	370.7	472.0	586.4	637.0	711.3	747.4	783.6	836.3	926.4
Standard deviation δ_{D^2}	μm^2	7.9	22.0	17.7	10.5	15.4	15.1	29.0	25.0	33.7	24.0	23.7

Pulse repetition rate f_R : 341 kHz												
Pulse energy Q_P (on target)	μJ	0.90	1.50	2.11	2.76	3.34	4.05	4.70	5.42	6.18	6.92	7.60
Fluence H_0	J/cm^2	0.33	0.56	0.78	1.03	1.24	1.50	1.75	2.01	2.29	2.57	2.82
Crater diameter D (*)	μm	13.5	18.4	20.8	24.5	25.6	26.1	27.6	28.3	29.9	30.6	31.4
Standard deviation δ_D	μm	0.8	0.3	0.4	0.3	0.2	0.5	0.3	0.4	0.5	0.4	0.3
Squared crater diameter D^2	μm^2	182.9	340.0	432.1	601.1	653.8	681.3	764.5	802.2	894.9	937.5	987.2
Standard deviation δ_{D^2}	μm^2	21.0	11.4	15.4	12.3	12.6	23.3	16.5	22.2	28.1	24.6	19.5

Pulse repetition rate f_R : 1.02 MHz												
Pulse energy Q_P (on target)	μJ	1.03	1.70	2.36	3.04	3.81	4.50	5.19	6.10	6.86	7.60	x
Fluence H_0	J/cm^2	0.38	0.63	0.87	1.13	1.41	1.67	1.93	2.26	2.55	2.82	x
Crater diameter D (*)	μm	18.3	22.4	24.8	26.1	28.2	28.9	30.0	31.0	31.8	32.5	x
Standard deviation δ_D	μm	0.4	0.4	0.4	0.4	0.2	0.3	0.5	0.5	0.6	0.3	x
Squared crater diameter D^2	μm^2	334.0	501.4	615.3	682.0	797.9	835.3	898.1	961.3	1010.3	1058.7	x
Standard deviation δ_{D^2}	μm^2	14.1	16.5	20.5	21.7	11.1	17.1	28.5	28.2	36.8	21.3	x

COPPER

Pulse repetition rate f_R : 20 kHz												
Pulse energy Q_P (on target)	μJ	1.30	1.88	2.49	3.02	3.74	4.32	4.97	5.61	6.50	7.01	7.55
Fluence H_0	J/cm^2	0.48	0.70	0.93	1.12	1.39	1.60	1.84	2.08	2.41	2.60	2.80
Crater diameter D (*)	μm	12.0	15.0	16.9	18.8	19.9	20.3	21.2	21.9	23.1	23.5	23.8
Standard deviation δ_D	μm	0.7	0.7	0.3	0.5	0.3	0.5	0.3	0.5	0.5	0.4	0.2
Squared crater diameter D^2	μm^2	144.7	225.9	285.0	354.0	395.1	411.0	448.6	477.6	532.2	549.9	567.0
Standard deviation δ_{D^2}	μm^2	17.3	21.8	9.4	18.8	12.2	19.2	12.7	21.1	21.4	19.3	11.6

Pulse repetition rate f_R : 102 kHz												
Pulse energy Q_P (on target)	μJ	1.53	2.13	2.91	3.72	4.17	4.80	5.45	6.01	6.69	7.13	7.52
Fluence H_0	J/cm^2	0.57	0.79	1.08	1.38	1.55	1.78	2.02	2.23	2.48	2.65	2.79
Crater diameter D (*)	μm	12.8	15.4	17.8	19.1	20.4	21.1	21.6	22.6	23.1	23.8	23.7
Standard deviation δ_D	μm	0.5	0.5	0.3	0.4	0.4	0.4	0.3	0.2	0.3	0.3	0.3
Squared crater diameter D^2	μm^2	164.8	237.6	316.7	365.3	416.5	444.8	466.0	511.2	533.9	567.1	562.1
Standard deviation δ_{D^2}	μm^2	12.8	15.4	11.2	13.4	15.4	15.7	13.1	11.0	12.6	13.3	12.4

Pulse repetition rate f_R : 341 kHz												
Pulse energy Q_P (on target)	μJ	1.60	2.38	2.78	3.35	3.88	4.52	4.95	5.59	6.31	6.93	7.50
Fluence H_0	J/cm^2	0.59	0.88	1.03	1.24	1.44	1.68	1.84	2.07	2.34	2.57	2.78
Crater diameter D ^(*)	μm	13.3	15.2	17.7	19.2	19.7	20.6	21.0	21.2	22.2	22.9	23.1
Standard deviation δ_D	μm	0.9	0.9	0.5	0.6	0.5	0.3	0.5	0.6	0.6	0.3	0.4
Squared crater diameter D^2	μm^2	177.2	231.5	312.4	367.0	387.5	423.5	438.9	448.8	491.9	523.7	534.9
Standard deviation δ_{D^2}	μm^2	22.3	25.6	18.7	23.3	21.0	13.6	20.3	25.8	26.5	14.2	17.6

Pulse repetition rate f_R : 1.02 MHz												
Pulse energy Q_P (on target)	μJ	1.22	1.82	2.35	2.91	3.72	4.37	5.04	5.56	6.16	6.79	7.50
Fluence H_0	J/cm^2	0.45	0.68	0.87	1.08	1.38	1.62	1.87	2.06	2.29	2.52	2.78
Crater diameter D ^(*)	μm	11.4	14.7	16.0	17.5	19.4	20.3	21.2	21.6	22.2	22.9	23.9
Standard deviation δ_D	μm	0.6	0.6	0.3	0.5	0.3	0.4	0.5	0.5	0.4	0.4	0.3
Squared crater diameter D^2	μm^2	129.3	217.4	256.2	307.3	376.2	411.9	450.8	468.1	494.9	525.4	572.5
Standard deviation δ_{D^2}	μm^2	13.6	17.6	11.0	16.5	11.5	17.4	19.0	21.2	18.4	17.8	14.0

STAINLESS STEEL

Pulse repetition rate f_R : 20 kHz												
Pulse energy Q_P (on target)	μJ	0.84	1.53	2.17	2.80	3.35	4.04	4.66	5.45	6.19	6.89	7.52
Fluence H_0	J/cm^2	0.31	0.57	0.81	1.04	1.24	1.50	1.73	2.02	2.30	2.56	2.79
Crater diameter D ^(*)	μm	18.6	23.3	25.1	26.3	27.9	28.9	29.7	30.4	31.1	31.8	32.7
Standard deviation δ_D	μm	0.5	0.2	0.7	0.4	0.5	0.4	0.8	0.4	0.3	0.4	0.5
Squared crater diameter D^2	μm^2	347.3	544.7	631.2	691.3	775.8	834.0	881.6	924.4	966.8	1014.4	1072.5
Standard deviation δ_{D^2}	μm^2	18.1	11.0	34.9	23.1	26.4	21.2	49.7	24.9	20.9	25.3	31.4

Pulse repetition rate f_R : 102 kHz												
Pulse energy Q_P (on target)	μJ	0.92	1.62	2.21	2.91	3.60	4.27	5.14	5.82	6.52	7.13	7.52
Fluence H_0	J/cm^2	0.34	0.60	0.82	1.08	1.34	1.58	1.91	2.16	2.42	2.65	2.79
Crater diameter D ^(*)	μm	19.9	22.9	25.3	26.6	28.4	29.0	30.0	30.8	31.7	32.1	32.6
Standard deviation δ_D	μm	0.5	0.4	0.3	0.4	0.4	0.5	0.5	0.5	0.4	0.8	0.6
Squared crater diameter D^2	μm^2	395.7	524.5	639.7	706.8	804.5	838.1	902.9	950.9	1002.7	1029.4	1062.6
Standard deviation δ_{D^2}	μm^2	18.5	17.1	16.5	21.9	24.0	28.1	28.5	30.4	26.7	49.1	38.4

Pulse repetition rate f_R : 341 kHz													
Pulse energy Q_P (on target)	μJ	0.95	1.58	2.01	2.62	3.20	3.88	4.62	5.24	5.82	6.45	6.94	7.52
Fluence H_0	J/cm^2	0.35	0.59	0.75	0.97	1.19	1.44	1.71	1.94	2.16	2.39	2.57	2.79
Crater diameter D ^(*)	μm	20.5	23.4	25.5	27.9	28.9	29.4	30.6	31.7	31.7	32.0	32.5	33.1
Standard deviation δ_D	μm	0.5	0.5	0.4	0.6	0.4	0.3	0.7	0.7	0.5	0.3	0.6	0.4
Squared crater diameter D^2	μm^2	420.4	546.4	647.9	777.1	834.3	865.5	939.0	1002.3	1003.8	1024.8	1058.1	1095.8
Standard deviation δ_{D^2}	μm^2	20.8	24.2	19.4	33.2	23.2	19.2	40.6	44.8	34.1	21.9	40.2	29.2

Pulse repetition rate f_R : 1.02 MHz													
Pulse energy Q_P (on target)	μJ	0.95	1.26	1.81	2.47	2.77	3.74	4.27	4.91	5.57	6.25	6.86	7.52
Fluence H_0	J/cm^2	0.35	0.47	0.67	0.92	1.03	1.39	1.58	1.82	2.07	2.32	2.55	2.79
Crater diameter D ^(*)	μm	21.3	24.1	25.8	27.2	27.9	29.9	31.1	31.1	31.7	32.3	33.4	34.2
Standard deviation δ_D	μm	0.4	0.7	0.4	0.4	0.5	0.4	1.0	0.6	0.5	0.5	0.6	1.1
Squared crater diameter D^2	μm^2	452.6	578.4	666.9	739.5	776.3	895.2	966.4	964.2	1006.7	1046.0	1116.9	1172.0
Standard deviation δ_{D^2}	μm^2	16.5	31.3	18.1	22.9	26.8	23.2	62.4	37.2	31.0	29.9	40.7	71.7

Annex 3: Ablation threshold calculation

- The data used for ablation threshold calculation are derived from **Figure 4-3**.

Metal	Repetition rate f_R [kHz]	Slope m	Y-intercept n	Threshold fluence H_{th} [J/cm ²]	Normalised Threshold related to 20kHz value [%]	Focus radius w_0 [μm]
Aluminium	20	356.87	395.27	0.33	100	13.4
	102	370.87	481.30	0.27	83	13.6
	341	377.63	565.65	0.22	68	13.7
	1,024	360.48	666.18	0.16	48	13.4
Copper	20	239.48	312.98	0.27	100	10.9
	102	257.21	299.23	0.31	115	11.3
	341	236.39	294.58	0.29	106	10.9
	1,024	238.44	302.78	0.28	104	10.9
Stainless steel	20	320.74	708.66	0.11	100	12.7
	102	321.47	707.46	0.11	101	12.7
	341	330.36	756.07	0.10	92	12.9
	1,024	326.12	792.73	0.09	80	12.8

Annex 4: Ablation rate calculation

- Ablation rates versus fluence, calculated from measured cavity depth by using **Equation 4-9**, standard deviations are presented

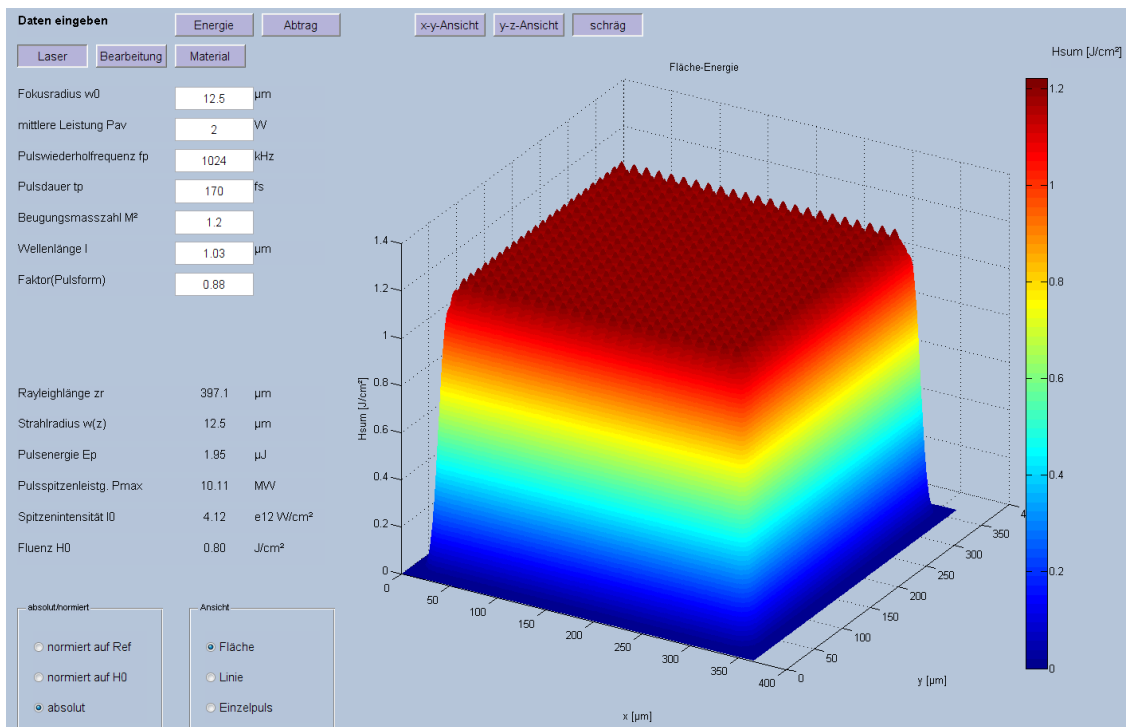
Aluminium				
Peak fluence H_0 [J/cm²]	Cavity depth l_z [μm]	Standard deviation δ_{l_z} [μm]	Ablation rate d_z [nm]	Standard deviation δ_{d_z} [nm]
0.90	2.67	0.58	3.77	0.82
1.02	4.30	0.14	6.08	0.20
1.14	4.63	0.12	6.55	0.16
1.29	5.97	0.45	8.44	0.64
1.41	7.53	0.50	10.66	0.71
1.54	9.67	0.42	13.68	0.59
1.68	11.07	0.50	15.66	0.71
1.81	11.25	0.07	15.92	0.10
1.90	12.05	0.21	17.05	0.30

Copper				
Peak fluence H_0 [J/cm²]	Cavity depth l_z [μm]	Standard deviation δ_{l_z} [μm]	Ablation rate d_z [nm]	Standard deviation δ_{d_z} [nm]
0.42	0.83	0.12	1.18	0.16
0.54	1.37	0.06	1.93	0.08
0.64	2.00	0.20	2.83	0.28
0.79	2.83	0.25	4.01	0.36
0.90	3.67	0.31	5.19	0.43
1.02	4.67	0.35	6.60	0.50
1.14	5.83	0.40	8.25	0.57
1.29	7.30	0.30	10.33	0.42
1.41	8.17	0.32	11.55	0.45
1.54	9.47	0.51	13.39	0.73
1.68	10.93	0.21	15.47	0.29
1.81	11.83	0.15	16.74	0.22
1.90	13.03	0.21	18.44	0.29

Stainless steel				
Peak fluence H_0 [J/cm ²]	Cavity depth l_z [μm]	Standard deviation δ_{l_z} [μm]	Ablation rate d_z [nm]	Standard deviation δ_{d_z} [nm]
0.19	1.27	0.12	1.79	0.16
0.27	2.57	0.15	3.63	0.22
0.36	3.53	0.12	5.00	0.16
0.46	5.20	0.28	7.36	0.40
0.57	6.63	0.15	9.38	0.22
0.70	8.17	0.25	11.55	0.36
0.83	9.73	0.21	13.77	0.29
0.94	10.73	0.40	15.18	0.57
1.06	11.93	0.49	16.88	0.70
1.20	13.03	0.32	18.44	0.45
1.31	13.93	0.59	19.71	0.83
1.43	15.43	0.64	21.83	0.91
1.54	15.87	0.46	22.45	0.65
1.67	17.13	0.57	24.24	0.80
1.81	18.13	0.32	25.65	0.45
1.90	18.77	0.38	26.55	0.54

Annex 5: Calculation program to calculate the accumulated irradiated laser fluence

- Input mask to calculate the accumulated irradiated laser fluence; laser parameter, machining parameter, and thermo-physical material properties can be varied.
- In the figure below the pulse energy is $1.95 \mu\text{J}$, the lateral pulse spacing is $12.5 \mu\text{m}$.
- The calculation program was programmed by Lutz Schneider using *Mathlab*.



Annex 6: Cavity depth and ablation rate calculation

- The cavity depths experimentally obtained for Aluminium, Copper, and Stainless steel represent mean values, each determined on three individual laser fabricated cavities.

Aluminium		Cavity depth l_z			
Pulse spacing d_x [μm]		5.0	7.5	10.0	12.5
Peak fluence H_0 [J/cm^2]	0.80	28.9	30.8	x	34.0
	1.07	29.9	30.5	29.1	30.7
	1.34	31.4	31.1	33.2	29.9
	1.61	29.4	27.0	37.8	31.5
	1.88	31.0	31.6	x	35.7
Standard deviation δ_{l_z}					
Pulse spacing d_x [μm]		5.0	7.5	10.0	12.5
Peak fluence H_0 [J/cm^2]	0.80	0.4	1.6	x	1.2
	1.07	0.4	0.6	1.2	0.9
	1.34	0.5	0.6	0.7	0.7
	1.61	0.4	0.5	1.3	1.1
	1.88	0.8	0.8	x	1.4
Number of scan passes n_s					
Pulse spacing d_x [μm]		5.0	7.5	10.0	12.5
Peak fluence H_0 [J/cm^2]	0.80	85	240	x	900
	1.07	60	140	275	400
	1.34	40	100	225	350
	1.61	30	70	175	300
	1.88	25	60	x	250
Ablation rate d_z [nm/pulse]					
Pulse spacing d_x [μm]		5.0	7.5	10.0	12.5
Peak fluence H_0 [J/cm^2]	0.80	12.0	10.2	x	8.3
	1.07	17.6	17.4	15.0	17.0
	1.34	27.8	24.7	20.9	18.9
	1.61	34.7	30.7	30.5	23.2
	1.88	44.2	42.0	x	31.6

Copper		Cavity depth l_z			
Pulse spacing d_x [μm]		5.0	7.5	10.0	12.5
Peak fluence H_0 [J/cm^2]	0.80	28.9	30.8	33.0	33.7
	1.07	30.1	30.5	29.5	30.6
	1.34	32.1	30.9	33.2	29.9
	1.61	29.6	27.1	37.3	31.5
	1.88	29.7	31.5	31.5	36.6
Standard deviation δ_{l_z}					
Pulse spacing d_x [μm]		5.0	7.5	10.0	12.5
Peak fluence H_0 [J/cm^2]	0.80	0.3	1.7	0.9	0.8
	1.07	0.5	0.5	1.2	0.8
	1.34	0.9	0.5	0.9	0.8
	1.61	0.3	0.5	1.0	0.8
	1.88	0.6	0.9	0.9	1.2
Number of scan passes n_s					
Pulse spacing d_x [μm]		5.0	7.5	10.0	12.5
Peak fluence H_0 [J/cm^2]	0.80	300	625	930	1300
	1.07	165	370	550	750
	1.34	110	250	450	600
	1.61	75	160	350	450
	1.88	55	140	240	400
Ablation rate d_z [mm/pulse]					
Pulse spacing d_x [μm]		5.0	7.5	10.0	12.5
Peak fluence H_0 [J/cm^2]	0.80	3.4	3.9	5.0	5.7
	1.07	6.4	6.6	7.6	9.0
	1.34	10.3	9.9	10.4	11.0
	1.61	14.0	13.5	15.1	15.5
	1.88	19.1	17.9	18.6	20.2

Stainless steel		Cavity depth l_z				
Pulse spacing d_x [μm]		2.5	5.0	7.5	10.0	12.5
Peak fluence H_0 [J/cm^2]	0.54	33.2	25.3	30.7	33.9	33.9
	0.80	27.5	29.4	30.7	30.7	33.5
	1.07	27.8	30.6	28.0	30.7	30.1
	1.34	30.0	29.7	29.7	31.0	31.9
Standard deviation δ_{l_z}						
Pulse spacing d_x [μm]		2.5	5.0	7.5	10.0	12.5
Peak fluence H_0 [J/cm^2]	0.54	1.1	0.4	0.7	2.2	0.5
	0.80	0.6	0.5	0.5	0.7	0.7
	1.07	0.6	0.2	0.6	0.4	0.6
	1.34	0.3	0.6	0.7	0.5	0.4
Number of scan passes n_s						
Pulse spacing d_x [μm]		2.5	5.0	7.5	10.0	12.5
Peak fluence H_0 [J/cm^2]	0.54	28	85	235	425	700
	0.80	14	65	160	300	515
	1.07	11	52	115	240	370
	1.34	11	45	105	200	330
Ablation rate d_z [nm/pulse]						
Pulse spacing d_x [μm]		2.5	5.0	7.5	10.0	12.5
Peak fluence H_0 [J/cm^2]	0.54	10.5	10.5	10.4	11.3	10.7
	0.80	17.4	16.0	15.3	14.5	14.4
	1.07	22.4	20.8	19.4	18.1	18.0
	1.34	24.1	23.3	22.5	21.9	21.4

Annex 7: Volume ablation rates

ALUMINIUM

Volume ablation rate V_{SP} [$\mu\text{m}^3/\text{pulse}$]

Peak fluence H_0 [J/cm^2]		0.54	0.80	1.07	1.34	1.61	1.88	2.14
Mechanism	depth [nm]							
Optical penetration depth	8.2	0.8	1.9	3.0	4.0	4.9	5.8	6.5
Effective penetration depth	18.4	1.8	4.3	6.7	8.9	11.0	12.9	14.7
Electron free path length	46.0	4.5	10.7	16.7	22.3	27.5	32.3	36.8
Thickness molten layer	40.0	3.9	9.3	14.5	19.4	23.9	28.1	32.0
Experiment		x	8.5	12.4	19.6	24.5	31.0	x

COPPER

Volume ablation rate V_{SP} [$\mu\text{m}^3/\text{pulse}$]

Peak fluence H_0 [J/cm^2]		0.54	0.80	1.07	1.34	1.61	1.88	2.14
Mechanism	depth [nm]							
Optical penetration depth	10.0	0.6	2.2	3.4	4.6	5.7	6.8	7.7
Effective penetration depth	18.7	1.2	4.0	6.4	8.7	10.7	12.6	14.4
Electron free path length	42.0	3.5	9.0	14.4	19.5	24.3	28.7	32.8
Experiment		x	4.0	6.4	8.8	10.9	14.3	x

STAINLESS STEEL

Volume ablation rate V_{SP} [$\mu\text{m}^3/\text{pulse}$]

Peak fluence H_0 [J/cm^2]		0.40	0.54	0.80	1.07	1.34	1.50
Mechanism	depth [nm]						
Optical penetration depth	10.0	6.1	9.0	14.0	18.3	21.9	23.9
Effective penetration depth	18.7	4.8	7.1	11.1	14.4	17.3	18.9
Experiment		x	7.5	11.3	14.7	16.5	x

Annex 8: Cavity depth depending on the repetition rate and percentage increase

Repetition rate f_R [kHz]		26	51	102	146	205	256	341	512	1,024
ALUMINIUM	Cavity depth l_Z [μm]	35.0	37.4	42.1	45.0	46.4	48.6	48.4	51.8	55.8
	Standard deviation δ_{lZ} [μm]	0.8	0.9	1.1	0.7	1.0	1.0	2.4	0.9	1.5
	Percentage increase of the cavity depth [%]	100.0	106.9	120.2	128.6	132.6	138.7	138.2	148.0	159.5
COPPER	Cavity depth l_Z [μm]	51.1	50.8	51.1	51.0	51.2	51.4	51.2	51.5	52.4
	Standard deviation δ_{lZ} [μm]	0.8	1.0	0.9	1.2	0.6	1.0	1.0	0.7	0.7
	Percentage increase of the cavity depth [%]	100.0	99.4	99.9	99.8	100.3	100.5	100.3	100.8	102.6
STAINLESS STEEL	Cavity depth l_Z [μm]	24.8	25.3	24.2	24.5	24.7	25.7	26.6	27.1	27.3
	Standard deviation δ_{lZ} [μm]	0.5	1.1	0.6	0.5	0.9	1.1	0.4	1.0	0.9
	Percentage increase of the cavity depth [%]	100.0	102.3	97.6	98.8	99.8	104.0	107.5	109.4	110.4

Annex 9: Calculation of energy losses induced by convective heat transfer and heat radiation

- Radiation losses Q_{RL} , calculated for Stainless steel according to Stephan-Boltzmann law [107]:

$$\dot{Q} = \frac{\partial Q}{\partial t} = \varepsilon \sigma A T^4$$

where ε is the emissivity, for Steel between 0.16 ... 0.77,

σ the Stephan-Boltzmann constant: $5.67 \cdot 10^{-8} \text{ Wm}^{-2}\text{K}^{-4}$,

A is the laser focus area as the surface area heat being transferred: $7.1 \cdot 10^{-10} \text{ m}^2$,

T is the temperature gradient between room temperature and melting temperature of about 1,400 K,

Δt is the time between two consecutive incident laser pulses of 20 μs at 50 kHz.

Calculation:

$$\begin{aligned} Q_{RL} &= \dot{Q} \cdot \Delta t \\ &= 0.77 \cdot 5.67 \cdot 10^{-8} \text{ Wm}^{-2}\text{K}^{-4} \cdot 7.1 \cdot 10^{-10} \text{ m}^2 \cdot (1,400 \text{ K})^4 \cdot 0.00002 \text{ s} \\ &= \mathbf{0.2 \cdot 10^{-8} \text{ J}} \end{aligned}$$

- **Calculation of convective heat transfer losses Q_{CL}**

$$Q_{CL} = \dot{Q} \cdot \Delta t = \alpha \cdot A \cdot \Delta T \cdot \Delta t$$

where α is the convective heat transfer coefficient, reported in [145] for metals ranging between $4.9 \text{ W m}^{-2}\text{K}^{-1}$ and $7.2 \text{ W m}^{-2}\text{K}^{-1}$,

A is the laser focus area as the surface area heat being transferred: $7.1 \cdot 10^{-10} \text{ m}^2$,

T is the temperature gradient between room temperature and melting temperature of about 1,400 K,

Δt is the time between two consecutive incident laser pulses of 20 μs at 50 kHz.

Calculation:

$$\begin{aligned} Q_{CL} &= \dot{Q} \cdot \Delta t \\ &= 7.2 \text{ Wm}^{-2}\text{K}^{-1} \cdot 7.1 \cdot 10^{-10} \text{ m}^2 \cdot 1,400 \text{ K} \cdot 0.00002 \text{ s} \\ &= \mathbf{1.4 \cdot 10^{-10} \text{ J}} \end{aligned}$$

Annex 10: Heat affected volume

Metal		ALUMINIUM				COPPER			STAINLESS STEEL		
Thermal diffusivity D [10^{-6} m ² /s]		64	64	64	20	115	115	115	3.9	3.9	3.9
Focus radius w ₀ [μm]		15	15	15	15	15	15	15	15	15	15
Repetition rate f _r [kHz]		51	205	1024	1024	51	205	1024	51	205	1024
Pulse number n _p / Thermal affected volume V [μm ³]	1	1166509	211051	37968	13765	2528896	424757	68184	46216	13246	4013
	2	2920714	484553	76243	25065	6504702	1015622	144106	94469	24029	6511
	3	5071781	805854	117904	36566	11441564	1724191	229338	147572	34972	8812
	4	7545181	1166509	162619	48406	17157523	2528896	322515	204942	46216	11028
	5	10297426	1561424	210094	60609	23546791	3416957	422728	266139	57792	13203
	6	13298985	1987075	260098	73174	30537813	4379661	529302	330825	69698	15359
	7	16528131	2440851	312453	86092	38077964	5410580	641736	398732	81926	17504
	8	19968043	2920714	367004	99348	46126428	6504702	759626	469650	94469	19647
	9	23605062	3425015	423627	112935	54650317	7657957	882646	543406	107315	21793
	10	27427995	3952377	482220	126838	63622455	8867027	1010513	619852	120454	23945
	11	31427300	4501636	542687	141047	73019845	10129045	1142993	698858	133876	26104
	12	35594739	5071781	604951	155553	82822696	11441564	1279885	780315	147572	28272
	13	39923268	5661946	668937	170347	93013701	12802467	1420997	864120	161533	30451
	14	44406483	6271349	734593	185419	103577716	14209844	1566189	950194	175754	32640
	15	49038798	6899299	801849	200760	114501105	15662042	1715301	1038457	190226	34842
	16	53815197	7545181	870664	216367	125771714	17157523	1868211	1128834	204942	37056
	17	58731077	8208424	940990	232230	137378539	18694919	2024805	1221270	219899	39282
	18	63782311	8888529	1012779	248344	149311605	20273023	2184978	1315695	235088	41520
	19	68965088	9585006	1085997	264703	161561603	21890656	2348620	1412059	250501	43773
	20	74275863	10297426	1160605	281303	174120118	23546791	2515651	1510315	266139	46038
	21	79711474	11025390	1236566	298136	186979410	25240426	2685984	1610416	281965	48316
	22	85268846	11768532	1313860	315197	200132166	26970691	2859547	1712322	298903	50608
	23	90945220	12526515	1392444	332483	213571670	28736757	3036254	1815985	313430	52912
	24	96737924	13298985	1472300	349993	227291675	30537813	3216054	1921379	330825	55231
	25	102644628	14085667	1553404	367715	241286149	32373103	3398871	2028453	347507	57562
	26	108662977	14886268	1635728	385653	255549725	34242021	3584651	2137186	364387	59907
	27	114790763	15700511	1719241	403799	270076979	36143829	3773337	2245747	381463	62264
	28	121025947	16528131	1803935	422149	284863180	38077964	3964872	2359504	398732	64635
	29	127366695	17368932	1889782	440704	299903472	40043794	4159203	2473028	416187	67017
	30	133811058	18222651	1976768	459455	315193667	42040866	4356292	2588091	433826	69414
	31	140357399	19089093	2064866	478403	330729272	44068528	4556092	2704667	451467	71824
	32	147003956	19968043	2154065	497546	346506661	46126428	4758557	2822739	469650	74245
	33	153749184	20859274	2244339	516881	362521737	48213959	4963645	2942273	487831	76681
	34	160591623	21762647	2335690	536400	378770919	50330734	5171314	3063268	506187	79127
	35	167529801	22677979	2428091	556104	395250772	52476312	5381537	3185669	524712	81588
	36	174562399	23605062	2521518	575992	411958058	54650317	5594251	3309488	543406	84059
	37	181687978	24543758	2615975	596060	428889535	56852293	5809462	3434694	562274	86545
	38	188905422	25493935	2711437	616311	446042234	59081895	6027105	3561267	581302	89042
	39	196213398	26455577	2807902	636734	463413029	61338704	6247162	3689188	600499	91551
	40	203610713	27427995	2905346	657330	480999328	63622455	6469586	3818440	619852	94072
	41	211096404	28411612	3003757	678097	498798237	65932752	6694377	3949006	639370	96606
	42	218669269	29406124	3103121	699038	516807234	68269312	6921474	4080880	659044	99151
	43	226528239	30411398	3203449	720142	535023897	70631763	7150880	4214034	678874	101708
	44	234072481	31427300	3304707	741416	553445628	73019845	7382551	4348465	698858	104278
	45	241900815	32453680	3406885	762852	572070034	75433259	7616446	4484148	718999	106858
	46	249812374	33490478	3509982	784456	590895097	77871715	7852586	4621064	739284	109451
	47	257806227	34537512	3613989	806214	609918599	80334934	8098099	4759229	759729	112054
	48	265881575	35594739	3718895	828135	629138226	82822696	8331391	4898601	780315	114670
	49	274037555	36662051	3824680	850217	648552041	85334689	8574025	5039168	801053	117297
	50	282273213	37739266	3931358	872449	668158024	87870658	8818774	5180930	821931	119934
	51	290587953	38826399	4038895	894838	687954217	90430407	9065657	5323874	842952	122584
	52	298980862	39923268	4147294	917379	707938853	93013701	9314595	5467991	864120	125244
	53	307451075	41029783	4256548	940076	728109952	95620307	9565622	5613266	885433	127916
	54	315998169	42145883	4366648	962920	748465852	98249940	9818665	5759689	906884	130960
	55	324621187	43271480	4477599	985918	769004813	100902502	10073759	5907236	928472	133292
	56	333319434	44406483	4589367	1009060	789725318	103577716	10330846	6055909	950194	135997
	57	342092319	45550765	4701958	1032353	810625354	106275312	10589928	6205713	972062	138712
	58	350939304	46704330	4815363	1055788	831703857	108995282	10850987	6356608	994057	141439
	59	359859501	47867046	4929575	1079365	852958886	111737235	11114005	6505899	1016188	144177
	60	368852386	49038798	5044602	1103088	874388929	114501105	11378946	6661693	1038457	146924
	61	377917334	50219589	5160421	1126956	895992844	117286642	11645812	6815848	1060854	149682
	62	387053879	51409302	5277015	1150961	917768823	120093729	11914587	6971088	1083386	152451
	63	396261295	52607862	5394402	1175103	939715817	122922122	12185256	7127370	1106044	155230
	64	405539138	53815197	5512577	1199393	961832254	125771714	12457802	7284719	1128834	158019
	65	414886718	55031281	5631506	1223811	984116789	128642336	12732212	7443110	1151755	160818
	66	424303609	56255999	5751210	1248375	1006568290	131533754	13008470	7602535	1174800	163628
	67	433789158	57489289	5871669	1273070	1029185280	134445873	13286562	7762985	1197968	166448
	68	443342957	58731077	5992878	1297897	1051966690	137378539	13566473	7924470	1221270	169279
	69	452964500	59981350	6114830	1322860	1074911290	140331595	13848190	8086947	1244686	172121
	70	462653287	61240046	6237535	1347958	1098017670	143304891	14131699	8250445	1268235	174970
	71	472408825	62507052	6360972	1373184	1121285070	146298276	14417009	8414936	1291903	177830
	72	482230635	63782311	6485153	1398544	1144712120	149311605	14704064	8580433	1315695	180701
	73	492118246	65065810	6610054	1424037	1168297500	152344667	14992871	8746909	1339604	183581
	74	502071196	66357494	6735673	1449654	1192040500	155397470	15283443	8914359	1363636	186472
	75	512089178	67657255	6862018	1475403	1215939840	158469799	15575744	9082777	1387790	189373
	76	522171466	68965088	6989070	1501274	1239994670	161561603	15869761	9252152	1412059	192281
	77	532317911	70280884	7116824	1527274	1264203720	164672595	16165484	9422499	1436448	195200
	78	542528094	71604701	7245290	1553404	1288565990	167802800	16462900	9593813	1460956	198131
	79	552801444	72936376	7374449	1579660	1313080690	170952015	16762023	9766065	1485577	201070
	80	563137566	74275863	7504311	1606037	1337746840	174120118	17062816	9939252	1510315	204018
	81	573536191	75623210	7634856	1632539	1362563250	177307065	17365271	10113368	1535172	206973
	82	583996788	76978269	7766080	1659159	1387529210	180512661	17669375	10288423	1560137	209942
	83	594519114	78341039	7897994	1685911	1412643770	183736787	17975144	10464394	1585219	212917
	84	605102795	79711474	8030596	1712780	1437905810	186979410	18282542	10641295	1610416	215904
	85	615747303	81089474	8163863	1739764	1463314910	190240334	18591559	10819101	1635728	218898
	86	626452427	82475104	8297790	1766878	1488869920	193519536	18902211	10997824	1661146	221902
	87	637217812	83868204	8432393	1794106	1514569780	196816819	19214461	11177442	1686678	224916
	88	648043103	85268846	8567667	1821455	1540410900	200132166				

Annex 11: Surface temperature calculated considering the remaining energy

Metal		ALUMINIUM			COPPER			STAINLESS STEEL		
Remaining energy Q_{rem} [μ J]		1.50	1.25	0.91	0.45	0.45	0.45	0.97	0.95	0.82
Repetition rate f_R [kHz]		51	205	1024	51	205	1024	51	205	1024
Pulse number n_p / Surface temperature T_{surf} [°C]	0	20.0	20.0	20.0	20.0	20.0	20.0	20.0	20.0	20.0
	1	20.5	22.3	29.4	20.1	20.3	21.9	25.6	39.2	74.8
	2	20.7	23.3	34.1	20.1	20.4	22.8	28.4	49.8	108.6
	3	20.8	23.9	37.2	20.1	20.5	23.4	30.1	57.1	133.5
	4	20.9	24.4	39.4	20.1	20.6	23.8	31.4	62.6	153.5
	5	21.0	24.7	41.1	20.1	20.6	24.1	32.4	67.0	170.1
	6	21.0	24.9	42.5	20.1	20.6	24.3	33.2	70.7	184.4
	7	21.0	25.1	43.6	20.1	20.6	24.5	33.8	73.8	197.0
	8	21.1	25.3	44.6	20.1	20.7	24.7	34.4	76.5	208.2
	9	21.1	25.4	45.4	20.1	20.7	24.8	34.9	78.9	218.3
	10	21.1	25.5	46.2	20.1	20.7	24.9	35.3	81.0	227.5
	11	21.1	25.7	46.8	20.1	20.7	25.1	35.7	82.9	235.9
	12	21.1	25.8	47.4	20.1	20.7	25.2	36.0	84.6	243.7
	13	21.2	25.8	48.0	20.1	20.7	25.3	36.3	86.2	250.9
	14	21.2	25.9	48.5	20.1	20.7	25.3	36.6	87.7	257.6
	15	21.2	26.0	48.9	20.1	20.8	25.4	36.8	89.0	263.9
	16	21.2	26.1	49.3	20.1	20.8	25.5	37.0	90.2	269.9
	17	21.2	26.1	49.7	20.1	20.8	25.5	37.3	91.4	275.5
	18	21.2	26.2	50.1	20.1	20.8	25.6	37.5	92.5	280.8
	19	21.2	26.2	50.4	20.1	20.8	25.7	37.6	93.5	285.8
	20	21.2	26.3	50.7	20.1	20.8	25.7	37.8	94.4	290.6
	21	21.2	26.3	51.0	20.1	20.8	25.8	38.0	95.4	295.1
	22	21.2	26.3	51.3	20.1	20.8	25.8	38.1	96.2	299.5
	23	21.3	26.4	51.5	20.1	20.8	25.8	38.3	97.0	303.6
	24	21.3	26.4	51.8	20.1	20.8	25.9	38.4	97.8	307.6
	25	21.3	26.5	52.0	20.1	20.8	25.9	38.5	98.5	311.4
	26	21.3	26.5	52.2	20.1	20.8	26.0	38.7	99.2	315.1
	27	21.3	26.5	52.4	20.1	20.8	26.0	38.8	99.9	318.6
	28	21.3	26.6	52.6	20.1	20.8	26.0	38.9	100.5	322.0
	29	21.3	26.6	52.8	20.1	20.8	26.1	39.0	101.1	325.3
	30	21.3	26.6	53.0	20.1	20.8	26.1	39.1	101.7	328.5
	31	21.3	26.6	53.2	20.1	20.8	26.1	39.2	102.3	331.6
	32	21.3	26.7	53.3	20.1	20.8	26.1	39.3	102.8	334.5
	33	21.3	26.7	53.5	20.1	20.8	26.2	39.4	103.4	337.4
	34	21.3	26.7	53.6	20.1	20.8	26.2	39.4	103.9	340.2
	35	21.3	26.7	53.8	20.1	20.8	26.2	39.5	104.3	342.9
	36	21.3	26.7	53.9	20.1	20.8	26.2	39.6	104.8	345.5
	37	21.3	26.8	54.1	20.1	20.8	26.3	39.7	105.3	348.0
	38	21.3	26.8	54.2	20.1	20.8	26.3	39.8	105.7	350.5
	39	21.3	26.8	54.3	20.1	20.8	26.3	39.8	106.1	352.9
	40	21.3	26.8	54.4	20.1	20.8	26.3	39.9	106.5	355.2
	41	21.3	26.8	54.6	20.1	20.8	26.3	40.0	106.9	357.5
	42	21.3	26.9	54.7	20.1	20.9	26.4	40.0	107.3	359.7
	43	21.3	26.9	54.8	20.1	20.9	26.4	40.1	107.7	361.9
	44	21.3	26.9	54.9	20.1	20.9	26.4	40.1	108.1	364.0
	45	21.3	26.9	55.0	20.1	20.9	26.4	40.2	108.4	366.0
	46	21.3	26.9	55.1	20.1	20.9	26.4	40.3	108.8	368.1
	47	21.3	26.9	55.2	20.1	20.9	26.4	40.3	109.1	370.0
	48	21.3	26.9	55.3	20.1	20.9	26.5	40.4	109.4	371.9
	49	21.3	27.0	55.4	20.1	20.9	26.5	40.4	109.7	373.8
	50	21.3	27.0	55.5	20.1	20.9	26.5	40.5	110.1	375.6
	51	21.4	27.0	55.6	20.1	20.9	26.5	40.5	110.4	377.4
	52	21.4	27.0	55.7	20.1	20.9	26.5	40.6	110.7	379.2
	53	21.4	27.0	55.8	20.1	20.9	26.5	40.6	110.9	380.9
	54	21.4	27.0	55.8	20.1	20.9	26.5	40.7	111.2	382.6
	55	21.4	27.0	55.9	20.1	20.9	26.6	40.7	111.5	384.2
	56	21.4	27.0	56.0	20.1	20.9	26.6	40.7	111.8	385.9
	57	21.4	27.1	56.1	20.1	20.9	26.6	40.8	112.0	387.4
	58	21.4	27.1	56.1	20.1	20.9	26.6	40.8	112.3	389.0
	59	21.4	27.1	56.2	20.1	20.9	26.6	40.9	112.5	390.5
	60	21.4	27.1	56.3	20.1	20.9	26.6	40.9	112.8	392.0
	61	21.4	27.1	56.4	20.1	20.9	26.6	40.9	113.0	393.5
	62	21.4	27.1	56.4	20.1	20.9	26.6	41.0	113.3	394.9
	63	21.4	27.1	56.5	20.1	20.9	26.7	41.0	113.5	396.4
	64	21.4	27.1	56.6	20.1	20.9	26.7	41.1	113.7	397.7
	65	21.4	27.1	56.6	20.1	20.9	26.7	41.1	113.9	399.1
	66	21.4	27.1	56.7	20.1	20.9	26.7	41.1	114.1	400.5
	67	21.4	27.1	56.7	20.1	20.9	26.7	41.2	114.4	401.8
	68	21.4	27.2	56.8	20.1	20.9	26.7	41.2	114.6	403.1
	69	21.4	27.2	56.9	20.1	20.9	26.7	41.2	114.8	404.4
	70	21.4	27.2	56.9	20.1	20.9	26.7	41.3	115.0	405.6
	71	21.4	27.2	57.0	20.1	20.9	26.7	41.3	115.2	406.8
	72	21.4	27.2	57.0	20.1	20.9	26.7	41.3	115.4	408.1
	73	21.4	27.2	57.1	20.1	20.9	26.7	41.3	115.6	409.3
	74	21.4	27.2	57.1	20.1	20.9	26.8	41.4	115.7	410.4
	75	21.4	27.2	57.2	20.1	20.9	26.8	41.4	115.9	411.6
	76	21.4	27.2	57.2	20.1	20.9	26.8	41.4	116.1	412.7
	77	21.4	27.2	57.3	20.1	20.9	26.8	41.5	116.3	413.9
	78	21.4	27.2	57.3	20.1	20.9	26.8	41.5	116.5	415.0
	79	21.4	27.2	57.4	20.1	20.9	26.8	41.5	116.6	416.1
	80	21.4	27.2	57.4	20.1	20.9	26.8	41.5	116.8	417.2
	81	21.4	27.3	57.5	20.1	20.9	26.8	41.6	117.0	418.2
	82	21.4	27.3	57.5	20.1	20.9	26.8	41.6	117.1	419.3
	83	21.4	27.3	57.6	20.1	20.9	26.8	41.6	117.3	420.3
	84	21.4	27.3	57.6	20.1	20.9	26.8	41.6	117.4	421.3
	85	21.4	27.3	57.7	20.1	20.9	26.8	41.7	117.6	422.3
	86	21.4	27.3	57.7	20.1	20.9	26.8	41.7	117.8	423.3
	87	21.4	27.3	57.7	20.1	20.9	26.9	41.7	117.9	424.3
	88	21.4	27.3	57.8	20.1	20.9	26.9	41.7	118.1	425.3
	89	21.4	27.3	57.8	20.1	20.9	26.9	41.8	118.2	426.2
	90	21.4	27.3	57.9	20.1	20.9	26.9	41.8	118.3	427.1
	91	21.4	27.3	57.9	20.1	20.9	26.9	41.8	118.5	428.1
	92	21.4	27.3	58.0	20.1	20.9	26.9	41.8	118.6	429.0
	93	21.4	27.3	58.0	20.1	20.9	26.9	41.8	118.8	429.9
	94	21.4	27.3	58.0	20.1	20.9	26.9	41.9	118.9	430.8
	95	21.4	27.3	58.1	20.1	20.9	26.9	41.9	119.0	431.7
	96	21.4	27.3	58.1	20.1	20.9	26.9	41.9	119.2	432.5
	97	21.4	27.3	58.1	20.1	20.9	26.9	41.9	119.3	433.4
	98	21.4	27.3	58.2	20.1	20.9	26.9	41.9	119.4	434.3
	99	21.4	27.3	58.2	20.1	20.9	26.9	42.0	119.6	435.1
100	21.4	27.4	58.2	20.1	20.9	26.9	42.0	119.7	435.9	

Annex 12: Surface temperature calculated considering enhanced energy coupling

Metal		ALUMINIUM					COPPER	STAINLESS STEEL				
Pulse energy Q _p [μJ]		3.00	4.00	5.00	6.00	7.00	7.00	2.00	3.74	4.27	5.00	
Residual energy coefficient k		0.80	0.80	0.80	0.80	0.80	0.50	0.70	0.70	0.70	0.70	
Thermal energy deposition Q [μJ]		2.40	3.20	4.00	4.80	5.60	3.50	1.40	2.62	2.99	3.50	
Pulse number n _p / Surface temperature T _{surf} [°C]	0	20.0	20.0	20.0	20.0	20.0	20.0	20.0	20.0	20.0	20.0	
	1	88.3	111.1	133.9	156.7	179.4	34.8	113.6	194.4	219.8	253.9	
	2	125.9	161.2	196.4	231.7	267.0	41.7	171.2	301.9	342.9	398.1	
	3	151.6	195.4	239.3	283.2	327.0	46.1	213.8	381.4	433.8	504.6	
	4	171.0	221.4	271.7	322.0	372.4	49.3	247.9	444.8	506.5	589.7	
	5	186.5	242.1	297.6	353.1	408.6	51.6	276.3	497.8	567.2	660.8	
	6	199.4	259.2	319.0	378.8	438.6	53.5	300.8	543.4	619.4	721.9	
	7	210.5	273.8	337.2	400.6	464.1	55.1	322.2	583.4	665.2	785.5	
	8	219.8	286.4	353.0	419.6	486.2	56.4	341.3	619.0	706.0	833.3	
	9	228.1	297.5	366.9	436.2	505.6	57.6	358.5	651.1	742.8	866.4	
	10	235.5	307.4	379.2	451.1	522.9	58.6	374.2	680.4	776.3	905.6	
	11	242.2	316.3	390.3	464.4	538.5	59.4	388.6	707.2	807.0	941.5	
	12	248.2	324.3	400.4	476.5	552.6	60.2	401.9	732.0	835.3	974.7	
	13	253.8	331.7	409.6	487.5	565.5	60.9	414.2	754.9	861.7	1005.6	
	14	258.8	338.5	418.1	497.7	577.3	61.6	425.7	776.4	886.2	1034.3	
	15	263.5	344.7	425.9	507.1	588.2	62.2	436.5	796.5	909.2	1061.2	
	16	267.9	350.5	433.1	515.8	598.4	62.7	446.6	815.4	930.9	1086.6	
	17	271.9	355.9	439.9	523.9	607.8	63.2	456.2	833.2	951.3	1110.5	
	18	275.7	361.0	446.2	531.4	616.7	63.7	465.2	850.0	970.6	1133.1	
	19	279.3	365.7	452.1	538.5	625.0	64.1	473.8	866.0	988.9	1154.5	
	20	282.6	370.1	457.7	545.2	632.8	64.5	482.0	881.2	1006.3	1174.9	
	21	285.8	374.4	462.9	551.5	640.1	64.9	489.7	895.7	1022.9	1194.3	
	22	288.7	378.3	467.9	557.5	647.1	65.2	497.2	909.6	1038.7	1212.9	
	23	291.6	382.1	472.6	563.2	653.7	65.6	504.2	922.8	1053.3	1230.6	
	24	294.3	385.7	477.1	568.5	660.0	65.9	511.0	935.5	1068.4	1247.6	
	25	296.8	389.1	481.4	573.6	665.9	66.2	517.6	947.6	1082.3	1263.9	
	26	299.3	392.4	485.4	578.5	671.6	66.4	523.8	959.3	1095.7	1279.6	
	27	301.6	395.5	489.3	583.2	677.1	66.7	529.9	970.5	1108.6	1294.7	
	28	303.8	398.4	493.0	587.6	682.2	67.0	535.7	981.4	1121.0	1309.2	
	29	306.0	401.3	496.6	591.9	687.2	67.2	541.3	991.8	1132.9	1323.2	
	30	308.0	404.0	500.0	596.0	692.0	67.4	546.7	1001.9	1144.5	1336.7	
	31	310.0	406.6	503.3	599.9	696.6	67.7	551.9	1011.6	1155.6	1349.8	
	32	311.9	409.1	506.4	603.7	701.0	67.9	557.0	1021.1	1166.4	1362.4	
	33	313.7	411.6	509.5	607.4	705.3	68.1	561.9	1030.2	1176.9	1374.7	
	34	315.4	413.9	512.4	610.9	709.3	68.3	566.6	1039.0	1187.0	1386.5	
	35	317.1	416.2	515.2	614.2	713.3	68.5	571.2	1047.6	1196.8	1398.0	
	36	318.8	418.3	517.9	617.5	717.1	68.6	575.7	1055.9	1206.4	1409.2	
	37	320.3	420.4	520.6	620.7	720.8	68.8	580.0	1064.0	1215.6	1420.1	
	38	321.9	422.5	523.1	623.7	724.3	69.0	584.2	1071.9	1224.6	1430.6	
	39	323.3	424.5	525.6	626.7	727.8	69.1	588.3	1079.5	1233.4	1440.8	
	40	324.8	426.4	527.9	629.5	731.1	69.3	592.3	1087.0	1241.9	1450.8	
	41	326.2	428.2	530.3	632.3	734.4	69.4	596.2	1094.2	1250.2	1460.5	
	42	327.5	430.0	532.5	635.0	737.5	69.6	600.0	1101.3	1258.3	1470.0	
	43	328.8	431.7	534.7	637.6	740.6	69.7	603.7	1108.2	1266.2	1479.2	
	44	330.1	433.4	536.8	640.2	743.5	69.9	607.3	1114.9	1273.9	1488.2	
	45	331.3	435.1	538.9	642.6	746.4	70.0	610.8	1121.4	1281.4	1497.0	
	46	332.5	436.7	540.8	645.0	749.2	70.1	614.2	1127.8	1288.7	1505.6	
	47	333.7	438.2	542.8	647.4	751.9	70.2	617.6	1134.1	1295.9	1514.0	
	48	334.8	439.7	544.7	649.6	754.6	70.4	620.9	1140.2	1302.8	1522.2	
	49	335.9	441.2	546.5	651.8	757.1	70.5	624.1	1146.1	1309.7	1530.2	
	50	337.0	442.7	548.3	654.0	759.7	70.6	627.2	1152.0	1316.4	1538.0	
	51	338.0	444.1	550.1	656.1	762.1	70.7	630.3	1157.7	1322.9	1545.6	
	52	339.1	445.4	551.8	658.1	764.5	70.8	633.3	1163.3	1329.3	1553.1	
	53	340.1	446.8	553.5	660.1	766.8	70.9	636.2	1168.8	1335.6	1560.5	
	54	341.1	448.1	555.1	662.1	769.1	71.0	639.1	1174.1	1341.7	1567.7	
	55	342.0	449.3	556.7	664.0	771.3	71.1	641.9	1179.4	1347.7	1574.7	
	56	342.9	450.6	558.2	665.9	773.5	71.2	644.6	1184.5	1353.6	1581.6	
	57	343.8	451.8	559.7	667.7	775.6	71.3	647.3	1189.6	1359.4	1588.4	
	58	344.7	453.0	561.2	669.5	777.7	71.4	650.0	1194.5	1365.1	1595.0	
	59	345.6	454.1	562.7	671.2	779.8	71.5	652.6	1199.4	1370.6	1601.5	
	60	346.5	455.3	564.1	672.9	781.7	71.6	655.2	1204.1	1376.1	1607.9	
	61	347.3	456.4	565.5	674.6	783.7	71.7	657.7	1208.8	1381.4	1614.2	
	62	348.1	457.5	566.9	676.2	785.6	71.8	660.1	1213.4	1386.7	1620.3	
	63	348.9	458.6	568.2	677.8	787.5	71.8	662.6	1217.9	1391.9	1626.4	
	64	349.7	459.6	569.5	679.4	789.3	71.9	664.9	1222.3	1396.9	1632.3	
	65	350.5	460.6	570.8	680.9	791.1	72.0	667.3	1226.7	1401.9	1638.2	
	66	351.2	461.6	572.0	682.4	792.9	72.1	669.6	1231.0	1406.8	1643.9	
	67	352.0	462.6	573.3	683.9	794.6	72.2	671.8	1235.2	1411.6	1649.5	
	68	352.7	463.6	574.5	685.4	796.3	72.2	674.0	1239.3	1416.4	1655.1	
	69	353.4	464.5	575.7	686.8	797.9	72.3	676.2	1243.4	1421.0	1660.5	
	70	354.1	465.5	576.8	688.2	799.6	72.4	678.4	1247.4	1425.6	1665.9	
	71	354.8	466.4	578.0	689.6	801.2	72.4	680.5	1251.3	1430.1	1671.2	
	72	355.5	467.3	579.1	690.9	802.7	72.5	682.5	1255.2	1434.5	1676.4	
	73	356.1	468.1	580.2	692.2	804.3	72.6	684.6	1259.0	1438.9	1681.5	
	74	356.8	469.0	581.3	693.5	805.8	72.6	686.6	1262.7	1443.2	1686.5	
	75	357.4	469.9	582.3	694.8	807.3	72.7	688.6	1266.4	1447.4	1691.5	
	76	358.0	470.7	583.4	696.1	808.7	72.8	690.5	1270.1	1451.6	1696.4	
	77	358.6	471.5	584.4	697.3	810.2	72.8	692.5	1273.7	1455.7	1701.2	
	78	359.2	472.3	585.4	698.5	811.6	72.9	694.4	1277.2	1459.8	1705.9	
	79	359.8	473.1	586.4	699.7	813.0	73.0	696.2	1280.7	1463.7	1710.6	
	80	360.4	473.9	587.4	700.9	814.3	73.0	698.1	1284.1	1467.7	1715.2	
	81	361.0	474.7	588.3	702.0	815.7	73.1	699.9	1287.5	1471.5	1719.7	
	82	361.6	475.4	589.3	703.1	817.0	73.1	701.7	1290.8	1475.4	1724.2	
	83	362.1	476.2	590.2	704.3	818.3	73.2	703.4	1294.1	1479.1	1728.6	
	84	362.7	476.9	591.1	705.4	819.6	73.2	705.2	1297.4	1482.8	1732.9	
	85	363.2	477.6	592.0	706.4	820.8	73.3	706.9	1300.6	1486.5	1737.2	
	86	363.8	478.3	592.9	707.5	822.1	73.3	708.6	1303.7	1490.1	1741.5	
	87	364.3	479.0	593.8	708.6	823.3	73.4	710.2	1306.8	1493.7	1745.6	
	88	364.8	479.7	594.7	709.6	824.5	73.5	711.9	1309.9	1497.2	1749.7	
	89	365.3	480.4	595.5	710.6	825.7	73.5	713.5	1312.9	1500.7	1753.8	
	90	365.8	481.1	596.3	711.6	826.9	73.6	715.1	1315.9	1504.1	1757.8	
	91	366.3	481.7	597.2	712.6	828.0	73.6	716.7	1318.9	1507.5	1761.8	
	92	366.8	482.4	598.0	713.6	829.2	73.7	718.3	1321.8	1510.8	1765.7	
	93	367.3	483.0	598.8	714.5	830.3	73.7	719.8	1324.7	1514.1	1769.5	
	94	367.7	483.6	599.6	715.5	831.4	73.7	721.3	1327.5	1517.4	1773.4	
	95	368.2	484.3	600.3	716.4	832.5	73.8	722.8	1330.3	1520.6	1777.1	
	96	368.7	484.9	601.1	717.3	833.5	73.8	724.3	1333.1	1523.8	1780.8	
	97	369.1	485.5	601.9	718.2	834.6	73.9	725.8	1335.8	1526.9	1784.5	
	98	369.6	486.1	602.6	719.1	835.6	73.9	727.3	1338.5	1530.0	1788.1	
	99	370.0	486.7	603.3	720.0	836.7	74.0	728.7	1341.2	1533.1	1791.7	
100	370.4	487.3	604.1	720.9	837.7	74.0	730.1	1343.8	1536.1	1795.3		

Annex 13: Energy balance calculation

- Ablation volume, experimentally obtained with 5 μJ pulse energy:

$$V (5 \mu\text{J}, 1.34 \text{ J/cm}^2) = 17.3 \mu\text{m}^3 \text{ (see Annex 7)}$$

- Mass calculation for 17.3 μm^3 Stainless steel

$$m (17.3 \mu\text{m}^3) = \rho \cdot V = 7,900 \frac{\text{kg}}{\text{m}^3} \cdot 17.3 \cdot 10^{-18} \text{ m}^3 = 1.37 \cdot 10^{-13} \text{ kg}$$

- Calculation of evaporation energy Q_{vap} to evaporate $1.37 \cdot 10^{-13}$ kg Stainless steel

with

- the specific heat capacity: $c_p = 472 \text{ J/(kg K)}$, given in [108] for Stainless steel,
- the latent heat of fusion: $L_{\text{melt}} = 272.1 \text{ kJ/kg}$, given in [108] for *St 37*, and
- the latent heat of evaporation: $L_{\text{vap}} = 6,364 \text{ kJ/kg}$, given in [108] for *St 37*.

$$\begin{aligned} Q_{\text{vap}} &= m \cdot c_p \cdot (T_{\text{vap}} - T_{\text{melt}}) + m \cdot L_{\text{melt}} + m \cdot L_{\text{vap}} \\ &= 1.37 \cdot 10^{-13} \text{ kg} \cdot 0.472 \frac{\text{kJ}}{\text{kg K}} \cdot (3,217 \text{ K} - 1,672 \text{ K}) \\ &\quad + 1.37 \cdot 10^{-13} \text{ kg} \cdot 272.1 \frac{\text{kJ}}{\text{kg}} \\ &\quad + 1.37 \cdot 10^{-13} \text{ kg} \cdot 6,364 \frac{\text{J}}{\text{kg}} \\ &= 1.01 \cdot 10^{-6} \text{ J} \end{aligned}$$

- Equations used in Energy balance calculation

Parameter	Equation
Irradiation energy, required for thermal coupling	$Q_{\text{R_th}} = Q_{\text{R}} / (1-\text{R})$
Irradiation energy, required for material evaporation	$Q_{\text{R_vap}} = Q_{\text{vap}} / (1-\text{R})$
Total irradiation energy need	$Q_{\text{t}} = Q_{\text{R_vap}} + Q_{\text{R_th}}$
Energy balance	$Q_{\text{P}} - Q_{\text{t}}$

▪ **Energy balance calculation (Stainless steel)**

Evaporation ratio	%	100	100	100	60	60	60
Pulse energy Q_p	μJ	5.00	5.00	5.00	5.00	5.00	5.00
Reflectivity R		0.30	0.20	0.10	0.30	0.20	0.10
Thermal coupling coefficient K		0.70	0.70	0.70	0.70	0.70	0.70
Thermal energy input Q_{res}	μJ	3.50	3.50	3.50	3.50	3.50	3.50
Evaporation energy Q_{vap}	μJ	1.01	1.01	1.01	0.61	0.61	0.61
Irradiated energy for thermal coupling Q_{r_th}	μJ	5.00	4.38	3.89	5.00	4.38	3.89
Required evaporation energy Q_{r_vap}	μJ	1.44	1.26	1.12	0.87	0.76	0.67
Total irradiation energy need Q_t	μJ	6.44	5.64	5.01	5.87	5.13	4.56
Energy balance	μJ	-1.44	-0.64	-0.01	-0.87	-0.13	0.44

Evaporation ratio	%	40	40	40	0	0	0
Pulse energy Q_p	μJ	5.00	5.00	5.00	5.00	5.00	5.00
Reflectivity R		0.30	0.20	0.10	0.30	0.20	0.10
Thermal coupling coefficient K		0.70	0.70	0.70	0.70	0.70	0.70
Thermal energy input Q_{res}	μJ	3.50	3.50	3.50	3.50	3.50	3.50
Evaporation energy Q_{vap}	μJ	0.40	0.40	0.40	0.00	0.00	0.00
Required thermal coupling energy Q_{R_th}	μJ	5.00	4.38	3.89	5.00	4.38	3.89
Required evaporation energy Q_{R_vap}	μJ	0.58	0.51	0.45	0.00	0.00	0.00
Total irradiation energy need Q_t	μJ	5.58	4.88	4.34	5.00	4.38	3.89
Energy balance	μJ	-0.58	0.12	0.66	0.00	0.63	1.11

References

1. Ancona, A., et al., *High speed laser drilling of metals using a high repetition rate, high average power ultrafast fiber CPA system*. Opt. Express, 2008. **16**(12): p. 8958-8968.
2. Döring, S., et al., *Microdrilling of metals using femtosecond laser pulses and high average powers at 515 nm and 1030 nm*. Applied Physics A: Materials Science & Processing, 2010. **100**(1): p. 53-56.
3. Nolte, S., et al. *High repetition rate ultrashort pulse micromachining with fiber lasers*. in *Fiber Laser Applications*. 2011: Optical Society of America.
4. Tan, B., S. Panchatsharam, and K. Venkatakrishnan, *High repetition rate femtosecond laser forming sub-10 μm diameter interconnection vias*. Journal of Physics D: Applied Physics, 2009. **42**(6): p. 065102.
5. Maiman, T.H., *Stimulated optical radiation in ruby*. Nature, 1960. **187**(4736): p. 493-494.
6. Ohse, R., *Laser application in high temperature materials*. Pure & Appl. Chem. **60**(3): p. 309-322.
7. Bäuerle, D., *Laser processing and chemistry*. 3rd ed. 2000: Springer-Verlag.
8. Hügel, H. and T. Graf, *Laser in der Fertigung (written in German)*. 2nd ed. 2009: Vieweg & Teubner. p. 404.
9. Breitling, D., A. Ruf, and F. Dausinger, *Fundamental aspects in machining of metals with short and ultrashort laser pulses*. 2004: p. 49-63.
10. Dausinger, F. *Femtosecond technology for precision manufacturing: fundamental and technical aspects*. in *Proc. SPIE 4830, 471* 2003.
11. Strickland, D. and G. Mourou, *Compression of amplified chirped optical pulses*. Optics Communications, 1985. **56**(3): p. 219-221.
12. Hertel, I.V., et al., *On the physics of material processing with femtosecond lasers*. RIKEN Rev, 2001. **32**: p. 23-30.
13. Ostendorf, A., et al. *Femtosecond versus picosecond laser ablation (Keynote Address)*. in *Proc. SPIE 5713, 1*. 2005.
14. Chichkov, B.N., et al., *Femtosecond, picosecond and nanosecond laser ablation of solids*. Applied Physics A: Materials Science & Processing, 1996. **63**(2): p. 109-115.
15. Meijer, J., et al., *Laser machining by short and ultrashort pulses, state of the art and new opportunities in the age of the photons*. CIRP Annals - Manufacturing Technology, 2002. **51**(2): p. 531-550.
16. Semerok, A., et al., *Femtosecond, picosecond, and nanosecond laser*

- microablation: Laser plasma and crater investigation*. Laser and Particle Beams, 2002. **20**(01): p. 67-72.
17. Kononenko, T.V., et al., *Comparative study of the ablation of materials by femtosecond and pico- or nanosecond laser pulses*. Quantum Electronics, 1999. **29**(8): p. 724.
 18. Le Harzic, R., et al., *Comparison of heat-affected zones due to nanosecond and femtosecond laser pulses using transmission electronic microscopy*. Applied Physics Letters, 2002. **80**(21).
 19. Tuennermann, A., S. Nolte, and J. Limpert, *Femtosecond versus picosecond Laser material processing*. Laser Technik Journal, 2010. **7**(1): p. 34-38.
 20. Jaeggi, B., et al., *Influence of the pulse duration in the ps-regime on the ablation efficiency of metals*. Physics Procedia, 2011. **12, Part B**(0): p. 164-171.
 21. Schmid, M., et al. *Processing of metals with ps-laser pulses in the range between 10ps and 100ps*. in *Laser Applications in Microelectronic and Optoelectronic Manufacturing (LAMOM) XVI*. 2011. San Francisco, California, USA: SPIE.
 22. Semerok, A., et al., *Experimental investigations of laser ablation efficiency of pure metals with femto, pico and nanosecond pulses*. Applied Surface Science, 1999. **138–139**: p. 311–314.
 23. von der Linde, D. and K. Sokolowski-Tinten, *The physical mechanisms of short-pulse laser ablation*. Applied Surface Science, 2000(154–155): p. 1–10.
 24. von Allmen, M., *Laser-beam interaction with materials*. 1987: Springer-Verlag.
 25. Bergström, D., *The absorption of laser light by rough metal surfaces*, in *Department of Applied Physics and Mechanical Engineering*. 2008, Luleå University of Technology: Luleå, Sweden.
 26. Chan, P.W., Y.W. Chan, and H.S. Ng, *Reflectivity of metals at high temperatures heated by pulsed laser*. Physics Letters A, 1977. **61**(3): p. 151-153.
 27. Kwon, H., et al., *Temperature-dependent absorptance of painted aluminum, stainless steel 304, and titanium for 1.07 μ m and 10.6 μ m laser beams*. Optics and Lasers in Engineering, 2012. **50**(2): p. 114-121.
 28. Ruf, A., *Modellierung des Perkussionsbohrens von Metallen mit kurz- und ultrakurzgepulsten Lasern (Doctoral Thesis, written in German)*, in *Fakultät für Maschinenbau der Universität Stuttgart*. 2004, Universität Stuttgart: Stuttgart, Germany.
 29. Poprawe, R., *Lasertechnik für die Fertigung (written in German)*. 1st ed. 2005: Springer-Verlag.
 30. Yahng, J.S., J.R. Nam, and S.C. Jeoung, *The influence of substrate temperature on femtosecond laser micro-processing of silicon, stainless steel and glass*. Optics and Lasers in Engineering, 2009. **47**(7-8): p. 815-820.

31. Rethfeld, B., et al., *Ultrafast dynamics of nonequilibrium electrons in metals under femtosecond laser irradiation*. Physical Review B, 2002. **65**(21): p. 214303.
32. Pedrotti, F., et al., *Optik für Ingenieure (written in German)*. 4th ed. 2008: Springer-Verlag. p. 848.
33. Bergmann, L. and C. Schäfer, *Lehrbuch der Experimentalphysik Band III Optik (written in German)*. 8th ed. 1987: Walter de Gruyter.
34. Weaver, J.H. and H.P.R. Frederikse, *Optical properties of metals and semiconductors*, in *CRC Handbook of Chemistry and Physics*. 74th Edition and subsequent printings (CRC Press, Boca Raton, Florida). p. 12-109 - 12-131.
35. Vorobyev, A.Y. and C. Guo, *Change in absorptance of metals following multi-pulse femtosecond laser ablation*. Journal of Physics: Conference Series, 2007. **59**(1): p. 579.
36. Vorobyev, A.Y. and C. Guo, *Reflection of femtosecond laser light in multipulse ablation of metals*. Journal of Applied Physics, 2011. **110**(4): p. 043102-9.
37. Kaakkunen, J.J.J., et al., *Morphology studies of the metal surfaces with enhanced absorption fabricated using interferometric femtosecond ablation*. Applied Physics A, 2009. **94**(2): p. 215-220.
38. von der Linde, D., K. Sokolowski-Tinten, and J. Bialkowski, *Laser-solid interaction in the femtosecond time regime*. Applied Surface Science, 1997. **109-110**: p. 1-10.
39. Rethfeld, B., et al., *Timescales in the response of materials to femtosecond laser excitation*. Applied Physics A: Materials Science & Processing, 2004. **79**(4): p. 767-769.
40. Fischer, A. and P. Lickschat, *Simulation der Temperaturfelder in Festkörpern infolge der Bestrahlung mit ultrakurzen Laserpulsen im Piko- und Femtosekundenbereich (written in German)*, in *Scientific Reports of 22th International Scientific Conference Mittweida*. 2012: Mittweida (Germany). p. 58-61.
41. Wellershoff, S.S., et al., *The role of electron-phonon coupling in femtosecond laser damage of metals*. Applied Physics A: Materials Science & Processing, 1999. **69**(7): p. S99.
42. Hohlfeld, J., et al., *Electron and lattice dynamics following optical excitation of metals*. Chemical Physics, 2000. **251**(1): p. 237-258.
43. Byskov-Nielsen, J., *Short-pulse laser ablation of metals: Fundamentals and applications for micro-mechanical interlocking*, in *Department of Physics and Astronomy*. 2010, University of Aarhus: Aarhus, Denmark.
44. Byskov-Nielsen, J., et al., *Ultra-short pulse laser ablation of copper, silver and tungsten: experimental data and two-temperature model simulations*. Applied Physics A: Materials Science & Processing, 2011. **103**(2): p. 447-453.

45. Schmidt, V., W. Husinsky, and G. Betz, *Ultrashort laser ablation of metals: pump-probe experiments, the role of ballistic electrons and the two-temperature model*. Applied Surface Science, 2002. **197-198**(0): p. 145-155.
46. Wellershoff, S.-S., *Untersuchungen zur Energierelaxationsdynamik in Metallen nach Anregung mit ultrakurzen Laserpulsen (written in German)*, in *Fachbereich Physik*. 2000, Freie Universität Berlin: Berlin.
47. Bukuk, O., et al., *Femtosecond laser ablation of metals and crater formation by phase explosion in the high-fluence regime*. Journal of Physics: Conference Series, 2007. **59**(1): p. 567.
48. Cheng, C. and X. Xu, *Mechanisms of decomposition of metal during femtosecond laser ablation*. Physical Review B, 2005. **72**(16): p. 165415.
49. Wu, B. and Y.C. Shin, *A simple model for high fluence ultra-short pulsed laser metal ablation*. Applied Surface Science, 2007. **253**(8): p. 4079-4084.
50. Margetic, V., *Femtosecond laser ablation*. Dissertation, 2002: p. 152.
51. Lewis, L.J. and D. Perez, *Laser ablation with short and ultrashort laser pulses: Basic mechanisms from molecular-dynamics simulations*. Applied Surface Science, 2009. **255**(10): p. 5101-5106.
52. Miotello, A. and R. Kelly, *Critical assessment of thermal models for laser sputtering at high fluences*. Applied Physics Letters, 1995. **67**(24): p. 3535-3537.
53. Miotello, A. and R. Kelly, *Laser-induced phase explosion: new physical problems when a condensed phase approaches the thermodynamic critical temperature*. Appl. Phys. A 1999. **69**: p. 67-73.
54. Xu, X., *Phase explosion and its time lag in nanosecond laser ablation*. Applied Surface Science, 2002. **197-198**: p. 61-66.
55. Martynyuk, M.M., *Phase explosion of a metastable fluid*. Sov. Phys. Tech.-Phys., 1974. **19**(793).
56. Mannion, P., et al. *Ablation thresholds in ultrafast laser micromachining of common metals in air*. in *Opto-Ireland 2002: Optics and Photonics Technologies and Applications*. 2003. Galway, Ireland: SPIE.
57. Mannion, P.T., et al., *The effect of damage accumulation behaviour on ablation thresholds and damage morphology in ultrafast laser micro-machining of common metals in air*. Applied Surface Science, 2004. **233**(1-4): p. 275-287.
58. Nedialkov, N.N., et al., *Ablation of metals by ultrashort laser pulses*. Journal of Physics D: Applied Physics, 2004. **37**(4): p. 638.
59. Mingareev, I. and A. Horn, *Time-resolved investigations of plasma and melt ejections in metals by pump-probe shadowgraphy*. Applied Physics A: Materials Science & Processing, 2008. **92**(4): p. 917-920.

60. Nolte, S., et al., *Ablation of metals by ultrashort laser pulses*. J. Opt. Soc. Am. B, 1997. **14**(10): p. 2716-2722.
61. Nedialkov, N.N., et al., *Laser ablation of iron by ultrashort laser pulses*. Thin Solid Films, 2004. **453-454**(0): p. 496-500.
62. Byskov-Nielsen, J., et al., *Ultra-short pulse laser ablation of metals: threshold fluence, incubation coefficient and ablation rates*. Applied Physics A: Materials Science & Processing, 2010. **101**(1): p. 97-101.
63. Maul, J., et al., *Onset of crater formation during short pulse laser ablation*. Applied Physics A: Materials Science & Processing, 2006. **82**(1): p. 43-47.
64. Banks, D.P., *Femtosecond laser induced forward transfer techniques for the deposition of nanoscale, intact, and solid phase material*, in *Optoelectronics Research Centre*. 2008, University of Southampton: Southampton, UK.
65. Vestentoft, K. and P. Balling, *Formation of an extended nanostructured metal surface by ultra-short laser pulses: single-pulse ablation in the high-fluence limit*. Applied Physics A: Materials Science & Processing, 2006. **84**(1): p. 207-213.
66. Birnbaum, M., *Semiconductor surface damage produced by ruby lasers*. Journal of Applied Physics, 1965. **36**(11): p. 3688-3689.
67. Rubahn, H.G. and F. Balzer, *Laseranwendungen an harten und weichen Oberflächen (written in German)*. 2005: Vieweg & Teubner 308.
68. Zhou, M., et al., *Sub-wavelength Ripple Formation on Silicon Induced by Femtosecond Laser Radiation*. Chinese Physics Letters. **26**(3): p. 037901.
69. Gottmann, J., D. Wortmann, and M. Hoerstmann-Jungemann, *Fabrication of sub-wavelength surface ripples and in-volume nanostructures by fs-laser induced selective etching*. Applied Surface Science, 2009. **255**(10): p. 5641-5646.
70. Wang, X., et al., *Femtosecond pulsed laser-induced periodic surface structures on GaN/sapphire*. Applied Surface Science, 2005. **252**(5): p. 1492-1497.
71. Hou, S., et al., *Formation of long-and short-periodic nanoripples on stainless steel irradiated by femtosecond laser pulses*. Journal of Physics D: Applied Physics, 2011. **44**(50): p. 505401.
72. Bonse, J., et al., *Femtosecond laser-induced periodic surface structures*. Journal of Laser Applications, 2012. **24**(4): p. 7.
73. Emmony, D.C., R.P. Howson, and L.J. Willis, *Laser mirror damage in germanium at 10.6 μm* . Applied Physics Letters, 1973. **23**(11): p. 598-600.
74. Emelianov, V.I. and V.N. Seminogov, *Laser excitation of coupled surface electromagnetic and acoustic waves and static surface structures in solids*. Sov. Phys. JETP, 1984. **59**(3): p. 598-604.

75. Sipe, J.E., et al., *Laser-induced periodic surface structure. I. Theory*. Physical Review B, 1983. **27**(2): p. 1141-1154.
76. Bonse, J., A. Rosenfeld, and J. Kruger, *On the role of surface plasmon polaritons in the formation of laser-induced periodic surface structures upon irradiation of silicon by femtosecond-laser pulses*. Journal of Applied Physics, 2009. **106**(10): p. 104910-5.
77. Garrelie, F., et al., *Evidence of surface plasmon resonance in ultrafast laser-induced ripples*. Opt. Express, 2011. **19**(10): p. 9035-9043.
78. Obara, G., et al., *Direct observation of surface plasmon far field for regular surface ripple formation by femtosecond laser pulse irradiation of gold nanostructures on silicon substrates*. Applied Physics Letters, 2011. **99**(6): p. 061106-061106-3.
79. Vorobyev, A.Y. and C. Guo, *Femtosecond laser-induced periodic surface structure formation on tungsten*. Journal of Applied Physics, 2008. **104**(6): p. 063523-3.
80. Reif, J., O. Varlamova, and F. Costache, *Femtosecond laser induced nanostructure formation: self-organization control parameters*. Applied Physics A: Materials Science & Processing, 2008. **92**(4): p. 1019-1024.
81. Reif, J., et al., *Self-organized regular surface patterning by pulsed laser ablation*. physica status solidi (c), 2009. **6**(3): p. 681-686.
82. Fauchet, P.M. and A.E. Siegman, *Observations of higher-order laser-induced surface ripples on 111 germanium*. Applied Physics A: Materials Science & Processing, 1983. **32**(3): p. 135-140.
83. Bensaoula, A., et al., *Micro column arrays (MCA) for thermal management of spacecraft environments*. ISSO Y2005 Annual Report, 2005.
84. Oliveira, V., F. Simões, and R. Vilar, *Column-growth mechanisms during KrF laser micromachining of Al₂O₃-TiC ceramics*. Applied Physics A: Materials Science & Processing, 2005. **81**(6): p. 1157-1162.
85. Ang, L.K., et al., *Surface instability of multipulse laser ablation on a metallic target*. Journal of Applied Physics, 1998. **83**(8): p. 4466-4471.
86. Brailovsky, A.B., S.V. Gaponov, and V.I. Luchin, *Mechanisms of melt droplets and solid-particle ejection from a target surface by pulsed laser action*. Applied Physics A: Materials Science & Processing, 1995. **61**(1): p. 81-86.
87. Dolgaev, S.I., et al., *Growth of large microcones in steel under multipulsed Nd:YAG laser irradiation*. Applied Physics A: Materials Science & Processing, 2006. **83**(3): p. 417-420.
88. Lloyd, R., et al., *Laser-assisted generation of self-assembled microstructures on stainless steel*. Applied Physics A: Materials Science & Processing, 2008. **93**(1): p. 117-122.

89. Groenendijk, M.N.W. and J. Meijer, *Surface microstructures obtained by femtosecond laser pulses*. CIRP Annals-Manufacturing Technology, 2006. **55**(1): p. 183-186.
90. Wu, P.H., et al., *Fabrication of large-area hydrophobic surfaces with femtosecond-laser-structured molds*. Journal of Micromechanics and Microengineering, 2011. **21**(11): p. 115032.
91. Wu, B., et al., *Superhydrophobic surfaces fabricated by microstructuring of stainless steel using a femtosecond laser*. Applied Surface Science, 2009. **256**(1): p. 61-66.
92. Kam, D.H., S. Bhattacharya, and J. Mazumder, *Control of the wetting properties of an AISI 316L stainless steel surface by femtosecond laser-induced surface modification*. Journal of Micromechanics and Microengineering, 2012. **22**(10): p. 105019.
93. Raciukaitis, G., et al. *Accumulation effects in laser ablation of metals with high-repetition-rate lasers*. in *High-Power Laser Ablation VII*. 2008. Taos, NM, USA: SPIE.
94. Luther-Davies, B., et al., *Picosecond high-repetition-rate pulsed laser ablation of dielectrics: the effect of energy accumulation between pulses*. Optical Engineering, 2005. **44**(5): p. 051102-051102-8.
95. Eaton, S., et al., *Heat accumulation effects in femtosecond laser-written waveguides with variable repetition rate*. Opt. Express, 2005. **13**(12): p. 4708-4716.
96. König, J., S. Nolte, and A. Tünnermann, *Plasma evolution during metal ablation with ultrashort laser pulses*. Opt. Express, 2005. **13**(26): p. 10597-10607.
97. Neuenschwander, B., et al. *Processing of metals and dielectric materials with ps-laserpulses: results, strategies, limitations and needs*. in *Laser Applications in Microelectronic and Optoelectronic Manufacturing XV*. 2010. San Francisco, California, USA: SPIE.
98. Bruening, S., et al., *Ultrafast scan techniques for 3D- μm structuring of metal surfaces with high repetitive ps-laser pulses*. Physics Procedia, 2011. **12, Part B**(0): p. 105-115.
99. Knappe, R., S. Brüning, and A. Gillner, *Kleinste Strukturen auf großen Flächen (written in German)*. Laser Technik Journal, 2011. **8**(4): p. 24-27.
100. Neuenschwander, B., et al. *Processing of dielectric materials and metals with ps laserpulses (paper M101)*. in *Proceedings of 29th Intern. Congress on Applications of Lasers & Electro-Optics (ICALEO)*. 2010. Anaheim, California, USA.
101. *Standard integrating spheres, gold*. [cited 30-05-2012]; Available from: http://www.lot-oriel.com/files/downloads/optosol/eu/standard_integrating_spheres_gold_eu.pdf.

102. Labsphere. *General purpose integrating spheres*. AQ-00001-000, Rev. 6 [cited 19/02/2013]; Available from:
<http://asumbe.eas.asu.edu/Documents/characterization/Integration%20Sphere/AQ-00001-000Rev6GeneralPurposeSpheres.pdf>.
103. Hagemann, H.J., W. Gudat, and C. Kunz, *Optical constants from the far infrared to the x-ray region: Mg, Al, Cu, Ag, Au, Bi, C, and Al₂O₃*. Journal of the Optical Society of America, 1975. **65**(6): p. 742-744.
104. *EN AW-6082 (AlMgSi1) T651*. [cited 07/05/2012]; Available from:
<http://www.haueselmann.ch/webautor-data/23/EN6082.pdf>.
105. *Aluminum 6061-T6*. [cited 07/05/2012]; Available from:
<http://asm.matweb.com/search/SpecificMaterial.asp?bassnum=MA6061t6>.
106. Wilson, J., *Thermal Diffusivity*, in *Electronics Cooling*. 2007.
107. Hering, E., R. Martin, and S. M., *Physik für Ingenieure (written in German)*. Vol. 7. 1999: Springer-Verlag 744.
108. Schmidt-Sandte, T., *Laserstrahlbasierte Entgratverfahren für feinwerktechnische Anwendungen (written in German)*, in *Fakultät für Maschinenbau und Elektrotechnik*. 2002, Technische Universität Carolo-Wilhelmina zu Braunschweig: Braunschweig.
109. Ebert, R., et al., *Rapid Microtooling mit laserbasierten Verfahren - anlagentechnische Realisierung (written in German)*. Lasermagazin, 2007.
110. Ebert, R., et al., *Rapid Microtooling mit laserbasierten Verfahren (written in German)*. Lasermagazin, 2007.
111. *Members of the Rapid Micro Tooling group with the Laser Institute at the University Mittweida (Germany): R. Ebert, U. Loeschner, A. Streek, J. Schille, T. Suess, L. Hartwig, S. Kloetzer, F. Ullmann*. 2006 -2011 [cited 01/06/2012]; Available from:
http://laz.htwm.de/43_rapidmicro/default.asp?content=%2F43%5Frapidmicro%2F20%5Fmitglieder%2Ehtml.
112. *ISO 11146-3, Lasers and laser-related equipment – Test methods for laser beam parameters – Beam width, divergence, angle and beam propagation factor - Part 3: Intrinsic and geometrical laser beam classification, propagation and details of test methods*.
113. Carr, K.F., *OPTICAL MATERIALS - Silicon carbide mirrors benefit high-speed laser scanning - Light weight, high stiffness, and good thermal conductivity make silicon carbide an ideal substrate for galvanometer mirrors in high-speed laser scanning systems*. Laser Focus World, 2008. **44**(4): p. 102-104.
114. *SKM DCAM 2009 (Ver. 5.2.1.0 Unicode)*. [cited 28-03-2013]; Available from:
<http://www.skm-dcam.com/>.
115. Stuart, B.C.D., et al., *Optical ablation by high-power short-pulse lasers*. 1996: Optical Society of America.

116. Jee, Y., M. F. Becker, and R.M. Walser, *Laser-induced damage on single-crystal metal surfaces*. J. Opt. Soc. Am. B, 1988. **5**(3): p. 648-659.
117. Regelskis, K., G. Raciukaitis, and P. Gecys. *Ripple formation at laser ablation of chromium thin film*. in *Advanced Optical Materials, Technologies, and Devices*. 2006: SPIE.
118. Baudach, S., J. Bonse, and W. Kautek, *Ablation experiments on polyimide with femtosecond laser pulses*. Applied Physics A: Materials Science & Processing, 1999. **69**(7): p. S395-S398.
119. Daminelli, G., J. Krüger, and W. Kautek, *Femtosecond laser interaction with silicon under water confinement*. Thin Solid Films, 2004. **467**(1&2): p. 334-341.
120. Cheng, J., et al., *Single-pulse drilling study on Au, Al and Ti alloy by using a picosecond laser*. Applied Physics A: Materials Science & Processing, 2009. **95**(3): p. 739-746.
121. Liu, J.M., *Simple technique for measurements of pulsed Gaussian-beam spot sizes*. Opt. Lett., 1982. **7**(5): p. 196-198.
122. Lickschat, P., et al., *Comparative study on microstructuring of steel using pico- and femtosecond laser pulses*, in *Proceedings of ICALEO - 31st International Congress on Applications of Lasers & Electro-Optics*. 2012: Anaheim, Ca. (USA). p. 1261-1268.
123. Sallé, B., et al., *Femtosecond and picosecond laser microablation: ablation efficiency and laser microplasma expansion*. Applied Physics A, 1999. **69**(1): p. 381-383.
124. Bejan, D., *Ballistic electron distribution for hot electron in metals*. Romanian Reports in Physics, 2006. **58**(2): p. 149.
125. Colombier, J.P., et al., *High shock release in ultrafast laser irradiated metals: Scenario for material ejection*. Physical Review B, 2007. **75**(10): p. 104105.
126. Li, Z.L., et al., *Direct patterning in sub-surface of stainless steel using laser pulses*. Opt. Express, 2010. **18**(15): p. 15990-15997.
127. Anisimov, S.I., B.L. Kapeliovich, and T.L.P.m. . *Electron emission from metal surfaces exposed to ultrashort laser pulses*. Soviet Physics JETP 1974. **39**(375).
128. Dyer, P.E., *Excimer laser polymer ablation: twenty years on*. Applied Physics A, 2003. **77**(2): p. 167-173.
129. Lazov, L. and N. Angelov, *Physical model about laser impact and metals and alloys*. Contemporary Materials I-2, 2010: p. 124–128
130. Vorobyev, A.Y., et al. *Thermal energy coupling to Al in ablation with ms-, ns-, and fs-laser pulses*. in *Laser and Fiber-Optical Networks Modeling, 2004. Proceedings of LFNM 2004. 6th International Conference on*. 2004.
131. Vorobyev, A.Y. and C. Guo, *Direct observation of enhanced residual thermal*

- energy coupling to solids in femtosecond laser ablation*. Applied Physics Letters, 2005. **86**(1): p. 011916-3.
132. Vorobyev, A.Y. and C. Guo, *Enhanced energy coupling in femtosecond laser-metal interactions at high intensities*. Opt. Express, 2006. **14**(26): p. 13113-13119.
133. Vorobyev, A.Y., *Reflection of pulsed ruby laser radiation by a copper target in air and in vacuum*. Soviet Journal of Quantum Electronics, 1985. **15**(4): p. 490.
134. Kahaly, S., et al., *Near-complete absorption of intense, ultrashort laser light by sub- λ gratings*. Physical Review Letters, 2008. **101**(14): p. 145001.
135. Tran, D.V., et al., *Quantification of thermal energy deposited in silicon by multiple femtosecond laser pulses*. Opt. Express, 2006. **14**(20): p. 9261-9268.
136. Tran, D.V., et al., *Direct observation of the temperature field during ablation of materials by multiple femtosecond laser pulses*. Applied Surface Science, 2007. **253**(17): p. 7290-7294.
137. Takahashi, Y., T. Azumi, and Y. Sekine, *Heat capacity of aluminum from 80 to 880 K*. Thermochemica Acta, 1989. **139**(0): p. 133-137.
138. Römer, G.R.B.E., et al., *On the formation of laser induced self-organizing nanostructures*. CIRP Annals - Manufacturing Technology, 2009. **58**(1): p. 201-204.
139. Li, L., et al., *Large-area laser nano-texturing with user-defined patterns*. Journal of Micromechanics and Microengineering, 2009. **19**(5): p. 054002.
140. Boulais, É., R. Lachaine, and M. Meunier, *Plasma-mediated nanocavitation and photothermal effects in ultrafast laser irradiation of gold nanorods in water*. The Journal of Physical Chemistry C. **117**(18): p. 9386-9396.
141. Kietzig, A.-M., S.G. Hatzikiriakos, and P. Englezos, *Patterned superhydrophobic metallic surfaces*. Langmuir, 2009. **25**(8): p. 4821-4827.
142. Engel, A., et al., *3D-Mikrostrukturierung von Metallen und Hartstoffen mit Femtosekundenlaserstrahlung (written in German)*. Scientific Reports of 20th IWKM – International Scientific Conference Mittweida (Germany), 2009. **Nr. 4**: p. 97-99.
143. Russbuedt, P., et al., *Compact diode-pumped 1.1 kW Yb:YAG Innoslab femtosecond amplifier*. Opt. Lett., 2010. **35**(24): p. 4169-4171.
144. Exner, H., et al., *High speed laser micro processing using high brilliance continuous wave laser radiation*. JLMN-Journal of Laser Micro/Nano-engineering 2012. **7**(1).
145. Nusser, K., *Thermische Simulation von temperaturkritischen Systemen (written in German)*, in *Lehrstuhl für Informatik 10 (Systemsimulation)*. 2010, Friedrich-Alexander-Universität Erlangen-Nürnberg. p. 40.